Catalytic conversion of biomass-derived compounds into specialty chemicals and diesel fuel precursor molecules

By: Paolo A. Cuello Peñaloza

A dissertation submitted in partial fulfillment of

the requirements for the degree of

Doctor of Philosophy

(Chemical Engineering)

at the

UNIVERSITY OF WISCONSIN-MADISON

2022

Date of final oral examination: 4/13/2022

This dissertation is approved by the following members of the Final Oral Committee:

George W. Huber, Professor, Chemical and Biological Engineering Department

James A. Dumesic, Professor, Chemical and Biological Engineering Department

Manos Mavrikakis, Professor, Chemical and Biological Engineering Department

Ive Hermans, Professor, Chemistry Department

David Rothamer, Professor, Mechanical Engineering Department

Abstract

Biomass offers a plethora of opportunities to obtain useful and unique products in a sustainable way, be it chemicals with specialty applications, or molecules that can be blended into our everyday fuels, potentially improving their desired properties. In this work, we study two processes involving the conversion of biomass-derived feedstocks into specialty chemicals and diesel fuel precursors using suitable solid catalysts for each application.

In Chapters 2 and 3, we delve into the production of hexane-1,2,5,6-tetrol from levoglucosanol, which is ultimately obtained from a cellulose direct derivate, and a potential application as a polymer precursor. In Chapter 2, we obtain kinetic information for the conversion of levoglucosanol into the polyol using a Pt-WO_x/TiO_2 catalyst at industrially relevant concentrations (10 – 30wt% reactant in water), showing that with this catalyst we can obtain selectively our product of interests, and also preserve over 90% of the reactant stereocenters. We also demonstrate the relative stability of this catalyst compared to what is known in literature, and its regenerability as well. In Chapter 3, we show a potential application for hexane-1,2,5,6-tetrol in the synthesis of tetrol-boronate copolymers when benzenediboronic acids are used. We prove that a facile synthesis is possible at room temperature with various solvents, and demonstrate that the properties of the polymers are impacted by the choice of a solvent, and the diastereomeric excess of the reactant, managing to obtain a first-known case of a chiral polymer when 98% d.e. (*S*,*R*)-hexane-1,2,5,6-tetrol is used.

In Chapters 4 and 5, we study the selective conversion of ethanol into larger molecules that can be ultimately converted into compounds that can be blended into diesel by different methods when MgAl mixed metal oxide catalysts that have very low loadings of Cu are used. In Chapter 4, we

demonstrate that when Cu loadings less than 0.6wt% are used in MgAl catalysts, very high diesel fuel precursor selectivities may be obtained, with the most significant products being larger alcohols and aldehydes, followed by large esters, and relatively minor amounts of ethyl acetate. We proved that changing the properties of the MgAl support does not greatly impact the performance of the catalyst, instead we found that the loading of Cu is the determinant factor in catalyst performance due to Cu acting more as a promoter of MgAl acid-base chemistry than as an actual catalyst for the Guerbet coupling reaction. The presence of Cu in low amounts also enables the selective production of esters with 6 or more carbons over ethyl acetate. The studied catalysts also promoted high product alcohol linearity, and the alcohol selectivity per carbon number fitted the Schultz-Flory distribution, showing that alcohol growth is dictated by chain growth behavior. In Chapter 5, we studied the performance of a single low Cu loading MgAl catalyst at different contact times, performed tests at varying ethanol-to-hydrogen partial pressure ratios, and performed cofeed studied of ethanol with acetaldehyde and ethyl acetate in order to elucidate the reaction network of ethanol oligomerization to larger oxygenates. We found that selectivity to higher alcohols was greater towards alcohols at all conversions, and alcohols exhibit chain-growth at all contact times. We found that ester and ketone selectivity increase with conversion, with their sizes becoming larger with conversion as well. Esters are series products from alcohols and aldehydes. Finally, we demonstrated that higher linear alcohols will be more selective to esters that ethanol, and that branched alcohols feeds may form esters selectively.

Finally, in Chapter 6, we cover the conclusions from all the performed studies, and provide an outlook on future research avenues that enable the effective conversion of biomass-derived feedstocks into products of added value using solid catalysts.

Acknowledgements

Going through the doctorate program of Chemical Engineering at the University of Wisconsin-Madison has been an amazing and highly enriching experience for me these last five years. I experienced world-class education and guidance from the top researchers of my field and made some good friends and family along the way. I have been able to prove myself as a man, as a scientist, and as a person of faith who believes I can accomplish anything through Him who strengthens me. I have witnessed how the process trained me to become a person capable of contributing to society using the best of my capabilities to produce knowledge that can transform the way we do things. I also learned that to do this, I needed to transform the way I think and approach things, and to know that I cannot accomplish these things or any meaningful endeavor alone, but only in cooperation with people sharing a common goal.

After 5 years of studies, I am very grateful to have had professors George W. Huber and James A. Dumesic as my advisors. With their guidance, my very thought process was transformed, and I learned how to think from the fundamental scientific principles to ask the appropriate questions to solve the problems I researched, and how to find the answers with a focus on practical applications of such scientific ideas.

I am also grateful to former members of the Huber and Dumesic Labs for useful discussions and help on my research. I would like to thank Professor Siddarth H. Krishna for his guidance in my first and second year as a PhD student, and for his collaboration in my publications from this research. I would like to thank Dr. Mario de Bruyn as well for his guidance and help in my first project, as well as for the nice, deep conversations we had during his time here at UW-Madison. I

would also like to thank Professor Nathaniel M. Eagan for his guidance during my second year, and his valuable input on the development of my second research project.

I would like to acknowledge the Exxon Mobil Research and Engineering Company (EMRE) for their funding in the Ethanol Oligomerization to distillate-range fuels project that I took part on as my second PhD research project, as part of the larger Catalytic Technologies for Production of Distillate Fuels from Biomass project funded by EMRE. I especially thank Dr. Michael P. Lanci for leading the project, and for the many useful discussions we had during our monthly meetings. I thank Dr. Yi Du for her collaboration in catalyst synthesis and for her advice. I thank Dr. Chenrong Wang for his useful advice and help in quantification techniques, and fellow past and present Huber Group members Dr. Peter H. Galebach, Dr. Alvin Jonathan, Anthony Anderson, and Raka G. Dastidar for the useful discussions we had about my research in the framework of the EMRE project we were part of.

I would also like to acknowledge the Department of Energy – Vehicle Technology Office (DOE-VTO) for their funding of the Ethanol Oligomerization to distillate-range fuels project based upon work supported by the U.S. Department of Energy's Office of Energy Efficiency and Renewable Energy (EERE) under the Bioenergy Technologies Office, Co-optimization of Fuels and Engines (Co-optima) initiative award number DE-EE0008480 (the views expressed herein do not necessarily represent the views of the U.S. Department of Energy or the United States Government.). I would like to thank Professor David Rothamer for leading the project discussions, and Emmanuel Canales and Dr. Juan Restrepo-Florez for collaborating closely with me in this project and for exchanging and discussing ideas. I would like to thank Professor Christos Maravelias, Professor Sage Kokjohn, Dustin Witkowski, Taylor Ross, and Srinath Subramanian for the useful discussions in the framework of the DOE-VTO project.

In addition, I am grateful for the present Huber and Dumesic fellow lab members for their useful input and exchange of ideas. I would also like to acknowledge and thank the members of the 2022 class I am part of for their companionship and help throughout my journey. I would like to thank Professor Manos Mavrikakis and Professor Ive Hermans for serving as part of several of my committees, including the present one. I also thank Professor Hermans for letting me use his lab facilities and collaborate with his students for the projects I worked with. I would like to thank Shao-Chun Wang and Edgard Rodriguez-Lebron for their help in characterization of materials.

I would like to thank the S.W. Bailey X-ray Diffraction Laboratory in the Department of Geoscience at the University of Wisconsin-Madison for use of their Rigaku Rapid II instrument. I would like to thank the Magnetic Resonance Facility in the Chemistry Department of the University of Wisconsin-Madison for use of the Bruker Avance III 500 gifted by Paul J. Bender.

I would like to acknowledge and thank the people who were with me and helped me in different stages of my journey in the PhD outside of the lab, bringing joy to my life and help when it was very much needed. I thank my family and friends who were with me here in Madison, as well as from a distance in Colombia. I am grateful to my mother Elizabeth for always lending her ear to me and for her wise counsels, and to my father Jorge for his very pointed and wise advice. I am grateful to my sister Isabella for always remembering my best qualities and for knowing I am within reach even if I am immersed in my daily occupations. I am also grateful to my brother Jorge Ivan for being there for the family back in Colombia.

I would also like to acknowledge the person who changed my world and became my wife, my most needed companion, and the source of my best joys to date. I am grateful to Rose for her unconditional love and affection, for the wonderful moments, for listening to me every day since

we met, for putting up with my silliness and with my long research talks in the car, for loving me and giving the best of herself every day.

And the best for last, I would like to acknowledge and give my thanks and my utmost praise to the one who thought of me before I was born, who gave me everything I have today, who never, ever disappoints, and whose unrelenting love I get to experience every day of my life, to whom I dedicate my life and works, and who I hope to be with in Eternity. Deo Omnis Gloria!

Table of Contents

List of Figures

List of Tables

Chapter 1. Introduction

1.1 Valorization of biomass-derived molecules by catalytic conversion to added value products

Biomass is an excellent source of platform molecules that can be used to obtain useful compounds depending on the functionality of the former and the application desired for the latter. Biomass is made up of cellulose, hemicellulose, and lignin accounting for over 90% of its total weight depending on the biomass source[1]. Consequently, the carbon-to-oxygen ratio in biomass is close to 1.[2] This means that depolymerized biomass is rich in both carbon and oxygen functionalities, that enable the obtention of molecules that would be much harder to produce from fossil fuels, that are mostly deoxygenated.[3] On the other hand, industrial-scale processes to produce daily use chemicals and fuels are based on oil-based feedstocks, processes that exhibit high carbon efficiency and low labor intensity, whereas those of biomass-based processes normally involve several processing steps and higher labor costs, meaning that most biomass-based products on their own would be outcompeted by oil-based counterparts.[4] However, increasing pushes for more sustainable processes and projected increased demands offer new opportunities for biomass-derived processes, especially if the molecules produced greatly resemble those obtained by fossil fuels,[5] or are able to use similar process designs.[6,7]

Conversion of biomass typically involves C-C, C-O and/or C-H bond formation or bond breaking reactions. For instance, cellulose may be depolymerized to monomeric sugars[8,9], that in turn may be converted to a variety of useful end products by dehydration as is the case of 5-(hydroxymethyl)furfural (HMF) from fructose[10] or by isomerization of levoglucosenone (LGO)[11], hydrogenation as in the case of HMF derivates such as tetrahydrofuran dimethanol (THFDM) or

The contents of this Chapter are partially adapted from the references detailed in Chapters 2 through 5.

those obtained by consecutive LGO hydrogenation that will be presented later. Other examples include oxidation of HMF to polymer precursor 2,5-furandicarboxylic acid (FDCA)[12], hydrodeoxygenation of monomeric sugars to lower chain oxygenates[13–15], or hydrogenolysis as in the case of oxygen-rich polyols derived from sugars to consecutively lower containing -OH alcohols such as hexanetetrols,[16–18] hexanetriols[13,14,16,19], hexanediols,[14,15,20] or hexanols[21]. Finally, biomass may be completely converted to small molecules that may be used to form larger useful molecules, as occurs in the conversion of sugarcane or corn bagasse into ethanol [22,23], which in turn can be directly blended into gasoline[24] or further upgraded into larger and/or more useful molecules by different processes [5,25–29]. One of these processes will also be studied in this work.

1.2. Conversion of biomass-derived levoglucosenone into useful platform chemicals

Levoglucosenone (LGO) is directly derived from cellulose via acid-catalyzed processes[30] or in an industrial level by mild-pyrolysis [31–33], and can be converted to several potentially useful products. Figure 1-1 shows the compounds that have been derived from LGO, all of them with potential or proven applications as solvents[34–36], polymer precursors[37] or pharmaceutical compounds or additives[38,39]. The European Union (EU) has shown increasing interest in developing green technologies to generate end-user high value chemicals, and LGO-based products are one of the most attractive options, as shown by the support of EU in the production of LGO-based renewable chemicals such as dihydrolevoglucosenone (Cyrene) for instance in the framework of the ReSolute Project[32,40] intended to replace toxic solvents with sizable market sizes such as N-methyl-2-pyrrolidone (US$ 956.7 Mn in 2022)[41] or dimethylformamide (US$ 687.8 Mn in 2021)[42] that are under increasing regulatory pressure.

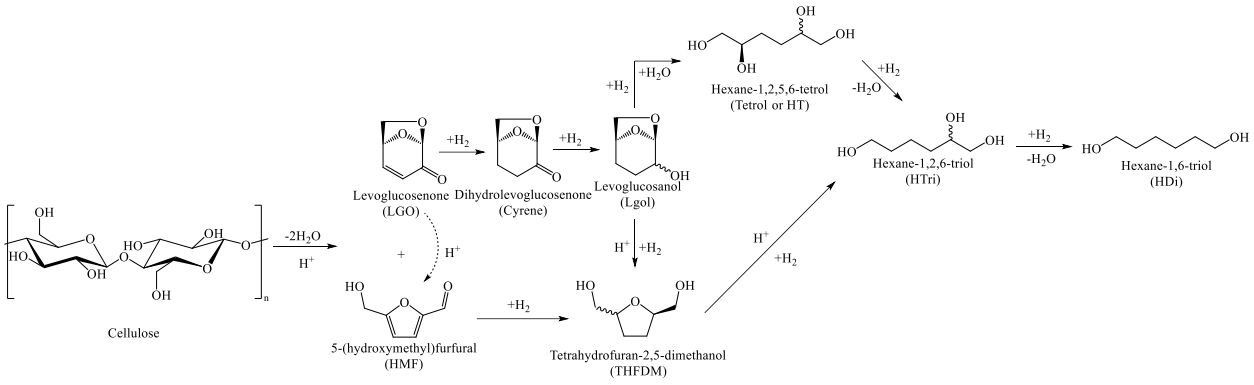

Figure 1-1. Several platform molecules derived from cellulose.

Other derivates include cyclic polyols such as tetrahydrofuran-2,5-dimethanol (THFDM), or lineal polyols such as hexane-1,2,5,6-tetrol (tetrol or HT), hexane-1,2,6-triol (HTri) and hexane-1,6-diol (HDi). HDi has an already established market as a feedstock for polyurethanes (US$ 70.67 Bn in 2020), and there is increasing demand for renewably sourced and easily recyclable polymers, including polyurethanes in the framework of circular economy which would theoretically enable a more sustainable product design and more responsible resource management[43] by using as little resources for as long as possible[44]. An example of this model can be found in the RENUVA™ program by The Dow Chemical Company in the company in cooperation with several partners recover used mattresses and use chemical recycling techniques to obtain polyols that can be reused in polyurethane production for other applications[45]. HTri[46] and THFDM can also serve as solvents and polymer precursors, but their use is not nearly as widespread as HDi. Tetrol on the other hand is a promising molecule for the production of chiral polymers[37] and asymmetric synthesis due to exhibiting two stereocenters. This feature will be explored in this work in the production of tetrol-boronate copolymers in Chapter 3. Finally, HMF applications are more known nowadays, as it is an already established platform molecule for the production of other useful polymer precursors

such as FDCA[47], and some of the aforementioned, or molecules with applications as biofuels such as 2,5-dimethylfuran.[48]

1.3. Conversion of ethanol to distillate-range fuels by Guerbet coupling and acid-catalyzed bimolecular dehydration

Ethanol is the most abundantly produced liquid fuel derived from biomass, accounting for 86% of total biofuel production in the United States (US)[5]. Ethanol has been widely used as a blendstock for gasoline-powered vehicles, with most gasoline blends containing 10% ethanol nowadays,[24] with blends containing up to 15% ethanol content being currently allowed by the US government on vehicles made on 2001 or later,[49] serving also as a partial fuel supply for light-duty applications in the event of fuel supply chain disruptions.[50] However, due to its thermodynamic and physical properties, it is not possible to blend ethanol into distillate-range fuels (e.g. jet and diesel fuels). It is projected that in the next 20 years, future demand for gasoline will decrease and demand for C_{8-22} distillate range-fuels such diesel and jet fuels will increase[51], as shown in Figure 1.2. On the other hand, ethanol production in the US has been increasing for the last two decades, as shown in Figure 1.3. Therefore, it is reasonable to attempt to satisfy the projected increased demand of distillate-range fuels with the readily available ethanol supply. Since ethanol itself cannot be blended into these fuels, several alternatives have been proposed in order to upgrade ethanol into larger sized molecules that can be used for this end. Some of these alternatives are summarized in Figure 1.4.[5] Ethanol may be either dehydrated to ethylene which then may undergo oligomerization to larger olefins,[52,53] or may be upgraded directly into larger oxygenates, particularly via Guerbet coupling mechanisms[25,26,54,55] that enable the obtention of higher alcohols

and aldehydes that may be blended into jet or diesel fuel depending on their size, or may be dehydrated to olefins and be subjected to additional oligomerization.[56]

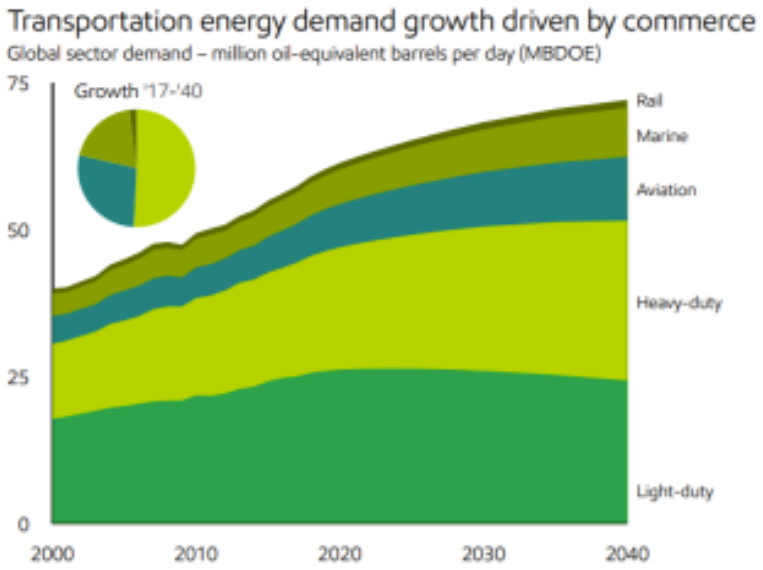

Figure 1-2. Projected fuel demands for 2040.[50] Reprinted from ExxonMobil 2019 Outlook for Energy: A perspective to 2040. ExxonMobil Copyright 2019.

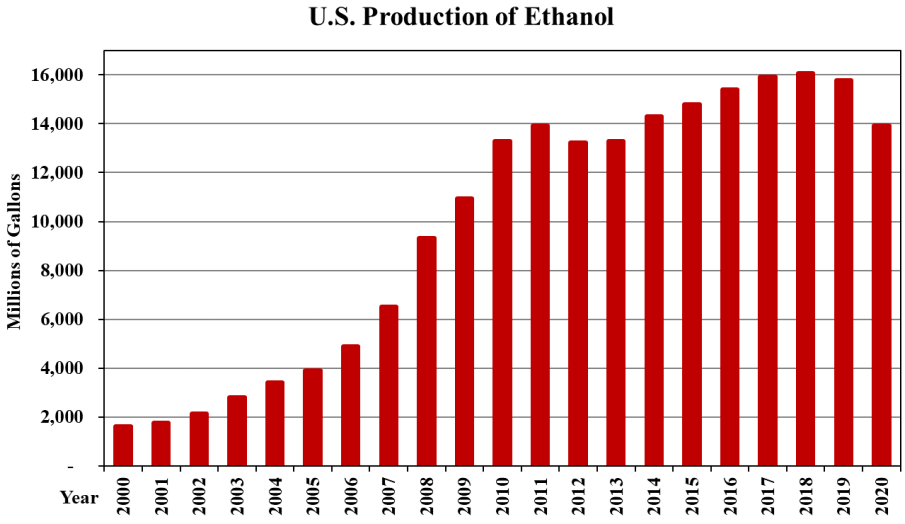

Figure 1-3. U.S. Ethanol production during the last two decades.[56] Data published by U.S. Energy Information Administration (EIA).

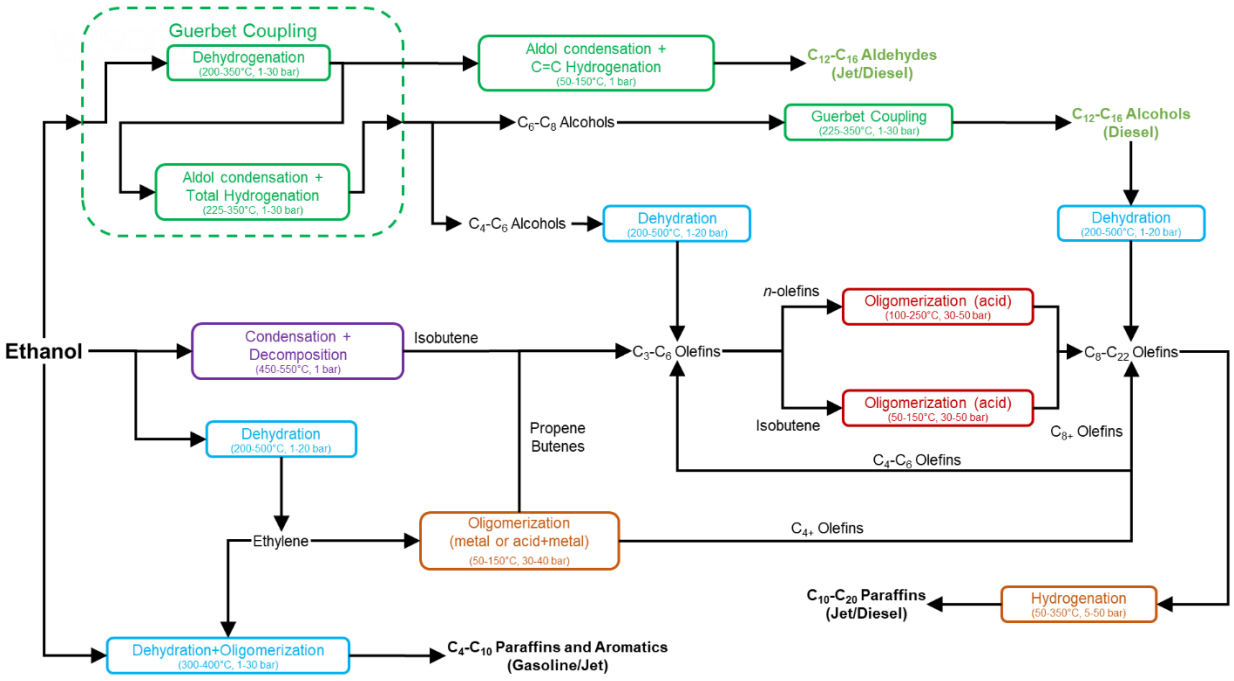

Figure 1-4. Different ethanol to distillate-range fuels synthesis routes.[5] Reprinted from the following reference with permission of Springer Nature: Eagan, N. M.; Kumbhalkar, M. D.; Buchanan, J. S.; Dumesic, J. A.; Huber, G. W. Chemistries and Processes for the Conversion of Ethanol into Middle-Distillate Fuels. *Nat. Rev. Chem.* 2019, 3 (4), 223–249. Copyright 2019.

Guerbet coupling chemistry to upgrade ethanol into larger alcohols is shown in Figure 1.5. It consists of an initial dehydrogenation of an alcohol into its corresponding aldehyde, which then is deprotonated on its α-C. The deprotonated aldehyde then undergoes aldol condensation by performing a nucleophilic attack to a neighboring adsorbed electrophilic aldehyde forming an aldol intermediate that undergoes dehydration to form an alkenal, which is finally successively hydrogenated to form a higher alcohol. Furthermore, some research [58–60] suggests that traditional Guerbet coupling might not be the only mechanism by which an alcohol chain may be grown, as the alcohols themselves may be able to perform a nucleophilic attack to a neighboring alcohol or aldehyde species to form a higher alcohol or aldehyde without forming an aldol intermediate.

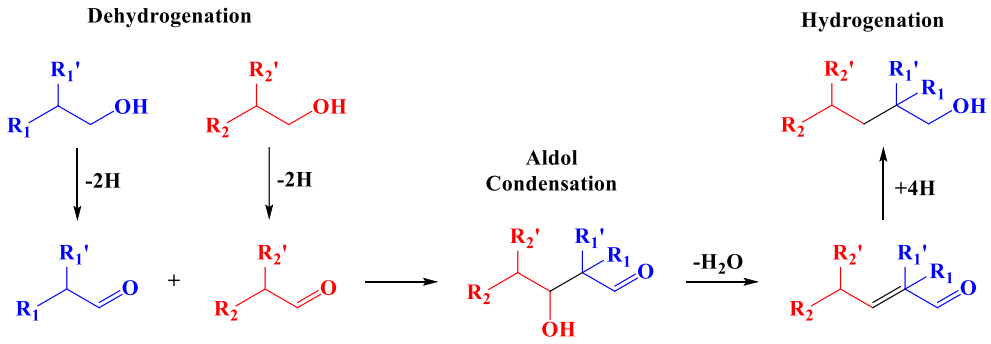

Figure 1-5. Traditional Guerbet coupling of alcohols via Aldol-condensation.[60] Adapted from the following reference with permission from the American Chemical Society: Eagan, N. M.; Lanci, M. P.; Huber, G. W. Kinetic Modeling of Alcohol Oligomerization over Calcium Hydroxyapatite. *ACS Catal.* 2020, 10 (5), 2978–2989. Copyright 2020 American Chemical Society.

Another point to consider is the suitability of larger alcohol species as potential jet or diesel blends when compared to similarly-sized molecules of other functionalities. Diesel fuel is mostly comprised of paraffins that range from 10 to 22 carbons long. Paraffins are apolar, whereas alcohols have some polarity. On the other hand, ethers of similar sizes than alcohols resemble more traditional diesel molecules than the alcohols themselves, and this is reflected in their properties being more suitable for diesel fuel applications than those of alcohols when compared at the same sizes. [25] Therefore, in prior research done in the last five years, our group proposed and patented a process[56] by which ethanol may be upgraded into diesel and jet fuel in three different stages, as shown in the scheme in Figure 1.6. First, higher alcohols are produced from ethanol via Guerbet coupling using appropriate acid-base or metal-acid-base catalysts, then the larger alcohols undergo bimolecular dehydration in a second stage using acid catalysts to form diesel-range ethers. Finally, any olefin byproducts are oligomerized in a third oligomerization reactor to produce jet fuel range molecules. Our group also found that only linear alcohols are suitable for upgrading into ethers, as β-branched alcohols will undergo unimolecular dehydration to form branched olefins with selectivities as high as 80%, whereas linear alcohols undergo bimolecular dehydration to ethers with up to 95% selectivity.[25]

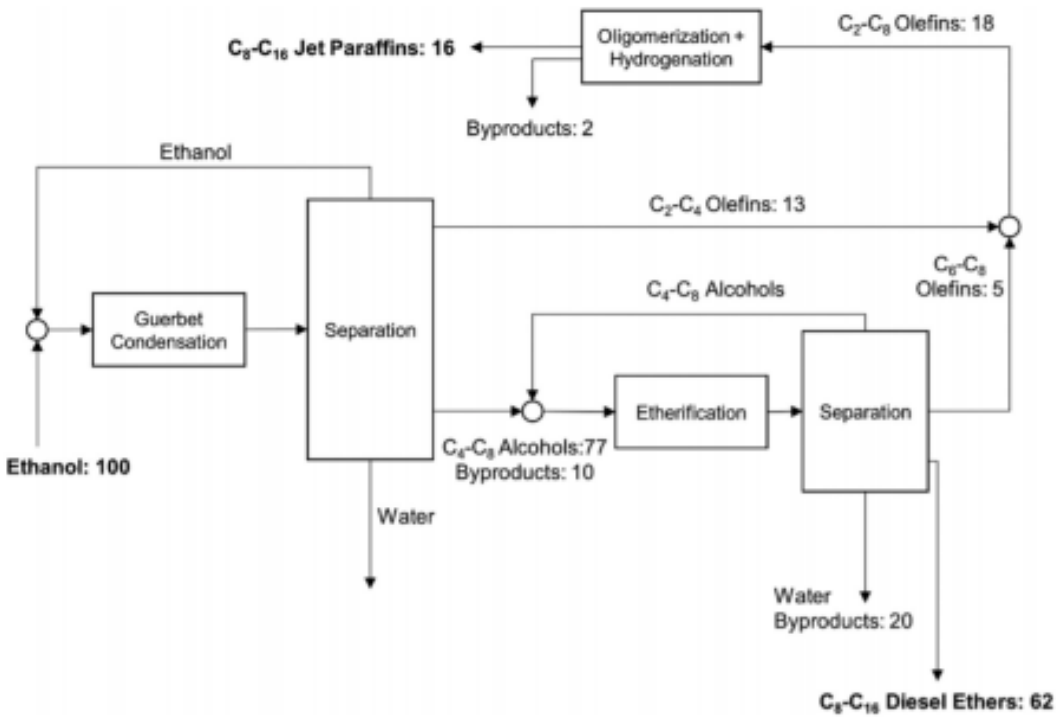

Figure 1-6. Ethanol to distillate range process involving production of larger alcohols by Guerbet coupling followed by acid-catalyzed bimolecular dehydration (etherification) and olefin oligomerization and hydrogenation. [25,55] Reprinted from the following reference with permission from the Royal Society of Chemistry: Eagan, N. M.; Moore, B. M.; McClelland, D. J.; Wittrig, A. M.; Canales, E.; Lanci, M. P.; Huber, G. W. Catalytic Synthesis of Distillate-Range Ethers and Olefins from Ethanol through Guerbet Coupling and Etherification. Green Chem. 2019, 21 (12), 3300–3318. Copyright 2019.

It is therefore essential to find catalysts that convert ethanol into larger alcohols at sufficiently high rates to facilitate process scale-up. Moreover, the catalyst will also have to be selective towards linear alcohols, as branching will 1) promote olefin formation in the etherification stage, and 2) branched alcohols are incapable of undergoing further coupling, as they cannot act as nucleophiles anymore[61] since their β-C (or the α-C of their aldehydes) will not be able to form the two bonds required for coupling, as the carbon in mention is tertiary and not secondary. Moreover, while the branched alcohol/aldehyde may be able to act as an electrophile, the carbon bound to the oxygen is sterically hindered by the vicinal carbon, making further coupling rates negligible compared to side-reaction rates such as dehydration. Therefore, in order to obtain increasing larger and linear

alcohols, a catalyst that promotes events in which ethanol (or acetaldehyde) acts as a nucleophile or decrease the events in which ethanol/acetaldehyde is attacked is required, since only when ethanol/acetaldehyde perform a nucleophilic attack may a larger alcohol be formed, as shown in Figure 1.7.

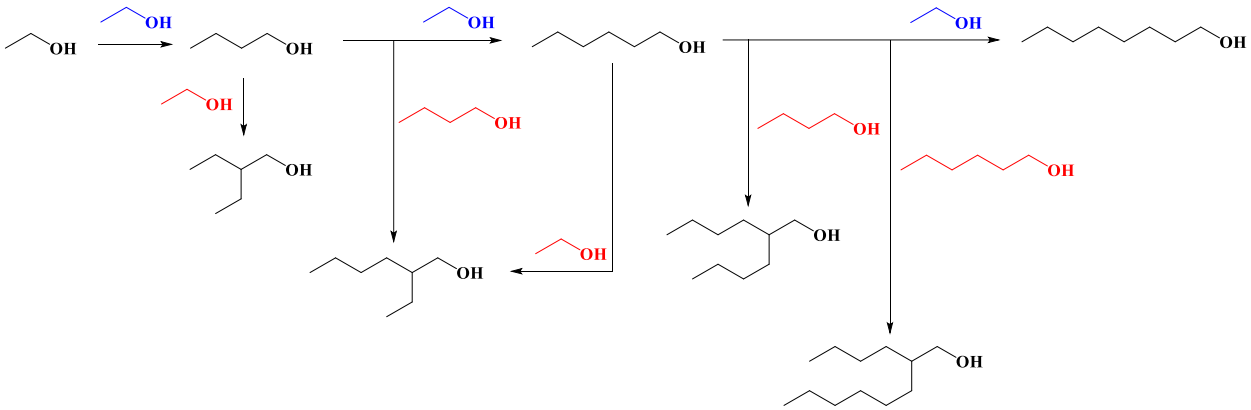

Figure 1-7. Chain-growth of higher alcohols derived from ethanol.

1.4. Scope of this work

This work is essentially divided in two major components. The first component consists in the production of specialty platform molecules and/or polymer precursors from cellulose-derived biomass and immediate applications. Chapter 2 of this work will cover a one-pot selective production of hexane-1,2,5,6-tetrol, from levoglucosanol under industrially-relevant conditions, namely high concentrations (up to 30wt% feeds). Kinetic and stability studies were carried out using a bifunctional Pt-WO_x/TiO_2 catalyst that has been found to be active, selective and relatively stable in other similar reactions[14,15]. The goal of this research is to show the feasibility of selective production of biomass-derived compounds in a single reaction stage at conditions applicable to eventual scaling up of process. A second stage of this research consisted in a facile synthesis and

characterization of polymers using the tetrol as one of the co-monomers at ambient conditions, showing an immediate application of the produced molecule as a polymer precursor with interesting chiral and structural properties. This latter research is explored in Chapter 3.

The second component of the research presented in this Thesis consists of the production of diesel-range precursor molecules from ethanol. Namely, the selective production of larger, linear alcohols from ethanol using Cu/Mg_xAlO_y mixed metal oxide catalysts with very low Cu loadings, as there is recent patent literature[62] that suggests that by using very low Cu loadings on Mg_xAlO_y, it would increase the rate of alcohol coupling reactions, while suppressing important side-reactions present at typical Cu loadings (>1wt%) such as esterification to ethyl acetate and ketone formation to acetone, 2-butanone and C_{5+} ketones.[63] Chapter 4 will cover the use of such mixed metal oxide catalysts with varying properties, and their impact on product selectivity in the ethanol conversion to larger oxygenate species, termed ethanol oligomerization from now on. We also show the nature of the Cu active sites involved, and how the addition of strictly low Cu amounts makes the Mg_xAlO_y component of the catalyst selective towards higher alcohols and higher esters (instead of ethyl acetate). Chapter 5 will explore the performance of a single Cu/Mg_xAlO_y catalyst formulation in the ethanol oligomerization reaction at different contact times and ethanol-to-hydrogen inlet partial pressures, as well as with acetaldehyde and ethyl acetate cofeed to the ethanol feed, elucidating the reaction network for ethanol with this catalyst, showing how the chain growth of the alcohols proceed, as well as the relevant termination reactions for molecular chain growth. Also, the potential uses of this catalyst in the selective formation of larger esters from alcohols different than ethanol are demonstrated. Finally, Chapter 6 will show the general conclusions and future directions derived from both major components of this thesis, and Chapter 7 will serve as an appendix containing a collection of additional information for Chapters 2 through 6.

1.5. References

(1) U.S. DOE. Lignocellulosic Biomass for Advanced Biofuels and Bioproducts: Workshop Report 2015. *U.S. Department of Energy Office of Science* **2015**, *DOE/SC-0170*.

(2) Vassilev, S. V.; Baxter, D.; Andersen, L. K.; Vassileva, C. G. An Overview of the Chemical Composition of Biomass. *Fuel* **2010**, *89* (5), 913–933. https://doi.org/10.1016/j.fuel.2009.10.022.

(3) Ringen, S.; Lanum, J.; Miknis, F. P. Calculating Heating Values from Elemental Compositions of Fossil Fuels. *Fuel* **1979**, *58* (1), 69–71. https://doi.org/10.1016/0016-2361(79)90056-5.

(4) Popp, J.; Kovács, S.; Oláh, J.; Divéki, Z.; Balázs, E. Bioeconomy: Biomass and Biomass-Based Energy Supply and Demand. *New Biotechnology* **2021**, *60*, 76–84. https://doi.org/10.1016/j.nbt.2020.10.004.

(5) Eagan, N. M.; Kumbhalkar, M. D.; Buchanan, J. S.; Dumesic, J. A.; Huber, G. W. Chemistries and Processes for the Conversion of Ethanol into Middle-Distillate Fuels. *Nature Reviews Chemistry* **2019**, *3* (4), 223–249. https://doi.org/10.1038/s41570-019-0084-4.

(6) Wilson, A. N.; Dutta, A.; Black, B. A.; Mukarakate, C.; Magrini, K.; Schaidle, J. A.; Michener, W. E.; Beckham, G. T.; Nimlos, M. R. Valorization of Aqueous Waste Streams from Thermochemical Biorefineries. *Green Chem.* **2019**, *21* (15), 4217–4230. https://doi.org/10.1039/C9GC00902G.

(7) Takkellapati, S.; Li, T.; Gonzalez, M. A. An Overview of Biorefinery-Derived Platform Chemicals from a Cellulose and Hemicellulose Biorefinery. *Clean Techn Environ Policy* **2018**, *20* (7), 1615–1630. https://doi.org/10.1007/s10098-018-1568-5.

(8) Galebach, P. H.; McClelland, D. J.; Eagan, N. M.; Wittrig, A. M.; Buchanan, J. S.; Dumesic, J. A.; Huber, G. W. Production of Alcohols from Cellulose by Supercritical Methanol Depolymerization and Hydrodeoxygenation. *ACS Sustainable Chem. Eng.* **2018**, *6* (3), 4330–4344. https://doi.org/10.1021/acssuschemeng.7b04820.

(9) Galebach, P. H.; Soeherman, J. K.; Wittrig, A. M.; Lanci, M. P.; Huber, G. W. Supercritical Methanol Depolymerization and Hydrodeoxygenation of Maple Wood and Biomass-Derived Oxygenates into Renewable Alcohols in a Continuous Flow Reactor. *ACS Sustainable Chem. Eng.* **2019**, *7* (18), 15361–15372. https://doi.org/10.1021/acssuschemeng.9b02704.

(10) Chia, M.; O'Neill, B. J.; Alamillo, R.; Dietrich, P. J.; Ribeiro, F. H.; Miller, J. T.; Dumesic, J. A. Bimetallic RhRe/C Catalysts for the Production of Biomass-Derived Chemicals. *Journal of Catalysis* **2013**, *308*, 226–236. https://doi.org/10.1016/j.jcat.2013.08.008.

(11) Krishna, S. H.; Walker, T. W.; Dumesic, J. A.; Huber, G. W. Kinetics of Levoglucosenone Isomerization. *ChemSusChem* **2017**, *10* (1), 129–138. https://doi.org/10.1002/cssc.201601308.

(12) Lewkowski, J. Synthesis, Chemistry and Applications of 5-Hydroxymethyl-Furfural and Its Derivatives. *ARKIVOC* **2001**, *2001* (1), 17–54. https://doi.org/10.3998/ark.5550190.0002.102.

(13) Chia, M.; Pagán-Torres, Y. J.; Hibbitts, D.; Tan, Q.; Pham, H. N.; Datye, A. K.; Neurock, M.; Davis, R. J.; Dumesic, J. A. Selective Hydrogenolysis of Polyols and Cyclic Ethers over Bifunctional Surface Sites on Rhodium–Rhenium Catalysts. *J. Am. Chem. Soc.* **2011**, *133* (32), 12675–12689. https://doi.org/10.1021/ja2038358.

(14) He, J.; Burt, S. P.; Ball, M. R.; Hermans, I.; Dumesic, J. A.; Huber, G. W. Catalytic C-O Bond Hydrogenolysis of Tetrahydrofuran-Dimethanol over Metal Supported WOx/TiO2 Catalysts. *Applied Catalysis B: Environmental* **2019**, *258*, 117945. https://doi.org/10.1016/j.apcatb.2019.117945.

(15) He, J.; Burt, S. P.; Ball, M.; Zhao, D.; Hermans, I.; Dumesic, J. A.; Huber, G. W. Synthesis of 1,6-Hexanediol from Cellulose Derived Tetrahydrofuran-Dimethanol with Pt-WO_x/TiO_2 Catalysts. *ACS Catal.* **2018**, *8* (2), 1427–1439. https://doi.org/10.1021/acscatal.7b03593.

(16) Krishna, S. H.; Cao, J.; Tamura, M.; Nakagawa, Y.; De Bruyn, M.; Jacobson, G. S.; Weckhuysen, B. M.; Dumesic, J. A.; Tomishige, K.; Huber, G. W. Synthesis of Hexane-Tetrols and -Triols with Fixed Hydroxyl Group Positions and Stereochemistry from Methyl Glycosides over Supported Metal Catalysts. *ACS Sustainable Chem. Eng.* **2020**, *8* (2), 800–805. https://doi.org/10.1021/acssuschemeng.9b04634.

(17) Krishna, S. H.; De bruyn, M.; Schmidt, Z. R.; Weckhuysen, B. M.; Dumesic, J. A.; Huber, G. W. Catalytic Production of Hexane-1,2,5,6-Tetrol from Bio-Renewable Levoglucosanol in Water: Effect of Metal and Acid Sites on (Stereo)-Selectivity. *Green Chem.* **2018**, *20* (19), 4557–4565. https://doi.org/10.1039/C8GC02455C.

(18) Cuello-Penaloza, P.; Krishna, S. H.; De bruyn, M.; Weckhuysen, B. M.; Lebrón-Rodríguez, E. A.; Hermans, I.; Dumesic, J. A.; Huber, G. W. Production of Hexane-1,2,5,6-Tetrol from Biorenewable Levoglucosanol over Pt-WOx/TiO2. *ACS Sustainable Chem. Eng.* **2021**, *9* (48), 16123–16132. https://doi.org/10.1021/acssuschemeng.1c04759.

(19) MacQueen, B.; Royko, M.; Crandall, B. S.; Heyden, A.; Pagán-Torres, Y. J.; Lauterbach, J. Kinetics Study of the Hydrodeoxygenation of Xylitol over a ReOx-Pd/CeO2 Catalyst. *Catalysts* **2021**, *11* (1), 108. https://doi.org/10.3390/catal11010108.

(20) Liu, L.; Cao, J.; Nakagawa, Y.; Betchaku, M.; Tamura, M.; Yabushita, M.; Tomishige, K. Hydrodeoxygenation of C4–C6 Sugar Alcohols to Diols or Mono-Alcohols with the Retention of the Carbon Chain over a Silica-Supported Tungsten Oxide-Modified Platinum Catalyst. *Green Chem.* **2021**, *23* (15), 5665–5679. https://doi.org/10.1039/D1GC01486B.

(21) Tamura, M.; Nakagawa, Y.; Tomishige, K. Reduction of Sugar Derivatives to Valuable Chemicals: Utilization of Asymmetric Carbons. *Catal. Sci. Technol.* **2020**, *10* (12), 3805–3824. https://doi.org/10.1039/D0CY00654H.

(22) Zang, G.; Sun, P.; Elgowainy, A.; Bafana, A.; Wang, M. Life Cycle Analysis of Electrofuels: Fischer–Tropsch Fuel Production from Hydrogen and Corn Ethanol Byproduct CO2. *Environ. Sci. Technol.* **2021**, *55* (6), 3888–3897. https://doi.org/10.1021/acs.est.0c05893.

(23) de Araujo Guilherme, A.; Dantas, P. V. F.; Padilha, C. E. de A.; dos Santos, E. S.; de Macedo, G. R. Ethanol Production from Sugarcane Bagasse: Use of Different Fermentation Strategies to Enhance an Environmental-Friendly Process. *Journal of Environmental Management* **2019**, *234*, 44–51. https://doi.org/10.1016/j.jenvman.2018.12.102.

(24) Almost all U.S. gasoline is blended with 10% ethanol - Today in Energy - U.S. Energy Information Administration (EIA) https://www.eia.gov/todayinenergy/detail.php?id=26092 (accessed 2022 -02 -11).

(25) Eagan, N. M.; Moore, B. M.; McClelland, D. J.; Wittrig, A. M.; Canales, E.; Lanci, M. P.; Huber, G. W. Catalytic Synthesis of Distillate-Range Ethers and Olefins from Ethanol through Guerbet Coupling and Etherification. *Green Chem.* **2019**, *21* (12), 3300–3318. https://doi.org/10.1039/C9GC01290G.

(26) Cuello-Penaloza, P. A.; Dastidar, R. G.; Wang, S.-C.; Du, Y.; Lanci, M. P.; Wooler, B.; Kliewer, C. E.; Hermans, I.; Dumesic, J. A.; Huber, G. W. Ethanol to Distillate-Range Molecules Using Cu/MgxAlOy Catalysts with Low Cu Loadings. *Applied Catalysis B: Environmental* **2022**, *304*, 120984. https://doi.org/10.1016/j.apcatb.2021.120984.

(27) Moteki, T.; Flaherty, D. W. Mechanistic Insight to C–C Bond Formation and Predictive Models for Cascade Reactions among Alcohols on Ca- and Sr-Hydroxyapatites. *ACS Catal.* **2016**, *6* (7), 4170–4183. https://doi.org/10.1021/acscatal.6b00556.

(28) Pomalaza, G.; Ponton, P. A.; Capron, M.; Dumeignil, F. Ethanol-to-Butadiene: The Reaction and Its Catalysts. *Catalysis Science & Technology* **2020**, *10* (15), 4860–4911. https://doi.org/10.1039/D0CY00784F.

(29) Ro, I.; Liu, Y.; Ball, M. R.; Jackson, D. H. K.; Chada, J. P.; Sener, C.; Kuech, T. F.; Madon, R. J.; Huber, G. W.; Dumesic, J. A. Role of the Cu-ZrO2 Interfacial Sites for Conversion of Ethanol to Ethyl Acetate and Synthesis of Methanol from CO2 and H2. *ACS Catal.* **2016**, *6* (10), 7040–7050. https://doi.org/10.1021/acscatal.6b01805.

(30) Cao, F.; Schwartz, T. J.; McClelland, D. J.; Krishna, S. H.; Dumesic, J. A.; Huber, G. W. Dehydration of Cellulose to Levoglucosenone Using Polar Aprotic Solvents. *Energy Environ. Sci.* **2015**, *8* (6), 1808–1815. https://doi.org/10.1039/C5EE00353A.

(31) Warmington, A. Consortium to build Cyrene plant https://www.specchemonline.com/consortium-build-cyrene-plant (accessed 2022 -02 -11).

(32) Flagship EU Project aiming to Replace Toxic Solvents with Renewable Alternatives Launches today https://circa-group.com/news/2020/10/24/9axo6z01ddll227lq24abjs2g5mbyz (accessed 2021 -03 -24).

(33) De Bruyn, M.; Fan, J.; Budarin, V. L.; Macquarrie, D. J.; Gomez, L. D.; Simister, R.; Farmer, T. J.; Raverty, W. D.; McQueen-Mason, S. J.; Clark, J. H. A New Perspective in Bio-Refining: Levoglucosenone and Cleaner Lignin from Waste Biorefinery Hydrolysis Lignin by Selective Conversion of Residual Saccharides. *Energy Environ. Sci.* **2016**, *9* (8), 2571–2574. https://doi.org/10.1039/C6EE01352J.

(34) Adaka, I. C.; Uzor, P. F. Chapter 12 - Cyrene as a Green Solvent in the Pharmaceutical Industry. In *Green Sustainable Process for Chemical and Environmental Engineering and Science*; Inamuddin, Boddula, R., Ahamed, M. I., Asiri, A. M., Eds.; Elsevier, 2021; pp 243–248. https://doi.org/10.1016/B978-0-12-821885-3.00001-3.

(35) Milescu, R. A.; Zhenova, A.; Vastano, M.; Gammons, R.; Lin, S.; Lau, C. H.; Clark, J. H.; McElroy, C. R.; Pellis, A. Polymer Chemistry Applications of Cyrene and Its Derivative Cygnet 0.0 as Safer Replacements for Polar Aprotic Solvents. *ChemSusChem* **2021**, *14* (16), 3367–3381. https://doi.org/10.1002/cssc.202101125.

(36) Sherwood, J.; De bruyn, M.; Constantinou, A.; Moity, L.; McElroy, C. R.; Farmer, T. J.; Duncan, T.; Raverty, W.; Hunt, A. J.; Clark, J. H. Dihydrolevoglucosenone (Cyrene) as a Bio-Based Alternative for Dipolar Aprotic Solvents. *Chem. Commun.* **2014**, *50* (68), 9650–9652. https://doi.org/10.1039/C4CC04133J.

(37) De bruyn, M.; Cuello-Penaloza, P.; Cendejas, M.; Hermans, I.; He, J.; Krishna, S. H.; Lynn, D. M.; Dumesic, J. A.; Huber, G. W.; Weckhuysen, B. M. Hexane-1,2,5,6-Tetrol as a Versatile and Biobased Building Block for the Synthesis of Sustainable (Chiral) Crystalline Mesoporous Polyboronates. *ACS Sustainable Chem. Eng.* **2019**, *7* (15), 13430–13436. https://doi.org/10.1021/acssuschemeng.9b02772.

(38) Giri, G. F.; Danielli, M.; Marinelli, R. A.; Spanevello, R. A. Cytotoxic Effect of Levoglucosenone and Related Derivatives against Human Hepatocarcinoma Cell Lines. *Bioorganic & Medicinal Chemistry Letters* **2016**, *26* (16), 3955–3957. https://doi.org/10.1016/j.bmcl.2016.07.007.

(39) Flourat, A. L.; Peru, A. A. M.; Teixeira, A. R. S.; Brunissen, F.; Allais, F. Chemo-Enzymatic Synthesis of Key Intermediates (S)-γ-Hydroxymethyl-α,β-Butenolide and (S)-γ-Hydroxymethyl-γ-Butyrolactone via Lipase-Mediated Baeyer–Villiger Oxidation of Levoglucosenone. *Green Chem.* **2015**, *17* (1), 404–412. https://doi.org/10.1039/C4GC01231C.

(40) About – Resolute Project https://www.resolute-project.eu/about-resolute/ (accessed 2022 -02 -07).

(41) N-Methyl-2-Pyrrolidone (NMP) Market https://www.futuremarketinsights.com/reports/global-n-methyl-2-pyrrolidone-market (accessed 2022 -02 -07).

(42) ltd, M. D. F. Dimethylformamide (DMF) Market | Share, Size | 2021 - 2026 http://www.marketdataforecast.com/ (accessed 2022 -02 -07).

(43) Circular economy: definition, importance and benefits | News | European Parliament https://www.europarl.europa.eu/news/en/headlines/economy/20151201STO05603/circular-economy-definition-importance-and-benefits (accessed 2022 -02 -07).

(44) Geissdoerfer, M.; Pieroni, M. P. P.; Pigosso, D. C. A.; Soufani, K. Circular Business Models: A Review. *Journal of Cleaner Production* **2020**, *277*, 123741. https://doi.org/10.1016/j.jclepro.2020.123741.

(45) The RENUVA™ Program Timeline https://corporate.dow.com/en-us/science-and-sustainability/2025-goals/renuva-program/timeline.html (accessed 2022 -02 -07).

(46) Whetstone, R. R.; Ballard, S. A. 1, 2, 6-Hexanetriol. US2768213A, October 23, 1956.

(47) van Putten, R.-J.; van der Waal, J. C.; de Jong, E.; Rasrendra, C. B.; Heeres, H. J.; de Vries, J. G. Hydroxymethylfurfural, A Versatile Platform Chemical Made from Renewable Resources. *Chem. Rev.* **2013**, *113* (3), 1499–1597. https://doi.org/10.1021/cr300182k.

(48) Román-Leshkov, Y.; Barrett, C. J.; Liu, Z. Y.; Dumesic, J. A. Production of Dimethylfuran for Liquid Fuels from Biomass-Derived Carbohydrates. *Nature* **2007**, *447* (7147), 982–985. https://doi.org/10.1038/nature05923.

(49) USDA Study Shows Significant Greenhouse Gas Benefits of Ethanol Compared with Gasoline https://www.usda.gov/media/press-releases/2019/04/02/usda-study-shows-significant-greenhouse-gas-benefits-ethanol (accessed 2022 -05 -11).

(50) Exxon Mobil Corporation. 2019 Outlook for Energy: A Perspective to 2040 https://corporate.exxonmobil.com/-/media/Global/Files/outlook-for-energy/2019-Outlook-for-Energy_v4.pdf (accessed 2021 -04 -19).

(51) Jonathan, A.; Eagan, N. M.; Bruns, D. L.; Stahl, S. S.; Lanci, M. P.; Dumesic, J. A.; Huber, G. W. Ethylene Oligomerization into Linear Olefins over Cobalt Oxide on Carbon Catalyst. *Catal. Sci. Technol.* **2021**, *11* (10), 3599–3608. https://doi.org/10.1039/D1CY00207D.

(52) Jonathan, A.; Tomashek, E. G.; Lanci, M. P.; Dumesic, J. A.; Huber, G. W. Reaction Kinetics Study of Ethylene Oligomerization into Linear Olefins over Carbon-Supported Cobalt Catalysts. *Journal of Catalysis* **2021**, *404*, 954–963. https://doi.org/10.1016/j.jcat.2021.05.035.

(53) Gines, M. J. L.; Iglesia, E. Bifunctional Condensation Reactions of Alcohols on Basic Oxides Modified by Copper and Potassium. *Journal of Catalysis* **1998**, *176* (1), 155–172. https://doi.org/10.1006/jcat.1998.2009.

(54) Kozlowski, J. T.; Davis, R. J. Heterogeneous Catalysts for the Guerbet Coupling of Alcohols. *ACS Catal.* **2013**, *3* (7), 1588–1600. https://doi.org/10.1021/cs400292f.

(55) Eagan, N. M.; Lanci, M. P.; Huber, G. W.; Penaloza, P. A. C.; Buchanan, J. S. Processes for Producing Ethers and Olefins from Primary Alcohols. US20210363085A1, November 25, 2021.

(56) Alternative Fuels Data Center: Maps and Data - U.S. Production, Consumption, and Trade of Ethanol https://afdc.energy.gov/data/10323 (accessed 2022 -05 -14).

(57) C. Meunier, F.; Scalbert, J.; Thibault-Starzyk, F. Unraveling the Mechanism of Catalytic Reactions through Combined Kinetic and Thermodynamic Analyses: Application to the Condensation of Ethanol. *Comptes Rendus Chimie* **2015**, *18* (3), 345–350. https://doi.org/10.1016/j.crci.2014.07.002.

(58) Iglesia, E.; Barton, D. G.; Biscardi, J. A.; Gines, M. J. L.; Soled, S. L. Bifunctional Pathways in Catalysis by Solid Acids and Bases. *Catalysis Today* **1997**, *38* (3), 339–360. https://doi.org/10.1016/S0920-5861(97)81503-7.

(59) Ogo, S.; Onda, A.; Iwasa, Y.; Hara, K.; Fukuoka, A.; Yanagisawa, K. 1-Butanol Synthesis from Ethanol over Strontium Phosphate Hydroxyapatite Catalysts with Various Sr/P Ratios. *Journal of Catalysis* **2012**, *296*, 24–30. https://doi.org/10.1016/j.jcat.2012.08.019.

(60) Eagan, N. M.; Lanci, M. P.; Huber, G. W. Kinetic Modeling of Alcohol Oligomerization over Calcium Hydroxyapatite. *ACS Catal.* **2020**, *10* (5), 2978–2989. https://doi.org/10.1021/acscatal.9b04734.

(61) Ramasamy, K. K.; Guo, M. F.; Gray, M. J.; Subramaniam, S. United States Patent: 10745330 - Method of Converting Ethanol to Higher Alcohols. 10745330, August 18, 2020.

(62) Bravo-Suárez, J. J.; Subramaniam, B.; Chaudhari, R. V. Vapor-Phase Methanol and Ethanol Coupling Reactions on CuMgAl Mixed Metal Oxides. *Applied Catalysis A: General* **2013**, *455*, 234–246. https://doi.org/10.1016/j.apcata.2013.01.025.

Chapter 2: Catalytic production of hexan-1,2,5,6-tetrol from biomass-derived levoglucosanol using Pt-WO_x/TiO_2 catalysts

2.1. Introduction

Channeling the production of commodity chemicals from petroleum-derived resources to renewable lignocellulosic feedstocks feedstocks is needed to effectively transition the chemical industry towards materials and products with a lower CO_2 footprint. Biomass-derived monomers can be used as important platform molecules for the synthesis of polymers, resins, solvents and surfactants among others[1–9]. Sugar derivatives have been shown to offer many opportunities to obtain such platform molecules[10,11]. Levoglucosenone (LGO) is a bio-based sugar-like compound, which can be produced from cellulose by mild pyrolysis[12–14]. Notably, based on the pyrolytic method developed by the Circa Group an actual 1,000 ton LGO/year plant is currently being developed in France[15]. LGO can also be produced at yields up to 51% using polar aprotic solvents and sulfuric acid at 170-230 °C[16]. LGO is a highly functionalized molecule that can be used in asymmetric synthesis[2,3], to create chiral pure pharmaceutical intermediates[4,5], and for the synthesis of chemicals useful to the creation of polymers, such as hydroxymethylfurfural[1,6] (HMF). It has equally been established that dihydrolevoglucosenone (Cyrene™) obtained from LGO hydrogenation[17] is a benign low-toxicity polar aprotic solvent with similar properties as dimethylformamide (DMF) or N-methylpyrrolidone (NMP)[7,9,18]. Also, when adding Cyrene to water a powerful hydrotrope is created, the central aspect to this phenomenon being Cyrene's

The content of this Chapter is adapted with permission of the American Chemical Society from the following reference: Cuello-Penaloza, P., Krishna, S.H., De bruyn, M., Weckhuysen, B.M., Lebrón-Rodríguez, E.A., Hermans, I., Dumesic, J.A. Huber, G.W. "Production of Hexane-1,2,5,6-Tetrol from Biorenewable Levoglucosanol over Pt-WO_x/TiO_2." *ACS Sustainable Chemistry & Engineering* 9, no. 48 (December 6, 2021): 16123–32. Copyright 2021 American Chemical Society. S.H.K, and E.A.L. performed data collection and analysis. S.H.K., M.de B., and B.M.W. performed revisions.

geminal diol[19]. Other potentially useful LGO-derived molecules are Lgol[17,20,21], tetrahydrofuran-dimethanol[21,22] (THFDM), hexane-1,2,6-triol (HTri)[23,24], hexane-1,6-diol[21,24–28], and tetrol[27,29]. The main reactants and products of interest for this work are shown in Figure 2-1.

Our group has recently demonstrated how Lgol can be selectively converted into tetrol[29]. Tetrol is a polyol of industrial interest[28,30,31], which could be potentially useful to the synthesis of a range of polymers.[8,30] as Also, in displaying two chiral centers, potential exist equally to use as a chiral synthon[28]. Tetrol is obtained by the selective C-O cleavage of the anhydrobridge of Lgol in water over a Brønsted acid catalyst, forming the dideoxy sugar intermediates 3,4-dideoxymannose (DDM) from t-Lgol and 3,4-dideoxyglucose (DDG) from e-Lgol. The latter intermediates are then respectively hydrogenated over metal sites to (*S,S*)-tetrol and (*S,R*)-tetrol[29]. As an alternative pathway it has also been established that DDM and DDG can isomerize to 3,4-dideoxyfructose (DDF) in the presence of a Lewis acid catalyst (at ≥ 100°C) or at a somewhat elevated temperature (150 °C)[29]. Subsequent hydrogenation of DDF leads to formation of equal amounts of (*S,S*) and (*S,R*)-tetrol[29], resulting in the complete loss of any of the initial Lgol stereochemistry. We have previously shown that these reactions can be carried out selectively using bifunctional metal-acid catalysts, such as Pt/SiO_2-Al_2O_3, in which hydrolysis of Lgol to DDM and DDG occurs on acid sites, and subsequent hydrogenation of DDM, DDG and DDF occurs on metal sites[29]. However, these reactions were done in a batch reactor where it is difficult to observe catalyst deactivation. In addition, while the selectivity to tetrol was 94%, this value was obtained at a reactant concentration of 2wt% in water, with the value decreasing to 85% when a 20wt% aqueous feed is used. It would be desirable to increase the reactant concentration and maintain high selectivity to tetrol with a stable catalyst for the process.

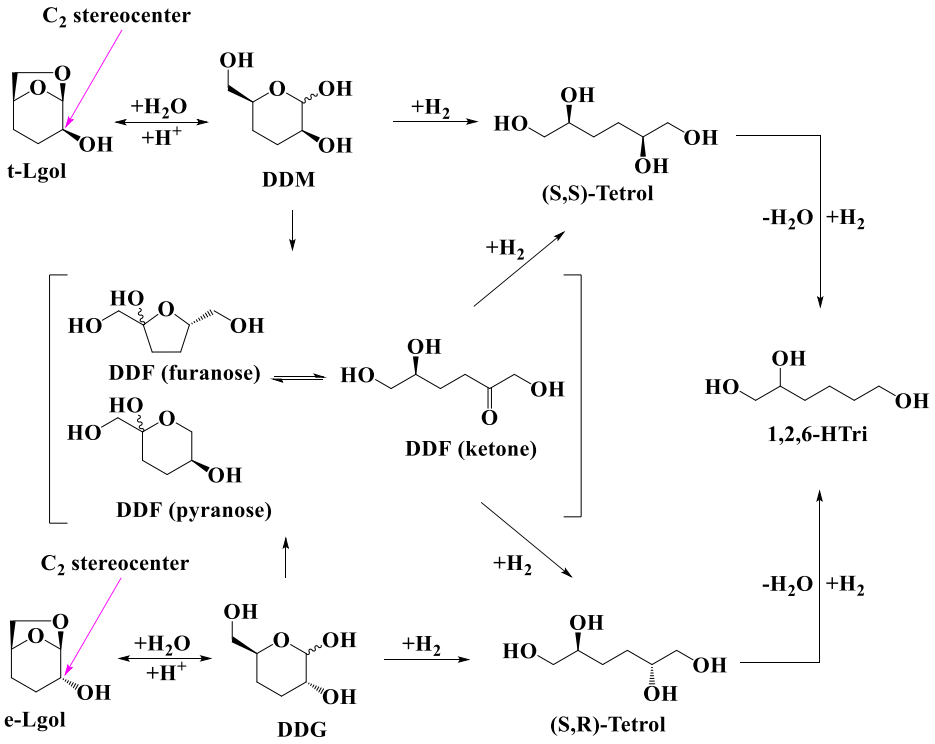

Figure 2-1. Lgol reaction network to tetrol[29] and HTri[25]. C_2 stereocenters of t-Lgol and e-Lgol and preserved (*S*,*S*) and (*S*,*R*) positions in tetrol shown.

Supported bifunctional catalysts have been shown very useful towards the hydrogenolysis of biomass-derived compounds.[10,24,26] These catalysts typically consist of a combination of reducible noble metals (e.g. Pt, Pd, Rh, Au), which engage in the adsorption and dissociation of H_2, and (reduced) oxophilic metal oxides (e.g. Mo, W, Re) , which comprise the required acid sites capable of C-O cleavage reactions.[24,32–38] Such bifunctional catalysts are highly active in the hydrogenolysis of secondary C-O bonds of linear (particularly with -OH in non-primary carbons) or cyclic polyoxygenates in which the carbon bonded to the oxygen or hydroxyl groups are vicinal due to the acid-catalyzed concerted formation of stable secondary oxocarbenium ion species in the former case, or primary oxocarbenium ion species stabilized with OH groups formed when the ring is protonated in the latter case[24], which in both cases is then followed by metal-catalyzed

hydrogenation. For example, Rh-ReO_x/C catalysts have been used in the hydrogenolysis of several cyclic polyoxygenates such as 2-(hydroxymethyl)tetrahydropyran (2-HMTHP) or tetrahydrofurfuryl alcohol to produce 1,6-hexandiol and 1,5-pentanediol respectively[24,32], as well as the hydrogenolysis of fructose into HMF[32], and of linear polyols such as butanediols and pentanediols. Pt-WO_x/TiO_2 catalysts have been used for similar hydrogenolysis reactions as reported for Rh-ReO_x/C catalysts to produce molecules such as 1,6-hexanediol from THFDM proving to be stable under dilute conditions[26] and exhibiting higher reaction rates at these hydrogenolyses than other noble metals[25] due to metal nanoparticle not being completely coated by the partially reduced support.

2.2. Experimental Methods

2.2.1. Pt-WO_x/TiO_2 catalyst synthesis and characterization

10wt%WO_x/TiO_2 supports were synthesized[26] by wet impregnation of ammonium tungsten oxide hydrate (Alfa Aesar #22640) on TiO_2 nanopowder (Sigma-Aldrich #718467). Ammonium tungsten oxide hydrate was first added to 100 mL of 18 MΩ water. HCl (Sigma-Aldrich #258148) was added dropwise to the mixture until it reached a pH of 1, and the mixture was then heated under reflux to 80 ˚C for 12 hours. 6 g of TiO_2 nanopowder was then added to the mixture and left to stir for an additional 30 minutes at 80 ˚C. Water was then evaporated by rotary evaporation using a water bath of 60 ˚C. WO_x/TiO_2 powders were then dried at 110 ˚C overnight and calcined under flowing air at 400 ˚C for three hours (1 ˚C min^{-1}).

(10wt%)Pt(10wt%)WO_x/TiO_2 catalysts (hereafter referred to as Pt-WO_x/TiO_2) was synthesized by wet impregnation of chloroplatinic acid on the 10wt%WO_x/TiO_2 support as indicated by He et al[26].

A chloroplatinic acid solution in water was added to 10wt%WO_x/TiO_2 support via wet impregnation. The mixture was then heated to 80 ˚C while stirring, then the resulting solid was dried at 80 ˚C in a vacuum oven overnight. The dry solid was then ground to a powder, and the powder was calcined under flowing air (Airgas, 19.5 – 23.5% O_2, 100 mL min^{-1}) at 400˚C for three hours (1˚C min^{-1}) and subsequently reduced under flowing H_2 (Airgas, 99.999%, 100 mL min^{-1}) at 250˚C for two hours (1˚C min^{-1}). After cooling down to room temperature, the catalysts were passivated under flowing 1% O_2 in Ar (Airgas, 99.999%) or transferred and stored in a glovebox.

Thermogravimetric analysis (TGA) of the spent and the fresh calcined materials was carried out using a TGA TA Q500. For analysis, 10 – 15mg of sample were added to the dish and heated up from room temperature to 650°C at a 10°C/min ramp under oxygen flow.

Total organic carbon (TOC) analysis of the spent and the fresh catalyst was made with a Shimadzu TOC-V CPH/CPN using the SSM-5000A solid sample module under 100mL min^{-1} oxygen flow. The instrument was calibrated with potassium phthalate (Acros Organics – 417955000) from 0 – 80 mg, and 45 – 55 mg of sample was weighed for the analysis.

Powder X-ray diffraction of the fresh and spent catalyst samples was carried out in Rigaku Rapid II diffractometer. A Mo Kα source (λ = 0.71 Å) was used for the measurements and the scanned zone was 2θ = 5 - 60°. All measurements were recalculated to Cu Kα source (λ = 1.54 Å) for ease of analysis and comparison with literature. Structures were matched with the use of JADE, PDF 4+ software, as well as from reports in literature.

Pt, W and Ti concentrations of the product effluents of the flow reactor were obtained by inductively coupled plasma optical emission spectroscopy (ICP-OES) with a Varian Vista-MPX after treating 1-1.5 g of the liquid samples with 1wt% HNO_3 (trace metal grade, Sigma-Aldrich –

438073) aqueous solution until pH < 1. Calibration curves of the metals were prepared from 1000 ppm standard solutions of Pt (Fluka – HONCE1046), W (Sigma Aldrich – 50334) and Ti (Fluka – FLE1125).

Additional characterization analyses carried out on these catalysts were acid site count by NH_3-TPD, Pt site count by CO chemisorption, and particle size distribution by STEM, whose data was taken from He et al[26].

2.2.2. Reactor systems

2.2.2.1. Batch reactors

For the production of levoglucosanol (Lgol) from Dihydrolevoglucosenone (Cyrene, 99% Circa Group), a 300 mL stainless steel Parr reactor was used. 100-150 mL Cyrene was added first to the reactor along with 5w% Ru/C catalyst added at a ~10mg catalyst/g Cyrene ratio. The reactor is then pressurized to 1000 psi by adding H_2 and maintaining the pressure by monitoring H_2 consumption until the conversion is complete. The solid Lgol product was then extracted with acetone and filtered with a Buchner funnel with a fine fritted 80 mm diameter disc and then purified with the use of a rotoevaporator (Heidolph Hei-vap Advantage) at 60 °C to remove the majority of the acetone solvent. Afterward, the Lgol solution was further purified by transferring the contents of the rotoevaporator to falcon vials and putting them into a Speedvac (Savant Thermo Scientific) at room temperature.

A 75 mL stainless steel Parr batch reactor with dip-tube was used to carry out the batch experiments. Reactions were carried out with 40 mL of reactant solution at 120˚C, 600 – 1000 psi H_2 (99.999%, Airgas), 750 rpm stir rate and the desired amount of the powder catalyst. H_2 pressure

was periodically replenished when the pressure fell to <90% of the desired value. Up to 6 samples were taken by first purging the dip-tube (0.3-0.5mL) and then collecting the sample (0.5 mL/sample). A stainless-steel mesh was added to the dip-tube to retain the catalyst during sampling. Samples were diluted in water to obtain a 1-2wt% solution that was then analyzed by HPLC (see section 3.3.).

2.2.2.2. Flow reactors

Lgol hydrogenolysis was carried out using a flow reactor to study its stability under time-on-stream (TOS). The reaction was carried out in a stainless-steel tubular flow reactor (2.0 in bed length, 1/4 in outer diameter), arranged in an up-flow configuration, and heated using a tube furnace (Applied Test Systems Inc. Series 3210). The catalyst (0.500 g) was sieved to 30-80 mesh sizes and added into the reactor with quartz wool packed on both sides without dilution. The material was reduced *in situ* under a H_2 flow (100 mL (STP)·min^{-1}) at 250 °C for 2 h before reaction. The reactor was then heated to 120 °C and pressurized to 620 psi H_2, with pressure maintained using a back-pressure regulator. An aqueous 30 wt % Lgol solution was pumped into the reactor using a Teledyne Series I Legacy HPLC pump, with H_2 (40 mL (STP)·min^{-1}) delivered by a mass flow controller (Brooks Instruments, 5850 Series E). A stainless-steel tank (150 mL) was used to accumulate the liquid products at the reactor outlet. The accumulated liquid product was collected periodically, filtered through a 0.22 μm PES syringe filter, diluted with water to 1-2wt% concentration and then analyzed by HPLC (section 3.3.). Feed solutions and liquid products were analyzed using HPLC as described for the batch experiments in section 3.3.

2.2.3. Product analysis and quantitation

A BioRad Aminex 87H column was used in a Shimadzu HPLC. The mobile phase was 5 mM H_2SO_4 (HPLC grade, Ricca Chemical) operated at a flow rate of 0.6 mL min^{-1}. with a column temperature of 30 °C and an injection volume of 3 μL. Lgol, HTri, DDM and tetrol plus intermediates DDG and DDF were quantified by HPLC using a refractive index (RI) detector. Lgol, tetrol and HTri response factors were obtained via calibration curves, whereas DDM, DDG and DDF were assumed to be equal to tetrol.

^{13}C qNMR was used to confirm the presence of Lgol, tetrol and HTri and quantify the stereoisomer ratios of Lgol and tetrol (Figure 7-1 A-E) using a Bruker Avance-500 with a DCH cryoprobe. MestreNova was used to process the spectra. Parameters used were as follow: 10%D_2O/90%H_2O solvent, NS = 112, AQ = 1s, TD1 = 30s. Referencing was done with water solvent 1H NMR peak at 4.69 ppm. Individual standards of each reactant were measured to assign.

2.2.4. Data analysis and considerations

Conversion of Lgol is defined in base of reactant concentration as:

$$X(\%) = \frac{C_{Lgol,0} - C_{Lgol}}{C_{Lgol,0}} \qquad (2-1)$$

Product selectivity is defined based on product concentration as:

$$S_i(\%) = \frac{\frac{C_i}{C_{Lgol,0}}}{X(\%)} = \frac{Y_i(\%)}{X(\%)} \qquad (2-2)$$

Where Y_i (%) is the yield of the *i*-th product.

In the development of this work, the reactant conversion was fitted to a first-order kinetic model in the form of:

$$r_{Lgol} = kC_{Lgol} \qquad (2-3)$$

Where r_{Lgol} is in mmol $g_{cat}^{-1}h^{-1}$. From this, it follows that in a batch reactor, $C_{Lgol}(t)$ is defined as:

$$C_{Lgol}(t) = C_{Lgol,0}\exp(-kt) \qquad (2-4)$$

Or alternatively as:

$$\frac{C_{Lgol}(t)}{C_{Lgol,0}} = \exp(-kt) \qquad (2-5)$$

The activation energy derived from batch experiments is obtained from a linear fit of the Arrhenius equation defined as:

$$E_a = -R\left[\frac{\partial \ln(r)}{\partial(1/\mathrm{T})}\right]_P \qquad (2-6)$$

Where E_{act} is the activation energy (KJ/mol), R is the universal gas constant (8.314×10^{-3} $KJmol^{-1}K^{-1}$, T is temperature and r are the initial rates of Lgol conversion obtained in the temperature range (100 – 130°C).

For first-order kinetics, the Lgol conversion may be calculated in the flow reactor as:

$$X(\%) = 100 \times [1 - \exp(-k\tau)] \qquad (2-7)$$

Where τ is the space-time which is defined in $g_{cat}g_{Lgol}^{-1}h$.

2.3. Results and discussion

2.3.1. Selectivity of Lgol conversion in water

2.3.1.1. Selectivity to different products with conversion

Irrespective the feed concentrations, the main observed products from Lgol conversion were tetrol and its three Lgol-derived intermediates DDM, DDG and DDF. At higher conversions, HTri can also be detected. Figure 2-2 shows the product selectivity as a function of conversion for three different initial Lgol concentrations (10, 20 and 30wt%). It can be observed that at conversions in excess of 10%, tetrol and its DDM/DDG/ DDF intermediates make up for over 90% of the products. The selectivity of products exceeds 100% for the 10wt% Lgol feed due to tetrol, DDG and DDF peaks fully overlapping (See Figure 7-2B), making quantitation difficult at low conversions as their individual response factors compound in that peak (remind that we assume DDM, DDG and DDF response factors equal to Tetrol). HTri is present at conversions in excess of 40% but it's overall yield remains small (< 3%, see Figure 7-2 B-D). Furthermore, from quantitative ^{13}C-NMR analysis (Figure 7-1 and Table 7-1) it could be concluded that HTri selectivity decreases with conversion, the values being 3.7% at 43% Lgol conversion and 3.5% at 91% Lgol conversion (see Table 7-1 for average of peaks). C-balances associated to these experiments can be found on the Supporting Information (Figure 7-6).

To further understand the reaction network of the process, the selectivity of DDG was estimated (it is reminded that its peak and that of DDF overlaps completely with the tetrol in HPLC analysis) by assuming that the ratio of produced DDM to DDG is proportional to the ratio of converted t-Lgol to converted e-Lgol, and that negligible amounts of DDF are formed (as Lgol stereocenters were mostly preserved as will be shown later), while DDM is calculated normally with its own distinctive peak. Figure 2-2 shows the resulting selectivity trends for DDM, the estimated DDG,

and the estimated tetrol selectivity obtained after subtracting DDG from the total selectivity of the tetrol + DDG + DDF peak (with DDF→0). It can be observed that tetrol now appears as a secondary stable product, whereas DDM and DDG appear as unstable products, reflecting their conversion to tetrol in a series mechanism, which is consistent with previous work done by our group on the reaction network of Lgol conversion to tetrol with Pt/SiO_2-Al_2O_3[29]. Regarding HTri, it can be asserted that it is an unstable product since its selectivity decreases with conversion. Moreover, since it can only be observed at >40% conversion, it cannot be asserted to what degree HTri may come from tetrol (or not) since concentrations before this conversion may just be below detection limits for HPLC and NMR. These results already constitute an improvement on our prior work[29] in regards the selective production of tetrol from Lgol at high concentration feeds, as now we are able to obtain >90% selectivity to tetrol with feeds as concentrated as 30wt%, whereas with Pt/SiO_2-Al_2O_3 selectivity would drop to 85% when a 20wt% aqueous Lgol feed is used, with expected decreases at higher concentrations. Moreover, using Pt-WO_x/TiO_2 is also shown to enable selective production of tetrol from Lgol among different possible products that may be obtained[27,28].

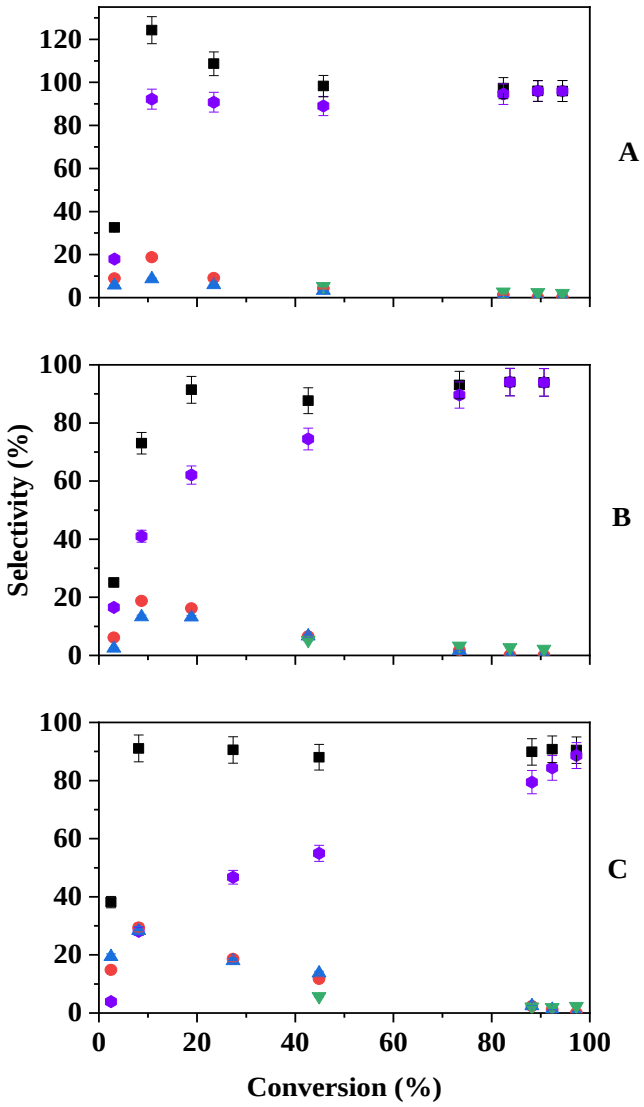

Figure 2-2. Calculated selectivities of tetrol + intermediates (■), DDM (●), HTri (▼) and estimated selectivities of tetrol (●) and DDG (▲) versus conversion using aqueous Lgol feed concentrations of A) 10wt%, B) 20wt% and C) 30wt%. **Conditions:** 120°C, 1000 psi H_2, 40-45 mL Lgol feed, 200 mg Pt-WO_x/TiO_2 catalyst.

Neither THFDM nor its isomer tetrahydropyran-2-methanol-5-hydroxyl (THP2M5H) were observed (refer to Figure 7-1 A-E). This is in contrast with prior work done by our group on the Pt/SiO_2-Al_2O_3 catalyzed Lgol to tetrol conversion.[29] It has been previously shown that THFDM can be produced as a main product from Lgol hydrogenolysis in organic solvent[22] or as a minor

byproduct in aqueous media[29]. THFDM has also been reported as a product of acid-catalyzed tetrol dehydration[20], and can also convert to HTri in a series mechanism[23]. Pt-WO_x/TiO_2 and similar catalysts are known to catalyze C-O bond hydrogenolysis reactions of other oxygenated molecules, such as THFDM and HTri[23,25,26]. Since the selectivity to HTri is very low (1-6%), this would indicate that if hydrogenolysis of tetrol to HTri is occurring (in a series mechanism), its rate is much lower than that of Lgol to tetrol. This would be consistent with previously reported higher reaction rates of -OH substituted cyclic ethers to linear polyols being superior to that of more substituted linear polyol to less substituted ones using similar catalysts. For instance, the reaction rate of 2-HMTHP to 1,6-hexanediol (90 μmol g min^{-1}) is greater compared to HTri conversion to 1,6-hexanediol (23 μmol g min^{-1}), which in turn is greater than the rate of conversion of 1,6-hexanediol to 1-hexanol (no visible reaction) at 100°C using $RhReO_x$/C as reported by Chia et al.[24]

2.3.1.2. Stereochemistry of Lgol conversion to tetrol with Pt-WO_x/TiO_2

We previously showed that the obtained Lgol t/e ratio depends on the choice of the catalyst used to hydrogenate Cyrene[21]. As shown in Figure 2-1 the C_2-OH stereocenter can either be preserved or erased depending on whether the intermediates DDM and DDG are rapidly hydrogenated to (*S*,*S*)- and (*S*,*R*)-tetrol, or isomerized to DDF prior to hydrogenation[29] . In this research, we used Lgol with a feedstock t/e ratio of 1.8 and obtained a tetrol (*S*,*S*)/(*S*,*R*) ratio of 1.7 at 91% Lgol conversion over Pt-WO_x/TiO_2 catalyst (T = 120°C). This corresponds to 91% preservation of the diastereomeric excess present in the Lgol feedstock. In contrast, a maximum of 64% preservation of diastereomeric excess in Lgol was obtained over a 5% Pt/SiO_2-Al_2O_3 catalyst at near-complete Lgol conversion (T = 150°C)[29]. A lower temperature (T = 100°C) two-step route using hydrolysis over an Amberlyst 70 acid catalyst, followed by hydrogenation over 5% Pt/SiO_2, was able to

largely preserve the Lgol stereochemistry (92%). However, in the latter case the initial Lgol hydrolysis step is equilibrium-limited, thus only allowing for a maximum t- and e-Lgol conversion of 58 and 83% respectively[29]. By using the Pt-WO_x/TiO_2 catalyst for the hydrogenolysis of Lgol to tetrol we achieved a high degree of stereochemistry preservation at near-complete Lgol conversion, because i) the rate of aldose-ketose isomerization that scrambles the C_2-OH stereocenter (observed in our previous work at 150°C)[22,29] is very low at 120°C, and ii) the bifunctional metal-acid catalyst hydrogenates DDM and DDG *in situ* at a higher rate than isomerization to DDF (evidenced by the absence of intermediates at ~90% conversion), enabling complete Lgol conversion.

2.3.2. Kinetic parameter measurements

2.3.2.1. Reaction orders of Lgol and H_2

Reaction orders and the apparent activation energy for Lgol conversion were measured in a batch reactor using 10, 20 and 30wt% aqueous Lgol solutions and a fixed pressure of 1000 psi H_2. Figure 2-3 shows the normalized reactant concentration versus time and the resulting first order model fit for the whole dataset done with equation (2-5). The value obtained for the first-order rate constant k is 0.071 ± 0.004 h^{-1} (95% confidence interval-based, as are all the function fits hereafter). This value is consistent with one calculated from the product concentration (See Figure 7-3) which has larger error of 0.006 h^{-1} due to the overlap of several of the products (tetrol and intermediates) at lower conversions (<20%) compared to higher ones (~40%). The maximum total number of turnovers for the batch reactions were 540 $mmol/mmol_{acid}$ and 5542 $mmol/mmol_{Pt}$ (surface sites).

Three experiments were carried out at 600, 800 or 1000 psi H_2 and 20 wt% Lgol to measure the reaction order with respect to H_2. As shown in Figure 2-4 the reaction is zero-order in H_2.

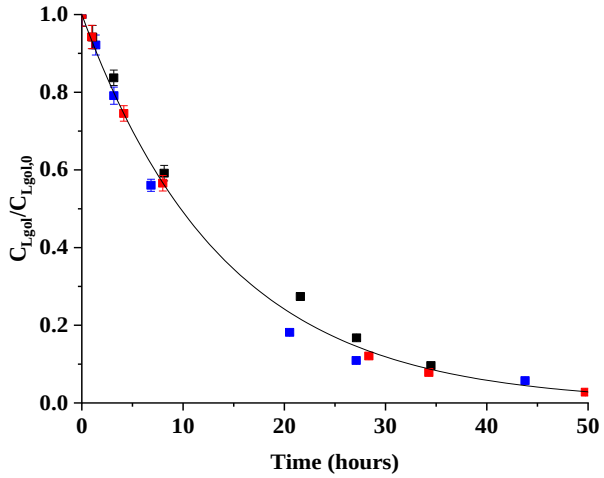

Figure 2-3. Normalized Lgol concentration vs time in batch reactor and first order fit for Lgol hydrogenolysis in water with Lgol concentration feeds of 10wt% (■), 20wt% (■) and 30wt% (■) using the Pt-WO_x/TiO_2 catalyst. Black line is Lgol first order function fit described by equation (2-5), where $\boldsymbol{k = 0.071 \pm 0.004}$, adjusted $R^2 = 0.9951$. Conditions: 120°C, 1000 psi H_2, 40-45 mL Lgol feed, 200 mg catalyst.

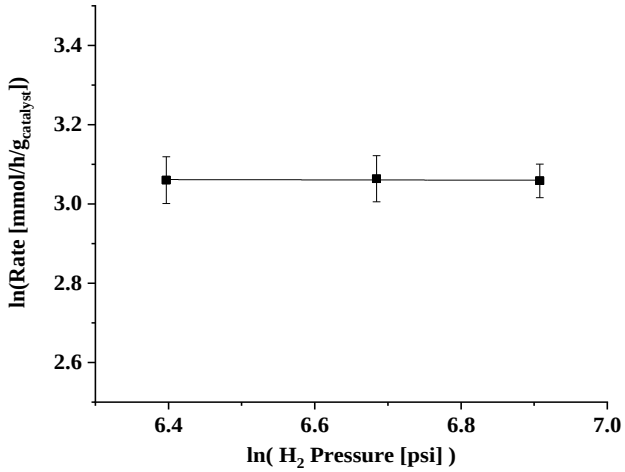

Figure 2-4. Hydrogen reaction order (n_{H2}) plot for Lgol hydrogenolysis in water in a batch reactor using the Pt-WO_x/TiO_2 catalyst. $\boldsymbol{n_{H2} = 0.00 \pm 0.02}$. Conditions: 120°C, 35-40 mL aqueous 20wt% Lgol feed, 175-200 mg catalyst, 600, 800 or 1000 psi H_2.

The reaction orders obtained for this work are similar to those obtained by Krishna et al.[22] for Lgol conversion in polar aprotic solvent (THF), where the major product (THFDM) is formed via irreversible, rate-limiting acid-catalyzed C-O bond cleavage followed by metal-catalyzed hydrogenation to THFDM.[22] The reaction orders obtained in this work fit the interpretation of an irreversible acid-catalyzed C-O bond cleavage step followed by hydrogenation on a metal site. If acid-catalyzed Lgol hydrolysis were reversible, a positive H_2 dependence might be expected because hydrogenation would promote the rate of Lgol hydrolysis by shifting the equilibrium to the products of that reaction step. However, it is also possible that the zeroth reaction order for H_2 is a consequence of metal sites being saturated by H_2.

2.3.2.2. Activation energy for Lgol conversion in water

The apparent activation energy of Lgol hydrogenolysis in water was calculated by performing experiments at 100 – 130 °C with 20wt% Lgol aqueous feeds. The apparent activation energy was found to be 151 ± 10 kJ/mol, as shown in Figure 2-5. This apparent activation energy value is higher than those reported in literature for hydrogenolysis of C-O bonds of cyclic ethers[24] (84 – 118 kJ/mol), and also higher than the computed activation energy of Lgol hydrolysis with H_2SO_4 catalyst (t-Lgol to DDM: 86 kJ/mol; e-Lgol to DDG: 98 kJ/mol) in water[38].

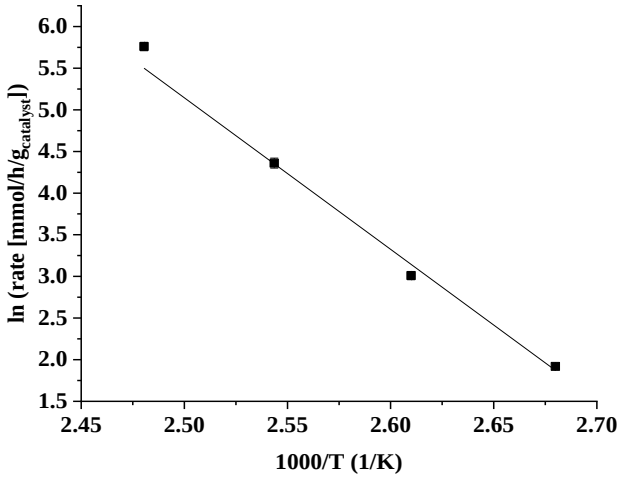

Figure 2-5. Activation energy plot for Lgol hydrogenolysis in water using the Pt-WO_x/TiO_2 catalyst done with equation (2 – 6). $\boldsymbol{E_{App}}$ **= 151 ± 10 KJ/mol**, adjusted R^2 = 0.9904. Reaction conditions: 1000 psi H_2, 40 mL aqueous 20wt% Lgol feed, 50-200 mg catalyst, 100, 110, 120 or 130°C.

2.3.3. Catalyst performance and stability and activity in flow reactor

Figure 2-6 shows the performance of the Pt-WO_x/TiO_2 catalyst for the hydrogenolysis of a 30wt% aqueous Lgol solution at 120°C over 51h time-on-stream (TOS). The number of turnovers for this catalyst during the time period (~51h) based on surface metal and acid sites are 1435 mmol/mmol$_{Pt}$ (CO chemisorption) and 400 mmol/mmol$_{acid}$ (NH_3-TPD) respectively. The catalyst deactivated with TOS. The catalyst was found to produce tetrol and its intermediates (DDM, DDG and DDF) initially in yields over 50% for conversions over 80%. HTri was also detected in the products, with yields being over 20% at initial times.

The selectivity of tetrol and its intermediates, and HTri is analyzed at the different conversions measured over time as observed in Figure 2-7. The tetrol selectivity decreases as conversion increases. The HTri selectivity decreases slightly with conversion from 23% at 88% conversion to 16% at 29% conversion. The HTri selectivity in the continuous flow reactor is much higher than

the values obtained for batch experiments (1-6%). We hypothesize this discrepancy between batch and flow experiments may occur either due to i) differences in the way the H_2 is added to the reactors if the HTri reaction is positive order in H_2 or due to ii) deactivation effects or a combination of both. In the former case, in a batch reactor H_2 will have to diffuse in water and then into the catalyst particle, whereas in the flow reactor the liquid will be saturated by H_2 when it comes in contact with the catalyst. An example of this effect is seen in the aqueous-phase hydrogenation of acetic acid using Ru catalysts, in which at 150 – 200°C, methane is the main product when the reaction is carried out in a batch reactor[39], but when the reaction is done in flow reactors, the main product is ethanol[40]. Such differences in H_2 supply will have an effect in HTri formation rates if it has non-zero order on H_2, favoring its formation if this reaction order is positive. In regards deactivation effects, by using the rate constant value calculated from the batch reactor adjusted for the catalyst amount, and volume and concentration differences between the batch and flow reactors, the calculated conversion obtained at the weight-hourly space velocity (WHSV) in the flow reactor (0.605 $g_{Lgol}g_{cat}^{-1}h^{-1}$), by replacing in equation (2-7), it can be observed that the estimated conversion would be close to 100%. The projected conversion at $t \rightarrow 0$ is >90%. Hence, deactivation would affect rates of product formations, having a higher impact on HTri since its rates are lower. Moreover, if we consider that HTri may be a series product from tetrol as would indicate the trend in Figure 2-7 and the fact that it is not observed at low conversion in the batch reactor experiments, it is then reasonable to assume that in the batch reactor by the time HTri is formed, catalyst deactivation would have a significant enough effect on its formation rate to lower its selectivity.

Often in biomass catalytic conversion reactions, increased reactant concentrations lead to lower selectivity to monomeric products due to oligomerization reactions that form undesired

degradation products ("humins").[41,42] In this work, product samples were dark brown, suggesting the formation of oligomeric humins. However, carbon balances (100%[1 - C_{out}/C_{in}]) were 98% on average, indicating that selectivity was mostly to detectable products. The full C-balance profile over time on stream can be observed in Figure 2-6. At initial data points (<10h TOS), C-balances were on the lower side, indicating potential carbon loss to undetectable products. At the last data point (51h TOS), C-balance shows an accumulation of ~10% carbon compared to the initial source, which may occur due to water evaporation.

The spent catalyst was calcined at 450°C for 4h (1°C/min) and re-reduced at 250°C for 2h (1°C/min), and the continuous flow reaction experiment was subsequently repeated. The result is shown in Figure 7-7. The catalyst regained some of its reactivity, but its initial conversion was 51%, being lower than the fresh catalyst (88%). Therefore, the catalyst was concluded to be only partially regenerable.

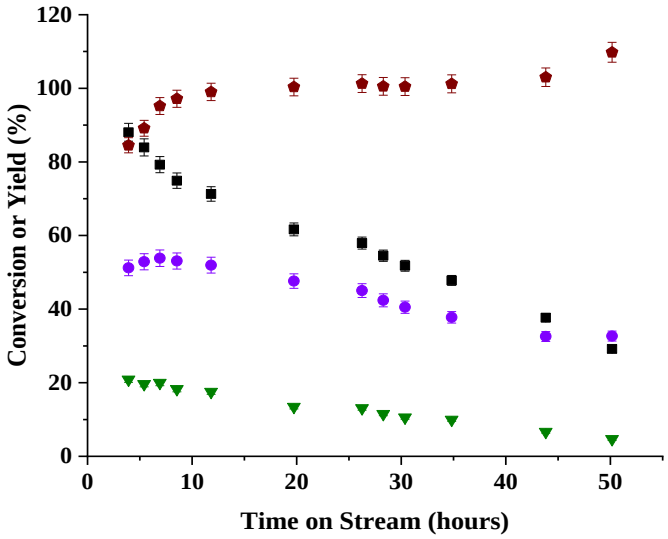

Figure 2-6. Conversion (■), yields of tetrol + intermediates (●) and HTri (▼), and carbon balances (⬟) vs time on stream for Lgol hydrogenolysis in a flow reactor using the Pt-WO_x/TiO_2 catalyst. **Reaction conditions:** 30wt% aqueous Lgol feed, 120°C, 620 psi H_2, 500 mg catalyst, 20 µL/min liquid flow, 40 mL/min H_2 flow.

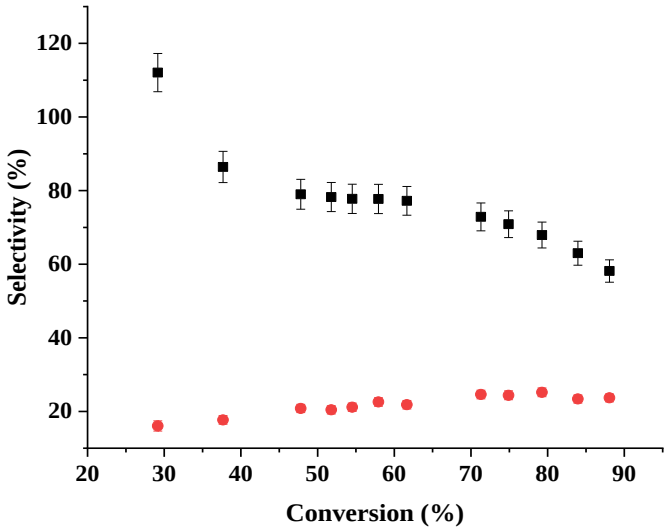

Figure 2-7. Selectivity of detected products tetrol + intermediates (■) and HTri (●) vs conversion for Lgol hydrogenolysis in a flow reactor using the Pt-WO_x/TiO_2 catalyst.
Conditions as described in Figure 2-6.

We measured the concentrations of Pt and W in the product effluent[25]. W was found to leach into the product effluent, while no Pt leaching was detected. The results of W-leaching for the first flow reaction run are shown in Figure 2-8. The concentration of leached W decreased with time on stream. The total amount of W leached in the continuous flow experiment with the fresh catalyst corresponds to 3.7% of the total W mass of the fresh catalyst. W-leaching during the second run (following catalyst regeneration) is shown in Figure 7-8. W-leaching rate is similar to that at the end of the first run, suggesting that W-leaching rate decreases and even stabilizes as more of the metal is lost to the product solution.

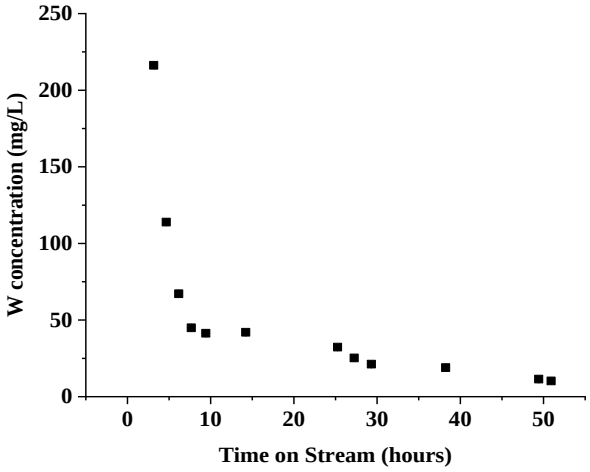

Figure 2-8. W leached detected in products as a function of time on stream in the first run with Pt-WO_x/TiO_2 over 51h. Conditions as described in Figure 2-6.

TGA and TOC analyses on the spent catalyst samples were used to determine the amount of carbon deposited on the catalyst during continuous flow experiments. Figure 2-9 contains the weight loss profile of the spent sample compared to the fresh. Two peaks at around 200°C and 225°C were observed. The TOC analysis showed that 11% of the catalyst mass was carbon compared to 2% of the fresh catalyst. The TOC results roughly match the weight loss showed between the two peaks attributed to carbon between 150 - 250°C by TGA. The wide peak that occurs at about 120°C then can be attributed mostly to water adsorbed in the catalyst from the reactant feed and the environment. The fresh calcined catalyst shows no significant mass loss over time (~1.5%). These results indicate that carbonaceous species are deposited on the catalyst surface during reaction and could thus contribute to catalyst deactivation. These species are removed by the regeneration treatment used here (450°C calcination followed by reduction in situ at 250°C). Deposition of carbonaceous species could contribute to catalyst deactivation but cannot explain the irreversible loss of reactivity despite regeneration treatments.

It is therefore noted that the different deactivation mechanisms at play may affect product selectivity and result in the discrepancies between batch and flow reactor results, especially if the rate in which each type of active site is deactivated differs significantly. Leaching for instance has the potential to be more pervasive for flow experiments than from batch due to W being completely lost in the liquid stream, whereas in the batch it may still remain active in solution. Also, intrinsic differences in the way H_2 is added between batch and flow reactors and initial conversion differences between the two of them may also affect the rate of coking of the catalyst, since it is noted that in batch experiments the reaction was able to be run at near-complete conversions for different Lgol feeds, requiring in some cases more turnovers for this than reported for the continuous flow experiment (up to 540 mmol/mmol$_{acid}$ in the batch vs 400 mmol/mmol$_{acid}$ in the flow reactor as shown in Figure 2-10).

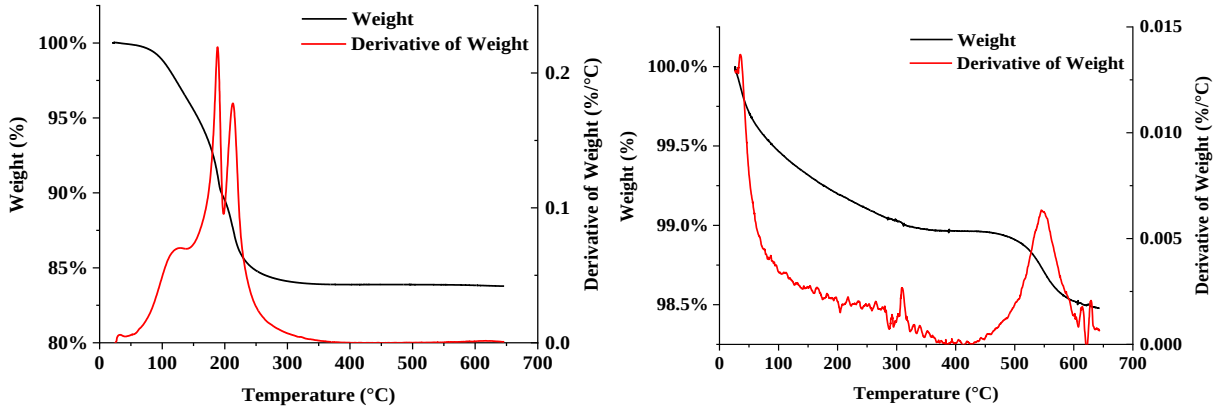

Figure 2-9. TGA weight loss profile for the Pt-WO_x/TiO_2 spent (left) and fresh (right) catalyst.

Finally, a (5wt%) Pt/SiO_2-Al_2O_3 catalyst was studied for Lgol hydrogenolysis with a 2wt% aqueous Lgol at 150°C. Figure 2-10 shows the number of turnovers (in surface acid sites) for Pt/SiO_2-Al_2O_3 and Pt-WO_x/TiO_2. The Pt-WO_x/TiO_2 is more stable and active than the Pt/SiO_2-Al_2O_3. Figure 7-9 shows the conversion vs time on stream profile for 5wt%Pt/SiO_2-Al_2O_3, it can

be observed that the catalyst deactivates over 45 h TOS. Treatment of the spent Pt/SiO_2-Al_2O_3 catalyst via calcination in air at 400°C and reduction at 260°C for 1h did not regenerate the catalytic reactivity (5% initial conversion was measured in a subsequent continuous flow experiment). Amorphous silica-aluminas are known to undergo irreversible deactivation in water at high temperature[42,43]. From this performance comparison and the information presented in this study it can be reasonably argued that 10wt%Pt-10wt%WO_x/TiO_2 can be used at lower temperatures and still retain significant activity.

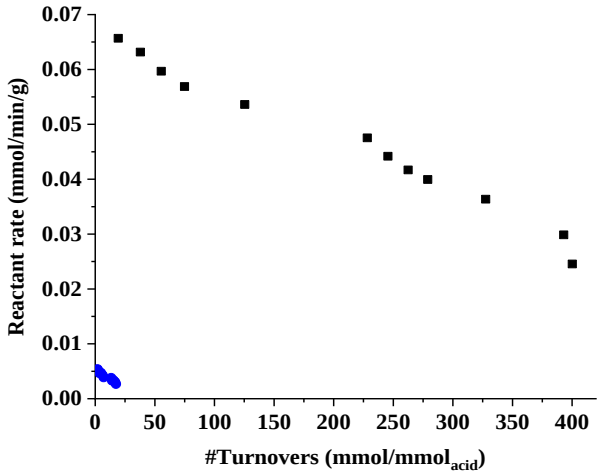

Figure 2-10. Reactant rates with number of turnovers (surface acid site basis) for Pt-WO_x/TiO_2 (■) and Pt/SiO_2-Al_2O_3 (●) catalysts. **Conditions:** For Pt-WO_x/TiO_2 as described in Figure 2-6. For Pt/SiO_2-Al_2O_3: 2 wt% aqueous Lgol feed, 130°C, 500 psi H_2, 200 mg catalyst, 30 µL/min feed flow, 6 mL/min H_2 flow.

2.4. Conclusions

Hydrogenolysis of Lgol was carried out in water under high reactant concentrations (i.e. 10-30 wt%) using (10wt%)Pt-(10wt%)WO_x/TiO_2 catalyst. The catalyst is highly selective to tetrol and its intermediates (e.g. >90% selectivity at >20% conversion in batch reactor). The catalyst showed deactivation but is more stable than a 5wt%Pt/SiO_2-Al_2O_3. The catalyst activity can be partially

recovered by a re-reduction/oxidation treatment. The reaction is first order with respect to Lgol and zero order with respect to H_2. The observed kinetics are consistent with irreversible acid-catalyzed C-O bond cleavage of Lgol to form intermediates that are then hydrogenated to tetrol. This route largely preserves the stereocenters in the Lgol feedstock, converting t-Lgol to (*S*,*S*)-tetrol and e-Lgol to (*S*,*R*)-tetrol with 91% overall preservation of the C_2 stereocenters. Stereocenter preservation implies that reactive aldose intermediates (DDM, DDG) formed over acid sites are rapidly hydrogenated over metal sites at rates much higher than their isomerization to ketose (DDF) intermediates that erase the C_2 stereocenter.

Future work on this research may be focused on lowering noble metal loadings to determine i) the effect of metal loading in product selectivity and confirm whether H_2 is strongly bound to the active sites or not to completely explain the interpretation provided on the reaction orders obtained and ii) determining recyclability of an optimized Pt-WO_x catalyst formulation. The use of less expensive hydrogenating metals for this reaction may be considered. Further work may also be done in the studying the kinetics of HTri from Lgol or Tetrol.

2.5. References

(1) Krishna, S. H.; Walker, T. W.; Dumesic, J. A.; Huber, G. W. Kinetics of Levoglucosenone Isomerization. *ChemSusChem* **2017**, *10* (1), 129–138. https://doi.org/10.1002/cssc.201601308.

(2) Flourat, A. L.; Peru, A. A. M.; Teixeira, A. R. S.; Brunissen, F.; Allais, F. Chemo-Enzymatic Synthesis of Key Intermediates (S)-γ-Hydroxymethyl-α,β-Butenolide and (S)-γ-Hydroxymethyl-γ-Butyrolactone via Lipase-Mediated Baeyer–Villiger Oxidation of Levoglucosenone. *Green Chem.* **2015**, *17* (1), 404–412. https://doi.org/10.1039/C4GC01231C.

(3) Stockton, K. P.; Greatrex, B. W. Synthesis of Enantiopure Cyclopropyl Esters from (−)-Levoglucosenone. *Org. Biomol. Chem.* **2016**, *14* (31), 7520–7528. https://doi.org/10.1039/C6OB00933F.

(4) Giri, G. F.; Danielli, M.; Marinelli, R. A.; Spanevello, R. A. Cytotoxic Effect of Levoglucosenone and Related Derivatives against Human Hepatocarcinoma Cell Lines. *Bioorganic & Medicinal Chemistry Letters* **2016**, *26* (16), 3955–3957. https://doi.org/10.1016/j.bmcl.2016.07.007.

(5) Giri, G. F.; Viarengo, G.; Furlán, R. L. E.; Suárez, A. G.; Garcia Véscovi, E.; Spanevello, R. A. Soybean Hulls, an Alternative Source of Bioactive Compounds: Combining Pyrolysis with Bioguided Fractionation. *Industrial Crops and Products* **2017**, *105*, 113–123. https://doi.org/10.1016/j.indcrop.2017.05.005.

(6) Shafizadeh, F.; Furneaux, R. H.; Stevenson, T. T. Some Reactions of Levoglucosenone. *Carbohydrate Research* **1979**, *71* (1), 169–191. https://doi.org/10.1016/S0008-6215(00)86069-3.

(7) Sherwood, J.; De bruyn, M.; Constantinou, A.; Moity, L.; McElroy, C. R.; Farmer, T. J.; Duncan, T.; Raverty, W.; Hunt, A. J.; Clark, J. H. Dihydrolevoglucosenone (Cyrene) as a Bio-Based Alternative for Dipolar Aprotic Solvents. *Chem. Commun.* **2014**, *50* (68), 9650–9652. https://doi.org/10.1039/C4CC04133J.

(8) De bruyn, M.; Cuello-Penaloza, P.; Cendejas, M.; Hermans, I.; He, J.; Krishna, S. H.; Lynn, D. M.; Dumesic, J. A.; Huber, G. W.; Weckhuysen, B. M. Hexane-1,2,5,6-Tetrol as a Versatile and Biobased Building Block for the Synthesis of Sustainable (Chiral) Crystalline Mesoporous Polyboronates. *ACS Sustainable Chem. Eng.* **2019**, *7* (15), 13430–13436. https://doi.org/10.1021/acssuschemeng.9b02772.

(9) Wilson, K. L.; Kennedy, A. R.; Murray, J.; Greatrex, B.; Jamieson, C.; Watson, A. J. B. Scope and Limitations of a DMF Bio-Alternative within Sonogashira Cross-Coupling and Cacchi-Type Annulation. *Beilstein J. Org. Chem.* **2016**, *12*, 2005–2011. https://doi.org/10.3762/bjoc.12.187.

(10) Tamura, M.; Nakagawa, Y.; Tomishige, K. Reduction of Sugar Derivatives to Valuable Chemicals: Utilization of Asymmetric Carbons. *Catal. Sci. Technol.* **2020**, *10* (12), 3805–3824. https://doi.org/10.1039/D0CY00654H.

(11) Krishna, S. H.; Cao, J.; Tamura, M.; Nakagawa, Y.; De Bruyn, M.; Jacobson, G. S.; Weckhuysen, B. M.; Dumesic, J. A.; Tomishige, K.; Huber, G. W. Synthesis of Hexane-Tetrols and -Triols with Fixed Hydroxyl Group Positions and Stereochemistry from Methyl Glycosides over Supported Metal Catalysts. *ACS Sustainable Chem. Eng.* **2020**, *8* (2), 800–805. https://doi.org/10.1021/acssuschemeng.9b04634.

(12) Warmington, A. Consortium to build Cyrene plant https://www.specchemonline.com/consortium-build-cyrene-plant (accessed 2020-05-12).

(13) Flagship EU Project aiming to Replace Toxic Solvents with Renewable Alternatives Launches today https://circa-group.com/news/2020/10/24/9axo6z01ddll227lq24abjs2g5mbyz (accessed 2021-03-24).

(14) De Bruyn, M.; Fan, J.; Budarin, V. L.; Macquarrie, D. J.; Gomez, L. D.; Simister, R.; Farmer, T. J.; Raverty, W. D.; McQueen-Mason, S. J.; Clark, J. H. A New Perspective in Bio-Refining: Levoglucosenone and Cleaner Lignin from Waste Biorefinery Hydrolysis Lignin by Selective Conversion of Residual Saccharides. *Energy Environ. Sci.* **2016**, *9* (8), 2571–2574. https://doi.org/10.1039/C6EE01352J.

(15) Stock announcements https://circa-group.com/stock-announcements (accessed 2021-06-11).

(16) Cao, F.; Schwartz, T. J.; McClelland, D. J.; Krishna, S. H.; Dumesic, J. A.; Huber, G. W. Dehydration of Cellulose to Levoglucosenone Using Polar Aprotic Solvents. *Energy Environ. Sci.* **2015**, *8* (6), 1808–1815. https://doi.org/10.1039/C5EE00353A.

(17) Mazarío, J.; Romero, M. P.; Concepción, P.; Chávez-Sifontes, M.; Spanevello, R. A.; Comba, M. B.; Suárez, A. G.; Domine, M. E. Tuning Zirconia-Supported Metal Catalysts for Selective One-Step Hydrogenation of Levoglucosenone. *Green Chem.* **2019**, *21* (17), 4769–4785. https://doi.org/10.1039/C9GC01857C.

(18) Milescu, R. A.; Zhenova, A.; Vastano, M.; Gammons, R.; Lin, S.; Lau, C. H.; Clark, J. H.; McElroy, C. R.; Pellis, A. Polymer Chemistry Applications of Cyrene and Its Derivative Cygnet 0.0 as Safer Replacements for Polar Aprotic Solvents. *ChemSusChem* **2021**, *14* (16), 3367–3381. https://doi.org/10.1002/cssc.202101125.

(19) De bruyn, M.; Budarin, V. L.; Misefari, A.; Shimizu, S.; Fish, H.; Cockett, M.; Hunt, A. J.; Hofstetter, H.; Weckhuysen, B. M.; Clark, J. H.; Macquarrie, D. J. Geminal Diol of Dihydrolevoglucosenone as a Switchable Hydrotrope: A Continuum of Green Nanostructured Solvents. *ACS Sustainable Chem. Eng.* **2019**, *7* (8), 7878–7883. https://doi.org/10.1021/acssuschemeng.9b00470.

(20) De bruyn, M.; Sener, C.; Petrolini, D. D.; McClelland, D. J.; He, J.; Ball, M. R.; Liu, Y.; Martins, L.; Dumesic, J. A.; Huber, G. W.; Weckhuysen, B. M. Catalytic Hydrogenation of Dihydrolevoglucosenone to Levoglucosanol with a Hydrotalcite/Mixed Oxide Copper Catalyst. *Green Chem.* **2019**, *21* (18), 5000–5007. https://doi.org/10.1039/C9GC00564A.

(21) Krishna, S. H.; McClelland, D. J.; Rashke, Q. A.; Dumesic, J. A.; Huber, G. W. Hydrogenation of Levoglucosenone to Renewable Chemicals. *Green Chem.* **2017**, *19* (5), 1278–1285. https://doi.org/10.1039/C6GC03028A.

(22) Krishna, S. H.; Assary, R. S.; Rashke, Q. A.; Schmidt, Z. R.; Curtiss, L. A.; Dumesic, J. A.; Huber, G. W. Mechanistic Insights into the Hydrogenolysis of Levoglucosanol over Bifunctional Platinum Silica–Alumina Catalysts. *ACS Catal.* **2018**, *8* (5), 3743–3753. https://doi.org/10.1021/acscatal.7b03764.

(23) Buntara, T.; Melián-Cabrera, I.; Tan, Q.; Fierro, J. L. G.; Neurock, M.; Vries, J. G. D.; Heeres, H. J. Catalyst Studies on the Ring Opening of Tetrahydrofuran-Dimethanol to 1,2,6-Hexanetriol. *Catalysis Today* **2013**, *210*, 106–116. https://doi.org/10.1016/j.cattod.2013.04.012.

(24) Chia, M.; Pagán-Torres, Y. J.; Hibbitts, D.; Tan, Q.; Pham, H. N.; Datye, A. K.; Neurock, M.; Davis, R. J.; Dumesic, J. A. Selective Hydrogenolysis of Polyols and Cyclic Ethers over Bifunctional Surface Sites on Rhodium–Rhenium Catalysts. *J. Am. Chem. Soc.* **2011**, *133* (32), 12675–12689. https://doi.org/10.1021/ja2038358.

(25) He, J.; Burt, S. P.; Ball, M. R.; Hermans, I.; Dumesic, J. A.; Huber, G. W. Catalytic C-O Bond Hydrogenolysis of Tetrahydrofuran-Dimethanol over Metal Supported WOx/TiO2 Catalysts. *Applied Catalysis B: Environmental* **2019**, *258*, 117945. https://doi.org/10.1016/j.apcatb.2019.117945.

(26) He, J.; Burt, S. P.; Ball, M.; Zhao, D.; Hermans, I.; Dumesic, J. A.; Huber, G. W. Synthesis of 1,6-Hexanediol from Cellulose Derived Tetrahydrofuran-Dimethanol with Pt-WO_x/TiO_2 Catalysts. *ACS Catal.* **2018**, *8* (2), 1427–1439. https://doi.org/10.1021/acscatal.7b03593.

(27) Allgeier, A. M.; Ritter, J. C.; Sengupta, S. K. Process for Preparing 1,6-Hexanediol. 20130231505, September 5, 2013.

(28) Allgeier, A. M.; Silva, W. I. N. D.; Korovessi, E.; Menning, C. A.; Ritter, J. C.; Sengupta, S. K.; Stauffer, C. S. Process for Preparing 1,6-Hexanediol. US8865940B2, October 21, 2014.

(29) Krishna, S. H.; De bruyn, M.; Schmidt, Z. R.; Weckhuysen, B. M.; Dumesic, J. A.; Huber, G. W. Catalytic Production of Hexane-1,2,5,6-Tetrol from Bio-Renewable Levoglucosanol in Water: Effect of Metal and Acid Sites on (Stereo)-Selectivity. *Green Chem.* **2018**, *20* (19), 4557–4565. https://doi.org/10.1039/C8GC02455C.

(30) Stensrud, K.; Ma, C.c. Synthesis of R-Glucosides, Sugar Alcohols, Reduced Sugar Alcohols, and Furan Derivatives of Reduced Sugar Alcohols. US20170044123A1, 2017.

(31) Smith, B.; Ma, C. Process for the Isolation of 1,2,5,6-Hexanetetrol from Sorbitol Hydrogenolysis Reaction Mixtures Using Simulated Moving Bed Chromatography. US20170066702A1, March 9, 2017.

(32) Chia, M.; O'Neill, B. J.; Alamillo, R.; Dietrich, P. J.; Ribeiro, F. H.; Miller, J. T.; Dumesic, J. A. Bimetallic RhRe/C Catalysts for the Production of Biomass-Derived Chemicals. *Journal of Catalysis* **2013**, *308*, 226–236. https://doi.org/10.1016/j.jcat.2013.08.008.

(33) Koso, S.; Ueda, N.; Shinmi, Y.; Okumura, K.; Kizuka, T.; Tomishige, K. Promoting Effect of Mo on the Hydrogenolysis of Tetrahydrofurfuryl Alcohol to 1,5-Pentanediol over Rh/SiO2. *Journal of Catalysis* **2009**, *267* (1), 89–92. https://doi.org/10.1016/j.jcat.2009.07.010.

(34) Koso, S.; Watanabe, H.; Okumura, K.; Nakagawa, Y.; Tomishige, K. Stable Low-Valence ReO_x Cluster Attached on Rh Metal Particles Formed by Hydrogen Reduction and Its Formation Mechanism. *J. Phys. Chem. C* **2012**, *116* (4), 3079–3090. https://doi.org/10.1021/jp2114225.

(35) Koso, S.; Watanabe, H.; Okumura, K.; Nakagawa, Y.; Tomishige, K. Comparative Study of Rh–MoOx and Rh–ReOx Supported on SiO2 for the Hydrogenolysis of Ethers and Polyols. *Applied Catalysis B: Environmental* **2012**, *111–112*, 27–37. https://doi.org/10.1016/j.apcatb.2011.09.015.

(36) Tamura, M.; Yuasa, N.; Cao, J.; Nakagawa, Y.; Tomishige, K. Transformation of Sugars into Chiral Polyols over a Heterogeneous Catalyst. *Angewandte Chemie International Edition* **2018**, *57* (27), 8058–8062. https://doi.org/10.1002/anie.201803043.

(37) Cao, J.; Tamura, M.; Nakagawa, Y.; Tomishige, K. Direct Synthesis of Unsaturated Sugars from Methyl Glycosides. *ACS Catal.* **2019**, *9* (4), 3725–3729. https://doi.org/10.1021/acscatal.9b00589.

(38) Cao, J.; Tamura, M.; Hosaka, R.; Nakayama, A.; Hasegawa, J. Y.; Nakagawa, Y.; Tomishige, K. Mechanistic Study on Deoxydehydration and Hydrogenation of Methyl Glycosides to Dideoxy Sugars over a ReO X-Pd/CeO2Catalyst. *ACS Catalysis* **2020**, *10* (20), 12040–12051. https://doi.org/10.1021/acscatal.0c02309.

(39) Zhou, M.; Krishna, S. H.; De bruyn, M.; Weckhuysen, B. M.; Curtiss, L. A.; Dumesic, J. A.; Huber, G. W.; Assary, R. S. Mechanistic Insights into the Conversion of Biorenewable Levoglucosanol to Dideoxysugars. *ACS Sustainable Chem. Eng.* **2020**, *8* (43), 16339–16349. https://doi.org/10.1021/acssuschemeng.0c06315.

(40) Wan, H.; Chaudhari, R. V.; Subramaniam, B. Aqueous Phase Hydrogenation of Acetic Acid and Its Promotional Effect on P-Cresol Hydrodeoxygenation. *Energy Fuels* **2013**, *27* (1), 487–493. https://doi.org/10.1021/ef301400c.

(41) Olcay, H.; Xu, Y.; Huber, G. W. Effects of Hydrogen and Water on the Activity and Selectivity of Acetic Acid Hydrogenation on Ruthenium. *Green Chem.* **2014**, *16* (2), 911–924. https://doi.org/10.1039/C4GC00011K.

(42) van Putten, R.-J.; van der Waal, J. C.; de Jong, E.; Rasrendra, C. B.; Heeres, H. J.; de Vries, J. G. Hydroxymethylfurfural, A Versatile Platform Chemical Made from Renewable Resources. *Chem. Rev.* **2013**, *113* (3), 1499–1597. https://doi.org/10.1021/cr300182k.

(43) *Reaction Pathways and Mechanisms in Thermocatalytic Biomass Conversion II: Homogeneously Catalyzed Transformations, Acrylics from Biomass, Theoretical Aspects, Lignin Valorization and Pyrolysis Pathways*; Schlaf, M., Zhang, Z. C., Eds.; Green Chemistry and Sustainable Technology; Springer Singapore: Singapore, 2016. https://doi.org/10.1007/978-981-287-769-7.

(44) Xiong, H.; Pham, H. N.; Datye, A. K. Hydrothermally Stable Heterogeneous Catalysts for Conversion of Biorenewables. *Green Chem.* **2014**, *16* (11), 4627–4643. https://doi.org/10.1039/C4GC01152J.

Chapter 3: Hexane-1,2,5,6-tetrol as a Versatile and Biobased Building Block for the Synthesis of Sustainable (Chiral) Crystalline Mesoporous Polyboronates

3.1. Introduction

Mesoporous materials have attracted significant attention as their wide pores (2−50 nm) allow for improved diffusion and accessibility, favoring applications as diverse as, controlled drug release, chromatography, adsorbents, electrodes, solar cells, and heterogeneous catalysis.[1,2] Exemplary are (non)siliceous mesoporous oxides, periodic mesoporous organic silicas (PMOs), mesoporous carbons, hyperconjugated porous polymers, and some metal−organic frameworks.[3–7] Often the introduction of mesopores in a material is linked to the use of (supra)molecular templates such as surfactants, but also other techniques are known like dealumination/desiliciation, nanoassemblies, and local associations of helices, among others.[1,8]

Boronate ester polymers (BEP) and their tendency to form hierarchical supramolecular structures have been widely reported in the literature.[9] However, few micro/mesoporous materials have been reported based on 1D polymeric boronate esters containing backbones not involving heteroatoms (e.g., nitrogen, sulfur). Exemplary are the flowerlike micro/mesoporous microparticles made by the condensation of 1,4-benzenediboronic acid (1,4-BDB) with pentaerythritol (PE). These

The content of this Chapter is adapted with permission of the American Chemical Society from the following reference: De bruyn, M.; Cuello-Penaloza, P.; Cendejas, M.; Hermans, I.; He, J.; Krishna, S. H.; Lynn, D. M.; Dumesic, J. A.; Huber, G. W.; Weckhuysen, B. M. Hexane-1,2,5,6-Tetrol as a Versatile and Biobased Building Block for the Synthesis of Sustainable (Chiral) Crystalline Mesoporous Polyboronates. *ACS Sustainable Chemistry and Engineering* 2019, 7 (15), 13430–13436. https://pubs.acs.org/doi/10.1021/acssuschemeng.9b02772. M.de B. led research into polyboronates, and performed polymer synthesis and reactant purification and analysis, P.C. edited the manuscript. P.C. and M.C. Performed characterizations, P.C., J. H. and S.H.K. provided revisions. P.C. and S.H.K. provided hexane-1,2,5,6-tetrol.

materials have a specific surface area of 184 $m^2 g^{-1}$ (BET), yet no data on pore volume and pore size has been published.[10,11] Notably, the functionalization of these materials with Au or Pd nanoparticles allowed for (chemoselective) catalytic reduction reactions. [10,11] Mixing diboronic acid with a chiral indacene-type *bis*(1,2-diol) gave trimeric microporous cages with surface areas (SAs) of 491 and 582 $m^2 g^{-1}$.[12] Hierarchical structures using dative B−N bonds have also been reported.[9,13] A relative recent addition are the covalent 2D/3D organic frameworks (COFs). These are micro/mesoporous materials where rigid building blocks, often with a specific geometry and/or symmetry, are interconnected through covalent bonds forming 2D/3D rigid crystalline porous structures.[14] Most typically, the boron-based COFs employ catechol building blocks. To date no COF has been reported with a pore diameter larger than 5 nm. In addition, only a few chiral COFs are known, typically using chiral pyrrolidine and tartaric acid derivatives as the linking or pendant groups[15] Presently, no chiral boron-based COFs have been reported.

Very recently a novel COF class was introduced where helical polymers are interwoven at regular intervals by means of copper complexes.[16] Demetalation of this structure (named COF-505) was shown to retain its morphology, at the expense of a certain decrease in crystallinity.[16] Most importantly, owing to the large flexibility of the 1D threads in demetalated COF- 505, a 10-fold increase of its elasticity was observed.[17] Besides weaving, entanglement in porous frameworks can also be achieved by the interpenetration of 2D/3D frameworks or interlocking of rings.[17] In spite of the high surface areas and pore volumes, and the related plethora of potential and promising applications, the commercial use of mesoporous materials is still quite a challenge due to their chemical instability, expensive synthesis approaches, and nonstraightforward processability.[18] The cost of the extended linkers, which is especially relevant for COFs and MOFs, is another major

concern with, for instance, only two commercialized MOFs employing linkers with more than one phenyl ring.[19]

Our group has reported on the sustainable synthesis of hexane-1,2,5,6-tetrol[20,21] (HT in this chapter) in the previous chapter and related research. HT has two 1,2-diol moieties are joined by a flexible ethane bridge, making it suitable to be used as a copolymer. Boronic acids are abundantly available due to their importance in Suzuki–Miyaura coupling reactions.[22,23] They are generally considered nontoxic and are easy to synthesize.[22,24] In this chapter, the synthesis of a novel porous organic polymer obtained by reactive dissolution of sparingly soluble HT with simple benzenediboronic acids (BDB) and concomitant precipitation of the mesoporous HT polyboronate is reported. The reaction is conducted at room temperature and requires no special reaction conditions such as vacuum, inert atmosphere, or controlled water removal. It is shown that the properties of the resulting mesoporous polymers are largely determined by the chirality of HT and the meta/para orientation of the boronic acids on the phenyl ring. Thereby HT's chirality is likely inducing coiling of the polymer chain, allowing for interweaving of the polymeric chains. These materials are crystalline and in spite of their lower surface areas (30–90 $m^2 g^{-1}$) display mesopore volumes up to 0.441 mL g^{-1}. Figure 3-1A provides a visual of the potential polymeric chains indicative of their stereocenters and points of potential molecular rotation. Hereafter these materials are denoted as "HT/polyboronates" or more specifically using the HT/1,x-BDB/solvent formalism.

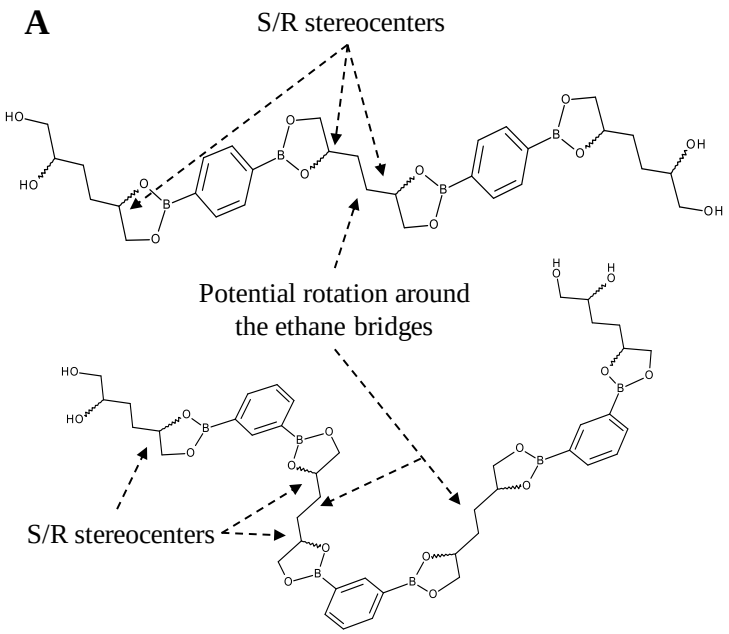

B: HT/polyboronate polymers using chiral (R,S)-HT:

(R-S)-BDB-(R-S)-BDB-(R-S)-
(R-S)-BDB-(R-S)-
(R-S)-BDB-(R-S)-BDB-(S-R)-
(R-S)-BDB *Extensive variability as the chiral polymeric chain grows*
(R-S)-BDB-(S-R)-BDB-(S-R)-
(R-S)-BDB-(S-R)-
(R-S)-BDB-(S-R)-BDB-(R-S)-

C: HT/polyboronate polymers using chiral (S,S)-HT:

(S-S)-BDB → (S,S)-BDB-(S,S)-BDB-(S,S)-BDB-(S,S)-BDB-(S,S)-BDB etc.

Unique chiral polymeric chain

Figure 3-1. A) Schematic visualization of two different HT-BDB polymeric chains with indication of the stereocenters and points of potential rotation of the molecular chains, and B) illustrative variability of the growing polymeric chain when incorporating chiral pure (R,S)-HT [shown as (R-S)] C) unique chiral polymer when constructing the polymeric chain from (*S*,*S*)-HT [shown as (S-S)].

3.2. Experimental Methods

3.2.1. Polymer synthesis

HT and a suitable multiboronic acid containing compound were added in equimolar quantities to a variable amount of a suitable solvent (typically 3-45 mL). The resulting suspension was allowed to stir for 48 h at RT, and in air, progressively dissolving the near insoluble HT while, at the same time, forming the polyboronate esters by reaction with a suitable diboronic acid and consequent precipitation. The resulting white product was filtered and washed with dried solvent (typically one of the following four: THF, acetone, acetonitrile, CH_2Cl_2 – see also Table 3-1 in section 3.3.) and dried overnight in air. Additionally drying was done in vacuum at 40 °C.

3.2.2. Polymer characterization

Scanning electron microscopy (SEM) was done using a LEO 1530 equipped with a Schottky-type field-emission electron source. This instrument uses a beam booster to maintain optimum electron optical performance at all accelerating voltages. In addition, the patented Gemini optical column has no crossovers and utilizes a magnetic/electrostatic objective lens for outstanding imaging capabilities, especially at low voltage (due to reduced chromatic aberration). Samples were prepared by putting them on a suitable dual side tape strip.

Attenuated total reflectance Fourier transform infrared (ATR-FTIR) spectroscopy measurements were recorded on a Bruker Vertex 70 spectrometer equipped with a liquid nitrogen-cooled MCT detector. The ATR cell was a MIRacle single reflection cell with a diamond crystal (Pike Technologies), which was internally purged with dry nitrogen flow. Each spectrum averaged 128 scans with a 4 cm-1 resolution. A measurement of the blank diamond crystal was used as the

background and subtracted from all sample measurements. All samples were ground without dilution and then clamped down onto the crystal with a manually tightened die. Sample collection and analysis was completed using the OPUS software package (Bruker). X-ray diffraction (XRD) patterns were recorded on a Rigaku D/Max Rapid II diffractometer with a curved two-dimensional imaging plate (2D IP). The Mo Ka X-ray tube operates at 50kV and 50mA (rated at 2.5 KW).

Solid-state magic angle spinning (MAS) nuclear magnetic resonance (NMR) was performed on a 500 MHz NMR spectrometer operating at 11.7 T with a 4 mm probe and a spinning rate of 10 kHz. All MAS NMR spectra were indirectly referenced to an adamantane standard (δiso = 1.6 ppm). 11B spin echo spectra were recorded with a recycle delay time of 30 s and the quadrupolar peaks were analytically simulated using the solids line shape analyzer in TopSpin. Spinning sidebands in the 13C CPMAS spectra were confirmed by spinning the samples at both 10 kHz and 8 kHz. 11B fitting parameters for (*S*,*R*)-HT/1,4-BDB: δiso = 30.6 ppm, CQ = 2.87 MHz, η = 0.55; 11B fitting parameters for (*S*,*R*)-HT/1,3-BDB: δiso = 30.7 ppm, CQ = 2.85 MHz, η = 0.6. N2 physisorption experiments were performed at -196 °C on a Micromeritics ASAP 2020 Surface Area and Pore Volume Analyzer. Typically, 100 mg of sample was analyzed. Before analysis the samples were outgassed at 120 °C for 5h at 10-3 mbar. The BET model was applied for surface area determination and the BJH model for the determination of the total pore volume (mesopore and micropore volume) and t-plot for micropore volume determination. All properties were calculated from the desorption branch.

3.3. Results and Discussion

Table 3-1 lists the obtained specific surface areas (SAs) and pore volumes (PVs) as a function of the type of diboronic acid used, the applied solvent and HT's diastereomeric excess. It is found that meta orientation of the diboronic acids on the phenyl ring (1,3-BDB) is favored over para orientation (1,4-BDB) (Table 3-1, entries a/b). This suggests for a distinct influence of the curvature of the polymeric chain. Interestingly, the use of 4,4'-biphenyldiboronic acid (4,4'-BPDB) led to quasi equal results as obtained with 1,3-BDB (Table 3-1, entry c). This can be rationalized by the non-planarity of biphenyl units and the consequent absence of p-p stacking of the aromatic rings. The use of acetone or CH_2Cl_2 as the reaction solvents gives higher SAs and PVs than when THF or AcCN are used (Table 3-1, d-g). Additionally, the SA and PV values benefit also from higher reaction volumes (Table 3-1 - d,h,i).

Partial enrichment of (*S*,*R*)-HT over (*S*,*S*)-HT was described in previous publications of our group depending on the catalyst used.[20,21] Specific crystallization of the (*S*,*R*)-HT diastereomer was achieved from 1,4-dioxane, allowing for the evaluation of HT's chirality on the properties of the HT/polyboronates. Unfortunately it has presently not been found possible to crystallize/purify (*S*,*S*)-HT. It is noteworthy that (*S*,*R*)-HT is a mesomer, making that it displays no net chirality on its own but does so effectively in a polymeric setting. As though (*S*,*R*)-HT can built into the polymeric chain as [SR] or [RS], substantial variability in the curvature of the polymeric chain is likely present (scheme 1B/C). Actual and distinct influences of the diastereomeric (*S*,*S*)/(*S*,*R*) ratio in HT on the properties of the materials are observable:

A) In using 38% d.e. (diastereomeric excess) (*S*,*R*)-HT a higher SA and PV is obtained then when 38% d.e. (*S*,*S*)-HT is used (Table 3-1, entries g vs j)

B) Elevating the d.e. in (*S*,*R*)-HT from 38 to 98% is found to increase both the SA and PV by around 30% for HT/1,3-BDB/THF (Table 3-1, k vs d). In the case of HT/1,3-BDB/acetone only an SA increase of 30% is observed with an already high PV (Table 3-1, m vs g).

C) Using diastereomerically pure (*S*,*R*)-HT magnifies the effect of the meta/para orientation of BDB on the spread in SA and PV (Table 3-1, entries a,b,k,and l).

Table 3-1. Survey of the specific surface areas and specific pore volumes for a range of HT containing polyboronate esters.

Entry	Component one	Component two	Solvent*	Specific surface area ($m^2 g^{-1}$)	Specific pore volume (mL g^{-1})
a	HT 38% 1<2	1,4-BDB	THF	42	0.227
b	HT 38% 1<2	1,3-BDB	THF	65.8	0.408
c	HT 38% 1<2	4,4'-BPDB	THF	64.5	0.359
d	HT 38% 1>2	1,3-BDB	THF	60.5	0.315
e	HT 38% 1>2	1,3-BDB	CH_2Cl_2	74.0	0.397
f	HT 38% 1>2	1,3-BDB	AcCN	61.2	0.290
g	HT 38% 1>2	1,3-BDB	Acetone	67.2	0.440
h	HT 38% 1>2	1,3-BDB	THF 5 mL	49.1	0.289
i	HT 38% 1>2	1,3-BDB	THF 45 mL	62.8	0.407
j	HT 38% 1<2	1,3-BDB	Acetone	51.3	0.271
k	HT 98% 1>2	1,3-BDB	THF	80.7	0.412
l	HT 98% 1>2	1,4-BDB	THF	32.8	0.148
m	HT 98% 1>2	1,3-BDB	Acetone	87.3	0.441

*Unless otherwise stated the used solvent volume is 15 mL; 1 = (*S*,*R*)-HT and 2 = (*S*,*S*)-HT; the 38 & 98 percentages refer to diastereomeric excesses (d.e.).

It is noteworthy that no cooperative stereochemical effect is present as hydrolysis of the formed HT/polyboronates does not reveal a preferential incorporation of one of the HT diastereomers.

Irrespective the nature of the HT/polyboronates, the obtained SA and PV values correlate to a certain degree (Figure 7-11).

The N_2 physisorption isotherms and associated pore size distribution of HT/1,3-BDB polymers made with different solvents are shown in Figure 3-2. As observed in Figure 3-2A, all materials display a type IV isotherm and an H3 hysteresis. The latter is indicative of aggregates of platelike particles forming slit-like pores.[25] This is reminiscent of the pentaerythrithol/1,4-BDB (PE/1,4-BDB) material reported by Fujiwara et al.[10] and Matsushima et al.[11] with that remark that here all measured N_2 desorption and N_2 adsorption curves re-join, strengthening our claim on sole mesoporous materials. Overall, larger variably sized mesopores spanning mainly the 5-50 nm Ø range (Figure 1B) are observed, with the apparent sharp peak denoting 3.7 nm Ø mesopores being an artifact of forced closure of the sorption hysteresis[26]. Thereby the use of THF as the reaction solvent favours apparently the occurrence of the 3.7 nm pore Ø while the larger mesopores are found to increase in dominance along the THF ~ CH_2Cl_2 < AcCN < acetone line.

The here reported maximal PV of 0.44 mL g^{-1} is comparable to the one reported for the [MeOAc]50-H2P (0.42 mL g^{-1}) COF.[27] The marked difference in SA between the HT/polyboronates and the latter COF material (90 $m^2 g^{-1}$ vs 754 $m^2 g^{-1}$) relates to the much larger pore diameters of the here reported materials (Ø 5-50 nm) vis-à-vis the one for the above stated COF (Ø 1.8 nm).

Scanning electron microscopy images of the synthesized polymers are shown in Figure 3-3. SEM analysis of 98% d.e. (R,S)-HT/1,4-BDB/THF (Figures 3-3 A-series), 98% d.e. (R,S)-HT/1,3-BDB/THF (Figures 3-3 B-series) and 98% d.e. (R,S)-HT/1,3-BDB/acetone (Figures 3-3 C-series) reveals:

- Micrometer-sized particles (Figure 3-3 A1/B1/C1)
- Aggregates of plates for 98% d.e. (R,S)-HT/1,4-BDB/THF (Figure 3-3 A2/A3)
- A more pronounced pore structure when 1,3-BDB is used over 1,4-BDB (Figure 3-3 B1/B2). Here the plate aggregates form channels and cell-like structures. Interestingly, some of the observed plate-like structures seem to have delaminated which may have contributed positively to the observed enhanced porosity (Figure 3-3 B3).
- Using acetone as the reaction solvent yields equally a highly porous structure yet with a substantially different fine-structure (on the micrometre level) than observed when THF is used (Figure 3-3 B2/B3 vs C2/C3).

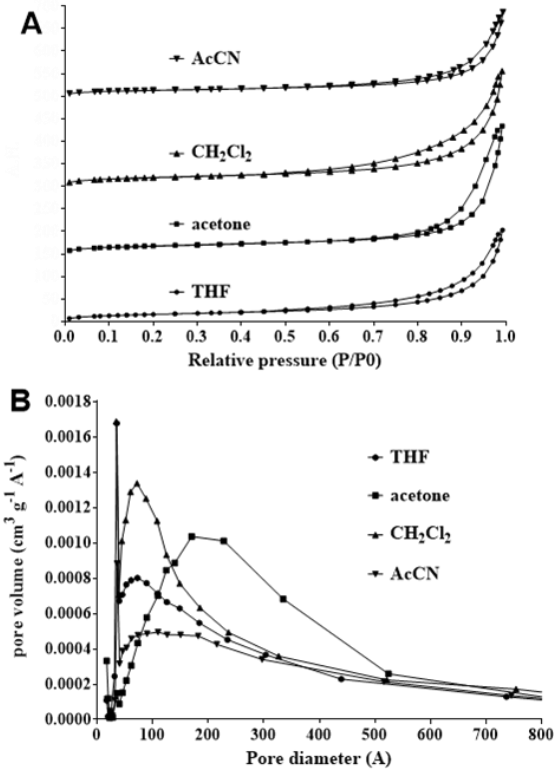

Figure 3-2. N_2 adsorption isotherms (A) and pore size distributions (B) for HT/1,3-BDB made with four different solvents.

Overall, the dimensions of the irregular voids between the platelets, as channels or cell-like structures, are in the tens of nanometers and thus consistent with the N_2 physisorption results and the appearance of an H3 hysteresis in the N_2 physisorption experiments. In spite of the high melting temperatures of the HT/polyboronates (~600K), TEM imaging was found impossible due to melting of materials under the electron beam. X-ray diffraction revealed a degree of crystallinity in all HT/polyboronates with the nature of the BDB (length, substitution pattern) affecting markedly the appearance of the different diffractograms, as it can be observed in Figure 3-4. Given the characteristic H3 hysteresis loop in the N_2 physisorption experiments, and the absence of order in the SEM images (Figure 3-3), we assume that the observed crystallinity reflects some ordering in the pore wall structure. The nature of the used solvent has no effect on the crystallinity (Figure 7-12). The diastereoselectivity of HT affects the crystallinity only in the case of the 1,4-BDB linker, as it can be observed in Figure 3-5.

The (*S,R*)-HT/1,4-BDB and (*S,R*)-HT/1,3-BDB polyboronates were characterized by ^{13}C CP-MAS and ^{11}B spin echo MAS NMR, and the results are shown in Figure 3-6. Analytical simulations of the ^{11}B spectra confirmed the existence of only one type of boron species and this irrespective the nature of the BDB unit. (Figure 3-6 B/D, red curve). FT-IR further confirmed the presence of boronate esters with characteristic peaks in the 1320-1300 cm^{-1} and 690-650 cm^{-1} ranges (Figure 7-13A).[11] In addition, FT-IR revealed a clear absence of OH groups, characteristic for the residual presence of HT or incomplete boronate ester formation, in the synthesized HT/polyboronates (Figures 7-13 B/C).

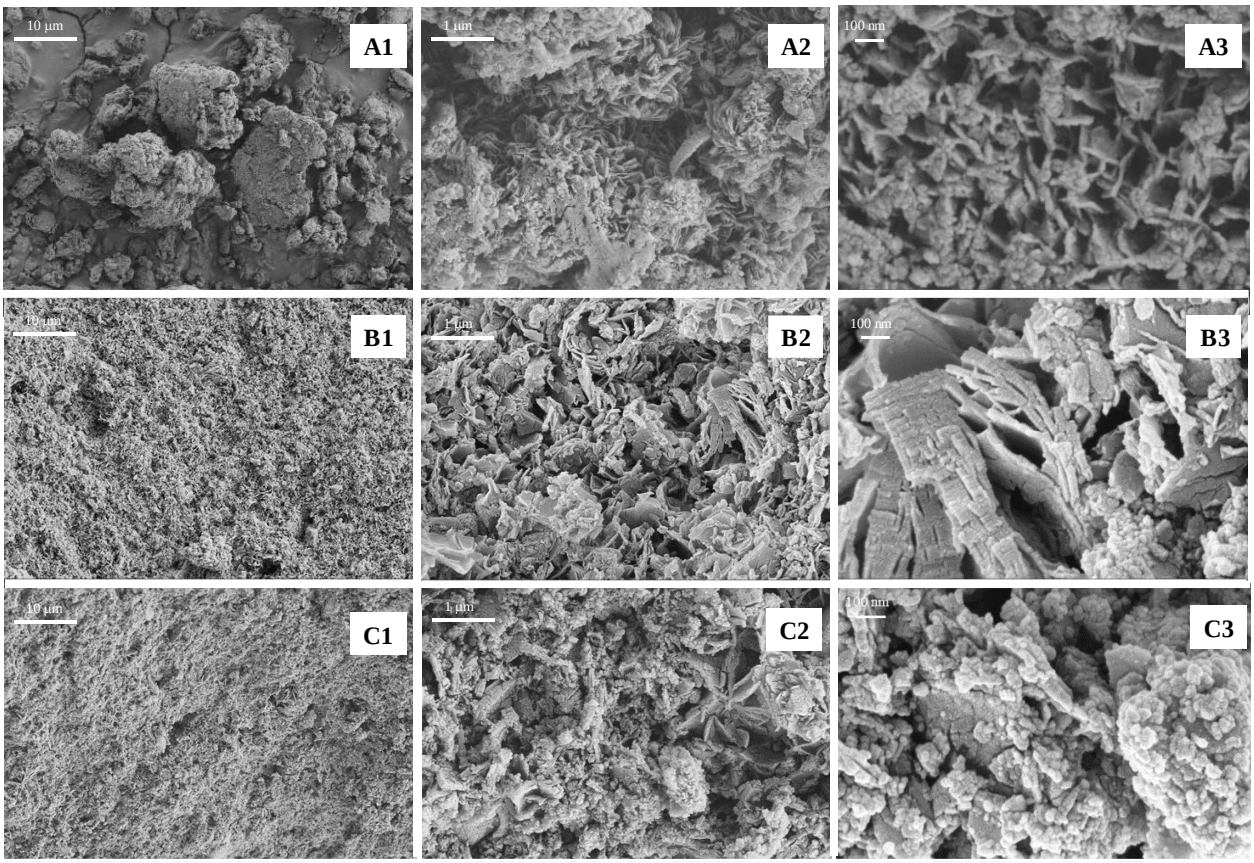

Figure 3-3. SEM images of 98% d.e. (R,S)-HT/1,4-BDB/THF (parts A1, A2 and A3), 98% d.e. (R,S)-HT/1,3-BDB/THF (parts B1, B2 and B3) and 98% d.e. (R,S)-HT/1,3-BDB/THF (parts C1, C2 and C3).

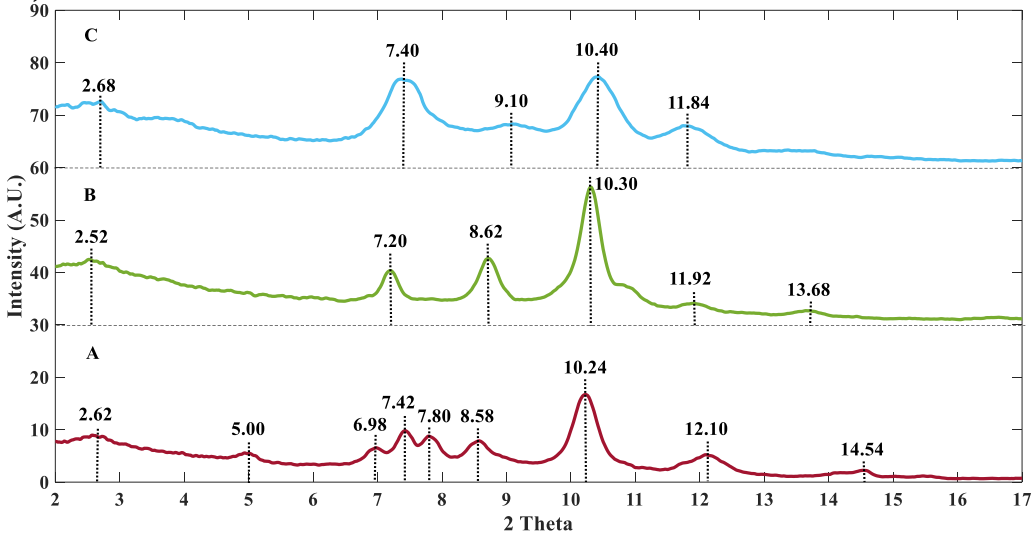

Figure 3-4. X-ray diffractograms (XRD) of (A) HT/1,4-BDB, (B) HT/1,3-BDB, and (C) HT/4,4′-BPDB; no background subtraction.

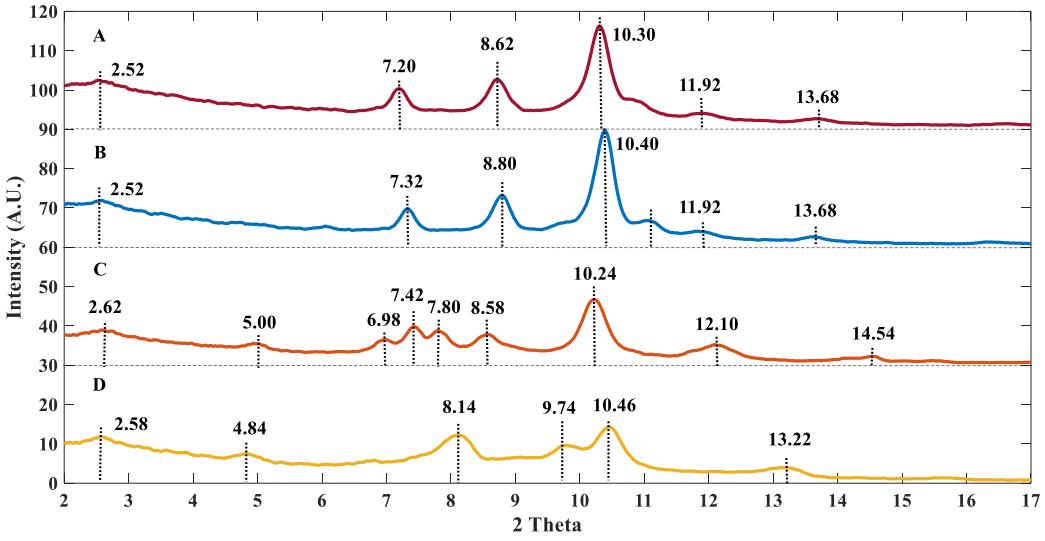

Figure 3-5. X-ray diffractograms (XRD) of HT/1,3-BDB (A 38% HT d.e.; B 98% HT d.e.) and HT/1,4-BDB (C 38% HT d.e.; D 98% HT d.e.); PHT = chirally pure HT.

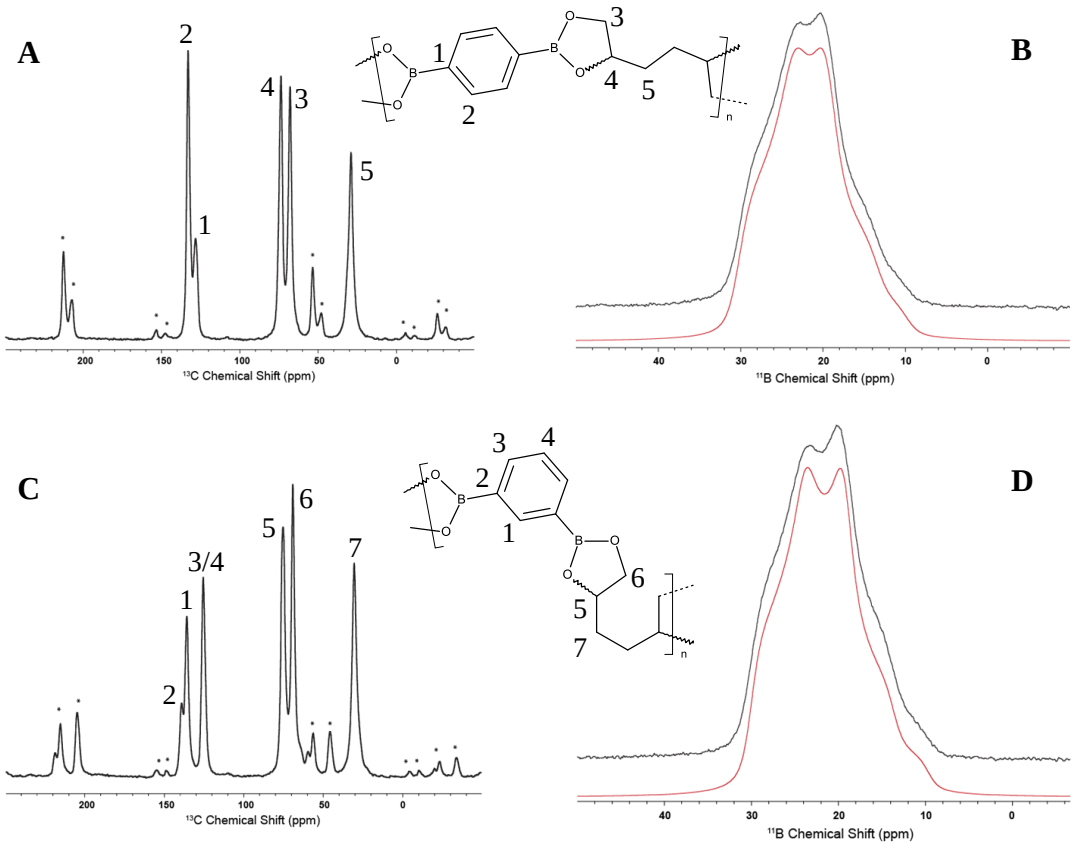

Figure 3-6. 13C CP-MAS NMR of a) (*S*,*R*)-HT/1,4-BDB and c) (*S*,*R*)-HT/1,3-BDB ; 11B spin echo MAS NMR of b) (*S*,*R*)-HT/1,4-BDB and d) (*S*,*R*)-HT/1,3-BDB; * = spinning side band.

3.4. Conclusion

A range of new crystalline (chiral) mesoporous materials were obtained by the facile and benign condensation of (chiral), biobased hexane-1,2,5,6-tetrol (HT) and simple aromatic diboronic acids. The so formed mesoporous HT/polyboronates are obtained by spontaneous precipitation from the reaction mixture, not requiring an extensive workup procedure. HT is easily accessible from cellulose and chiral pure (R,S)-HT is straightforward to crystallize. The applied simple diboronic acids are abundantly available due to their commercial use in Miyaura−Suzuki reactions, easy to synthesize, and generally considered nontoxic.[35−37] The low cost of these materials is ultimately considered to benefit potential commercial applications. The reported materials show an appreciable pore volume of up to 0.44 mL g−1, rivalling the pore volumes of some reported COF materials yet obtained in a less expensive way. Importantly, presently no COF has been reported with pore diameters in excess of 5 nm. The (R,S)-HT (98% d.e.)/polyboronate represents a first example of a chiral mesoporous polyboronate. The high pore volume and the larger pore sizes of 5−50 nm offer great potential to the incorporation of enzymes or as supports to immobilize catalysts to convert bulkier substrates. The meta/para orientation of the boronic acids on the phenyl ring was shown to influence the obtainable surface areas and pore volumes. Uniquely, a distinct influence of HT's chirality (its d.e. value) on the materials' properties was evidenced. Future work will focus on testing these new materials toward a wide range of different applications, thereby hopefully demonstrating its potential as a valuable material.

3.5. References

(1) Linares, N.; Silvestre-Albero, A. M.; Serrano, E.; Silvestre-Albero, J.; García-Martínez, J. Mesoporous Materials for Clean Energy Technologies. *Chem. Soc. Rev.* **2014**, *43* (22), 7681–7717. https://doi.org/10.1039/C3CS60435G.

(2) Libbrecht, W.; Verberckmoes, A.; Thybaut, J. W.; Van Der Voort, P.; De Clercq, J. Soft Templated Mesoporous Carbons: Tuning the Porosity for the Adsorption of Large Organic Pollutants. *Carbon* **2017**, *116*, 528–546. https://doi.org/10.1016/j.carbon.2017.02.016.

(3) Gu, D.; Schüth, F. Synthesis of Non-Siliceous Mesoporous Oxides. *Chemical Society Reviews* **2014**, *43* (1), 313–344. https://doi.org/10.1039/C3CS60155B.

(4) Suib, S. L. A Review of Recent Developments of Mesoporous Materials. *The Chemical Record* **2017**, *17* (12), 1169–1183. https://doi.org/10.1002/tcr.201700025.

(5) Liu, D.; Zou, D.; Zhu, H.; Zhang, J. Mesoporous Metal–Organic Frameworks: Synthetic Strategies and Emerging Applications. *Small* **2018**, *14* (37), 1801454. https://doi.org/10.1002/smll.201801454.

(6) Xin, W.; Song, Y. Mesoporous Carbons: Recent Advances in Synthesis and Typical Applications. *RSC Adv.* **2015**, *5* (101), 83239–83285. https://doi.org/10.1039/C5RA16864C.

(7) G. Croissant, J.; Cattoën, X.; Man, M. W. C.; Durand, J.-O.; M. Khashab, N. Syntheses and Applications of Periodic Mesoporous Organosilica Nanoparticles. *Nanoscale* **2015**, *7* (48), 20318–20334. https://doi.org/10.1039/C5NR05649G.

(8) White, R. J.; Shuttleworth, P. S.; Budarin, V. L.; Bruyn, M. D.; Fischer, A.; Clark, J. H. An Interesting Class of Porous Polymer—Revisiting the Structure of Mesoporous α-d-Polysaccharide Gels. *ChemSusChem* **2016**, *9* (3), 280–288. https://doi.org/10.1002/cssc.201501354.

(9) Kubo, Y.; Nishiyabu, R.; James, T. D. Hierarchical Supramolecules and Organization Using Boronic Acid Building Blocks. *Chem. Commun.* **2015**, *51* (11), 2005–2020. https://doi.org/10.1039/C4CC07712A.

(10) Fujiwara, S.; Takanashi, N.; Nishiyabu, R.; Kubo, Y. Boronate Microparticle-Supported Nano-Palladium and Nano-Gold Catalysts for Chemoselective Hydrogenation of Cinnamaldehyde in Environmentally Preferable Solvents. *Green Chem.* **2014**, *16* (6), 3230–3236. https://doi.org/10.1039/C4GC00383G.

(11) Matsushima, Y.; Nishiyabu, R.; Takanashi, N.; Haruta, M.; Kimura, H.; Kubo, Y. Boronate Self-Assemblies with Embedded Au Nanoparticles: Preparation, Characterization and Their Catalytic Activities for the Reduction of Nitroaromatic Compounds. *J. Mater. Chem.* **2012**, *22* (45), 24124–24131. https://doi.org/10.1039/C2JM34797K.

(12) Ono, K.; Aizawa, R.; Yamano, T.; Ito, S.; Yasuda, N.; Johmoto, K.; Uekusa, H.; Iwasawa, N. Procedure-Dependent Construction of Two Isomers of Trimeric Self-Assembled Boronic Esters. *Chem. Commun.* **2014**, *50* (89), 13683–13686. https://doi.org/10.1039/C4CC05836D.

(13) Dhara, A.; Beuerle, F. Reversible Assembly of a Supramolecular Cage Linked by Boron–Nitrogen Dative Bonds. *Chemistry – A European Journal* **2015**, *21* (48), 17391–17396. https://doi.org/10.1002/chem.201502841.

(14) Lohse, M. S.; Bein, T. Covalent Organic Frameworks: Structures, Synthesis, and Applications. *Advanced Functional Materials* **2018**, *28* (33), 1705553. https://doi.org/10.1002/adfm.201705553.

(15) Han, X.; Zhang, J.; Huang, J.; Wu, X.; Yuan, D.; Liu, Y.; Cui, Y. Chiral Induction in Covalent Organic Frameworks. *Nat Commun* **2018**, *9* (1), 1294. https://doi.org/10.1038/s41467-018-03689-9.

(16) Liu, Y.; Ma, Y.; Zhao, Y.; Sun, X.; Gándara, F.; Furukawa, H.; Liu, Z.; Zhu, H.; Zhu, C.; Suenaga, K.; Oleynikov, P.; Alshammari, A. S.; Zhang, X.; Terasaki, O.; Yaghi, O. M. Weaving of Organic Threads into a Crystalline Covalent Organic Framework. *Science* **2016**. https://doi.org/10.1126/science.aad4011.

(17) Diercks, C. S.; Yaghi, O. M. The Atom, the Molecule, and the Covalent Organic Framework. *Science* **2017**. https://doi.org/10.1126/science.aal1585.

(18) Kandambeth, S.; Dey, K.; Banerjee, R. Covalent Organic Frameworks: Chemistry beyond the Structure. *J. Am. Chem. Soc.* **2019**, *141* (5), 1807–1822. https://doi.org/10.1021/jacs.8b10334.

(19) Peh, S. B.; Wang, Y.; Zhao, D. Scalable and Sustainable Synthesis of Advanced Porous Materials. *ACS Sustainable Chem. Eng.* **2019**, *7* (4), 3647–3670. https://doi.org/10.1021/acssuschemeng.8b05463.

(20) Krishna, S. H.; De bruyn, M.; Schmidt, Z. R.; Weckhuysen, B. M.; Dumesic, J. A.; Huber, G. W. Catalytic Production of Hexane-1,2,5,6-Tetrol from Bio-Renewable Levoglucosanol in Water: Effect of Metal and Acid Sites on (Stereo)-Selectivity. *Green Chem.* **2018**, *20* (19), 4557–4565. https://doi.org/10.1039/C8GC02455C.

(21) Cuello-Penaloza, P.; Krishna, S. H.; De bruyn, M.; Weckhuysen, B. M.; Lebrón-Rodríguez, E. A.; Hermans, I.; Dumesic, J. A.; Huber, G. W. Production of Hexane-1,2,5,6-Tetrol from Biorenewable Levoglucosanol over Pt-WOx/TiO2. *ACS Sustainable Chem. Eng.* **2021**, *9* (48), 16123–16132. https://doi.org/10.1021/acssuschemeng.1c04759.

(22) Lennox, A. J. J.; Lloyd-Jones, G. C. Selection of Boron Reagents for Suzuki–Miyaura Coupling. *Chem. Soc. Rev.* **2013**, *43* (1), 412–443. https://doi.org/10.1039/C3CS60197H.

(23) Polshettiwar, V.; Decottignies, A.; Len, C.; Fihri, A. Suzuki–Miyaura Cross-Coupling Reactions in Aqueous Media: Green and Sustainable Syntheses of Biaryls. *ChemSusChem* **2010**, *3* (5), 502–522. https://doi.org/10.1002/cssc.200900221.

(24) Hooshmand, S. E.; Heidari, B.; Sedghi, R.; Varma, R. S. Recent Advances in the Suzuki–Miyaura Cross-Coupling Reaction Using Efficient Catalysts in Eco-Friendly Media. *Green Chem.* **2019**, *21* (3), 381–405. https://doi.org/10.1039/C8GC02860E.

(25) Sing, K. S. W. Reporting physisorption data for gas/solid systems with special reference to the determination of surface area and porosity (Recommendations 1984). *Pure and Applied Chemistry* **1985**, *57* (4), 603–619. https://doi.org/10.1351/pac198557040603.

(26) Schüth, F.; Ward, M. D.; Buriak, J. M. Common Pitfalls of Catalysis Manuscripts Submitted to Chemistry of Materials. *Chem. Mater.* **2018**, *30* (11), 3599–3600. https://doi.org/10.1021/acs.chemmater.8b01831.

(27) Zhu, L.; Zhang, Y.-B. Crystallization of Covalent Organic Frameworks for Gas Storage Applications. *Molecules* **2017**, *22* (7), 1149. https://doi.org/10.3390/molecules22071149.

Chapter 4: Ethanol to Distillate-Range Molecules using Cu/Mg_xAlO_y catalysts with low Cu loadings

4.1. Introduction

The production of C_8-C_{22} distillate-range fuels has been a topic of increasing importance in the last few decades. In the next 20 years, an increase in demand for heavy-duty fuels is projected[1], with a concomitant decrease in demand for light duty fuels, such as gasoline. Moreover, there is a strong drive to produce fuels with lower greenhouse gas (GHG) emissions[2,3]. The most commonly produced low carbon liquid fuel is ethanol which has been reported to have 39 - 108% reduction in GHG emissions compared to gasoline, depending on the biomass source it is produced from, and also on the ethanol production technology[4,5]. Several approaches have been proposed to convert ethanol into diesel, none of which are commercially practiced today[3]. Our group has previously proposed a route to convert ethanol into distillate-range fuel molecules by a two-step approach that involves Guerbet coupling of ethanol to longer alcohols and subsequent acid-catalyzed etherification of the alcohols[6]. The ethers produced have properties that are similar to diesel fuels[7]. The key challenge of the Guerbet step is to selectively oligomerize the alcohols into C_{4+} primary linear alcohols in high yields, which can then undergo etherification. Branched alcohols produce olefins as major products during the acid catalyzed etherification step.

One of the most researched catalysts for the production of 1-butanol and higher alcohols from ethanol are stoichiometric hydroxyapatites (HAP) of Ca and Sr[8,9]. HAPs are particularly selective

The contents of this Chapter are adapted from the following publication: Cuello-Penaloza, P. A.; Dastidar, R. G.; Wang, S.-C.; Du, Y.; Lanci, M. P.; Wooler, B.; Kliewer, C. E.; Hermans, I.; Dumesic, J. A.; Huber, G. W. Ethanol to Distillate-Range Molecules Using Cu/Mg_xAlO_y Catalysts with Low Cu Loadings. *Applied Catalysis B: Environmental* **2022**, *304*, 120984. R.G.D., S-C.W., and C.E.K. collaborated with characterization of materials, Y.D. and B.W. collaborated with catalyst synthesis, M.P.L. collaborated with conceptualization and revision of manuscript.

to 1-butanol (>70% at <15% conversion) and higher alcohols due to its good balance of acid and base sites[10]. Moteki and Flaherty[11] have previously studied ethanol conversion over Ca and Sr-HAP catalysts and proposed a series of relevant kinetic steps to describe this reaction proceeding via aldol condensation. They found that the linear-to-branched ratio of C_6 alcohols was found to be a weak function of temperature, always being slightly lower than 1; and more importantly, that selectivities to alcohols and aldehydes decreased with conversion and could be described by a modified step-growth model. However, our group[6] demonstrated that chain growth with Ca-HAP is limited for the Guerbet coupling of ethanol after 50% conversion because branched alcohols are essentially inactive as nucleophiles in the Guerbet coupling reaction[12], tending instead to undergo dehydration to form olefins. Moreover, selectivity to dehydration products also increases with concomitant decrease of selectivity to coupling products due to water inhibition[12] affecting more severely the latter reactions, as also reported by Hanspal et al.[10] Our group also proposed a kinetic model for the Guerbet coupling of ethanol and several dehydration side reactions using Ca-HAP[12], which was capable of accurately predicting conversion and product selectivities in all conversion ranges. According to the kinetic model, a good catalyst for alcohol coupling must either favor increased events of ethanol attacking other alcohols (higher nucleophilicity of ethanol relative to that of higher alcohols) or decreased events of higher alcohols attacking ethanol (lower electrophilicity of ethanol relative to that of higher alcohols) to produce larger linear chain alcohols capable of undergoing subsequent coupling reactions. The C_{6+} primary branched alcohols produced by Guerbet coupling are highly selective (>80%) to olefins in the acid catalyzed etherification step of alcohols to ethers[6] and the linear-to-branched chain alcohol ratios of C_6 molecules was only 0.8 for HAP, which is consistent with Moteki and Flaherty findings and also was found to decrease as the alcohols increase in molecular weight. Consequently, these factors

limit both the ability of HAP to produce increasingly larger alcohols as conversion increases, and the suitability of the produced alcohols for upgrading by acid-catalyzed etherification as branching is significant and more of it will occur the higher the conversion is.

A handful of other catalysts have been studied for ethanol oligomerization. These include base metals such as Cu or Ni supported on Mg_xAlO_y mixed metal oxides derived from calcination of layered double hydroxides (LDH)[13]. The performance of these catalysts varies depending on the reaction conditions and the nature of the catalysts. Marcu et al.[14] used Cu/Mg_xAlO_y catalysts with 1.1-22.9 wt% Cu loadings for Guerbet coupling of ethanol using batch reactors at 200°C, obtaining 1-butanol selectivity up to 50% at low conversion. Bravo-Suarez et al.[15] used methanol/ethanol mixtures in a flow reactor and observed low selectivities to alcohols (5-10%) but higher selectivities to esters(~50%). Cheng et al.[16] tested Mg_xAlO_y doped with 1wt% Cu in the coupling of methanol/ethanol mixtures, varying the Mg/Al ratio from 1 to 5. They found that the conversion rates and space-time yields of C_{3+} products increased with the exposed Cu^0 area, which in turn was affected non-monotonically by the Mg/Al ratio. A particular approach to tune Cu/Mg_xAlO_y catalysts to be more selective to higher alcohols in the ethanol oligomerization reaction was proposed by Guo et al. [17–19] The researchers observed that catalysts with ≤ 0.1 wt% Cu were able to catalyze the conversion of ethanol to 1-butanol and higher alcohols with selectivities up to 75%, while side-reactions such as esterification and ketone formation were suppressed. They proposed that at very low Cu loadings the active site is Cu^{+1}, not metallic Cu, as indicated from *in-situ* XANES and EXAFS. However, no articles have been published about this approach applied to alcohol coupling as of present, and no mention of the branching patterns of the product alcohols is reported in any literature.

Numerous methods are available in literature to synthesize well-defined mixed metal oxide catalysts (particularly MgAl) by co-precipitation[20,21]. It is possible to vary the surface area and porosity of the LDH precursor by changing process parameters, including pH of titration, temperature, and organic solvent washing (acetone/ methanol)[22,23]. It is also possible to synthesize materials with varying M^{+2}/M^{+3} ratios (where M is the metal and +2/+3 are the valences) to promote desired base or acid-catalyzed reactions[24–26].The solid phase composition of the resulting material differs with the metal function ratios. For instance, in the case of MgAl mixed oxides it is possible to obtain a homogeneous MgO-like structure active in alcohol dehydrogenation reactions if Mg/Al > 1.[24] For lower Mg/Al ratios, combined $MgAl_2O_4$, MgO and Al_2O_3 heterogeneous phases may be obtained, and the performance of the resulting catalyst will increasingly lean towards acid-catalyzed reactions such as dehydrations. When a metal function such as Cu is added, the resulting material properties such as base site counts and reduction profile will change, having an impact on the performance of reactions such as dehydrogenations or dehydration of alcohols and coupling of alcohols and aldehydes[15,16].Therefore, LDH catalysts can be flexibly synthesized and the variation of the resulting properties of the materials may be studied in regards any reaction by employing co-precipitation synthesis techniques. Finally, calcination temperatures can also impact the performance of these catalysts in ethanol condensation reactions, as this parameter can affect the relative amounts of acid-to-base sites as well as the bulk structure and cation environment of the metals as argued by Ramasamy et al.[21] who found that for ethanol condensation the best calcination temperature of MgAl LDH to obtain higher C-number products was 600°C.

The objective of study of this chapter is the production of diesel fuel precursors from ethanol by using low Cu loading catalysts supported on high surface area LDH-derived MgAl mixed oxides.

Diesel fuel precursors (DFP) are defined as any alcohol, aldehyde or ketone with 4 or more carbon atoms, or any ester, ether, hemiacetal or acetal with more than 6 carbon atoms, as these species are either in the distillate-range (C_{10+} sizes) or can ultimately be upgraded via acid catalysis to higher molecular weight ethers (bimolecular dehydration) or esters (transesterification). As we will show in this chapter, these catalysts produce linear alcohols, esters and other diesel fuel precursors from ethanol at high selectivity.

4.2. Experimental Methods

4.2.1. Synthesis and characterization of Cu/Mg_xAlO_y catalysts

Cu/Mg_xAlO_y catalysts were done by co-precipitation techniques carried out by our group in other research[27], with the use of solvents (acetone, methanol)[22], or by incipient wetness impregnation. The materials were labeled as wtCuMMO(d), where 'wt' is the Cu wt% nominal loading, and d is a description of the catalyst depending on the BET surface area (vl = very low, l = low, m = medium, h =high), the method of preparation (i – incipient wetness impregnation), a physical mixture (pm), and a regenerated catalyst(r). Target materials prepared were: 0CuMMO, 0.1CuMMO, 0.3CuMMO(vl), 0.3CuMMO(l), 0.3CuMMO(m), 0.3CuMMO(h), 0.3CuMMO(i) and 1.2CuMMO.

Three aqueous solutions were prepared: solution 1 contains aqueous solutions of $Mg(NO_3)_2{\cdot}6(H_2O)$ (Sigma-Aldrich 237175), $Al(NO_3)_3{\cdot}9(H_2O)$ (Sigma-Aldrich 237973), and $Cu(NO_3)_2{\cdot}3(H_2O)$ (Sigma-Aldrich 61194) in appropriate amounts, solution 2 is a 0.133M (for 0.1CuMMO) or 0.512M aqueous Na_2CO_3 (Sigma-Aldrich 223530) solution, and solution 3 contains a 1M (for 0.1CuMMO) or 50wt% NaOH (Sigma-Aldrich 795429) aqueous solution. The

Na_2CO_3 solution was added to a 1 L beaker and either heated to 60 °C (for 0.1CuMMO) or maintained at room temperature and stirred with a magnetic stir bar. Solution 1 containing Cu, Mg and Al metals and solution 3 containing NaOH were slowly added to the 1 L beaker using a syringe pump. The flow rates of solution 1 and 3 were controlled so that addition would take place over 1 h and so the pH was maintained at 10 (or 11 for 0.1CuMMO) during the addition. A temperature/pH probe (Ohaus ST20) was used to monitor the pH and temperature of the solution. After all solutions were added, the mixed solution was aged differently depending on the catalyst. For 0.1CuMMO, the aging was done for 20 hours in a 1 L bottle at 60°C with stirring, for 0.3CuMMO(vl) and 0.3CuMMO(l) catalyst, aging was done at 60°C for 12h, for all other catalysts aging was done at room temperature for 24h. After the aging process, the mixed solution was washed and filtered to remove residual nitrates and sodium. The filter cake was dissolved in 300 mL of 1 M Na_2CO_3 solution and then washed with 500 mL of DI water and filtered. The filter cake was dissolved in 500 mL of DI water and washed and filtered 2 more times for 0.1CuMMO and for 0.3CuMMO(vl) (due to having more residual Na content to be removed than other materials). For all other materials, washing was done with water and acetone, and for 0.3CuMMO(h) the resultant gel was redispersed in 1L of acetone at 60°C for 2h after washing. The filter cakes were dried overnight in a 110 °C oven or in a vacuum oven at room temperature (0.3CuMMO(h)). The dry catalysts were then crushed and calcined at 600 °C for 2 h on a 4 °C min^{-1} temperature ramp. The catalyst is then sieved to 30 – 80 mesh and packed into the reactor where it is reduced in situ at 325°C for 12 h with a 4°C min^{-1} temperature ramp under 50 mL min^{-1} H_2 flow before the start of any run.

For the 0.3CuMMO(i) catalyst, Cu addition was done using incipient wetness impregnation by dropwise addition of $Cu(NO_3)_2 \cdot 3(H_2O)$ (Sigma-Aldrich 61194) aqueous solution to MgAl

hydrotalcite (Sigma-Aldrich 652288), then drying, calcining and reducing the catalyst as described in the previous paragraph. A physical mixture of 0CuMMO catalyst (no Cu content) with 1.2CuMMO catalyst was prepared by mixing 0.9213 ± 0.0001 g of the undoped material with 0.0832g ± 0.0001 g of 1.2CuMMO. This mixture was labeled 0.1CuMMO(pm).

CuMMO catalysts textural properties were determined via N_2 physisorption using a Micromeritics ASAP 2020 instrument. Properties obtained were BET surface area, BJH pore size distribution and pore volume. The catalysts acid and base sites were determined via NH_3-TPD and CO_2-TPD respectively using modified methods reported in literature [25,26]. For this, a Micromeritics 2720 II equipment was used. Samples were pre-reduced at 350°C before being treated with 25 mL of NH_3 or CO_2. The temperature range of the analyses were 150 – 600 °C for NH_3-TPD and 50 – 600 °C for CO_2-TPD. Actual compositions of Mg, Al and Cu of the catalysts were obtained by ICP-OES (Varian Vista-MPX) after digesting 10 - 15 mg of the solid samples in 10 mL of 10 wt% HNO_3 (trace metal grade, Sigma-Aldrich no. 438073) aqueous solution and diluting the digestate to 1 wt% HNO_3. Calibration curves of the metals were prepared from 1000 ppm standard solutions of Cu (Fluka – 68921), Mg (Ricca – RV010077) and Al (Fluka – 61935). Powder X-ray diffraction of the catalyst samples was carried out in Rigaku Rapid II diffractometer. A Mo Kα source (λ = 0.71 Å) was used for the measurements and the scanned zone was $2\theta = 5 - 60°$. All measurements were recalculated to Cu Kα source ($\lambda = 1.54$ Å) for ease of analysis and comparison with literature. Structures were matched with the use of JADE, PDF 4+ software, as well as from reports in literature. Thermogravimetric analysis was carried out using a TGA TA Q500. For analysis, 10 – 15mg of sample were added to the dish and heated up from room temperature to 650°C at a 10°C min^{-1} ramp under oxygen flow. Total organic carbon (TOC) analysis of the fresh calcined and spent 0.1CuMMO and 0.3CuMMO(m) catalysts were made with a Shimadzu TOC-V CPH/CPN

using the SSM-5000A solid sample module under a 100mL min^{-1} O_2 flow. The instrument was calibrated with potassium phthalate (Sigma-Aldrich P1088) from 0 – 80 mg, and 48-62 mg of sample were weighed for the analysis. For TEM, the catalyst powder was prepared for characterization by crushing it into small pieces (<100 nm thick) using an agate mortar and pestle. The fines were dusted onto a 200 mesh, holey-carbon-coated, copper TEM grid. The grid was examined in the bright field (BF) TEM imaging mode of a Philips CM200F electron microscope that was operated at an accelerating voltage of 200 kV. Digital images were collected from randomly selected areas using a Gatan CCD camera and Digital Micrograph v. 2.5.4 software.

Fourier Transform Infrared Spectroscopy (FT-IR) was done to some of the samples after dosing CO in order to determine the nature of Cu sites on the catalytic surface. In order to make measurements comparable between samples, 5 ± 0.1 mg of these were weighed before they were pelletized under 2 ton of pressure for 30 seconds. The sample pellets are heated under 40 mL min^{-1} 4%H_2/N_2 flow to 325°C with 4oC/min ramp and held for 5 min, then cooled down to room temperature while maintaining %H_2/N_2 flow. When cooling down to room temperature, the cell was evacuated to 10-6 hPa, and then liquid nitrogen was used to further cool down to -150°C with background scan. CO adsorption FT-IR (Bruker Vertex 70) spectra are collected after dosing 60 Torr 5%CO/He for 5 minutes. Finally, the CO is evacuated from the system, and another spectrum is then collected after 9 minutes.

4.2.2. Flow reaction system

Ethanol oligomerization reactions were performed in stainless-steel fixed-bed reactors (40 cm long, 2.54 cm catalyst bed, 0.95 cm outer diameter) using the scheme shown in Figure 4-1 and

described next. The reactors were packed with 1g of CuMMO catalysts pelletized and sieved to a particle size of 250–354 μm. Prior to reaction, the catalysts were reduced in situ as described in the previous section. Ethanol was fed with a syringe pump (Teledyne ISCO) at 21–244 μL min^{-1}, with H_2 cofeed at 2–50 mL min^{-1} in the downflow configuration at atmospheric pressure through a preheated evaporation region maintained at >200 °C prior to entering the reactor, ensuring that the feed is completely in the gas phase before contacting the catalyst. The gas composition entering the reactor was 80 mole% ethanol and 20 mole% H_2.

The reactor was heated with a tube furnace (Lindberg Blue M Mini-Mite) with the temperature kept uniform via an aluminum block (30 cm long) positioned between the reactor and furnace coils. Below the furnace, the products were kept heated at >150 °C prior to passing through either a removable 110 mL glass condenser (Ace Glass) or a 150 mL stainless-steel condenser (Swagelok) submerged in an ice bath. Gases which did not condense were sent to a three-way valve positioned to flow either through a bubble-flow meter and then to vent or to an online gas GC (Shimadzu 2010). Gas and liquid samples were collected simultaneously every 1.5–6 hours. Gas samples were first injected into the GC via a six-way valve, after which the gas flow rate was measured via the bubble flow meter. For the experiments with glass condensers, the outlet flow from the reactor was redirected from the product collection condenser to a waste condenser on the side where the liquid would drop and the gas flow would emerge and be redirected to vent, then the ice bath was lowered in order for the condenser containing the collected product to be removed and immediately replaced with another, after which the outlet flow would finally be redirected from the waste condenser to the new product collection condenser. To reduce sampling error caused by transient vapor–liquid equilibria and low product volumes, 10 – 20 mL of 1-propanol was generally added to the condenser prior to collection. For the experiments with a stainless-steel

condenser, the liquid flow is stopped and the inlet and outlet valves in the flow reactor were closed before the ice bath was lowered, then the condenser was emptied into a vial with 5-10 mL of 1-propanol, and the system was re-pressurized in both the inlet and the outlet before restarting the pump again. This entire process took <3 min.

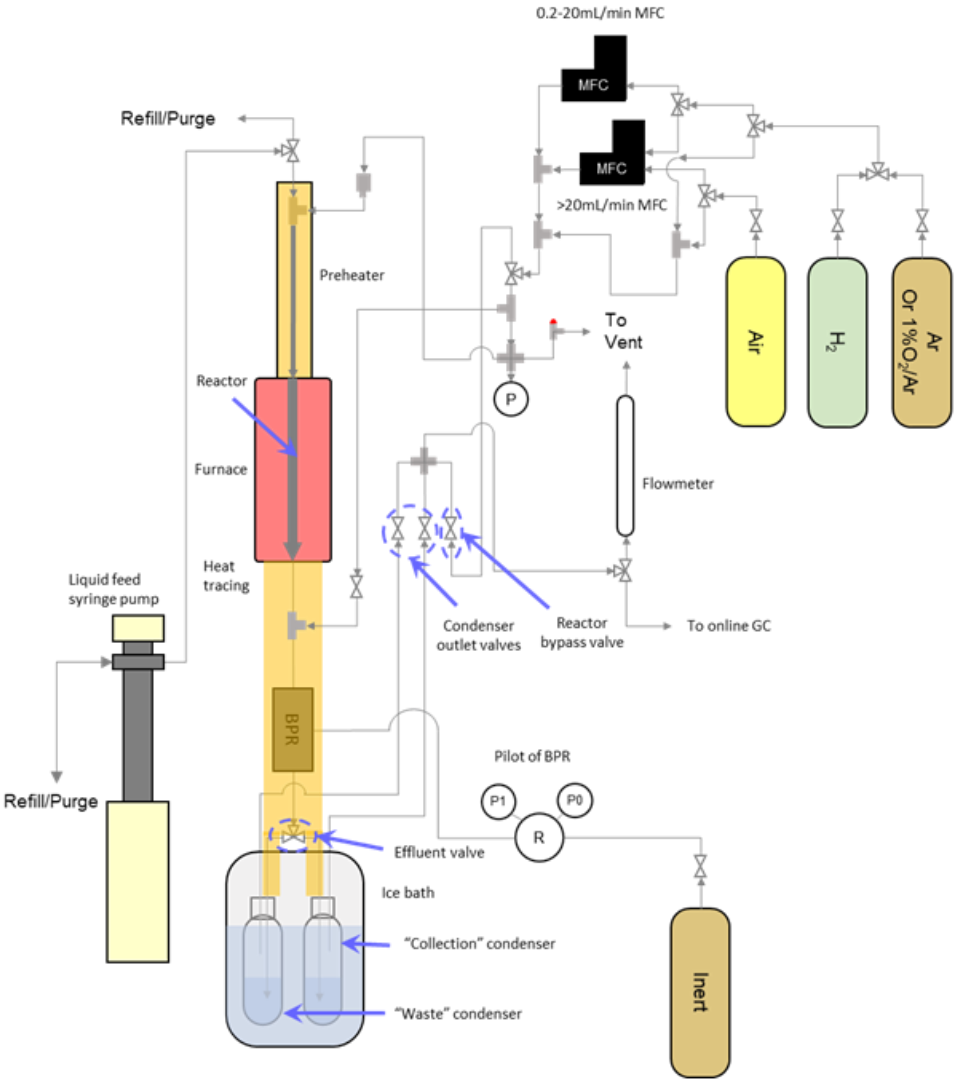

Figure 4-1. Schematic of the flow reaction system used for the Ethanol Oligomerization reactions.

4.2.3. Product analysis and quantitation

After collection, the sample mass was weighed, and the liquid was diluted with 1-propanol including a known amount of 1-pentanol as an internal standard. The liquid products were then analyzed and quantified via GC-FID (Shimadzu 2014) equipped with a RTX-VMS column (Restek). Products were quantified with GC-FID via external standards when reference compounds could be obtained. When they could not, response factors were estimated via the effective carbon number method. Products were identified via external standards when available, or via GC-MS suggestions. The gas products were analyzed via GC-FID (Shimadzu 2010) equipped with a flame ionization detector (FID) and a thermal conductivity detector (TCD). The FID line utilized a Rt-Q-BOND column (Restek), while the TCD line utilized a Hayesep D column (Supelco). Negligible permanent gases were detected via the TCD, thus this line was not used for quantification.

4.2.4. Data analysis and considerations

Yield of each species was calculated using the following formula:

$$Y_i = \frac{n_{C,i,out}}{n_{C,in}} \qquad (4-1)$$

Conversion was calculated using the following formula:

$$X = \sum_{i=1}^{n} Y_i \qquad (4-2)$$

Selectivity was calculated in product yield-basis using this formula:

$$S_i = \frac{Y_i}{\sum_{i=1}^{n} Y_i} = \frac{Y_i}{X} \qquad (4-3)$$

Diesel fuel precursors (DFP) are defined as any alcohol, aldehyde or ketone with 4 or more carbon atoms, or any ester, ether, hemiacetal or acetal with more than 6 carbon atoms. Diesel fuel precursor selectivity (DFPS) is then defined as:

$$DFPS = \sum_{i=1}^{n} S_{C4+alcohols} + \sum_{i=1}^{n} S_{C4+aldehydes} + \sum_{i=1}^{n} S_{C4+ketones} + \sum_{i=1}^{n} S_{C6+esters} \sum_{i=1}^{n} S_{C6+ethers} + \sum_{i=1}^{n} S_{C6+hemiacetals} + \sum_{i=1}^{n} S_{C6+acetals} \qquad (4-4)$$

Another feature investigated in this reaction is the selectivity distribution of alcohols and esters according to the Schultz-Flory model[27,28]. This model is defined by the following equation:

$$ln\left(\frac{\boldsymbol{C_n}}{\boldsymbol{n}}\right) = (\boldsymbol{n}-\mathbf{1})\, ln(\boldsymbol{\alpha}) + \mathbf{2}\, ln(\mathbf{1}-\boldsymbol{\alpha}) \qquad (4-5)$$

Where n is repeat unit defined as ethanol, C_n is carbon selectivity of alcohol (or ester), α is the chain-growth probability which in this case is the probability of an adsorbed C_n alcohol chain to grow to C_{n+2} (since ethanol is the monomer), and (1-α) is the desorption probability which in this case is the probability of obtaining a C_n alcohol product[28]. The α parameter is then calculated from the slope of an $\ln(C_n/n)$ vs n plot.

We also studied catalyst deactivation with time on stream (TOS) at different WHSV. In Equation (6), x(t) is conversion at TOS and $x_{0,WHSV\_i}$ is the initial conversion at the ith WHSV. We plotted the catalyst activity (a), as defined in Equation (4 – 6) against the number of turnovers for the catalyst.

$$\frac{x(t)}{x_{0,WHSV_i}} = a \qquad (4-6)$$

4.3. Results and discussion

4.3.1. Catalyst characterization and properties

The measured properties of the prepared catalysts are in Table 4-1. The BET surface area of the low surface area catalysts (vl and l) increased after calcination, while the BET surface area of the other materials decreased after calcination. For the low surface area materials, the increase in surface area may be explained by calcination-induced turbostractic disorder formation of the former LDH, in which the layers of the material (now-MMO) undergo small distortions after the anions and the water is removed from the layers of the material, exposing more surfaces. The reduction in area for the higher surface area materials could be explained by thermal sintering of the material, by which the layers stack up on top of each other upon calcination, reducing available surface area. The pore volume of the catalysts is proportional to the BET surface area. As shown in Figures 7-14 and 7-15 the catalysts are almost exclusively mesoporous. As shown in Figure 4-2, the concentration of base sites is proportional to the pore volume for the Cu containing catalysts, suggesting that most base sites may be located inside the pores of the catalyst due to incorporation of Cu in the materials. This positive correlation still holds if the density of base sites (μmol/m^2) is considered as shown in Figure 7-17. Catalysts have varying acid site concentrations, with 0.3CuMMO(vl) having more than twice the acidity of the catalyst with next lowest acid site count (0.3CuMMO(m)), potentially because of requiring a more extensive wash to remove its higher residual Na content compared to the other materials. Unfortunately, we were not able to measure the number of Cu active sites on the catalysts in this work due to the low loading of the Cu catalysts. Improved chemisorption techniques will be required to accurately measure the concentration of Cu metallic sites for such low Cu loading catalysts in the future.

Table 4-1. Properties of the synthesized catalysts.

Catalyst	0.3CuMMO(vl)	0.3CuMMO(l)	0.3CuMMO(m)	0.3CuMMO(h)	0.3CuMMO(i)	0.1CuMMO	1.2CuMMO	0CuMMO
Actual Cu wt%[a,b]	0.4	0.3	0.3	0.4	0.6	0.2	1.5	0
Cu:Al[a]	0.01	0.009	0.008	0.009	0.02	0.006	0.04	0
Mg:Al[a]	2.8	3.0	2.9	2.8	3.0	3.3	2.8	2.9
LDH BET surface area (m^2/g)	82	98	250	382	388	-	235	388
Calcined LDH BET surface area (m^2/g)	148	129	172	192	176	187	208	268
Pore Volume (cm^3/g)	0.3	0.5	0.5	0.9	0.6	0.3	0.9	1.2
Base sites (µmol/g)	209	263	325	549	332	215	512	327
Acid sites (µmol/g)	1698	589	861	788	401	751	535	818

[a] Elemental composition of the catalysts from ICP-OES.
[b] Calculated Cu wt% loading is based on a fully decomposed hydrotalcite at the obtained Cu:Mg:Al ratio.

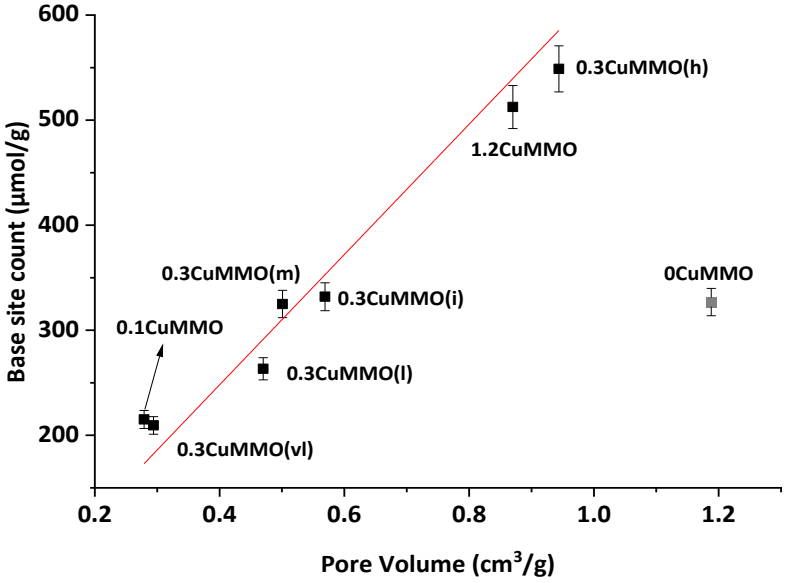

Figure 4-2. Base site vs pore volume correlation for Cu/Mg_xAlO_y catalysts. Red line is linear fit of base site counts vs pore volume, Pearson's r = 0.9943; Adjusted R^2 = 0.9867, 0CuMMO catalyst (shown in translucent black) is left out of the correlation.

As seen from X-ray diffractograms in Figure 7-3, all calcined materials had visible peaks resembling a periclase MgO phase (PDF # 04-002-3057), indicating that the materials are solid solutions in which Al is incorporated in the MgO-like lattice of the MMO [21,29] which is reported to occur when Mg/Al ratio is >1 [24]. The 0.3CuMMO(vl) catalyst had some visible Al_2O_3 peaks (PDF # 00-010-0425), explaining its higher acidity. The 0.3CuMMO(i) in which Cu was added via incipient wetness impregnation exhibits a peak that may be matched to CuO (PDF # 01-078-

0428) at 74.0°, but its presence as crystalline nanoparticles is ambiguous given that any higher intensity peak of CuO (36.6 and 42.6°) will be masked by MgO signals. Neither Cu nor CuO were observed in the other XRD peaks, indicating that it is probably well dispersed in the MMO.

4.3.2. Catalyst activity and selectivities to key species in the alcohol oligomerization reaction

More than 160 products were detected after reaction. Table 4-2 shows the ethanol selectivity, diesel fuel precursor selectivity (DFPS), C_6 linear to branched alcohol ratios, α-values (chain growth) of alcohols and α-values of esters assuming ethanol as the monomer unit, and selectivity of major classes of products. Table 7-4 shows the selectivities of each of the tested catalyst to the different product categories detected, whereas the detailed product distribution per C-size over each catalyst is in Tables 7-5 – 7-12. In general, the low loading catalysts (0.1-0.6 Cu wt%) exhibit high selectivity towards higher alcohols, followed by esters, then aldehydes, then ketones and other products at the same reaction conditions. 0.3CuMMO(vl), 0.3CuMMO(l), 0.3CuMMO(m) and 0.3CuMMO(h) catalysts exhibited approximately the same conversion (49 – 54%), whereas 0.3CuMMO(i), 1.2CuMMO, 0.1CuMMO and the physical mixture of 1.2CuMMO and 0CuMMO showed lower conversions (39 – 45%). The DFPS was similar for all low Cu loading catalysts, ranging between 75 – 84%. The DFPS decreased to 49% for the 1.2 CuMMO catalyst because of the higher selectivities exhibited towards smaller molecules, particularly ethyl acetate and acetone for this material. All catalysts had linear-to-branched C_6 alcohol ratios greater than 3. Ca-HAP had a linear to branched C_6 alcohol ratio of 0.8.[6] This suggests that for the CuMMO catalysts chain growth occurs either by an increased frequency of nucleophilic attacks of an ethanol-derived intermediate to any other alcohol-derived intermediate compared to that of Ca-HAP, or by a decreased frequency of nucleophilic attacks to ethanol. Large amounts of C_{6+} esters were also observed including ethyl butyrate, butyl acetate, butyl butyrate, ethyl hexanoate, hexyl acetate,

butyl hexanoate, hexyl butyrate, butyl-2-ethylbutyrate, ethyl octanoate, octyl acetate and other combinations that arise from the different linear and branched alcohols, up to C_{14} sizes. Aldehydes observed were acetaldehyde, butyraldehyde, hexanal, 2-ethylbutanal, octanal and 2-ethylhexanal. No alkenals (such as crotonaldehyde) were observed in the products, but alkenols such as crotyl alcohols were seen.

Table 4-2. Diesel fuel precursor compounds selectivity (DFPS), C_{4+} alcohol and aldehyde selectivities, C_{6+} ester selectivity and acetaldehyde, ethyl acetate and 1-ethoxyethanol selectivities for CuMMO catalyst formulations.

Catalyst (wt%CuMMO (d))[a]	0.3(vl)	0.3(l)	0.3(m)	0.3(h)	0.3(i)	1.2	0.1	0.1(r)	0.1(pm)[b]
Conversion (%)[c]	49	51	54	54	43	44	45	47	39
DFPS (%)	75	81	75	77	75	49	79	78	84
C_6 L:B[d]	3.4	3.3	3.5	3.3	3.7	3.0	3.2	3.1	3.7
C_{4+} Alcohols (%)	55	57	50	49	51	27	56	54	63
C_{4+} Aldehydes (%)	10	11	11	9	10	6	11	10	13
C_{6+} Esters (%)	5	11	12	15	10	11	9	10	6
Others[e] (%)	30	21	27	27	29	56	24	26	18
Acetaldehyde (%)	4	3	4	5	7	5	6	5	6
Ethyl acetate (%)	3	9	9	10	13	30	9	7	3
1-ethoxyethanol (%)	2	1	1	1	1	1	2	1	2
α-Alcohols[f]	0.210	0.182	0.162	0.21	0.147	0.050	0.158	0.186	0.26
α-Esters[f]	0.43	0.32	0.30	0.39	0.21	0.19	0.29	0.33	0.21

[a] Labels only contain Cu wt% and descriptor (d) if any, as all materials are CuMMO.

[b] This experiment is a physical mixture of 1.2CuMMO and 0CuMMO that has a total nominal Cu wt% of 0.1%.

[c] Conversion is defined as average of data points before 5000 turnovers on total Cu content basis of each catalyst by ICP-OES. Data typically is taken in the first 2500 turnovers.

[d] C_6 L:B = linear to branched C_6 alcohol ratio.

[e] Others include Acetaldehyde, ethyl acetate, ethers, ketones, paraffins, olefins, hemiacetals and acetals (Refer to Tables 7-4 – 7-12).

[f] These are the propagation probability (α-values) calculated from the Schultz-Flory distribution (Equation (4-5)).

Conditions: 325°C, 300 psi, 6.56 h^{-1}, 1.00 g catalyst, 0.139 mL/min EtOH, 18.1 mL/min H_2, p_{EtOH}:p_{H2} = 4.

As shown in Figure 4-3, alcohol selectivity varies inversely with BET surface area for the 0.3CuMMO catalysts. Base site concentration or base site density do not have a large impact on

alcohol selectivity (Figure 7-18). The 1.2CuMMO catalyst has a lower alcohol selectivity while having a similar base site count compared to 0.3CuMMO(h), showing that Cu loading is a more important parameter in catalyst performance than base sites. 0.3CuMMO(i) being present in the correlation indicates that the preparation method for the MMO does not impact on its own selectivity to alcohols. A monotonic increase of ester selectivity with base sites is observed for 0.2-0.4wt%Cu loading materials as shown in Figure 4-4. The ethyl acetate selectivity is very similar for these catalysts as well. The selectivity to higher esters increases monotonically with base sites for similar Cu wt% loading catalysts (0.2-0.4wt%Cu). The 0.3CuMMO(vl) catalyst is excluded from Figure 4-4 since this catalyst had at least two times higher acid site concentration than other 0.3CuMMO which caused an increase in olefin selectivity. The incipient wetness impregnation prepared 0.3CuMMO(i) catalyst is displayed in Figure 4-4 but excluded from this correlation since it is observed that this material has a higher Cu content (~0.6wt%) than the other 0.3CuMMO samples, which leads to a higher ethyl acetate selectivity. Similar observations for ester selectivity as a function of density of base sites are also observed (Figure 7-19). The increase of ester formation related to base site counts can be explained by the promotion by these sites of hemiacetal species formation from alcohols and aldehydes which eventually leads to ester formation by dehydrogenation on Cu sites[14,30,31].

The 1.2CuMMO catalyst exhibited a higher ester and ketone selectivity and lower alcohol selectivity than any of the studied catalysts. These results are consistent with prior work done by our group[32], as well as the work of Ramasamy et al. [18,19] and others[15,16,33] who reported that higher loading Cu catalysts are more selective to esters and ketones. Ramasamy et al. particularly claimed that the low loading Cu catalysts had a higher selectivity to alcohols than ethyl acetate because the Cu was in a +1 oxidation state, whereas higher loading Cu catalysts ($\geq$ 0.25 wt%) had a Cu^0

oxidation state[18,19]. They observed the Cu oxidation state using XANES and EXAFS which are bulk techniques. This observation would not extend to catalyst prepared via incipient wetness impregnation[19]. However, the selectivity of a physical mixture of 1.2 CuMMO and MMO (0.1 CuMMO (pm)) is similar in selectivity to the low loading Cu catalysts, and so is the one obtained by 0.3CuMMO(i) prepared by incipient wetness impregnation (which would have Cu as Cu^0 on the surface). This indicates that Cu^0 based catalysts can also have a similar selectivity to alcohols and esters as lower loading Cu catalysts regardless of synthesis method.

We obtained FT-IR spectra of 0CuMMO, 0.1CuMMO, 0.1CuMMO(pm) and 1.2CuMMO after dosing CO at -150°C to further study the oxidation state of Cu in these catalysts. Low temperature CO adsorption on Cu catalysts has been reported to be an accurate approach to measure the oxidation state of Cu in the catalyst surface as Cu^0 and Cu^{+1} have distant bands in the FTIR at 2091-2117 cm^{-1} for Cu^0, [34] and 2145-2160 cm^{-1} for Cu^{+1}.[35] The CO dosing and evacuation FT-IR spectra are shown in Figure 4-5. It is observed that all materials aside from 0CuHT show a peak at 2104 cm^{-1}, corresponding to the CO-Cu^0 band[34] indicative of Cu^0 species. There are also peaks at 2150 and 2162 cm^{-1} observed for all the analyzed materials including 0CuHT. This indicates that these peaks come from the MgAl oxide itself rather than Cu^{+1} species. Furthermore, these two peaks completely disappear after evacuation for all but 1.2CuHT material, in which the height of the remnant peak is $1/40^{th}$ of the original peak. Since CO is known to strongly adsorb in the surface of Cu^{+1} sites[35], we would have expected that whichever peak that could correspond to Cu^{+1} (2150 or 2162 cm^{-1}) remained present after evacuation with little change. Because no peaks remained after evacuation, we can conclude that none of the catalysts analyzed exhibit Cu^{+1} sites on the surface. This observation would then apply by extension to all the materials synthesized in this work.

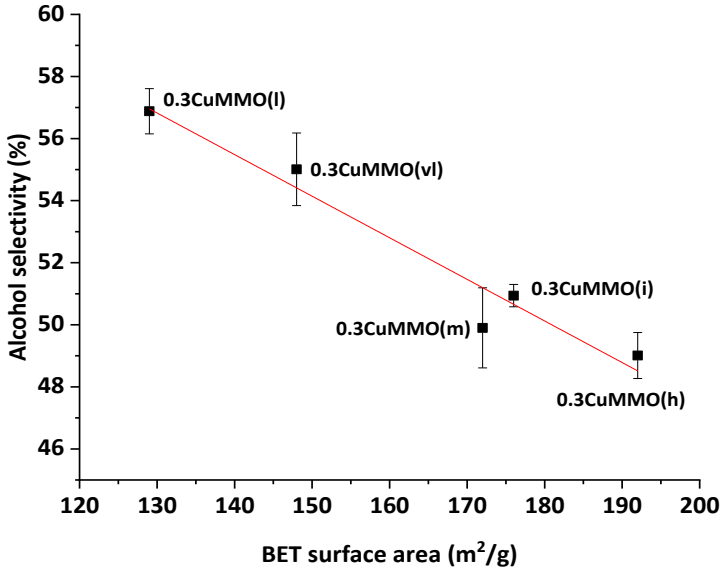

Figure 4-3. Alcohol selectivity vs BET surface area in 0.3wt%Cu (nominal) CuMMO catalysts. Conditions as described in Table 4-2. Red line is linear fit of alcohol selectivity vs BET surface area. Pearson's r = - 0.9744, Adjusted R^2 = 0.9325.

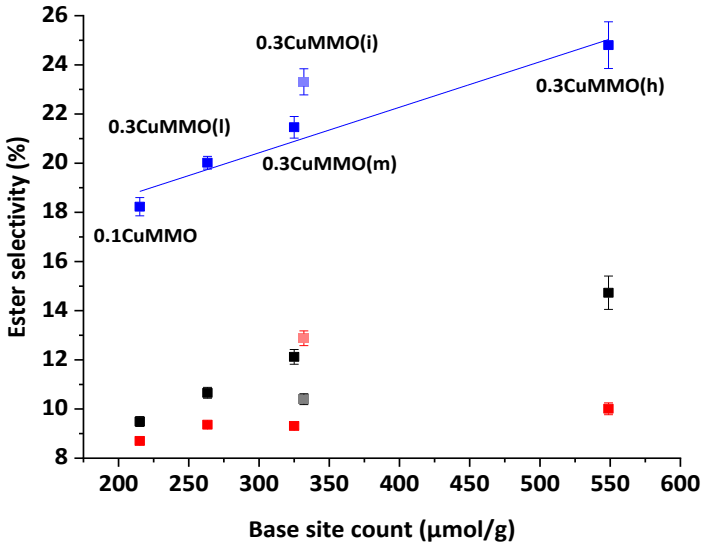

Figure 4-4. Total ester selectivity (■), C_{6+} ester selectivity (■) and ethyl acetate selectivity (■) vs base site count in select low-loading (0.2-0.6 wt%Cu) CuMMO catalysts. Conditions as described in Table 4-2. Blue line is linear fit of total ester selectivity vs base site count excluding 0.3CuMMO(i) (shown in translucent colors). Pearson's r = 0.9816, Adjusted R^2 = 0.9454.

The peak at 2104cm^{-1} (CO-Cu^0 band) for 0.1CuMMO, 0.1CuMMO(pm) and 1.2CuMMO was deconvoluted using a Gaussian function in order to obtain its area (please refer to Table 7-13 and Figure 7-20). We note that the area of this peak on the 1.2CuMMO material is only 2.8 times greater than that of the 0.1CuMMO material. The former material has about 7.5 times more Cu than the latter. This indicates that the dispersion of Cu of 0.1CuMMO is much greater than that of the 1.2CuMMO, which is expected of a lower loading material. The area of the same peak of the 0.1CuMMO material in turn is about 1.7 times greater than that of the peak in the physical mixture, which is more consistent to the ratio of Cu loadings between 0.1CuMMO and 0.1CuMMO(pm) being about 1.4.

The 0.1CuMMO catalyst exhibited a similar performance to that of the 0.3CuMMO catalysts, with slightly higher alcohol selectivity and similarly lower ester selectivity. Moreover, the physical mixture experiment results show that by mixing a higher loading CuMMO material such as 1.2CuMMO with undoped calcined LDH (0CuMMO), it is possible to obtain even higher alcohol selectivities and lower ester selectivities at just a slightly lower conversion than the other CuMMO catalysts at the same conditions. The higher C_{4+} alcohol selectivity and lower C_{6+} ester selectivity obtained from the physical mixture experiment might also be the result of having less actual Cu wt% in the mixture (~0.1wt%) than in the 0.1CuMMO catalyst (~0.2wt%).

Overall, all of the results obtained for the different catalysts suggest that Cu has a promotional role in the rates of reaction steps that involve H-transfers, including ethanol dehydrogenation to acetaldehyde. More importantly, such H-transfer role may be accomplished by very small amounts of Cu, regardless of how Cu is added to the catalyst as shown by the similar performance between 0.3CuMMO(i) to the other 0.3CuMMO, and more remarkably, the slightly better performance of 0.1CuMMO(pm) compared to 0.1CuMMO. Once Cu is added in larger quantities, rates to side

reactions proper to the Cu element such as esterification and ketone formation will become significant, resulting in lower DFP selectivity as shown by 1.2CuMMO and as reported in literature[3,14,15,32].

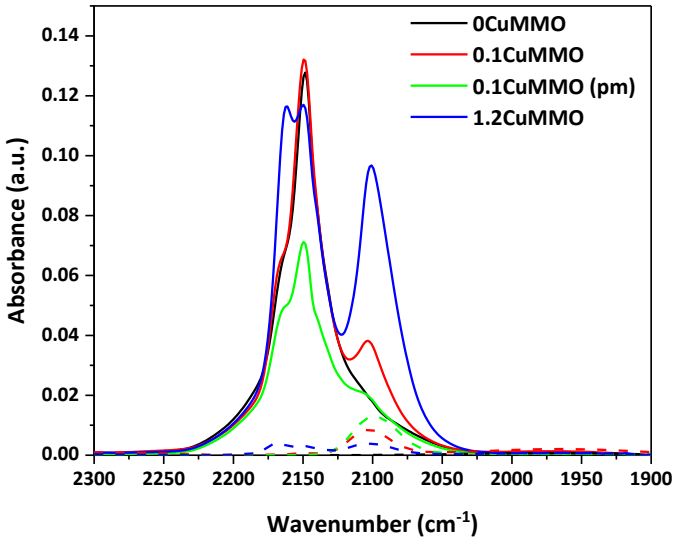

Figure 4-5. IR spectra at 3 Torr of CO on 0CuMMO, 0.1CuMMO, 0.1CuMMO(pm) and 1.2CuMMO recorded at -150°C. Solid lines represent spectra obtained after CO dosing. Dashed lines represent spectra obtained after 9 min evacuation. Catalysts were reduced in situ in flowing 4% H_2/N_2 at 325°C before spectra were collected. Baselines of measurements were subtracted in the 1900-2300 cm^{-1} range so that new baseline is zero for all data.

4.3.3. Schultz-Flory selectivity distributions of alcohols and esters and general reaction pathways

The alcohol selectivities fit the Schultz-Flory model (R^2 = 0.9933 to 0.9997) regardless of Cu loading as shown in Figure 4-6. The chain growth propagation for the alcohols (α) of the 0.1 – 0.6wt% Cu catalysts ranges from 0.147 to 0.210 with no apparent correlation to surface area, base sites counts or product selectivity. The 1.2 wt% Cu catalyst had a lower α value of 0.050, which can be related to the fact that this catalyst has lower selectivity to alcohols. The physical mixture had an α value of 0.26 which is slightly greater than the values for the 0.1-0.6 wt% Cu catalysts. This shows that chain growth occurs in all catalysts by a step growth mechanism and that

electrophilicity of all alcohols is similar regardless of the alcohol size as per the distribution model assumption in which all chains have the same reactivity as described by the model[28] and other authors[11]. Only linear alcohols can continue acting as nucleophiles to form higher alcohols. α-branched alcohols are unable to act as nucleophiles as shown by Eagan et al[6,12]. Moreover, in the present work we did not observe any alcohol that could be formed from the attack of a linear alcohol to an α-branched alcohol. This could be explained by steric effects on the region close to the C-O bond preventing C-C bonding to occur. This result and that of the C_6 linear:branched alcohol ratio being greater than 1 allows us to therefore conclude that CuMMO catalysts promote coupling by increasing the relative nucleophilicity (i.e. tendency to attack and form C-C bonds) of ethanol with respect to other alcohols.

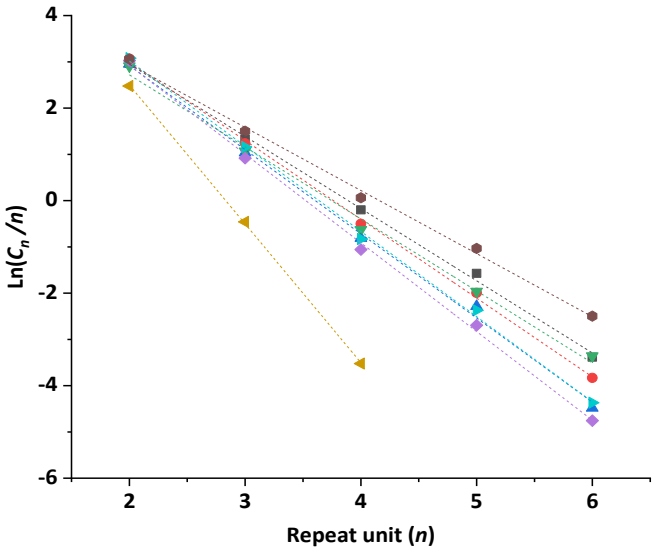

Figure 4-6. Schultz-Flory distribution plots for primary alcohols for 0.3CuMMO(vl) (■, α = 0.210 ± 0.008), 0.3CuMMO(l) (●, α = 0.182 ± 0.006), 0.3CuMMO(m) (▲, α = 0.162 ± 0.009), 0.3CuMMO(h) (▼, α = 0.21 ± 0.01), 0.3CuMMO(i) (◆, α = 0.147 ± 0.006), 1.2CuMMO (◀, α = 0.050 ± 0.002), 0.1CuMMO (▶, α = 0.158 ± 0.007) and 0.1CuMMO (pm) (⬢, α = 0.26 ± 0.01). Dashed lines denote linear fits defined in equation 4-5. Conditions as described in Table 4-2.

Ester products also fit the Schultz-Flory distribution chain growth model as shown in Figure 4-7. Their degree of fit is lower than that of the alcohol selectivities (R^2 = 0.9606 – 0.9902). The α-

value for 0.1-0.6wt% Cu-doped materials varies widely between 0.29 and 0.43, again with no apparent correlation to any property as was the case for alcohols. The α-value for the 1.2CuMMO catalyst is 0.19, which is closer to the obtained for the 0.3CuMMO(i) made by incipient wetness impregnation of 0.21. The α-value for the physical mixture is 0.51, being the largest among all materials. This may be explained if an alcohol-to-ester series mechanism is taking place as it is reported in literature for Cu-containing MMO[15,30], which can be assumed to be the case since hemiacetals (particularly 1-ethoxyethanol) were observed in the products. The larger esters could also be produced by transesterification reactions, in which a part of the alcohol moiety of the ester may be substituted by another one. Also, ester selectivity following Schultz-Flory distribution may indicate that the electrophilicity of aldehydes to form C-O bonds is similar regardless of their size.

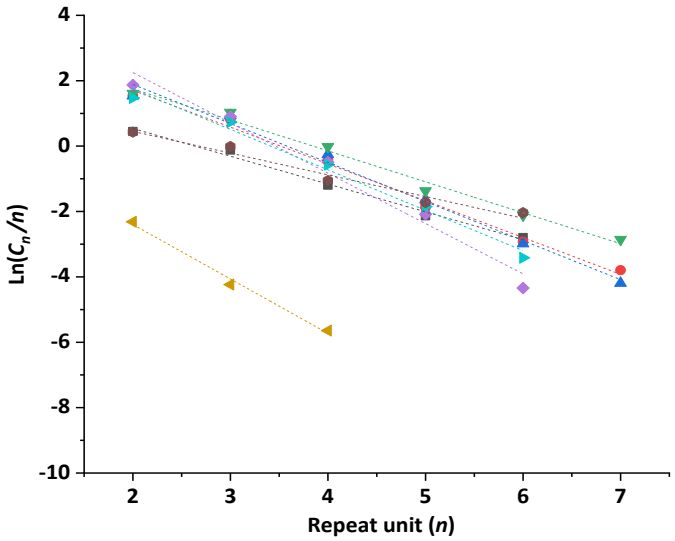

Figure 4-7. Schultz-Flory distribution plots for esters for 0.3CuMMO(vl) (■, α = 0.43 ± 0.02), 0.3CuMMO(l) (●, α = 0.32 ± 0.02), 0.3CuMMO(m) (▲, α = 0.30 ± 0.02), 0.3CuMMO(h) (▼, α = 0.39 ± 0.02), 0.3CuMMO(i) (◆, α = 0.21 ± 0.03), 1.2CuMMO (◀ , α = 0.19 ± 0.03), 0.1CuMMO (▶ , α = 0.29 ± 0.02) and 0.1CuMMO(pm) (⬢ , α = 0.51 ± 0.01). Dashed lines denote linear fits defined in equation 4-5. Conditions as described in Table 4-2.

To further understand the reasons behind the favorable selectivity of low Cu-loading catalysts towards diesel fuel precursors, particularly towards C_{4+} alcohols, we need to consider the

contribution of each type of site in the catalysts towards the most important reactions occurring. In Figure 4-8 we outline the most important reactions that happen on the Cu sites and the acid-base sites of Mg_xAlO_y. Ethanol dehydrogenation to acetaldehyde can be catalyzed by both acid-base sites (1a)[8,24,25,25,33], and Cu sites (1b)[15,33,36]. Alcohol condensation either via direct condensation (2a and 3a for ethanol) mechanisms, Aldol condensation (4a) or a combination of both mechanisms [37] may be catalyzed mostly by acid-base sites [24,25,33,36,38,38,39] of Mg_xAlO_y, in which H-transfer steps occur through intermolecular exchanges via Meerwein–Ponndorf–Verley (MPV) mechanisms (5a) that are equilibrium-limited. Cu sites catalyze decarbonylation of the aldol intermediate to a ketone (2b for acetone)[33,40]. However, Cu sites enable an increase of the concentration of surface H and allows transport of such species across the catalyst surface. This H-transfer capabilities to the material allows for H removal in deprotonation steps by forming gas phase H_2. The addition of Cu can thus increase rates of deprotonation of the β-C of ethanol and α-C of acetaldehyde (involved in steps of 2a-4a). The increased surface H concentration also increases rates of hydrogenation/dehydrogenation reactions from which the larger alcohols are increased (via 3b-6b rather than 5a). Such H-transfer reactions are reported to be the rate-limiting step of higher alcohol formation [38,41,42]. The kinetic model for ethanol coupling based on Aldol condensation developed by our group with Ca-HAP in prior work assumes deprotonation of the α-C of acetaldehyde as the rate-limiting step[12]. The low loading (0.2-0.6wt%Cu) catalysts in this work have high C_{4+} alcohol selectivity (49 – 56%) likely because surface H can be quickly removed from deprotonation steps when Cu is added to the Mg_xAlO_y. The concentration of surface hydrogen can be increased by raising total pressure allowing for more facile hydrogenation of alcohol coupling intermediates (note that the $P_{ethanol}>P_{H2}$ to boost H_2 formation from surface H via

favorable equilibrium in ethanol deprotonation steps to obtain high conversion). It is remarkable then that only a very small amount of Cu is required for this to occur.

It can be concluded that Cu does not need to be atomically close to acid-base sites for two main reasons: 1) The performance of the physical mixture of 1.2CuMMO and 0CuMMO is similar to that of low Cu loading catalysts and 2) the low temperature CO adsorption experiments show that the 1.2CuMMO and 0.3CuMMO catalysts have similar types of Cu sites. The product selectivity may be expressed as a combination of the rates by each type of site separately. The higher alcohol selectivity for low Cu loading catalysts is then due to the rates of acid-base catalyzed alcohol coupling being greater than those of Cu-catalyzed esterification and ketone formation [33,36,40,43]. If Cu loadings are further increased, decarbonylation (3b) and esterification (7b, 8b) will increase, and product selectivity will shift towards ketones and lighter esters (7b particularly).

Finally, another unexpected effect of having low Cu loadings in the catalysts is that since higher alcohol formation is favored (7a, 8a), it is possible to form higher esters in relatively high selectivity compared to ethyl acetate, since the higher alcohols and aldehydes would form these via formation of hemiacetals (9a rather than 6a) that can subsequently be dehydrogenated by Cu sites, which are also capable on their own to fully form the higher esters (8b).

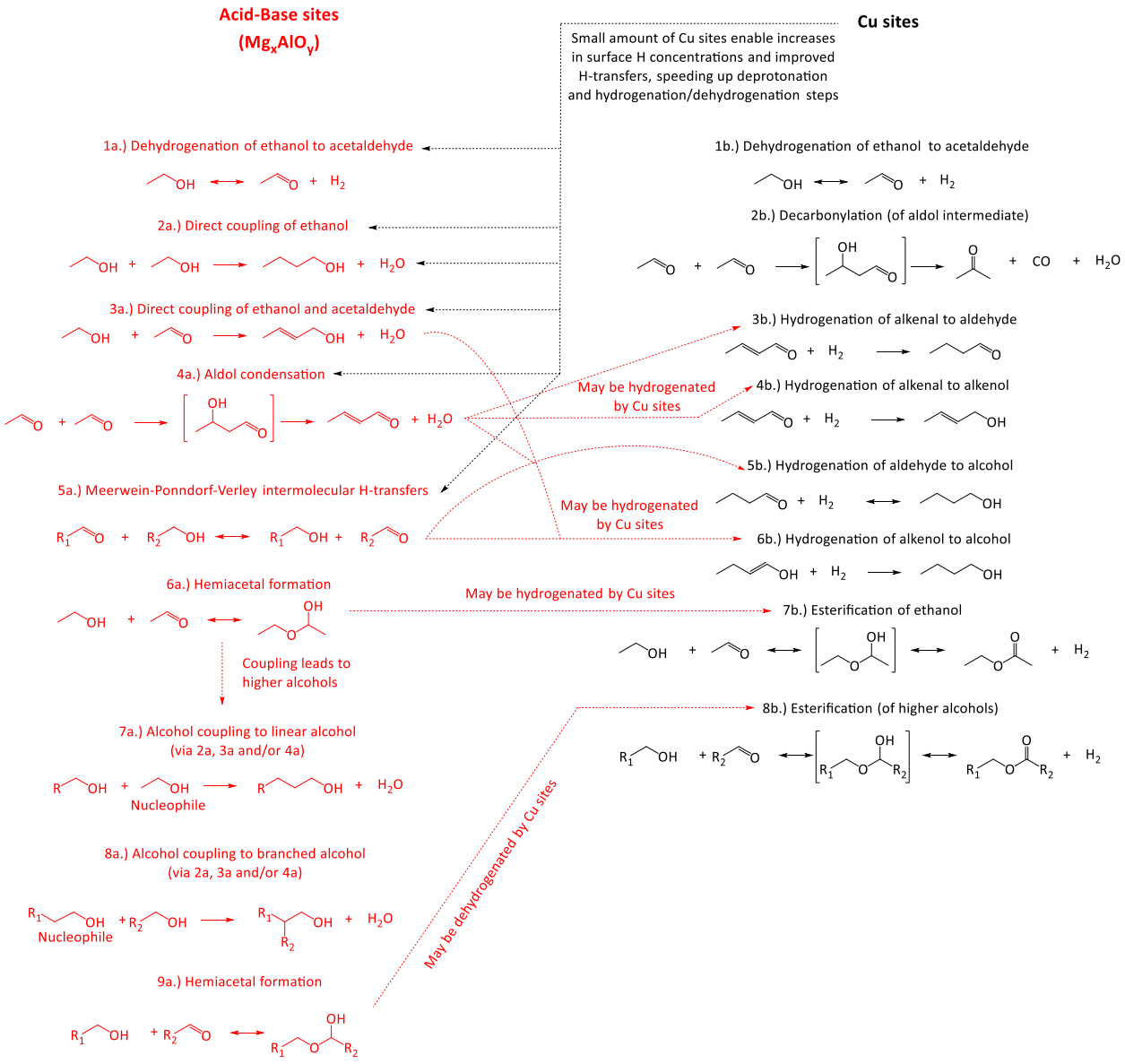

Figure 4-8. List of main reactions catalyzed by Cu/Mg_xAlO_y catalysts. Main reactions catalyzed by acid-base sites are shown in red. Main reactions catalyzed by Cu sites are shown in black. Synergies between reaction steps on Cu sites and products from acid-base catalyzed steps are indicated in red dashed arrows. Synergies between reaction steps of acid-base catalyzed reactions and small amounts of Cu sites are shown in dashed black arrows.

4.3.4. Catalyst stability and deactivation mechanism

All catalysts were observed to undergo deactivation. Figure 4-9 shows the conversion of 0.1CuMMO over 170 h at two different WHSV. It can be observed that at 6.56 h^{-1} deactivation seems to be proceeding faster than at 1.48 h^{-1} (for species selectivities changes over time please refer to Figure 7-21). Therefore, we decided to compare loss of activity over number of turnovers in Cu loading base to obtain a normalized way of measuring deactivation since it seems to be the most influencing parameter in catalyst selectivity. Activity is defined as the ratio of conversion at a given TOS to the initial conversion as defined by equation (6). Figure 4-10 shows the catalyst activity as a function of turnovers for 0.1CuMMO. It can be observed that deactivation is proportional to the number of turnovers. This trend was observed for the other 0.3CuMMO catalysts as shown in Figures 7-22 to 7-26 for select catalysts.

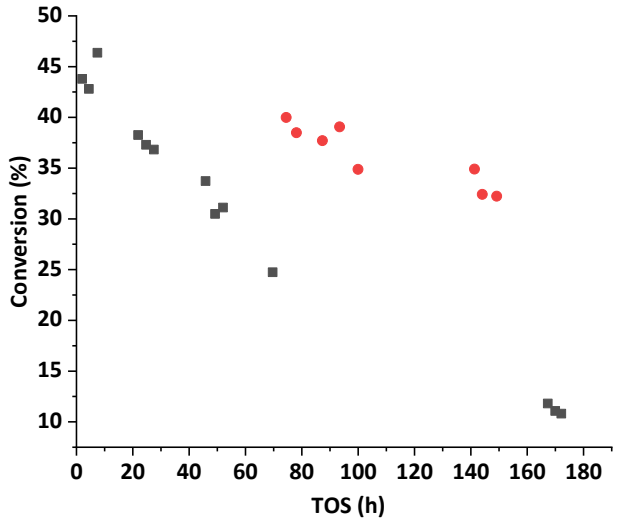

Figure 4-9. Stability test of 0.1CuMMO at 6.56 h^{-1} (■) and 1.48 h^{-1} (●). **Conditions:** 325°C, 300 psi, 1.00 g catalyst, p_{EtOH}:p_{H2} = 4.

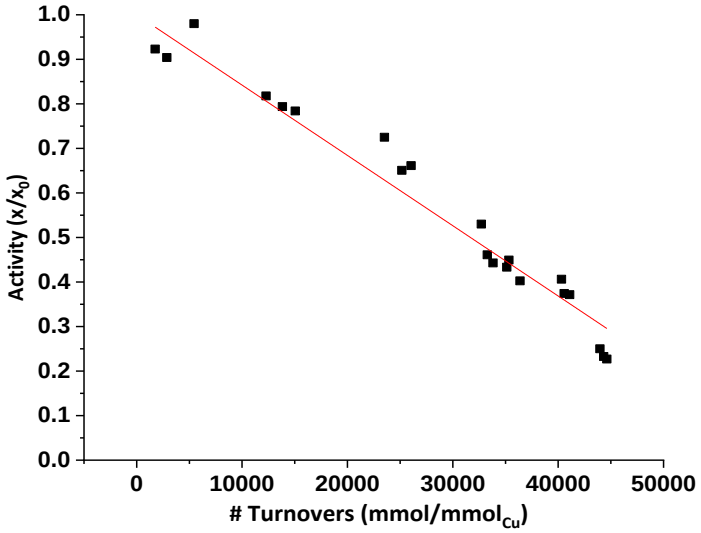

Figure 4-10. Normalized activity vs turnovers for 0.1CuMMO. **Conditions** as in Figure 4-9. Red line is fit of activity vs #Turnovers, with activity as defined by equation 4-6: $a = x/x_0 = 1 - 1.58 \times 10^{-5} T_n$, where $R^2 = 0.9939$ and slope = $(1.58 \pm 0.03) \times 10^{-5}$.

Deactivation of these catalysts has been reported to occur via oligomerization of aldehyde species[15], at least when no metal is incorporated. It is also possible that olefins may also undergo oligomerization in the acid sites of the catalyst and generate coke. Water generated in the alcohol coupling and dehydration reactions may rehydrate the LDH structure, promoting deactivation. X-ray diffractograms of the spent 0.1CuMMO catalyst compared to the fresh calcined material are shown in Figure 4-11. The X-ray diffraction pattern of the spent catalyst compared to the fresh sample shows that the crystalline structure of the fresh and spent material correspond to the MgO-like phase expected from a solid solution of MgO and Al_2O_3 with Mg/Al > 1 [24], which allows us to conclude that no rehydration occurred. However, we do note that a ~15% decrease on peak width occurred in the spent material compared to the fresh suggesting increase of crystallite sizes. Thermogravimetric analysis (TGA) of the spent and fresh 0.1CuMMO is shown in Figure 4-12. TGA shows that about 18% of the mass of the catalyst was lost when it was heated from room temperature to 650°C. It can be observed that from 200 – 400°C, a major part of the mass loss occurs, which is consistent with loss of carbon species on the surface of the catalyst, whereas the

loss that occurs at lower temperatures can be attributed mostly to water, as the fresh sample TGA shows a major mass loss only before 200°C. An additional confirmation of the observations made above was done by analyzing the 0.3CuMMO(m) spent sample. The results are shown in Figures 7-27 and 7-28, where a comparison between the fresh and spent samples of 0.3CuMMO(m) catalyst is done, corroborating the results for the 0.1CuMMO material. A final piece of evidence was obtained by performing TOC analysis to the 0.1CuMMO and 0.3CuMMO(m) samples, showing that 13% and 14% of each sample mass respectively was carbon versus 1% and 2% of each fresh sample, which is consistent with deactivation via coking. We also carried out quantification of metal content analysis of select product samples by ICP-OES, and all the analyses showed no leaching of the metals into the products (i.e. metal content no different from baseline).

Another possible deactivation mechanism that occurs with metal particles is sintering. To verify if sintering is occurring, several micrographs of freshly calcined catalysts were taken and compared to micrographs of catalysts reduced at reaction conditions and then passivated with 1 O_2/Ar pulses to determine whether metal aggregation occurred. A comparison between fresh calcined and reduced and passivated images of 0.1CuMMO, 0.3CuMMO(m) and 1.2CuMMO is shown in Figure 4-13. Larger areas of darker domains are observed in the reduced and passivated samples compared to the fresh materials, suggesting particle aggregation occurs. Coupling this observation to that of the decrease of peak width from the XRD analysis, we conclude that sintering is a possible deactivation mechanism. Sintering of Cu nanoparticles has been observed on similar catalysts with higher Cu loadings for the catalytic upgrading of glycerol[44–46] and sugar fractions, with minimal decrease in activity even after 100 h TOS[44]. The same observations hold for the rest of catalysts, as shown in Figure 7-29.

Finally, we regenerated 0.1CuMMO catalyst as described at the end of the Ethanol Oligomerization Reactions section. The results of the run with the regenerated catalyst compared to the fresh one is shown in Table 4-2 and Table 7-4. Overall, reaction performance is very similar between fresh and regenerated batches, with the regenerated batch producing small amounts of aromatic species. Therefore, it can be concluded that the catalyst is regenerable and that the primary mechanism of deactivation within the timeframe studied is coking.

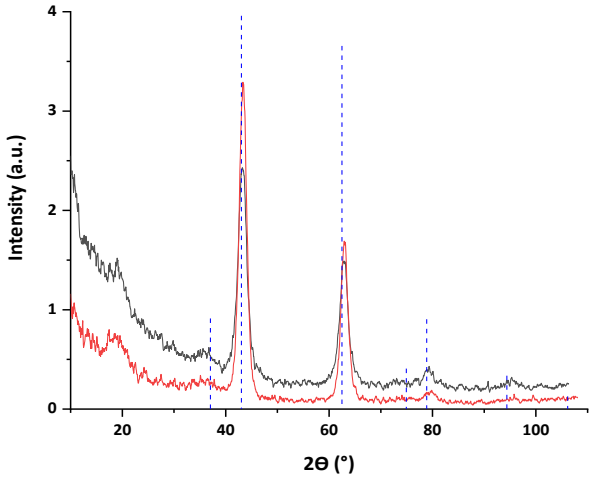

Figure 4-11. Powder XRD of fresh (black) and spent (red) calcined 0.1CuMMO. Blue dashed lines represent MgO periclase peaks (PDF# 04-002-3057). X-ray source used was Cu kα (λ = 1.54 Å).

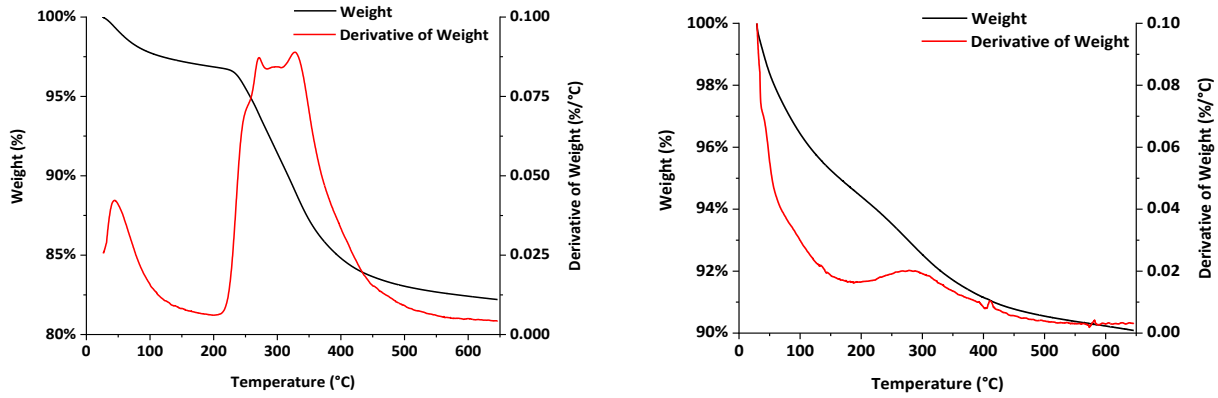

Figure 4-12. TGA of 0.1CuMMO spent (left) and fresh calcined (right). **TGA conditions:** 25-650°C (10°C/min). 50mL/min O_2, 10-15mg sample.

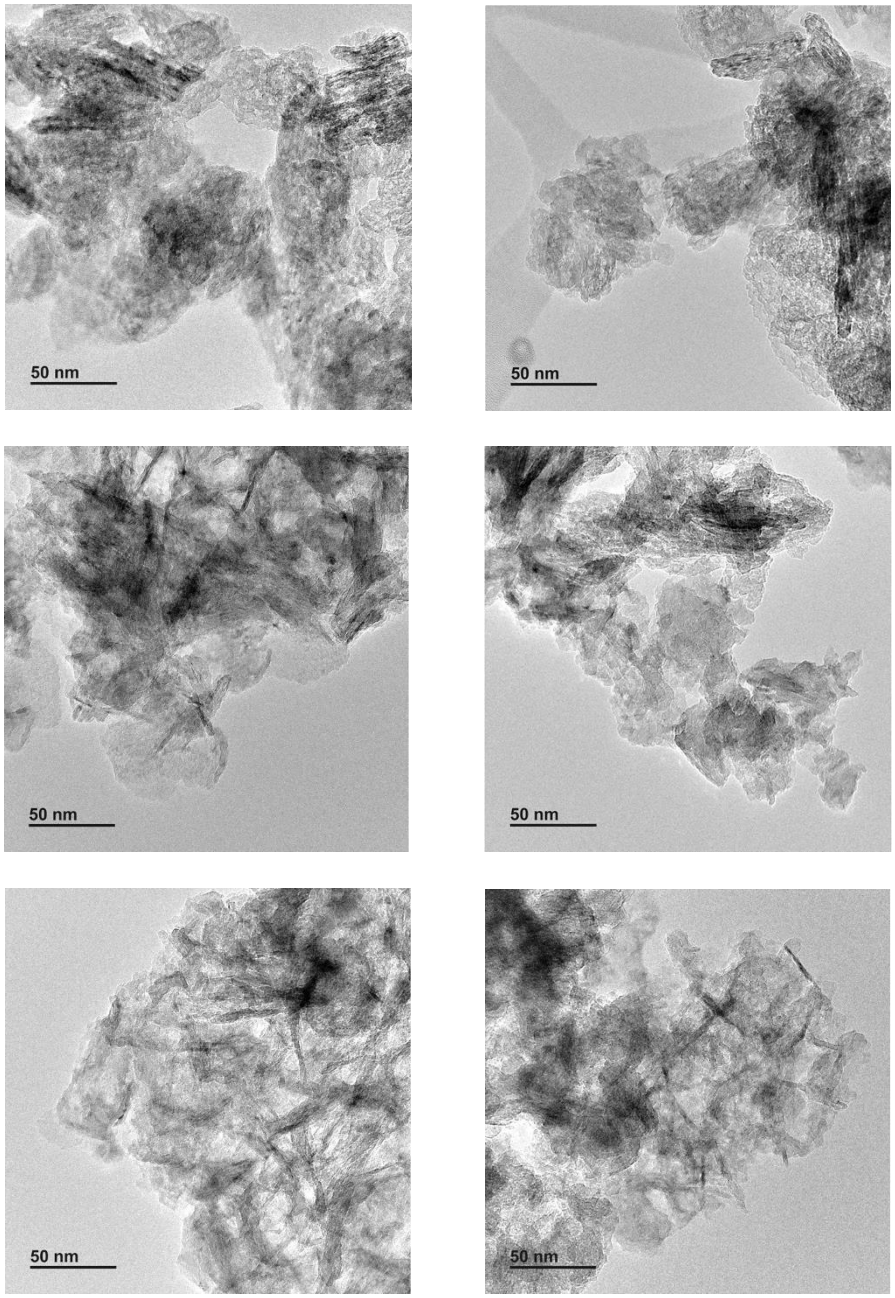

Figure 4-13. TEM micrographs of 0.1CuMMO (upper), 0.3CuMMO(m) (middle) and 1.2CuMMO(lower). Micrographs to the left are of freshly calcined catalysts (600°C, 2h, 4°C/min, static air). Micrographs to the right are of reduced (50mL/min H_2, 325°C, 1.33h) then passivated (1% O_2/Ar pulses) catalysts.

4.4. Conclusions

Low (0.1 - 0.6 wt%) Cu loadings catalysts supported on Mg_xAlO_y can promote coupling of ethanol to higher predominately linear alcohols and aldehydes with high selectivity regardless of how the Cu is added to the catalyst. The low Cu catalysts exhibited high selectivities (75-84%) towards diesel-fuel precursor compounds. C_{6+} esters are another product of this reaction. The esters are combinations of the several mostly linear alcohols produced and can potentially be used as diesel fuel additives. Moreover, we found that varying surface area of the catalyst has an impact in properties such as pore volume and base site counts, but this does not translate into significant changes in catalyst performance as does varying the Cu loading. In contrast, higher loading of Cu (>1.2 wt%) on Mg_xAlO_y produces higher amounts of ethyl acetate and ketones, significantly reducing selectivity to diesel-fuel precursor compounds. Increasing the acidity of the catalyst can increase the olefin yield at the expense of ester yields.

By adding small Cu amounts to Mg_xAlO_y catalysts, the materials become able to promote higher alcohol coupling by facilitating H-transfers on the catalyst surface and enabling H_2 scission and proton recombination, accelerating acid-base-catalyzed deprotonation and hydrogenation/dehydrogenation reaction steps that would be carried out via equilibrated MPV mechanisms otherwise. Alcohol coupling then involves ethanol coupling to 1-butanol either via aldol condensation or direct condensation. 1-butanol then is attacked by an ethanol-derived active species to form 1-hexanol, and a similar process occurs with any combination of alcohols in which the ethanol-derived species performs the nucleophilic attack to form increasingly larger alcohols. In any other case, primary branched alcohols are formed, and these are incapable of undergoing coupling in an appreciable manner. Ethanol may also dehydrogenate to acetaldehyde, which in turn can participate in the coupling reaction to higher alcohols depending on the mechanism, and

also participates in the formation of esters such as ethyl acetate by forming C-O bonds with alcohols. Esters are formed from alcohols and aldehydes produced via hemiacetal-based mechanisms that can be catalyzed by Cu sites, and may be further helped by acid-base sites. Additional reactions include decarbonylation that gives rise to ketones, unimolecular dehydration to olefins and bimolecular dehydration to ethers.

The alcohols and esters follow a Schultz-Flory distribution chain growth model. The alcohol and ester molecules have similar electrophilicities, therefore the driving force of alcohol growth is an increased nucleophilicity of ethanol relative to the other alcohols when Cu/Mg_xAlO_y catalysts are used.

The studied catalysts deactivated proportional to the number of turnovers mainly by coking. Deactivation was reversible and the catalyst activity can be recovered by calcination. Therefore, we discovered that using sufficiently low Cu loadings, a series of inexpensive LDH calcined catalysts that can be used to produce diesel fuel precursor compounds in high selectivities was uncovered in this work.

4.5. References

(1) Exxon Mobil Corporation. 2019 Outlook for Energy: A Perspective to 2040 https://corporate.exxonmobil.com/-/media/Global/Files/outlook-for-energy/2019-Outlook-for-Energy_v4.pdf (accessed 2021-04-19).

(2) FedCenter - EO 13693 (Archive) - revoked by EO 13834 on May 17, 2018, Sec. 8 https://www.fedcenter.gov/programs/eo13693/ (accessed 2021-04-19).

(3) Eagan, N. M.; Kumbhalkar, M. D.; Buchanan, J. S.; Dumesic, J. A.; Huber, G. W. Chemistries and Processes for the Conversion of Ethanol into Middle-Distillate Fuels. *Nature Reviews Chemistry* **2019**, *3* (4), 223–249. https://doi.org/10.1038/s41570-019-0084-4.

(4) USDA Study Shows Significant Greenhouse Gas Benefits of Ethanol Compared with Gasoline https://www.usda.gov/media/press-releases/2019/04/02/usda-study-shows-significant-greenhouse-gas-benefits-ethanol (accessed 2021-04-19).

(5) Zang, G.; Sun, P.; Elgowainy, A.; Bafana, A.; Wang, M. Life Cycle Analysis of Electrofuels: Fischer–Tropsch Fuel Production from Hydrogen and Corn Ethanol Byproduct CO2. *Environ. Sci. Technol.* **2021**, *55* (6), 3888–3897. https://doi.org/10.1021/acs.est.0c05893.

(6) Eagan, N. M.; Moore, B. M.; McClelland, D. J.; Wittrig, A. M.; Canales, E.; Lanci, M. P.; Huber, G. W. Catalytic Synthesis of Distillate-Range Ethers and Olefins from Ethanol through Guerbet Coupling and Etherification. *Green Chem.* **2019**, *21* (12), 3300–3318. https://doi.org/10.1039/C9GC01290G.

(7) Huq, N. A.; Huo, X.; Hafenstine, G. R.; Tifft, S. M.; Stunkel, J.; Christensen, E. D.; Fioroni, G. M.; Fouts, L.; McCormick, R. L.; Cherry, P. A.; McEnally, C. S.; Pfefferle, L. D.; Wiatrowski, M. R.; Benavides, P. T.; Biddy, M. J.; Connatser, R. M.; Kass, M. D.; Alleman, T. L.; John, P. C. S.; Kim, S.; Vardon, D. R. Performance-Advantaged Ether Diesel Bioblendstock Production by a Priori Design. *PNAS* **2019**, *116* (52), 26421–26430. https://doi.org/10.1073/pnas.1911107116.

(8) Kozlowski, J. T.; Davis, R. J. Heterogeneous Catalysts for the Guerbet Coupling of Alcohols. *ACS Catal.* **2013**, *3* (7), 1588–1600. https://doi.org/10.1021/cs400292f.

(9) Silvester, L.; Lamonier, J.-F.; Lamonier, C.; Capron, M.; Vannier, R.-N.; Mamede, A.-S.; Dumeignil, F. Guerbet Reaction over Strontium-Substituted Hydroxyapatite Catalysts Prepared at Various (Ca+Sr)/P Ratios. *ChemCatChem* **2017**, *9* (12), 2250–2261. https://doi.org/10.1002/cctc.201601480.

(10) Hanspal, S.; Young, Z. D.; Prillaman, J. T.; Davis, R. J. Influence of Surface Acid and Base Sites on the Guerbet Coupling of Ethanol to Butanol over Metal Phosphate Catalysts. *Journal of Catalysis* **2017**, *352*, 182–190. https://doi.org/10.1016/j.jcat.2017.04.036.

(11) Moteki, T.; Flaherty, D. W. Mechanistic Insight to C–C Bond Formation and Predictive Models for Cascade Reactions among Alcohols on Ca- and Sr-Hydroxyapatites. *ACS Catal.* **2016**, *6* (7), 4170–4183. https://doi.org/10.1021/acscatal.6b00556.

(12) Eagan, N. M.; Lanci, M. P.; Huber, G. W. Kinetic Modeling of Alcohol Oligomerization over Calcium Hydroxyapatite. *ACS Catal.* **2020**, *10* (5), 2978–2989. https://doi.org/10.1021/acscatal.9b04734.

(13) De Bruyn, M.; Sun, Z.; Barta, K. Chapter Three - The Thousand Faces of Cu-Doped Porous Mixed Oxides (Cu-PMO) in the Conversion of Renewable Resources and Beyond. In *Advances in Inorganic Chemistry*; Ford, P. C., van Eldik, R., Eds.; Catalysis in Biomass Conversion; Academic Press, 2021; Vol. 77, pp 59–98. https://doi.org/10.1016/bs.adioch.2020.12.002.

(14) Marcu, I.-C.; Tichit, D.; Fajula, F.; Tanchoux, N. Catalytic Valorization of Bioethanol over Cu-Mg-Al Mixed Oxide Catalysts. *Catalysis Today* **2009**, *147* (3), 231–238. https://doi.org/10.1016/j.cattod.2009.04.004.

(15) Bravo-Suárez, J. J.; Subramaniam, B.; Chaudhari, R. V. Vapor-Phase Methanol and Ethanol Coupling Reactions on CuMgAl Mixed Metal Oxides. *Applied Catalysis A: General* **2013**, *455*, 234–246. https://doi.org/10.1016/j.apcata.2013.01.025.

(16) Cheng, F.; Guo, H.; Cui, J.; Hou, B.; Li, D. Guerbet Reaction of Methanol and Ethanol Catalyzed by CuMgAlOx Mixed Oxides: Effect of M2+/Al3+ Ratio. *Journal of Fuel Chemistry and Technology* **2018**, *46* (12), 1472–1481. https://doi.org/10.1016/S1872-5813(18)30061-6.

(17) H. M. Job. Reaction Mechanism Studies of Ethanol Coupling over Mixed Oxide Catalyst, 2016.

(18) Gray, M. J.; Alvarez-Vasco, C.; Guo, M.; Ramasamy, K. K. Distillate Generation via Guerbet Alcohol Coupling from Biomass, 2016.

(19) Ramasamy, K. K.; Guo, M. F.; Gray, M. J.; Subramaniam, S. United States Patent: 10745330 - Method of Converting Ethanol to Higher Alcohols. 10745330, August 18, 2020.

(20) Ramasamy, K. K.; Gray, M.; Job, H.; Smith, C.; Wang, Y. Tunable Catalytic Properties of Bi-Functional Mixed Oxides in Ethanol Conversion to High Value Compounds. *Catalysis Today* **2016**, *269*, 82–87. https://doi.org/10.1016/j.cattod.2015.11.045.

(21) Ramasamy, K. K.; Gray, M.; Job, H.; Santosa, D.; Li, X. S.; Devaraj, A.; Karkamkar, A.; Wang, Y. Role of Calcination Temperature on the Hydrotalcite Derived MgO–Al2O3 in Converting Ethanol to Butanol. *Top Catal* **2016**, *59* (1), 46–54. https://doi.org/10.1007/s11244-015-0504-8.

(22) Chen, C.; Yang, M.; Wang, Q.; Buffet, J.-C.; O'Hare, D. Synthesis and Characterisation of Aqueous Miscible Organic-Layered Double Hydroxides. *J. Mater. Chem. A* **2014**, *2* (36), 15102–15110. https://doi.org/10.1039/C4TA02277G.

(23) Wang, Q.; O'Hare, D. Large-Scale Synthesis of Highly Dispersed Layered Double Hydroxide Powders Containing Delaminated Single Layer Nanosheets. *Chem. Commun.* **2013**, *49* (56), 6301–6303. https://doi.org/10.1039/C3CC42918K.

(24) Díez, V. K.; Apesteguía, C. R.; Di Cosimo, J. I. Effect of the Chemical Composition on the Catalytic Performance of MgyAlOx Catalysts for Alcohol Elimination Reactions. *Journal of Catalysis* **2003**, *215* (2), 220–233. https://doi.org/10.1016/S0021-9517(03)00010-1.

(25) Di Cosimo, J. I.; Apesteguı&́a, C. R.; Ginés, M. J. L.; Iglesia, E. Structural Requirements and Reaction Pathways in Condensation Reactions of Alcohols on MgyAlOx Catalysts. *Journal of Catalysis* **2000**, *190* (2), 261–275. https://doi.org/10.1006/jcat.1999.2734.

(26) Di Cosimo, J. I.; Díez, V. K.; Xu, M.; Iglesia, E.; Apesteguía, C. R. Structure and Surface and Catalytic Properties of Mg-Al Basic Oxides. *Journal of Catalysis* **1998**, *178* (2), 499–510. https://doi.org/10.1006/jcat.1998.2161.

(27) Takeuchi, D.; Osakada, K. Oligomerization of Olefins. In *Organometallic Reactions and Polymerization*; Osakada, K., Ed.; Lecture Notes in Chemistry; Springer: Berlin, Heidelberg, 2014; pp 169–215. https://doi.org/10.1007/978-3-662-43539-7_5.

(28) Young, C. T.; von Goetze, R.; Tomov, A. K.; Zaccaria, F.; Britovsek, G. J. P. The Mathematics of Ethylene Oligomerisation and Polymerisation. *Top Catal* **2020**, *63* (3), 294–318. https://doi.org/10.1007/s11244-019-01210-0.

(29) Kuśtrowski, P.; Chmielarz, L.; Bożek, E.; Sawalha, M.; Roessner, F. Acidity and Basicity of Hydrotalcite Derived Mixed Mg–Al Oxides Studied by Test Reaction of MBOH Conversion and Temperature Programmed Desorption of NH3 and CO2. *Materials Research Bulletin* **2004**, *39* (2), 263–281. https://doi.org/10.1016/j.materresbull.2003.09.032.

(30) Inui, K.; Kurabayashi, T.; Sato, S. Direct Synthesis of Ethyl Acetate from Ethanol Carried Out under Pressure. *Journal of Catalysis* **2002**, *212* (2), 207–215. https://doi.org/10.1006/jcat.2002.3769.

(31) Hronec, M.; Fulajtárová, K.; Horváth, B.; Liptaj, T.; Dobročka, E. A Facile Conversion of Furfural to Novel Tetrahydrofurfuryl Hemiacetals. *Applied Catalysis A: General* **2020**, *594*, 117471. https://doi.org/10.1016/j.apcata.2020.117471.

(32) Petrolini, D. D.; Eagan, N.; Ball, M. R.; Burt, S. P.; Hermans, I.; Huber, G. W.; Dumesic, J. A.; Martins, L. Ethanol Condensation at Elevated Pressure over Copper on AlMgO and AlCaO Porous Mixed-Oxide Supports. *Catal. Sci. Technol.* **2019**, *9* (8), 2032–2042. https://doi.org/10.1039/C9CY00316A.

(33) Iglesia, E.; Barton, D. G.; Biscardi, J. A.; Gines, M. J. L.; Soled, S. L. Bifunctional Pathways in Catalysis by Solid Acids and Bases. *Catalysis Today* **1997**, *38* (3), 339–360. https://doi.org/10.1016/S0920-5861(97)81503-7.

(34) Ro, I.; Liu, Y.; Ball, M. R.; Jackson, D. H. K.; Chada, J. P.; Sener, C.; Kuech, T. F.; Madon, R. J.; Huber, G. W.; Dumesic, J. A. Role of the Cu-ZrO2 Interfacial Sites for Conversion of Ethanol to Ethyl Acetate and Synthesis of Methanol from CO2 and H2. *ACS Catal.* **2016**, *6* (10), 7040–7050. https://doi.org/10.1021/acscatal.6b01805.

(35) Borgard, G. D.; Molvik, S.; Balaraman, P.; Root, T. W.; Dumesic, J. A. Microcalorimetric and Infrared Spectroscopic Studies of CO, C2H4, N2O, and O2 Adsorption on Cu-Y Zeolite. *Langmuir* **1995**, *11* (6), 2065–2070. https://doi.org/10.1021/la00006a037.

(36) Gines, M. J. L.; Iglesia, E. Bifunctional Condensation Reactions of Alcohols on Basic Oxides Modified by Copper and Potassium. *Journal of Catalysis* **1998**, *176* (1), 155–172. https://doi.org/10.1006/jcat.1998.2009.

(37) de Souza, E. F.; Pacheco, H. P.; Miyake, N.; Davis, R. J.; Toniolo, F. S. Computational and Experimental Mechanistic Insights into the Ethanol-to-Butanol Upgrading Reaction over MgO. *ACS Catal.* **2020**, *10* (24), 15162–15177. https://doi.org/10.1021/acscatal.0c04616.

(38) C. Meunier, F.; Scalbert, J.; Thibault-Starzyk, F. Unraveling the Mechanism of Catalytic Reactions through Combined Kinetic and Thermodynamic Analyses: Application to the Condensation of Ethanol. *Comptes Rendus Chimie* **2015**, *18* (3), 345–350. https://doi.org/10.1016/j.crci.2014.07.002.

(39) Ndou, A. S.; Plint, N.; Coville, N. J. Dimerisation of Ethanol to Butanol over Solid-Base Catalysts. *Applied Catalysis A: General* **2003**, *251* (2), 337–345. https://doi.org/10.1016/S0926-860X(03)00363-6.

(40) Neurock, M.; Tao, Z.; Chemburkar, A.; Hibbitts, D. D.; Iglesia, E. Theoretical Insights into the Sites and Mechanisms for Base Catalyzed Esterification and Aldol Condensation Reactions over Cu. *Faraday Discuss.* **2017**, *197*, 59–86. https://doi.org/10.1039/C6FD00226A.

(41) Pang, J.; Zheng, M.; He, L.; Li, L.; Pan, X.; Wang, A.; Wang, X.; Zhang, T. Upgrading Ethanol to N-Butanol over Highly Dispersed Ni–MgAlO Catalysts. *Journal of Catalysis* **2016**, *344*, 184–193. https://doi.org/10.1016/j.jcat.2016.08.024.

(42) Ogo, S.; Onda, A.; Iwasa, Y.; Hara, K.; Fukuoka, A.; Yanagisawa, K. 1-Butanol Synthesis from Ethanol over Strontium Phosphate Hydroxyapatite Catalysts with Various Sr/P Ratios. *Journal of Catalysis* **2012**, *296*, 24–30. https://doi.org/10.1016/j.jcat.2012.08.019.

(43) Sad, M. E.; Neurock, M.; Iglesia, E. Formation of C–C and C–O Bonds and Oxygen Removal in Reactions of Alkanediols, Alkanols, and Alkanals on Copper Catalysts. *J. Am. Chem. Soc.* **2011**, *133* (50), 20384–20398. https://doi.org/10.1021/ja207551f.

(44) Galebach, P. H.; Soeherman, J. K.; Wittrig, A. M.; Lanci, M. P.; Huber, G. W. Supercritical Methanol Depolymerization and Hydrodeoxygenation of Maple Wood and Biomass-Derived Oxygenates into Renewable Alcohols in a Continuous Flow Reactor. *ACS Sustainable Chem. Eng.* **2019**, *7* (18), 15361–15372. https://doi.org/10.1021/acssuschemeng.9b02704.

(45) Galebach, P. H.; Beussman, M.; Johnson, J.; Fredriksen, T.; Wang, C.; Lanci, M. P.; Huber, G. W. Catalytic Conversion of Pyrolysis Oil to Alcohols and Alkanes in Supercritical Methanol over the CuMgAlOx Catalyst. *ACS Sustainable Chem. Eng.* **2021**, *9* (5), 2067–2079. https://doi.org/10.1021/acssuschemeng.0c07020.

(46) Yin, W.; Venderbosch, R. H.; Bottari, G.; Krawzcyk, K. K.; Barta, K.; Heeres, H. J. Catalytic Upgrading of Sugar Fractions from Pyrolysis Oils in Supercritical Mono-Alcohols over Cu Doped Porous Metal Oxide. *Applied Catalysis B: Environmental* **2015**, *166–167*, 56–65. https://doi.org/10.1016/j.apcatb.2014.10.065.

Chapter 5: Reaction chemistry of ethanol oligomerization to Distillate-range molecules using low loading Cu/Mg_xAlO_y catalysts

5.1. Introduction

Ethanol is the most commonly produced liquid biofuel in the world, with 86% of total liquid biofuel in the United States being ethanol [1]. The main use of ethanol is blending with gasoline. Gasoline demand may decrease by up to 1.2 million oil-equivalent barrels in the next 20 years depending on electric vehicle demand [2]. On the other hand, heavy-duty fuels will have an increased demand for the next 20 years [2], particularly for diesel fuel in transportation and heavy machinery applications, as well as jet fuels for aviation, mostly accounting for a total energy demand increase of over 25% in this time period. Ethanol cannot be blended into heavy-duty fuels such as diesel due to its high volatility. However, longer molecules compatible with diesel can be produced from ethanol, opening the possibility to produce diesel fuel from ethanol in a sustainable way with appropriate chemistries, catalysts, and processes [3–5].

We have previously proposed and patented a process to convert ethanol into diesel-fuel ethers by combining Guerbet coupling with acid-catalyzed bimolecular dehydration (etherification) to form diesel-range ethers [5]. Guerbet coupling allows the production of higher oxygenate molecules from ethanol [6–14]. Our group has studied the Guerbet coupling of ethanol with hydroxyapatites [4], 8-9wt% Cu/Mg_xAlO_y [15] and 0.1-0.3wt% Cu/Mg_xAlO_y [16]. The C_{4+} alcohols produced by Guerbet coupling must be linear to provide feeds that will selectively undergo etherification reactions. Branched alcohol formation is a chain termination step in Guerbet coupling and are formed when any

The contents of this Chapter are adapted from the following submitted paper: Cuello-Penaloza, P. A.; Du, Y.; Lanci, M. P.; Maedke, D. A, Dumesic, J. A.; Huber, G. W. Ethanol to Distillate-Range Molecules Using Cu/Mg_xAlO_y Catalysts with Low Cu Loadings. Y.D. collaborated with catalyst synthesis, M.P.L. collaborated with revision of manuscript.

alcohol-derived active species different from the ones derived from ethanol are the nucleophile in this reaction. High alcohol linearity may be attained with a catalyst that either promotes higher nucleophilicity of the ethanol-derived active species compared to that of the species derived from higher alcohols, or lower electrophilicity of the ethanol derived species compared to that of higher alcohols [17]. It is possible to selectively produce linear C_{4+} alcohols from ethanol (selectivities around 60% at 45 – 55% conversion) with low Cu-loadings (0.1 – 0.6wt% Cu) added to Mg_xAlO_y [16,18]. C_{6+} esters are co-products in the reaction. These larger esters may also be blended directly into diesel fuel or find applications as flavorings and fragrances [19,20]. It is then important to understand the reaction network of ethanol oligomerization, especially how alcohols grow with conversion and how larger esters are produced to adjust process conditions to selectively produce one or another product, and to eventually create processes that can selectively produce specific desired products.

The objective of this study is to elucidate the reaction network that occurs for ethanol oligomerization with a 0.3wt%Cu/$Mg_{2.9}$AlO catalyst. We study the catalyst performance with contact time and performed several cofeed experiments to elucidate the reaction network at play in the production of higher oxygenates, mostly alcohols, aldehydes, esters, and ketones, from ethanol when this catalyst is used. We also probed the performance of our low Cu loading catalyst with higher alcohol feeds, such as 1-butanol, 1-hexanol and 2-ethyl-1-butanol.

5.2. Experimental Methods

5.2.1. Catalyst Synthesis

Catalyst used was a 0.3wt%Cu/$Mg_{2.9}$AlO prepared as indicated in Section 4.2.1. of this thesis. It corresponds to the 0.3CuMMO(m) material.

5.2.2. Flow reaction system and product analysis and quantitation

The flow reactor system used is as detailed in Section 4.2.2. of this thesis. Product analysis was conducted in the manner described in Section 4.2.3. of this report.

For high conversion (low WHSV) experiments, as well as for 1-butanol, 1-hexanol and 2-ethyl-1-butanol feed experiments, and ethyl acetate cofeed experiments, a stainless-steel condenser was used instead of the dual glass condenser system described in Section 4.2.2., due to concerns with the backpressure regulator failing with condensing high molecular and highly viscous products. For the experiments with a stainless-steel condenser, the liquid flow is stopped and the inlet and outlet valves in the flow reactor were closed before the ice bath was lowered, then the condenser was emptied into a vial with 5-10 mL of 1-propanol, and the system was re-pressurized in both the inlet and the outlet before restarting the pump again. This entire process took <3 min. After collection, the sample mass was weighed, and the liquid was diluted with 1-propanol including a known amount of 1-pentanol as an internal standard. The product analysis then continues as described in Section 4.2.3.

5.2.3. Data analysis and considerations

For species yield, conversion and selectivity calculations, equations (4-1), (4-2) and (4-3) were used for the relevant calculations done in the present Chapter. Likewise, for diesel fuel precursor selectivity calculation (DFPS) and determination of Schultz-Flory distribution of alcohol selectivity, equations (4-4) and (4-5) were used respectively.

In addition, an effective conversion, where ethanol is in equilibrium with acetaldehyde, 1-ethoxyethanol and ethyl acetate, was also calculated as described in Equation 5-1.

$$X_{eff}(\%) = \sum_{i=1}^{n} Y_i - Y_{Acetaldehyde} - Y_{1-ethoxyethanol} - Y_{ethyl\ acetate} \qquad (5-1)$$

Similarly, an effective DFPS may also be defined as shown in Equation 5-2.

$$DFPS_{eff} = DFPS * \frac{X}{X_{eff}} \qquad (5-2)$$

5.3. Results and discussion

5.3.1. Contact time tests

Table 5-1 shows the yields of different products as a function of the contact time. It can be observed that the most abundant products at all conditions are C_{4+} alcohols, reaching a peak of 38.9% at 68% conversion. The C_6 linear-to-branched alcohol ratio decreases with conversion. C_{4+} aldehyde

yields increase with conversion, reaching a maximum of 6.8% at 54% conversion. Acetaldehyde yields are high at low conversion, reaching a maximum of 5.5% at 20% conversion, then decreasing until almost disappearing. C_{6+} ester yields increase monotonically with conversion, with ethyl acetate reaching a maximum of 5.4% at 54% conversion. C_{5+} ketones increase with conversion. Other products include methanol, acetone, ethers, olefins, paraffins and hemiacetals and acetals. Total diesel fuel precursor yield increased with conversion, to values up to 63%. C-balances decreased with conversion, probably due to increasing coke formation, as was shown in our previous publication [16]. Coke formation is the main cause of catalyst deactivation. More detailed product selectivity information is provided in Tables 7-14 through 7-21 in the Appendix on Chapter 7.

Table 5-1. Yields of main compound categories at different contact times. **Conditions:** 325 °C, 300 psig total, P_{EtOH}:P_{H2} = 4.

WHSV (h^{-1})	328.8	52.7	26.2	13.2	6.6	1.3	0.7
Contact time (s kg_{cat}/mol)	0.5	3.2	6.3	12.6	25.2	125.1	228.5
C-balance (%)	101.9	99.9	97.0	96.1	97.5	89.8	87.3
C6 L:B	6.5	3.6	4.1	3.5	3.5	2.9	2.3
Conversion (%)	4.8	20.0	23.3	27.5	54.2	68.2	69.7
Diesel Fuel Precursor Yield (%)	2.4	10.8	14.7	18.0	34.3	62.0	62.8
C4+ Alcohol	2.0	8.8	11.6	13.3	26.6	38.9	31.7
C4+ Aldehydes	0.4	1.3	2.3	2.4	6.1	6.2	4.7
C6+ Esters	0.0	0.3	0.5	1.6	6.6	11.5	16.4
C5+ Ketones	0.0	0.0	0.1	0.2	0.6	2.6	7.8
Others	2.4	9.5	8.8	9.9	14.2	9.1	9.0
Acetaldehyde (%)	1.5	5.5	5.8	5.2	2.0	0.8	0.6
Ethyl acetate (%)	0.1	1.1	1.5	1.8	5.0	1.8	2.3

Figure 5-1 shows the overall and effective conversion as a function of contact time. There appear to be three different conversion regimes in Figure 5-1. First a linear increase from 0 to 27% conversion, then a more rapid increase from 30-68%, followed by a very slow increase from 68 to

70%. This trend may be explained by inhibition occurring both at low contact times due to acetaldehyde [9], and at higher contact times due to additional causes. The DFPS increases with conversion until they reach a plateau of 90% at ~70% conversion. The effective conversion trends are very similar to that of the nominal conversion, whereas the effective diesel fuel precursor selectivity based on this conversion was found to be roughly constant after 20% ethanol conversion.

The product selectivity (grouped by major species) as a function of contact time is shown in Figure 5-2. The C_{4+} alcohol selectivity initially increases rapidly with conversion until to around 54%, and then going through a maximum of 60% at 68% conversion before decreasing to less than 50% at 70% conversion. The C_{4+} aldehyde selectivity increases until it reaches a maximum of 11% at 54% conversion, then decreases with conversion. The C_{6+} ester and C_{4+} ketone selectivity both increase with conversion monotonically. The increase of ester selectivity with conversion is relatively steady. The ketone selectivity increases from 4% at 68% conversion to 12% at 70% conversion. The average carbon number of products increases with increasing contact time.

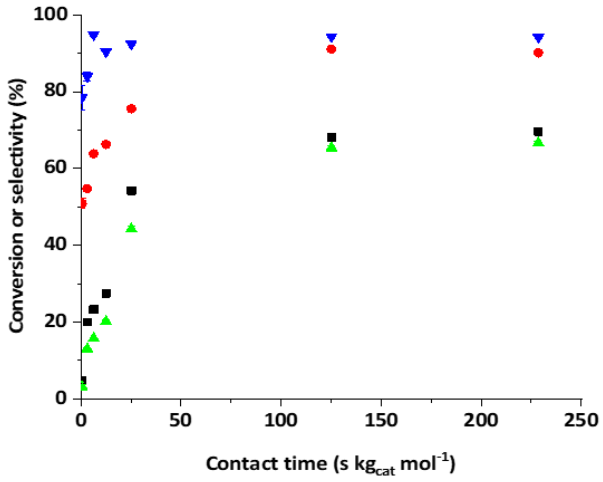

Figure 5-1. Conversion (■), effective conversion (▲), diesel fuel precursor selectivity (●) and effective DFPS (▼) vs contact time. Conditions as described in Table 5-1.

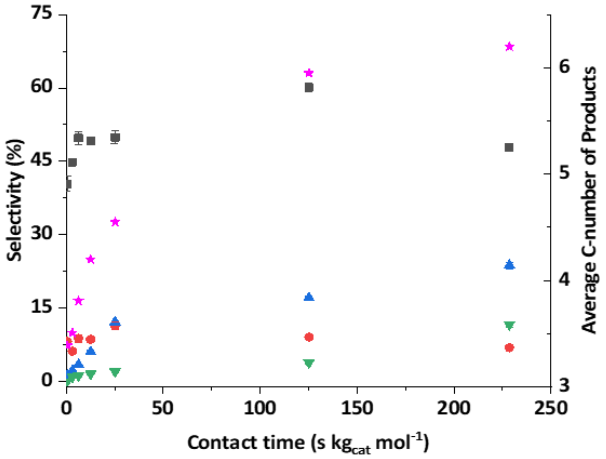

Figure 5-2. Selectivity (left y-axis) towards C_{4+} alcohols (■), C_{4+} aldehydes (●), C_{6+} esters (▲), and C_{4+} ketones (▼), and average carbon number of products (★ – right y-axis) vs contact time. Conditions as described in Table 5-1.

Alcohol selectivities fit the Schultz-Flory distribution as defined in Equation (4-5) at all studied conversions as shown in Figure 5-3a. This is in agreement with our prior findings [16]. Figure 5-3b shows the α-value obtained as a function of ethanol conversion. A non-monotonic increase in the propagation value with conversion is observed. Overall, the probability for an alcohol chain to grow seems to increase with conversion, which is consistent with finding larger alcohols at high conversion, up to C_{14} (1-tetradecanol and β-branched alcohols).

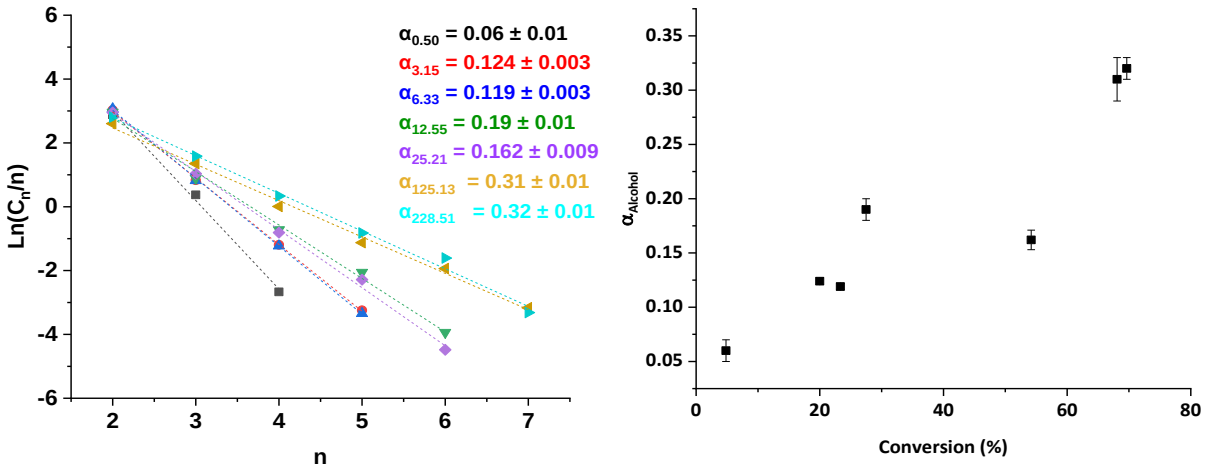

Figure 5-3. a) Schultz-Flory distribution plots for primary alcohols at different contact times (left) and b) α-values (right) variation with conversion. The color of the font matches the respective color on the plot to the left. Conditions as described in Table 5-1.

Several individual species yields were plotted against conversion in Figures 5-4, 5 and 7, with complementary plots of yields vs contact time in the supporting information (Figures 7-30 through 7-32). Figure 5-4 shows the profile for 1-butanol, the most abundantly produced species, as well as for acetaldehyde, butyraldehyde and crotyl alcohols (2-buten-1-ol). 1-butanol shows a linear increase in yield until 54% conversion (125 s kg_{cat} mol^{-1}), then reaching a maximum at 68% conversion, and then decreasing between 68-70% (125 – 229 s kg_{cat} mol^{-1}), meaning that 1-butanol is eventually consumed to form larger products. The slope at contact time zero is non-zero (Figure 7-30), indicating that 1-butanol is a mostly primary product from ethanol, which is further confirmed by its initial rate plot (please refer to Figure 7-33) and linear trend until 54% in Figure 4. 1-butanol can be formed from two main routes: 1) direct coupling of adsorbed ethanol, and 2) hydrogenation of butyraldehyde and crotyl alcohol which are formed from aldol condensation of acetaldehyde, or direct coupling of ethanol and acetaldehyde.

Acetaldehyde shows a maximum yield at 23% conversion where the inflection for 1-butanol occurs. This indicates that 1) acetaldehyde is a reaction intermediate and 2) that it is probably the species that causes non-linear behavior in conversion. Acetaldehyde is a primary product that is further converted (Please refer to Figures 7-30 and 7-33 for further reference). Butyraldehyde and crotyl alcohols show an initial increase with contact time with an inflection at 23% conversion, and a maximum at 54% followed by a decrease, indicating their nature as secondary products. However, the contact time slopes (Figure 7-30) and initial rates (Figure 7-33) for butyraldehyde and crotyl alcohols at time zero are non-zero, indicating that these are also primary products that eventually are consumed to form larger products.

Figure 5-5 shows the variation of yield with conversion for 1-hexanol, 2-ethyl-1-butanol, and 2-pentanone. It can be observed that the plots of the C_6 alcohols both show inflections at 23%

conversion, showing that an amount of these species are generated as secondary products from ethanol/acetaldehyde and 1-butanol/butyraldehyde. However, it must be noted that these species also have a finite slope at contact time zero (Figure 7-31), indicating that an amount of these is also produced as primary products. Their initial rates are also non-zero (Figure 7-34), giving further support to the partially primary nature of these species. Since alcohol selectivities follow Schultz-Flory distribution at all studied conversions, this fact may provide an explanation on why 1-butanol, 1-hexanol, 2-ethyl-1-butanol and even 1-octanol (Figure 7-34), as well as butyraldehyde (and crotyl alcohols), and even hexanal appear as seemingly primary (in addition to secondary) products (Figure 7-35). Figure 5-6 shows a schematic illustrating the chain growth of ethanol into larger alcohols. As shown in Figure 5-6, ethanol would first adsorb and create the active monomer surface species (that may come from ethanol or even from acetaldehyde) that would undergo successive chain growth by addition of further ethanol-based monomers, forming the higher alcohols (or aldehydes). To form any oligomeric alcohol/aldehyde C_n species, it is not necessary for the C_{n-1} species to desorb in principle. This allows for the interpretation that any higher alcohol or aldehyde may appear partially as a primary product, as ethanol might directly form the active surface species that continues to react or might form surface acetaldehyde that in turn forms the active species on the surface without desorbing. The probability of the coupling event is in fact given by the α parameter. The diagram does not consider any other alcohol-derived nucleophile species other than that of ethanol since that would constitute a chain-termination step, as a β-branched alcohol is formed, and their relative nucleophilicity is negligible. The plot for 2-pentanone is more straightforward to explain since it appears as a clearly non-primary product that is formed at high conversion. Notably, its sharp yield increase after 68% conversion matches a decrease in C_6 alcohol yields (as well as that of 1-butanol) between 125 and 228.5 s kg_{cat} mol^{-1}

(Figure 7-31). This suggests that 2-pentanone is formed at higher rates than C_6 alcohols from ethanol and 1-butanol, or that C_6 alcohols are consumed faster than they are formed to form higher products (ketones and esters). These observations may be extended to the formation of higher ketones (heptanones, nonanones, undecanones, etc.) from alcohols/aldehydes, as the selectivities towards these were also found to increase at ~70% conversion (Please refer to Tables 7-14 – 7-21), which overall would be consistent with an interpretation that ketones are non-primary products of ethanol oligomerization. Lower alcohol formation rates at high conversions may be explained by larger amounts of water produced from coupling reactions inhibiting further alcohol formation more than other reactions.[17]

The yield of ethyl-acetate, 1-ethoxyethanol and acetaldehyde (for reference) vs conversion is shown in Figure 5-7. Ethyl acetate is a secondary product since its initial rate extrapolates to zero (Figure 7-36). The 1-ethoxyethanol yield plot follows a strikingly similar trend compared to acetaldehyde, suggesting that these two species are in a series pathway. The acetaldehyde and 1-ethoxyethanol yields decrease while the ethyl acetate yield increases at 54% (25.2 s kg_{cat} mol^{-1}, please refer to Figure 7-32 for yield vs contact time plots). This indicates that acetaldehyde can reacts with ethanol to form 1-ethoxyethanol which is then dehydrogenated to ethyl acetate. The C_6 ester and other higher esters form similar trends (Figure 7-36) indicating they are all secondary products. Ethyl acetate goes through a maximum yield at a conversion of 54%. This latter trend indicates that ethyl acetate is consumed to form other products, such as esters via transesterification as will be shown later. Figure 5-8 shows the selectivity of esters per carbon size at different contact times. Esters were found to progressively grow with conversion, with C_6 ester selectivity eventually being greater than that of ethyl acetate, and C_{8+} ester selectivity being collectively greater than that of ethyl acetate as well at high contact times, as observed in Figure 5-8.

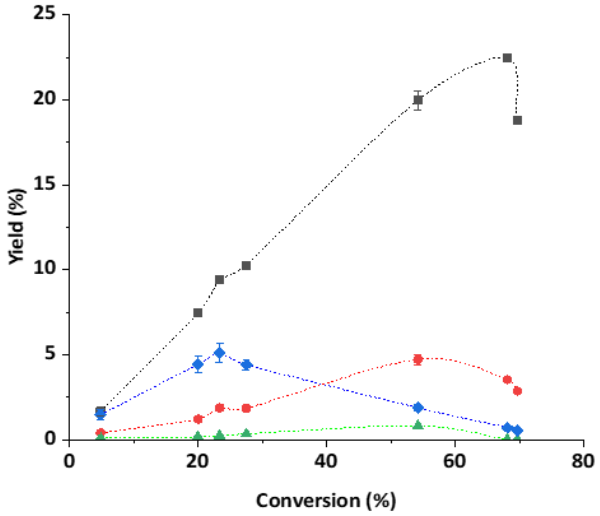

Figure 5-4. Yield *vs* contact time plots for 1-butanol (■), acetaldehyde (◆), butyraldehyde (●) and crotyl alcohols (▲). Conditions as described in Table 5-1.

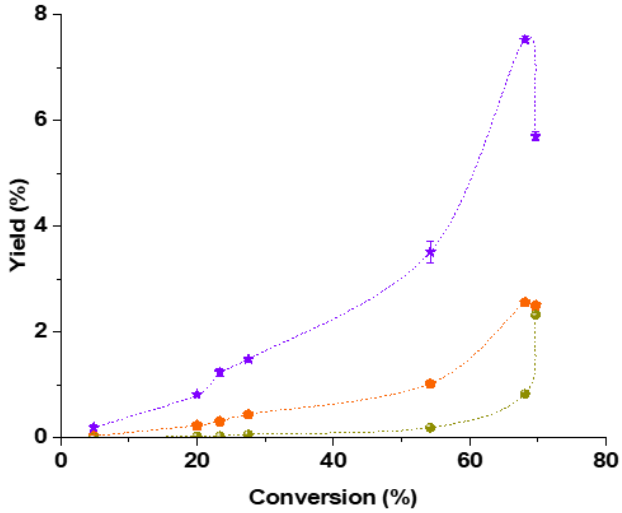

Figure 5-5. Yield *vs* contact time plots for 1-hexanol (★), 2-ethyl-1-butanol (⬟), and 2-pentanone (●). Conditions as described in Table 5-1.

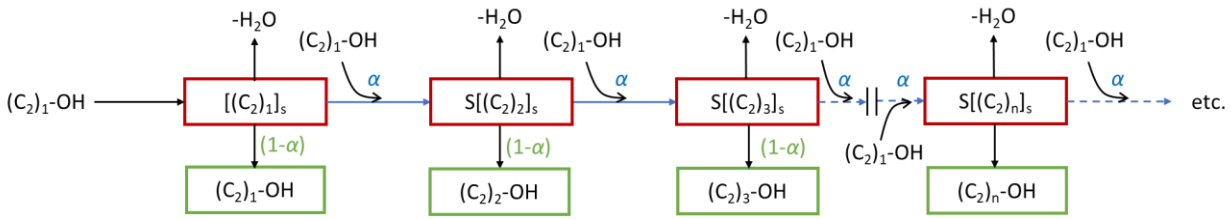

Figure 5-6. Illustrated chain-growth of ethanol to higher alcohols based on Schultz-Flory distribution. The diagram assumes the monomeric nucleophilic species comes from ethanol and any monomeric or oligomeric surface species is the electrophile. Ethanol may adsorb and form a C_2 surface active species that can grow or desorb back as ethanol (or acetaldehyde). Surface species of any given size are shown in red rectangles. Chain growth is shown in blue arrows, with the probability of each growth event being α, and monomer addition is represented by curved arrows. Desorption to product is shown in green arrows, the probability being (1-α), and alcohol (or aldehyde) products are shown in green boxes. Dashed lines denote either a skipped segment of chain growth or its indefinite continuation.

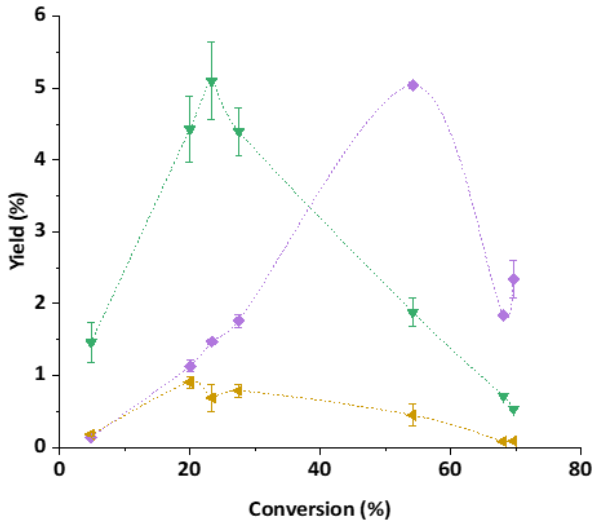

Figure 5-7. Yield vs conversion plots for acetaldehyde (▼), ethyl acetate (◆) and 1-ethoxyethanol (◀). Conditions as described in Table 5-1.

Figure 5-9 shows the ratio of the partial pressure of alcohols-to-aldehydes found at each contact time divided by the same ratio at equilibrium for ethanol/acetaldehyde, 1-butanol/butyraldehyde and 1-hexanol/hexanal. The ethanol-to-acetaldehyde ratio decreases with contact time and is 10 times above the equilibrium value. The alcohol-to-aldehyde ratio for 1-butanol is always close to equilibrium (e.g. 1), with the value at 0.5 s kgcat mol-1 being 0.9. The 1-hexanol/hexanal ratios

are also close to equilibrium, being typically above 1. These trends could be explained in the case of ethanol and acetaldehyde if the reaction rate of adsorbed acetaldehyde is faster than the rate of its desorption, therefore equilibrium concentrations are not observed. For the higher aldehydes, it could be occurring that the enolates formed from these aldehydes are considerably more hindered, allowing them to be equilibrated with their alcohols. Another plausible explanation for the equilibrium in the higher alcohols may be that their rate of formation via Guerbet coupling is similar to that of direct coupling if the latter reaction is indeed occurring.

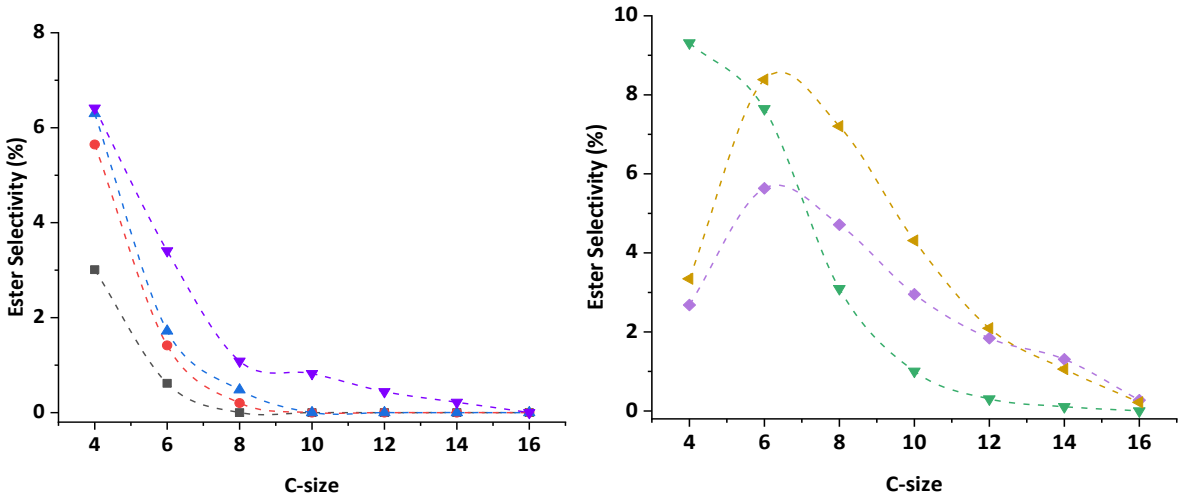

Figure 5-8. Ester selectivity per carbon size for contact times (s kg_{cat} mol^{-1}) 0.5 (■ , left), 3.15 (● , left), 6.33 (▲ , left), 13.22 (▼ , left), 25.21 (▼ , right), 125.13 (◆ , right) and 228.51 (◀ , right). Conditions as described in Table 5-1.

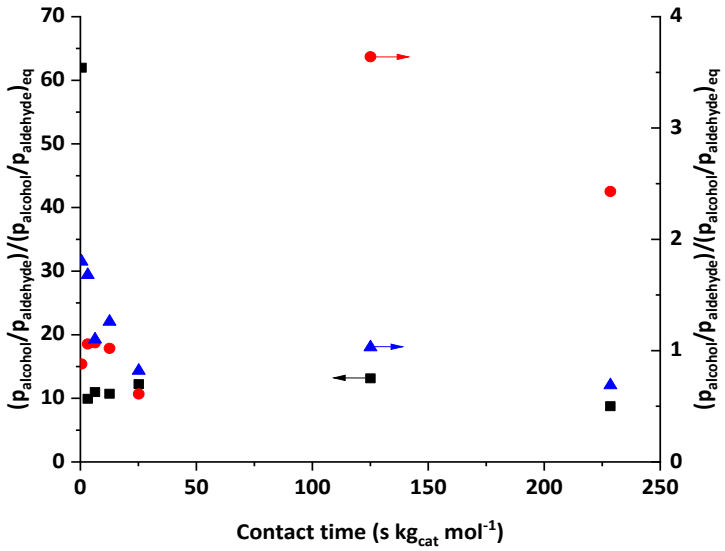

Figure 5-9. Alcohol-to-aldehyde pressure ratios between experiment and equilibrium values for ethanol and acetaldehyde (■, left y-axis), 1-butanol/butyraldehyde (●, right y-axis) and 1-hexanol/hexanal (▲, right y-axis) at different contact times. A value of 1 indicates equilibrium.

5.3.2. Role of ethanol-to-hydrogen partial pressure ratios

Table 5-2 shows the product yield as a function of the ethanol to H_2 partial pressure ratio from 0.5 to 4. The ethanol conversion decreases from 27.4% to 24.9% as the ethanol-to-hydrogen partial pressure decreases. The linearity of the alcohol products is similar across the three pressure ratio conditions, with the C_6 linear-to-branched alcohol ratio varying non-monotonically between 3.6 to 4.0 with pressure ratios. The propagation probability (α) of alcohol chain growth increases with decreasing H_2 content relative to ethanol. The DFPS is higher for experiments with enriched H_2 contents (76-78% for P_{EtOH}:P_{H2} 1 and 0.5) compared to H_2 scarce experiments (70% for P_{EtOH}:P_{H2} of 4). The C_{4+} alcohol selectivity increases dramatically with increasing H_2 contents, the value jumping from 49.7% to 63.8% between ratios 4 and 1, and then modestly increasing to 67.8% at ratio 0.5. The trend for C_{4+} aldehydes and C_{6+} esters is the opposite of that of alcohols with increasing H_2 contents. C_{4+} aldehyde selectivity drops from 9.5% to 5.7% between ratios 4 to 1,

and then decreases to 5.3% for ratio 0.5. C_{6+} ester selectivity decreases from 6.1% to 5.5% between ratios 4 and 1, and then drops to 2.5% for ratio 0.5. Finally, acetaldehyde selectivity is similar between all pressure ratios, hovering around 12%, whereas ethyl acetate selectivity decreases with increasing H_2 pressure, varying from 6.2% to 5.7% between ratios 4 and 1, then dropping to 4.8% at ratio 0.5.

Table 5-2. Product yields from varying P_{EtOH}:P_{H2} ratio. **Conditions:** 325°C, 300 psig, WHSV = 26.2 h^{-1}.

P_{EtOH}:P_{H2} ratio	0.5	1	4
Ethanol p.p (kPa)	688.3	1045.1	1660.3
H_2 p.p (kPa)	1380.2	1023.4	408.2
C-balance (%)	101.7	100.5	98.3
C_6 L:B	4.0	3.6	3.7
Alcohol propagation probability (α)	0.13	0.15	0.18
Average conversion (%)	24.9	26.7	27.4
DFPS (%)	76.4	77.6	70.0
C_{4+} Alcohol	67.8	63.8	49.7
C_{4+} Aldehydes	5.3	5.7	9.5
C_{6+} Esters	2.5	5.5	6.1
Others	24.5	25.0	34.7
Acetaldehyde	12.5	11.1	12.8
Ethyl acetate	4.8	5.7	6.2

[a]p.p is partial pressure.
[b] C_6 L:B is linear C_6 alcohol/branched C_6 alcohol ratio.

The trends of varying ethanol-to-hydrogen pressure ratios illustrate that increasing H_2 pressure will shift the product selectivities towards alcohols, at the expense of aldehydes and esters. This is to be expected since both aldehyde and ester formation involve the release of H_2. Therefore, inhibition of reactions involving dehydrogenation is consistent with the trends of the data. It can also be noted that acetaldehyde selectivity was relatively constant across the pressure ratio range, whereas ethyl acetate selectivity steadily decreased, suggesting that ester formation reactions are affected first when H_2 pressure is increased. We would expect acetaldehyde selectivity to decrease

at lower P_{EtOH}:P_{H2}, since ethanol, acetaldehyde and ethyl acetate are expected to influence one another as they would tend to be in equilibrium. Another important point to note is the moderate conversion decrease with increasing H_2 contents and decreasing ethanol contents. Conversion only varied 2.5% across a 2.4-fold ethanol partial pressure decrease (and 3.4-fold H_2 partial pressure increase), suggesting that ethanol reaction order is positive, but close to zero, since the main reaction is alcohol coupling and H_2 is not a stoichiometric reactant for this reaction.

Another point to consider is how the alcohol-to-aldehyde pressure ratios vary with ethanol-to-hydrogen changing pressure ratios. Table 5-3 describes the ratio of pressure ratios between alcohols and aldehydes at each experiment divided by their expected equilibrium ratios for ethanol/acetaldehyde, 1-butanol/butyraldehyde and 1-hexanol/hexanal. Ethanol-to-aldehyde ratio of ratios comes closer to equilibrium as the P_{EtOH}:P_{H2} ratio is decreased (i.e. H_2 pressure in the feed is increased, ethanol pressure is decreased). This is to be expected since dehydrogenation reactions are usually equilibrated or quasi-equilibrated. The value is still far from equilibrium (e.g. 1), but this suggests that further increases in P_{EtOH}:P_{H2} will eventually lead to an equilibrium between ethanol and acetaldehyde. Moreover, the value could also be higher than 1 due to acetaldehyde being a more reactive molecule than ethanol. 1-butanol/butyraldehyde and 1-hexanol/hexanal ratio of ratios are close to equilibrium. 1-butanol/butyraldehyde ratios show that as H_2 pressure is decreased, the ratio comes closer to equilibrium, but still stays below it. For 1-hexanol/hexanal, the ratio value is below equilibrium for P_{EtOH}:P_{H2} of 0.5, but then increases to slightly above equilibrium with increasing P_{EtOH}:P_{H2} ratios. These results show that dehydrogenation reactions are favored at H_2 depleted conditions, indicating the equilibrated nature of higher alcohol and aldehydes reactions compared to ethanol/acetaldehyde.

Table 5-3. Alcohol/aldehyde-to-equilibrium alcohol/aldehyde pressure ratios for experiments varying P_{EtOH}:P_{H2} ratios. Conditions as defined in Table 5-2.

P_{EtOH}:P_{H2} ratio	0.5	1	4
$\frac{\left(\frac{p_{Ethanol}}{p_{Acetaldehyde}}\right)_{exp}}{\left(\frac{p_{Ethanol}}{p_{Acetaldehyde}}\right)_{eq}}$	5.65	7.35	12.39
$\frac{\left(\frac{p_{1-Butanol}}{p_{Butyraldehyde}}\right)_{exp}}{\left(\frac{p_{1-Butanol}}{p_{Butyraldehyde}}\right)_{eq}}$	0.80	0.84	0.85
$\frac{\left(\frac{p_{1-Hexanol}}{p_{Hexanal}}\right)_{exp}}{\left(\frac{p_{1-Hexanol}}{p_{Hexanal}}\right)_{eq}}$	0.94	1.06	1.29

5.3.3. Role of acetaldehyde and ethyl acetate in the reaction network

We performed several experiments in which we cofed acetaldehyde and ethyl acetate with ethanol. We plot the outlet partial pressures of different species as a function of the acetaldehyde feed mole fraction in Figure 5-10 to assess the impact of acetaldehyde in the feed. Ethanol conversion does not vary significantly at acetaldehyde mole fractions below 0.08. The 1-butanol partial pressure increases with acetaldehyde cofeed content, suggesting that acetaldehyde undergoes formal Guerbet coupling (e.g. aldol condensation to alkenal and consecutive hydrogenation of alkenal to alcohol). A similar trend can be observed for 1-hexanol and 2-ethyl-1-butanol. Ethyl acetate follows a similar trend to the alcohols. Interestingly, hexanal and 2-ethylbutanal formation is barely sensitive to acetaldehyde molar concentration, whereas butyraldehyde partial pressure increases with acetaldehyde molar fraction, as well as that of crotyl alcohols. This suggests that acetaldehyde mainly reacts via formal Guerbet coupling to butyraldehyde and crotyl alcohols with

very fast hydrogenation of crotonaldehyde, which is never observed in the products. Overall, the presence of small amounts of acetaldehyde favors the formation of higher alcohols, as well as those of esters. The larger increase in partial pressure observed for butyraldehyde and 1-butanol compared to ethyl acetate suggest that alcohol formation reactions are more favored with the acetaldehyde cofeed.

Table 5-4 shows the partial pressure ratios of alcohols-to-aldehydes are compared to their equilibrium counterparts in the acetaldehyde cofeed experiments, in a similar fashion as shown in Figure 5-9 and Table 5-3 for the varying contact time and varying P_{EtOH}:P_{H2} experiments respectively. It can be observed that the ratio of ratios for ethanol/acetaldehyde comes closer to equilibrium the more acetaldehyde is added to the system as expected, but it is still far away from equilibrium, albeit this could also be due to acetaldehyde being a more reactive molecule than ethanol, disappearing faster. Interestingly, 1-butanol/butyraldehyde and 1-hexanol/hexanal ratio of ratios plunge well below equilibrium with high enough acetaldehyde molar fractions, with the trend being downward as the acetaldehyde molar fraction is increased. This can be explained by increasing formal Guerbet coupling of acetaldehyde molecules to higher aldehydes that eventually form the higher alcohols as the acetaldehyde content is increased. This might also explain the non-linearity in the 20-30% conversion range, since it seems that the higher contents of acetaldehyde might drive the coupling chemistry towards formal Guerbet coupling in addition to direct ethanol coupling, until the acetaldehyde is consumed, and direct coupling becomes the main driving force of the reaction afterwards. Each coupling chemistry might have different rates, which would be consistent with non-linearity with varying acetaldehyde contents. Also, acetaldehyde itself may adsorb and cause deactivation [9] or reaction inhibition, as when the molar fraction is increased to 0.13, conversion and partial pressures of most species decrease, save for that of butyraldehyde and

crotyl alcohols that register an increase, as it can be observed in Table 7-22. Therefore, these results combined with the ones from the different ethanol-to-H_2 partial pressure ratios allows us to conclude that acetaldehyde controls the reaction chemistry of ethanol oligomerization, with conditions favorable to larger concentrations of acetaldehyde resulting in larger rates of higher alcohol coupling and esterification, and conditions favorable to lower concentrations of acetaldehyde (e.g. high H_2 partial pressures) resulting in higher alcohol selectivity at the expense of ester and higher aldehydes selectivities.

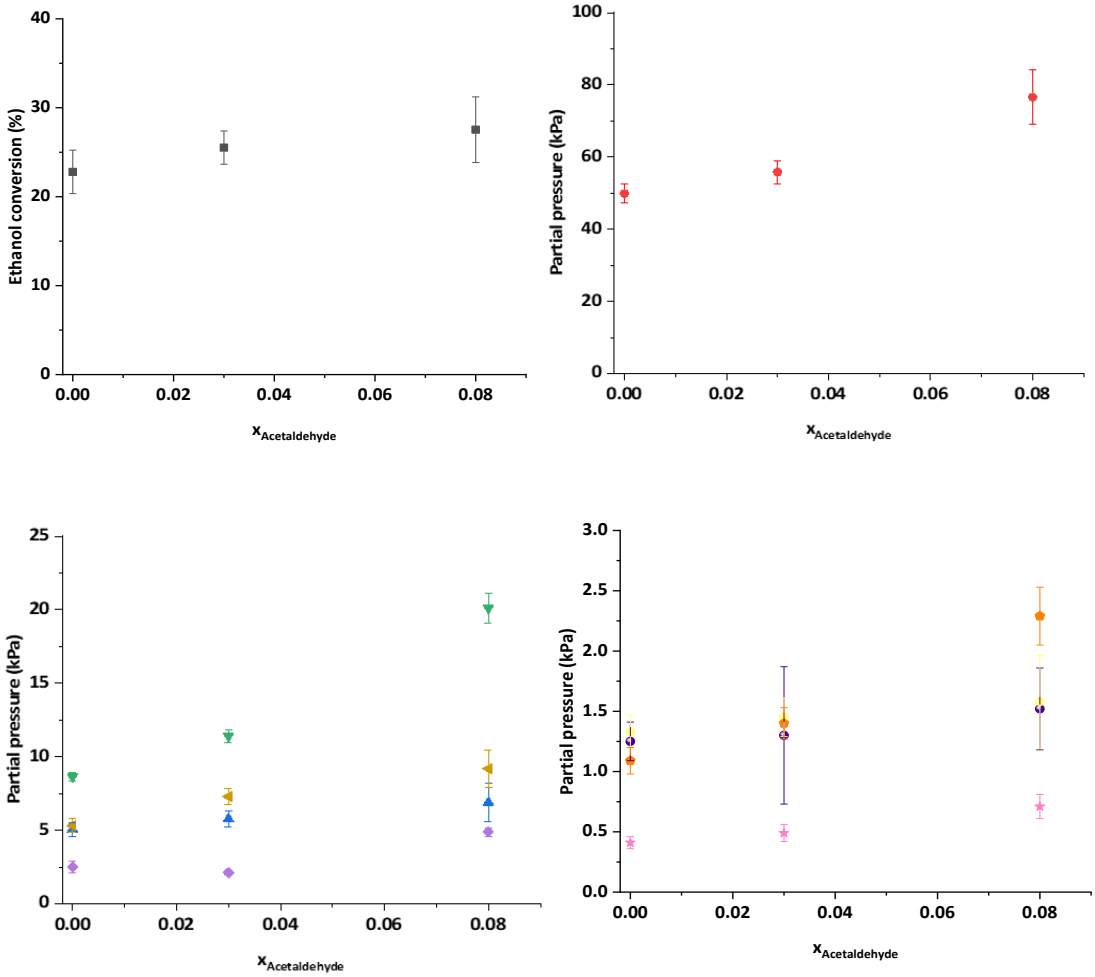

Figure 5-10. Conversion (■, upper left) and partial pressures of 1-butanol (●, upper right), 1-hexanol (▲, lower left), butyraldehyde (▼, lower left), 1-ethoxyethanol (◆, lower left), ethyl acetate (◀, lower left), crotyl alcohols (●, lower right), 2-ethyl-1-butanol (⬢, lower right), hexanal (⬟, lower right) and 2-ethylbutanal (★, lower right) as a function of acetaldehyde molar fraction in the inlet. **Conditions:** 325°C, 300 psig total, P_{EtOH}:P_{H2} = 1, $WHSV_{EtOH}$ = 26.23 – 26.58

h^{-1}. N-hexane is added as an inert species to substitute progressively with acetaldehyde while maintaining ethanol partial pressure constant.

Table 5-4. Alcohol/aldehyde-to-equilibrium alcohol/aldehyde ratios for experiments varying acetaldehyde molar ratios. Conditions as defined in Figure 5-10.

Acetaldehyde molar fraction	0.00	0.03	0.08
$\frac{\left(\frac{p_{Ethanol}}{p_{Acetaldehyde}}\right)_{exp}}{\left(\frac{p_{Ethanol}}{p_{Acetaldehyde}}\right)_{eq}}$	9.92	8.15	5.13
$\frac{\left(\frac{p_{1-Butanol}}{p_{Butyraldehyde}}\right)_{exp}}{\left(\frac{p_{1-Butanol}}{p_{Butyraldehyde}}\right)_{eq}}$	0.94	0.81	0.64
$\frac{\left(\frac{p_{1-Hexanol}}{p_{Hexanal}}\right)_{exp}}{\left(\frac{p_{1-Hexanol}}{p_{Hexanal}}\right)_{eq}}$	1.05	0.97	0.71

For the ethyl acetate cofeed experiments, the partial pressures of several relevant species were plotted against the molar fraction of ethyl acetate in the inlet, this is shown in Figure 5-11. Overall, conversion does not vary significantly with ethyl acetate content. Acetaldehyde and 1-ethoxyethanol production increases with ethyl acetate content, which is to be expected if these species are in equilibrium with one another. Butyraldehyde partial pressure decreased slightly with ethyl acetate content, meaning that its production is inhibited by ester content. Interestingly, ethyl butyrate and butyl acetate production increased with ethyl acetate content. This can be explained by two reasons: 1) larger amounts of acetaldehyde can promote esterification, particularly towards butyl acetate if acetaldehyde undergoes a nucleophilic attack by the oxygen in 1-butanol, and 2) transesterification of ethyl acetate to higher esters is possible with larger alcohols being produced, since the 0.3wt%Cu/$Mg_{2.9}$AlO has both acid and base sites. C_{4+} alcohols, production is decreased with increasing ethyl acetate content, suggesting inhibition of larger species formation by competitive adsorption of ethyl acetate.

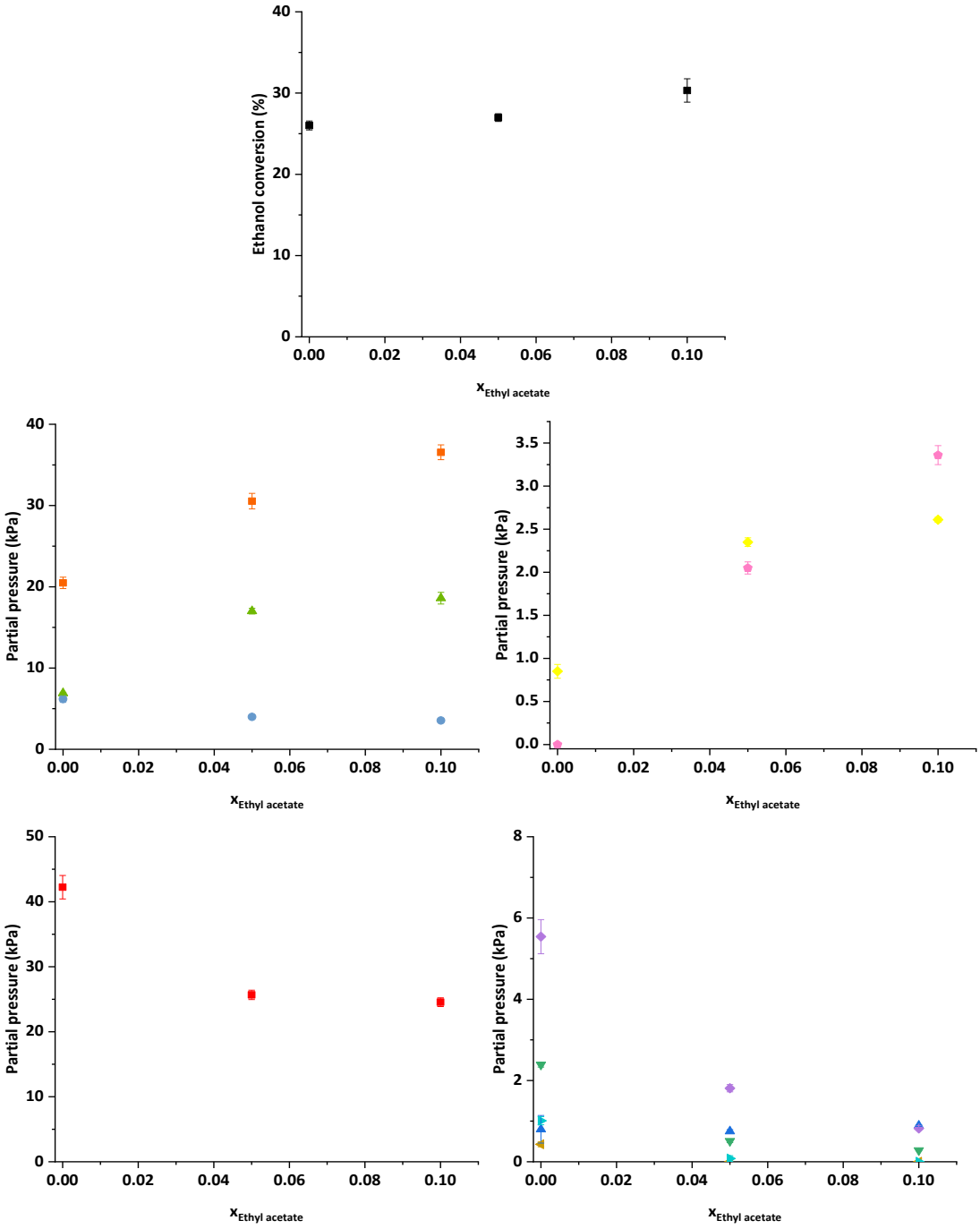

Figure 5-11. Conversion (■, upper center) and partial pressures of acetaldehyde (■, middle left), 1-ethoxyethanol (▲, middle left), butyraldehyde (●, middle left), ethyl butyrate (◆, middle right), butyl acetate (⬟, middle right), 1-butanol (■, lower left), 1-hexanol (◆, lower right), 2-ethyl-1-butanol (▼, lower right), 1-octanol (▶, lower right), 2-ethyl-1-hexanol (◀, lower right) and crotyl alcohols (▲, lower right) with varying ethyl acetate molar fraction in the inlet. **Conditions:** 325°C, 300 psig total, P_{EtOH}:P_{H2} = 1, $WHSV_{EtOH}$ = 26.24 – 26.62 h^{-1}. N-hexane is added as an inert species to substitute progressively with ethyl acetate while maintaining ethanol partial pressure constant.

Since ethyl acetate selectivity reaches a maximum at 54% ethanol conversion, and the molar fraction of ethyl acetate at its maximum yield/selectivity point (54% conversion) is less than what was cofeed in the present experiments (~0.03 vs 0.05), we do not expect transesterification to be important in our reaction network for the contact times studied. Butyraldehyde and 1-butanol partial pressures, as well as that of higher alcohols (except crotyl alcohols) decreased with ethyl acetate content, meaning that their production is inhibited by ester content. This might be due to these species reacting to form esters, particularly the alcohols, and the aldehyde pressures would then also decrease since these would tend to be in equilibrium with the alcohols. Another explanation may be that ethyl acetate competes for active sites with the alcohol/aldehyde species that promote coupling. We found no crotyl alcohol-based esters, hence might explain why its partial pressure remained relatively constant with increasing ethyl acetate contents.

5.3.4. Higher alcohol reactions with low-loading Cu/$Mg_{2.9}$AlO catalyst

We tested higher alcohol (1-butanol, 1-hexanol and 2-ethyl-1-butanol) conversion with the 0.3wt%Cu/$Mg_{2.9}$AlO catalyst. 1-butanol was tested at two different contact times as shown in Table 5-5. It can be observed that butyraldehyde, 2-ethylhexanal, 2-ethyl-1-hexanol and butyl butyrate are the main products. Since butyraldehyde selectivity decreases with contact time with a concomitant increase of 2-ethyl-1-hexanol, and the species 2-ethyl-2-butenal was detected, we conclude that 1-butanol undergoes formal Guerbet coupling with itself and hydrogenate to form 2-ethyl-1-hexanol, the expected Guerbet alcohol. Butyl butyrate is the expected self-esterification product, expected from a nucleophilic attack of 1-butanol to butyraldehyde followed by dehydrogenation. It is worth noting that the cross esters from 1-butanol, butyraldehyde, 2-ethyl-1-

hexanol and 2-ethylhexanal were observed. The ester 2-ethylhexyl-2-ethylxhexanoate was observed at very small quantities, whereas no C_{16} alcohol was observed, which shows that while the β-C of a β-branched alcohol (2-ethyl-1-hexanol) cannot act as a nucleophile [17], the oxygen of the alcohol can. It is also possible for a linear aldehyde to attack a α-branched aldehyde to form a larger alcohol, as a C12 alcohol was observed (by GC-MS). However, the frequency of such event is low, and further attacks are not expected considering the steric hindrance of the already formed alcohol.

1-hexanol was tested at 10.2 s kg_{cat} mol^{-1} as shown in Table 5-6. It can be observed that the alkenal 2-butyl-2-octenal was observed, and that main products were hexanal, the Guerbet alcohol 2-buty-1-octanol and the self -ester hexyl hexanoate. This is consistent with the results for 1-butanol in regards the higher alcohol formation by Guerbet coupling with the main reactions being dehydrogenation to aldehyde, Guerbet coupling and esterification.

Table 5-5. Results of test with 1-butanol. Conditions: 325°C, 300 psig, $P_{1\text{-ButOH}}$:P_{H2} = 4, $WHSV_{1\text{-ButOH}}$ = 26.16 or 6.55 h^{-1}.

	Contact time (s kg_{cat} mol^{-1})	**10.20**	**20.40**
	Conversion (%)	22.5	32.4
Selectivities (%)	**butyraldehyde**	34.51	18.18
	2-ethylhexanal	9.14	10.28
	2-ethyl-1-hexanol	29.33	38.18
	C12 alcohol	0.17	0.40
	butyl butyrate	16.47	21.05
	2-ethylhexyl butyrate	0.93	2.69
	butyl -2-ethylhexanoate	0.49	1.30
	2-ethylhexyl-2-ethylhexanoate	0.00	0.12
	4-heptanone	1.68	2.22
	3-methyl-4-heptanone	0.28	0.25
	others	7.00	5.33

Table 5-6. Results of test with 1-hexanol. Conditions: 325°C, 300 psig, $P_{1\text{-HexOH}}$:P_{H2} = 4, $WHSV_{1\text{-HexOH}}$ = 25.58 h^{-1}.

	Contact time (s kg_{cat} mol^{-1})	14.37
	Conversion (%)	18.39
Selectivities (%)	**hexanal**	39.76
	2-butyl-2-octenal	3.01
	2-butyloctanal	4.81
	2-butyl-1-octanol	25.08
	hexyl hexanoate	14.58
	C18 ester	0.78
	4-undecanone	1.45
	others	10.53

Another feature to explore with this catalyst is the tendency for an alcohol to form higher alcohols compared to esters [4]. Table 5-7 shows 1) the ratio of formed self-coupling alcohols to self-forming esters, and 2) the ratio of total higher alcohols to total higher esters formed for ethanol, 1-butanol and 1-hexanol. Ethanol has a much higher alcohol/ester ratio compared to 1-butanol and 1-hexanol. The ethanol self-alcohol/self-ester ratio (1-butanol/ethyl acetate) is higher than the total alcohol/total ester, whereas this ratio for 1-butanol and 1-hexanol is mostly unchanged. This is because ethanol undergoes successive coupling while higher alcohols do not. The self-alcohol/self-ester ratio of ethanol is much higher than that of 1-butanol and 1-hexanol, which can be explained with a higher nucleophilicity of the ethanol-derived active species compared to higher alcohols. Alcohol coupling by 1-butanol and 1-hexanol is by formal Guerbet coupling mechanisms thus this indicates that ethanol coupling occurs by Guerbet coupling, as well as by a direct C-C coupling step.

Table 5-7. Ratios of higher alcohols to esters for ethanol, 1-butanol and 1-hexanol reactant feeds at 25 – 27 h^{-1}.

Reactant	Conversion (%)	Immediate higher alcohol to self-ester ratio of rates		Total higher alcohol to higher ester ratio of rates
Ethanol	23	6.7	1-butanol to ethyl acetate	6.2
1-butanol	23	1.8	2-ethyl-1-hexanol to butyl butyrate	1.7
1-hexanol	18	1.7	2-butyl-1-octanol to hexyl hexanoate	1.7

Finally, we also tested the performance of the first produced branched alcohol, 2-ethyl-1-butanol as shown in Table 5-8. It mainly produced the aldehyde and its self-ester, 2-ethylbutyl-2-ethylbutanoate. This also means that esterification is a termination reaction for alcohols, that will continue to react until they form a branch on their β-C position.

Table 5-8. Results of test with 2-ethyl-1-butanol. Conditions: 325°C, 300 psig, $P_{2\text{-Et-1-ButOH}}$:P_{H2} = 4, $WHSV_{2\text{-Et-1-ButOH}}$ = 26.11 h^{-1}.

Contact time(s kg_{cat} mol^{-1})	14.09
Conversion (%)	18.95
Selectivities (%)	
2-ethylbutanal	88.21
2-ethylbutyl 2-ethylbutanoate	9.38
Others	2.41

5.3.5. Elucidated reaction network for Ethanol Oligomerization

With all the information collected from our experiments, we know delve into the reaction network for ethanol oligomerization to higher alcohols, aldehydes, esters, ketones and additional products. First, ethanol may be converted primarily to acetaldehyde via dehydrogenation, this reaction is far from equilibrium at our reaction conditions. Then, ethanol may be converted to C_4 oxygenates by

different C-C coupling mechanisms involving an alcohol- or aldehyde-derived nucleophile attacking an electrophilic alcohol/aldehyde-derived species. Stoichiometric reactions illustrating the production of C_4 alcohols and aldehydes are illustrated in Figure 5-12. Ethanol may directly couple [7,12,21,22] with itself to form 1-butanol and water (described by 1 in Figure 5-12), or with acetaldehyde to form butyraldehyde (described by 2 in Figure 5-12) or crotyl alcohols (described by 3 in Figure 5-12) depending on where the dehydration occurs, and in the fact that crotyl alcohols and butyraldehyde are tautomers to each other. Moreover, butyraldehyde is known to be very close to equilibrium with 1-butanol, as our data showed. Both crotyl alcohol and butyraldehyde may hydrogenate to 1-butanol, with the hydrogenation of crotyl alcohol being probably irreversible. Acetaldehyde may also undergo formal Guerbet coupling [10,11,17,22] with itself via aldol condensation forming an unstable intermediate that is dehydrated very quickly to crotonaldehyde, which is then presumably hydrogenated also very quickly to butyraldehyde or crotyl alcohols, since we do not observe crotonaldehyde when pure ethanol is the feed. From this scheme, we can observe that 1-butanol can be a primary product of ethanol, but butyraldehyde and crotyl alcohols should not be, unless these are formed via surface mechanisms that do not require the desorption of intermediate species. It would then be conceivable that even at very low conversions, ethanol may dehydrogenate to acetaldehyde surface species which would then couple with ethanol (or with another similarly formed acetaldehyde surface species that has not desorbed yet) to form butyraldehyde or crotyl alcohols. This logic would extend to higher alcohols as well, as 1-hexanol, 2-ethyl-1-butanol and even 1-octanol were shown to be apparently primary products.

The formation of esters is then explained by a series mechanism in which an alcohol would perform a nucleophilic attack to an aldehyde, forming a hemiacetal which would then undergo dehydrogenation to form an ester. This stoichiometric reaction is illustrated in Figure 5-12

(described by 5) for the formation of ethyl acetate from ethanol and acetaldehyde, which combine to form 1-ethoxyethanol that then undergoes dehydrogenation to ethyl acetate. This also explains why increasing H_2 pressures decrease ester selectivity (and eventually aldehyde selectivity as well).

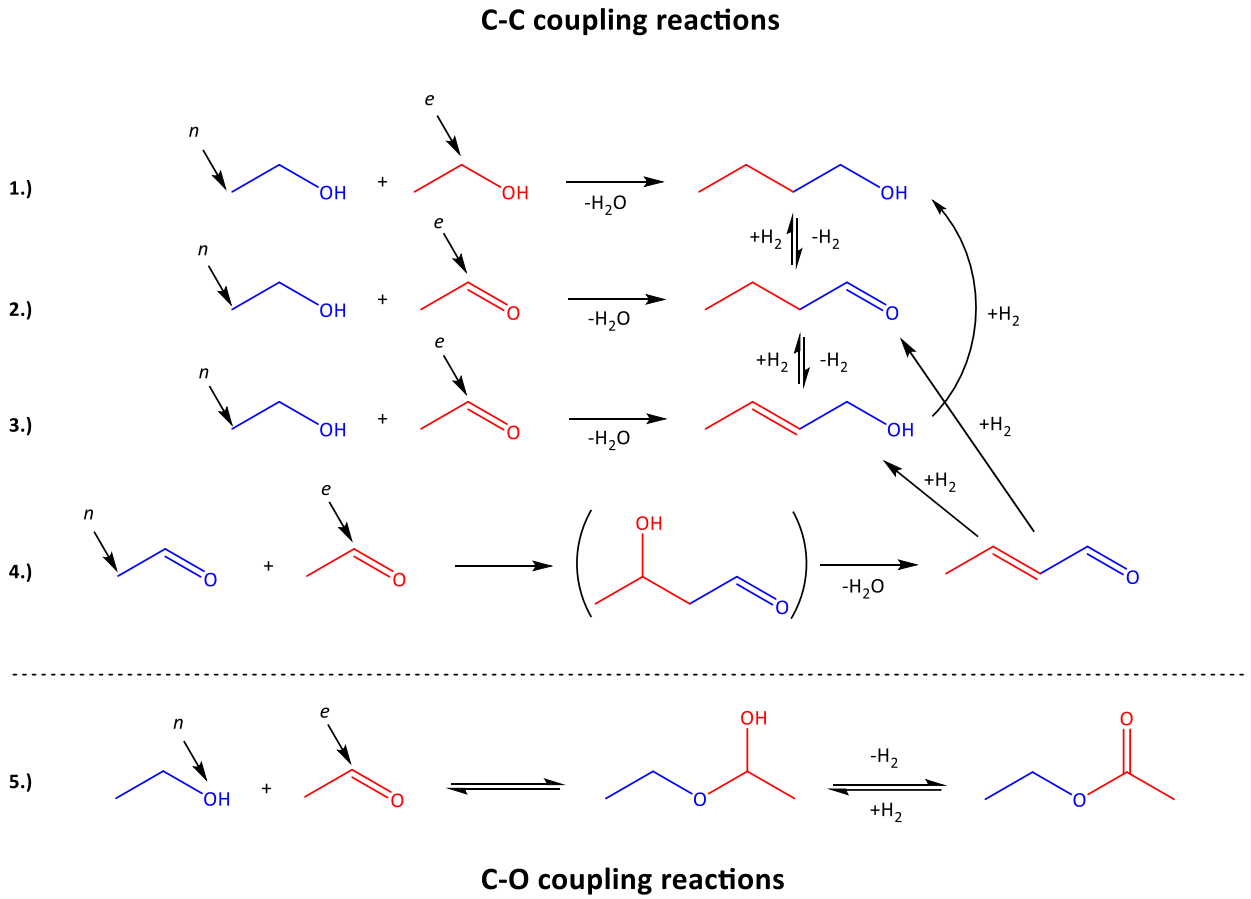

Figure 5-12. C-C coupling and C-O coupling reactions of ethanol to form C_4 alcohols/aldehydes and ethyl acetate respectively, including dehydration and hydrogenation steps of each. Blue color refers to nucleophilic molecules or their components into larger molecules. Red color refers to electrophilic molecules or their components into larger molecules. Nucleophilic carbons or oxygen positions are denoted by *n*, and electrophilic carbons are denoted by *e*. Reactions 1) through 4) are C-C coupling, where 1) refers to ethanol direct coupling with itself, 2) and 3) refer to ethanol direct coupling with acetaldehyde to form butyraldehyde and crotyl alcohols respectively, and 4) refers to formal Guerbet coupling of acetaldehyde via aldol condensation. Higher alcohol formation involves analogous steps at varying degrees on each type of reaction. Reaction 5) is C-O coupling of ethanol and acetaldehyde to form ethyl acetate via hemiacetal formation and subsequent dehydrogenation. Higher ester formation mechanism is analogous to the one presented here with different alcohol and aldehyde combinations.

Extending the logic of the mechanisms applied to the formation of C_4 alcohol and aldehydes, as well as ethyl acetate from ethanol by C-C and C-O coupling to larger oxygenate species, ethanol oligomerization to larger species can be described by Figure 5-13. Larger species may be consecutively formed via C-C coupling reactions of alcohols/aldehydes, with the chain-growth continuing for linear alcohols, which in turn require ethanol/acetaldehyde to be the nucleophile. Any other C-C coupling reaction in which ethanol does not participate as a nucleophile will result in a termination reaction for C-C coupling (e.g. no further higher alcohol formation). However, branched alcohols are capable of undergoing C-O coupling to form higher esters. Esters will always come from C-O coupling reactions of alcohols and aldehydes, and are referred to as condensation reactions, with H_2 being released after the reaction. Esters may be able to also grow via transesterification reactions with alcohols, but such behavior is not expected to widely occur at the studied reaction conditions, hence ester formation reactions are termination reactions for molecular weight growth.

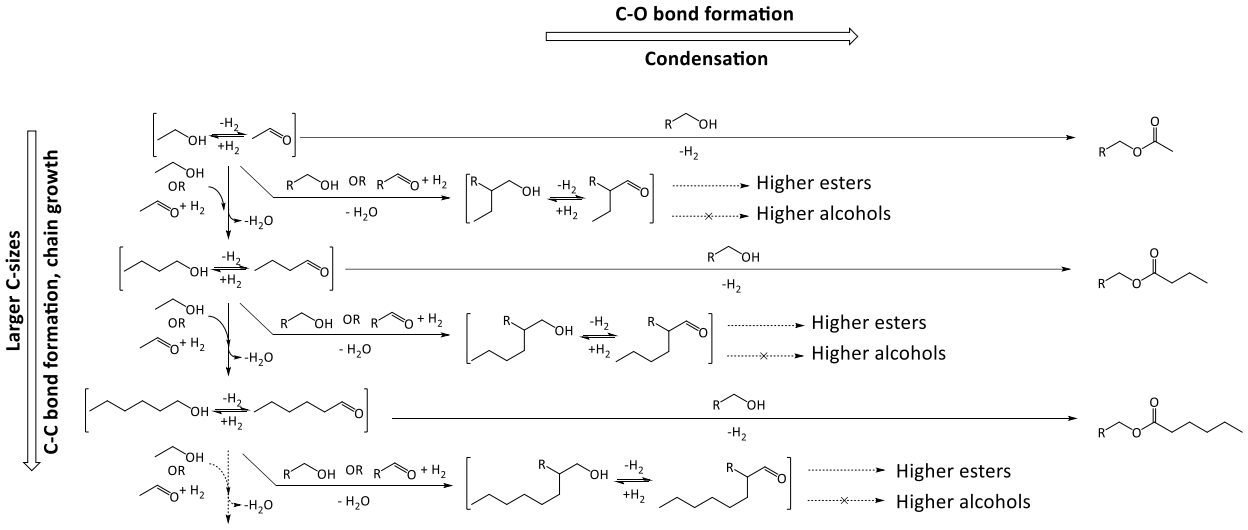

Figure 5-13. Successive higher alcohol and ester formation by C-C and C-O coupling reactions. Alcohols and aldehydes are considered to be in equilibrium. Ester formation reactions are considered termination reactions.

Considering the previous reasonings, we propose the following reaction network for the formation of species, shown in Figure 5-14. Ethanol may couple to form higher alcohols via aldol condensation mechanisms in which acetaldehyde performs the coupling [3,7,10], or via direct alcohol coupling. [7,21,22] There is recent literature about first-principles calculations that shows that it is possible to have one or both alcohol coupling mechanisms depending on the reaction conditions, particularly the temperature. [22] Esters are formed from the combination of an alcohol and an aldehyde that gives rise to a hemiacetal which is then dehydrogenated to the ester. Both Cu sites and base sites are capable of this reaction. [23,24] Finally, minor reactions of ethanol include retro-aldol condensation in which ketones are formed (especially at higher conversions), dehydration to olefins (unimolecular) and to ethers (bimolecular). Retro-aldol condensations are expected to be more favorable on Cu sites than dehydration of aldol and subsequent hydrogenation as Cu sites catalyze decarbonylation of the aldol intermediates after they undergo isomerization to their keto form via hydride shift [7,23,25]. In contrast, dehydration reactions are most likely occurring on acid sites [26,27].

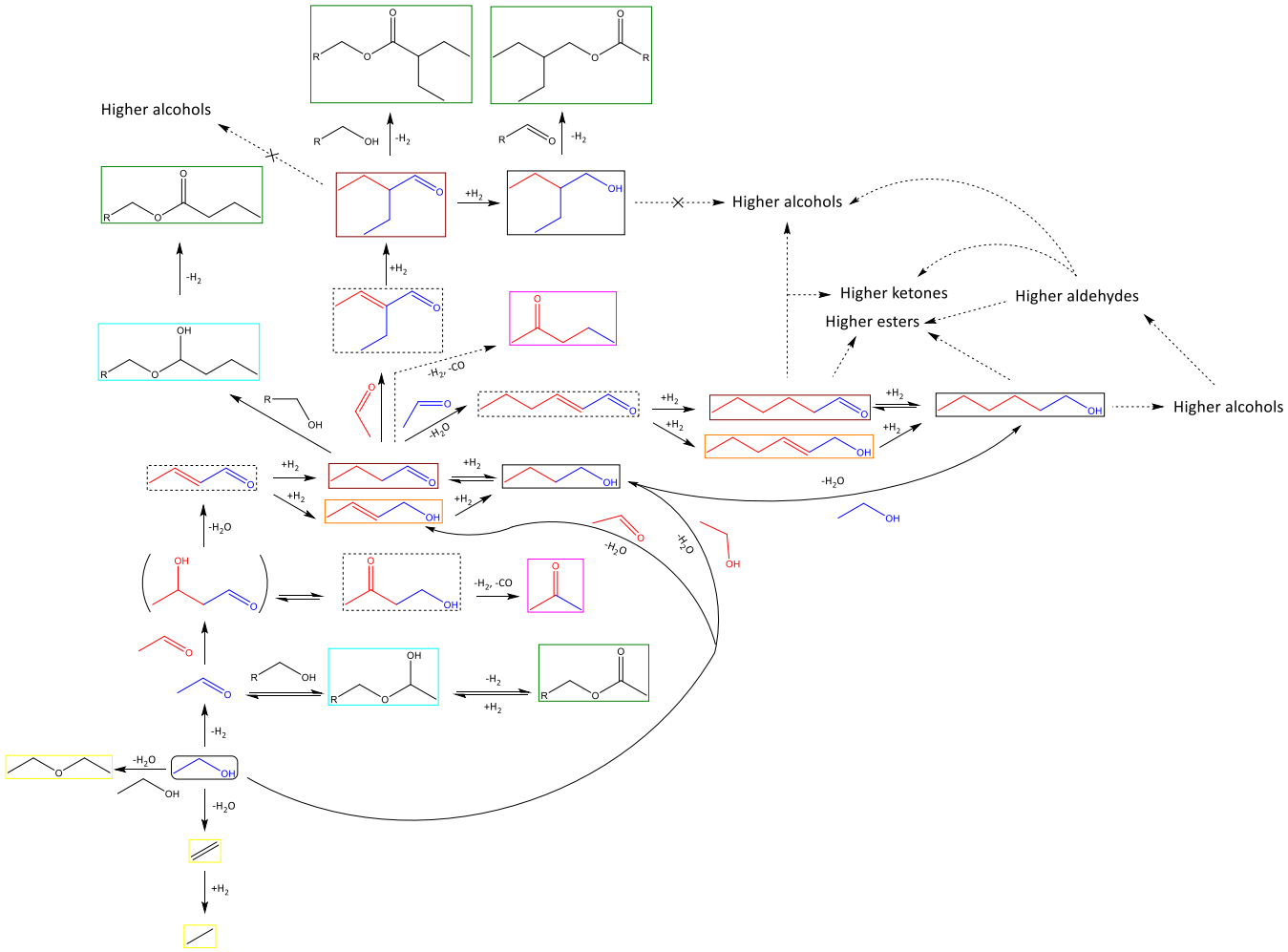

Figure 5-14. Reaction network proposed for ethanol oligomerization using 0.3wt%Cu/$Mg_{2.9}$AlO catalyst. Molecules in solid rectangles denote observed products, molecules in dashed rectangles denote expected, but non-detected products, and molecule in parentheses is unstable aldol adduct that undergoes dehydration in the surface. Ethanol is in a black, rounded rectangle, product alcohols are in black rectangles, aldehydes are in brown rectangles, alkenols are in orange rectangles, esters are in green rectangles, hemiacetals are in cyan rectangles, ketones are in violet rectangles, and ethers, olefins and paraffins (only those derived from ethanol are shown) are in yellow rectangles. Blue alcohol and aldehyde molecules denote a nucleophile in direct or formal Guerbet coupling, whereas red colored molecules denote the electrophile. Alcohol, aldehyde, alkenol and alkenal molecules are shown in a combination of blue and red colors to denote the nucleophilic and the electrophilic component that comes together to form it.

5.4. Conclusions

In this work, we have elucidated the reaction pathway for production of diesel fuel precursor compounds from ethanol oligomerization reaction with low Cu loading $Cu/Mg_{2.9}AlO$ catalysts. Conversion increases non-linearly at 0 – 70% range, suggesting that chemistry transition takes place between 20 – 30% and ethanol conversion inhibition occurs after 70%. Alcohols are formed at low to mid-conversions, with size increases being predicted by the Schultz-Flory distribution at all conversions, showing that alcohols grow via chain-growth mechanisms. Alcohols may be formed from ethanol by direct coupling mechanisms in which alcohols couple directly, as well as from formal Guerbet coupling mechanisms in which aldehydes are formed from alcohols and then undergo aldol condensation followed by successive hydrogenation steps until the alcohol is formed. For higher alcohol feeds, Guerbet coupling is confirmed to occur by the presence of expected alkenal intermediates, and an increase in alcohol selectivity accompanied by a decrease in aldehyde selectivity for 1-butanol.

Esterification is found to occur via reactions of alcohols and aldehydes forming hemiacetals that are dehydrogenated to form esters in a series pathway. Higher ester formation occurs predominantly over ethyl acetate formation as higher alcohol contents increase with conversion. Ketones on the other hand, are found to be formed predominantly at very high conversions, seemingly at the expense of alcohols. Ketone selectivity increases at around 70% conversion, where inhibition of ethanol conversion occurs, suggesting a shift in chemistry.

Higher alcohols such as 1-butanol, 1-hexanol and 2-ethyl-1-butanol show lower higher alcohol-to-ester product ratios than ethanol, which is attributed to ethanol higher nucleophilicity and its capability to couple to higher alcohols. On the other hand, it is possible to obtain esters more selectively from any alcohol different from ethanol using $0.3w\%Cu/Mg_{2.9}AlO$, which was found

to be especially true when branched alcohols such as 2-ethyl-1-butanol are used. It can be concluded from these tests that while the β-C of a β-branched alcohol (or the α-C of the corresponding α-branched aldehyde) is inactive towards Guerbet coupling, the oxygen of the same compound is active towards esterification.

Increasing the H2 partial pressure relative to ethanol results in alcohol formation being favored due to the suppression of H2 releasing reactions such as esterification and aldehyde formation. Increasing acetaldehyde molar fraction in the feeds promotes formal Guerbet coupling mechanisms. At high enough concentration in the feed, acetaldehyde promotes high selectivity to butyraldehyde and inhibits ethanol conversion and the formation of higher molecular weight products. Leading to the conclusion that controlling acetaldehyde formation enables control of the overall reaction chemistry. Finally, it was found that ethyl acetate inhibits higher species formation in general, favoring higher ester formation at the expense of higher alcohols and aldehydes.

5.5. References

(1) Alternative Fuels Data Center: Maps and Data - U.S. Production, Consumption, and Trade of Ethanol https://afdc.energy.gov/data/10323 (accessed 2021 -11 -22).

(2) Exxon Mobil Corporation. 2019 Outlook for Energy: A Perspective to 2040 https://corporate.exxonmobil.com/-/media/Global/Files/outlook-for-energy/2019-Outlook-for-Energy_v4.pdf (accessed 2021 -04 -19).

(3) Eagan, N. M.; Kumbhalkar, M. D.; Buchanan, J. S.; Dumesic, J. A.; Huber, G. W. Chemistries and Processes for the Conversion of Ethanol into Middle-Distillate Fuels. *Nature Reviews Chemistry* **2019**, *3* (4), 223–249. https://doi.org/10.1038/s41570-019-0084-4.

(4) Eagan, N. M.; Moore, B. M.; McClelland, D. J.; Wittrig, A. M.; Canales, E.; Lanci, M. P.; Huber, G. W. Catalytic Synthesis of Distillate-Range Ethers and Olefins from Ethanol through Guerbet Coupling and Etherification. *Green Chem.* **2019**, *21* (12), 3300–3318. https://doi.org/10.1039/C9GC01290G.

(5) Eagan, N. M.; Lanci, M. P.; Huber, G. W.; Penaloza, P. A. C.; Buchanan, J. S. Processes for Producing Ethers and Olefins from Primary Alcohols. US20210363085A1, November 25, 2021.

(6) Di Cosimo, J. I.; Díez, V. K.; Xu, M.; Iglesia, E.; Apesteguía, C. R. Structure and Surface and Catalytic Properties of Mg-Al Basic Oxides. *Journal of Catalysis* **1998**, *178* (2), 499–510. https://doi.org/10.1006/jcat.1998.2161.

(7) Gines, M. J. L.; Iglesia, E. Bifunctional Condensation Reactions of Alcohols on Basic Oxides Modified by Copper and Potassium. *Journal of Catalysis* **1998**, *176* (1), 155–172. https://doi.org/10.1006/jcat.1998.2009.

(8) Di Cosimo, J. I.; Apesteguı&́a, C. R.; Ginés, M. J. L.; Iglesia, E. Structural Requirements and Reaction Pathways in Condensation Reactions of Alcohols on MgyAlOx Catalysts. *Journal of Catalysis* **2000**, *190* (2), 261–275. https://doi.org/10.1006/jcat.1999.2734.

(9) Bravo-Suárez, J. J.; Subramaniam, B.; Chaudhari, R. V. Vapor-Phase Methanol and Ethanol Coupling Reactions on CuMgAl Mixed Metal Oxides. *Applied Catalysis A: General* **2013**, *455*, 234–246. https://doi.org/10.1016/j.apcata.2013.01.025.

(10) Kozlowski, J. T.; Davis, R. J. Heterogeneous Catalysts for the Guerbet Coupling of Alcohols. *ACS Catal.* **2013**, *3* (7), 1588–1600. https://doi.org/10.1021/cs400292f.

(11) Moteki, T.; Flaherty, D. W. Mechanistic Insight to C–C Bond Formation and Predictive Models for Cascade Reactions among Alcohols on Ca- and Sr-Hydroxyapatites. *ACS Catal.* **2016**, *6* (7), 4170–4183. https://doi.org/10.1021/acscatal.6b00556.

(12) Ogo, S.; Onda, A.; Iwasa, Y.; Hara, K.; Fukuoka, A.; Yanagisawa, K. 1-Butanol Synthesis from Ethanol over Strontium Phosphate Hydroxyapatite Catalysts with Various Sr/P Ratios. *Journal of Catalysis* **2012**, *296*, 24–30. https://doi.org/10.1016/j.jcat.2012.08.019.

(13) Marcu, I.-C.; Tichit, D.; Fajula, F.; Tanchoux, N. Catalytic Valorization of Bioethanol over Cu-Mg-Al Mixed Oxide Catalysts. *Catalysis Today* **2009**, *147* (3), 231–238. https://doi.org/10.1016/j.cattod.2009.04.004.

(14) Cheng, F.; Guo, H.; Cui, J.; Hou, B.; Li, D. Guerbet Reaction of Methanol and Ethanol Catalyzed by CuMgAlOx Mixed Oxides: Effect of M2+/Al3+ Ratio. *Journal of Fuel Chemistry and Technology* **2018**, *46* (12), 1472–1481. https://doi.org/10.1016/S1872-5813(18)30061-6.

(15) Petrolini, D. D.; Eagan, N.; Ball, M. R.; Burt, S. P.; Hermans, I.; Huber, G. W.; Dumesic, J. A.; Martins, L. Ethanol Condensation at Elevated Pressure over Copper on AlMgO and AlCaO Porous Mixed-Oxide Supports. *Catal. Sci. Technol.* **2019**, *9* (8), 2032–2042. https://doi.org/10.1039/C9CY00316A.

(16) Cuello-Penaloza, P. A.; Dastidar, R. G.; Wang, S.-C.; Du, Y.; Lanci, M. P.; Wooler, B.; Kliewer, C. E.; Hermans, I.; Dumesic, J. A.; Huber, G. W. Ethanol to Distillate-Range Molecules Using Cu/MgxAlOy Catalysts with Low Cu Loadings. *Applied Catalysis B: Environmental* **2022**, *304*, 120984. https://doi.org/10.1016/j.apcatb.2021.120984.

(17) Eagan, N. M.; Lanci, M. P.; Huber, G. W. Kinetic Modeling of Alcohol Oligomerization over Calcium Hydroxyapatite. *ACS Catal.* **2020**, *10* (5), 2978–2989. https://doi.org/10.1021/acscatal.9b04734.

(18) Ramasamy, K. K.; Guo, M. F.; Gray, M. J.; Subramaniam, S. United States Patent: 10745330 - Method of Converting Ethanol to Higher Alcohols. 10745330, August 18, 2020.

(19) Lee, J.-W.; Trinh, C. T. Towards Renewable Flavors, Fragrances, and Beyond. *Current Opinion in Biotechnology* **2020**, *61*, 168–180. https://doi.org/10.1016/j.copbio.2019.12.017.

(20) Kim, J.; Altreuter, D. H.; Clark, D. S.; Dordick, J. S. Rapid Synthesis of Fatty Acid Esters for Use as Potential Food Flavors. *Journal of the American Oil Chemists' Society* **1998**, *75* (12), 1109–1113. https://doi.org/10.1007/s11746-998-0298-y.

(21) C. Meunier, F.; Scalbert, J.; Thibault-Starzyk, F. Unraveling the Mechanism of Catalytic Reactions through Combined Kinetic and Thermodynamic Analyses: Application to the Condensation of Ethanol. *Comptes Rendus Chimie* **2015**, *18* (3), 345–350. https://doi.org/10.1016/j.crci.2014.07.002.

(22) de Souza, E. F.; Pacheco, H. P.; Miyake, N.; Davis, R. J.; Toniolo, F. S. Computational and Experimental Mechanistic Insights into the Ethanol-to-Butanol Upgrading Reaction over MgO. *ACS Catal.* **2020**, *10* (24), 15162–15177. https://doi.org/10.1021/acscatal.0c04616.

(23) Neurock, M.; Tao, Z.; Chemburkar, A.; Hibbitts, D. D.; Iglesia, E. Theoretical Insights into the Sites and Mechanisms for Base Catalyzed Esterification and Aldol Condensation Reactions over Cu. *Faraday Discuss.* **2017**, *197*, 59–86. https://doi.org/10.1039/C6FD00226A.

(24) Ndou, A. S.; Plint, N.; Coville, N. J. Dimerisation of Ethanol to Butanol over Solid-Base Catalysts. *Applied Catalysis A: General* **2003**, *251* (2), 337–345. https://doi.org/10.1016/S0926-860X(03)00363-6.

(25) Sad, M. E.; Neurock, M.; Iglesia, E. Formation of C–C and C–O Bonds and Oxygen Removal in Reactions of Alkanediols, Alkanols, and Alkanals on Copper Catalysts. *J. Am. Chem. Soc.* **2011**, *133* (50), 20384–20398. https://doi.org/10.1021/ja207551f.

(26) Song, W.; Liu, Y.; Baráth, E.; Wang, L. L.; Zhao, C.; Mei, D.; Lercher, J. A. Dehydration of 1-Octadecanol over H-BEA: A Combined Experimental and Computational Study. *ACS Catal.* **2016**, *6* (2), 878–889. https://doi.org/10.1021/acscatal.5b01217.

(27) Rorrer, J.; Pindi, S.; Toste, F. D.; Bell, A. T. Effect of Alcohol Structure on the Kinetics of Etherification and Dehydration over Tungstated Zirconia. *ChemSusChem* **2018**, *11* (18), 3104–3111. https://doi.org/10.1002/cssc.201801067.

Chapter 6: Conclusions and Future directions

6.1. Conclusions

In this work, the conversion of biomass-derived feedstocks into valuable fuels chemicals using selective catalysts at industrially relevant conditions has been investigated. Particularly, in Chapter 2, we have investigated the conversion of levoglucosanol (Lgol) into hexane-1,2,5,6-tetrol (tetrol) at industrially relevant feed concentrations up to 30wt% with a Pt-WO_x/TiO_2 catalyst. We concluded that tetrol can be produced with over 90% selectivity using a 10wt%Pt-(10wt%)WO_x/TiO_2 catalyst. The relative stability of this catalyst compared to other studied[1] allowed us to obtain the kinetics for this reaction at high concentrations. The hydrogenolysis of Lgol into tetrol in aqueous media was found to be first order in Lgol and zeroth order in H_2, therefore allowing us to conclude that the acid-catalyzed step of this reaction is irreversible, and that the metal-catalyzed hydrogenation is not equilibrated. The activation energy barrier for this reaction was found to be 151 ± 10 KJ/mol, which is higher than the measured and calculated value for Lgol hydrolysis to dideoxymannose (DDM) and dideoxyglucose (DDG) of ~80 KJ/mol [2]. The 10wt%Pt-(10wt%)WO_x/TiO_2 catalyst used for this reaction was found to deactivate with time-on-stream, but was much more stable than 5wt%Pt/SiO_2-Al_2O_3, which deactivated irreversibly, whereas our Pt-WO_x/TiO_2 catalyst was found to be partially regenerable, and last through at least 400 turnovers (Acid-site based) at 120°C compared to less than 30 for Pt/SiO_2-Al_2O_3 at 150°C. Finally, the Pt-WO_x/TiO_2 catalyst also enable over 90% preservation of Lgol stereocenters in a one-pot synthesis, which is much higher than the 64% achieved with Pt/SiO_2-Al_2O_3 and very similar to the 95% achieved by a two-stage reaction scheme consisting of Lgol hydrolysis to

The contents of this Chapter are partially adapted from the references detailed in Chapters 2 through 5.

intermediates with H_2SO_4 followed by hydrogenation. The stereochemistry is presumed to be preserved due to hydrogenation occurring very fast compared to isomerization of intermediates DDM and DDG to dideoxyfructose (DDF) due to metal site proximity to acid sites, as well as the higher activity of Pt-WO_x/TiO_2 compared to Pt/SiO_2-Al_2O_3, and also due to the lower temperature the reaction is carried out with our catalyst (120 °C *vs* 150 °C) that further limits any isomerization of DDM/DDG into DDF[1].

We also explored a potential application of biomass-derived tetrol as a monomer in the synthesis of tetrol-benzenediboronic acid (BDB) copolymers in Chapter 3. 1,3- and 1,4-BDB, as well as 4,4'-biphenyldiboronic acid (4,4-BPDB) were tested as comonomers with tetrol. We found that the meta orientation of 1,3-BDB favored the obtention of higher surface areas and pore volumes, probably due to the induced curvature of this position over the para position. 1,4-BDB-tetrol and 4,4'BPDB-tetrol copolymers had similar properties. The solvent used in the synthesis was found to have significant effect on the resulting polymer properties, with acetone leading to larger pore volumes compared to THF, CH_3CN and CH_2Cl_2. Moreover, the diastereomeric purity of the tetrol was found to have an impact in the polymer properties, with a 98%(*S*,*R*)-tetrol-based polymer exhibiting larger surface area and pore volume than a 38%-based (*S*,*R*)- or (*S*,*S*)-tetrol-based polymers. This last polymer also serves as an example of a rare chiral polymer.

In this work, we have explored the use of mixed metal oxides to produce diesel fuel precursors from ethanol. Particularly, we have demonstrated that by using very low Cu loadings (<0.6wt%) in Mg_xAlO_y acid-base catalysts, we are able to obtain high selectivities towards diesel fuel precursors, namely C4+ alcohols (up to 61%), C4+ aldehydes (up to 12%), C6+ esters (up to 27%) and C5+ ketones (up to 13%). C4+ alcohols obtained are mostly linear, and these may be upgraded to diesel fuel ethers by bimolecular dehydration (etherification) using acid catalysts[3,4]. C4+

aldehydes may be hydrogenated to alcohols that may undergo etherification. Esters with more than 8 carbons may be blended into diesel directly or hydrogenated back into alcohols that may undergo etherification. Ketones may also be hydrogenated to secondary alcohols that may be subjected to etherification, and olefins may be obtained from these and branched alcohols that undergo unimolecular dehydration preferentially over bimolecular dehydration[3,4].

In Chapter 4, we demonstrated that low Cu loadings make Cu/Mg_xAlO_y catalysts effective for ethanol oligomerization by acting as a promoter that speeds up hydrogen transfers typically carried out in acid-base catalysts by intermolecular transfers (Meerwein-Ponndorf-Verley mechanisms), favoring alcohol coupling while keeping side reaction rates proper to Cu (esterification, ketone formation) at a minimum. We also demonstrated that the synthesis method does not impact greatly catalyst performance, that only having low amounts of Cu in the catalytic material was required, and that active site proximity between Cu and the acid-base sites of Mg_xAlO_y was not required to make it effective. We concluded by infrared spectroscopy of CO-dosed catalysts at low temperature that the active Cu site for the low Cu-loading Mg_xAlO_y catalysts studied in this work was Cu^0. The catalysts were found to deactivate in proportion to number of turnovers but were found to be regenerable by a calcination procedure followed by reduction. Catalyst deactivation was found to proceed mostly via coking, with sintering occurring, but not impeding full catalyst activity recovery. We also found that higher alcohol selectivity follows Schultz-Flory distribution, meaning that alcohols grow via chain-growth mechanisms, and also hinting that higher alcohol linearity is due to ethanol-derived active species being more nucleophilic than those derived from higher alcohols[5].

In Chapter 5 we tested 0.3wt% Cu/$Mg_{2.9}AlO$ catalysts at different weight hourly space velocities (WHSV), varied $P_{Ethanol}$:P_{H2} feed rations and performed cofeed experiments with acetaldehyde and

ethyl acetate to elucidate the reaction network of ethanol oligomerization. We found that alcohol selectivity follows Schultz-Flory distribution at all conversions, with the probability of chain-growth increasing with conversion generally. Aldehydes are intermediates to obtain esters by reacting with alcohols via hemiacetal-based mechanisms[6]. Ketones are only formed significantly at very high conversions (~70%), indicating that these are secondary products from alcohols and aldehydes. We also found that acetaldehyde promotes minimally higher alcohol formation, eventually hindering this and all other reactions and ethanol conversion, with the exception of butyraldehyde formation, which is consistent with an interpretation that acetaldehyde undergoes Guerbet coupling, and that it may also strongly adsorb in the surface or undergo significant oligomerization that inhibits activity[7]. Ethyl acetate in general inhibited higher alcohol and aldehyde formation, and promoted C6 ester formation, probably by transesterification. When the partial pressure of H_2 is increased in the system with reduction in ethanol partial pressure, selectivity towards higher alcohols was promoted at the expense of ester selectivity, and eventually higher aldehyde selectivity, with a minimal decrease in conversion. This indicates that alcohols, aldehydes and esters are influenced by equilibria, but not dominated at our reaction conditions. Finally, we also tested higher alcohols, namely 1-butanol, 1-hexanol and 2-ethyl-1-butanol as feeds using Cu/$Mg_{2.9}$AlO catalysts. We found that 1-butanol and 1-hexanol undergo formal Guerbet coupling by forming their aldehydes first, then undergoing aldol condensation and hydrogenation as evidenced by the presence of alkenol intermediates[8]. We found that the relative rate of alcohol-to-ester production for 1-butanol and 1-hexanol was similar, and much lower than that of ethanol, being consistent with an interpretation that ethanol is a better nucleophile. We found that branched alcohols may be able to undergo esterification from 1-butanol, 1-hexanol and most remarkably 2-

ethyl-1-butanol, demonstrating that the oxygen of branched alcohols/aldehydes is not impeded to act as a nucleophile as the carbon proximal to the C-OH/C=O is.

6.2. Future directions and outlook

6.2.1. Future directions

6.2.1.1. Scale up of levoglucosanol hydrogenolysis to hexane-1,2,5,6-tetrol and potential markets

Having obtained kinetic information at industrially-relevant conditions using a 10wt%Pt-(10wt%)WO_x/TiO_2 catalyst, our attention now turns to how to scale up the hydrogenolysis of Lgol to tetrol while maintaining selectivity and process feasibility. Two important factors come to mind, capital costs and operational costs.

In regards capital costs, alternative catalytic approaches must be considered, as Pt is one of the most expensive metals in the market being a noble metal, and W-based acid catalysts are also more expensive alternative compared to inexpensive SiO_2-Al_2O_3 or zeolites. The main reasons for using WO_x are its better hydrothermal stability, regenerability and superior activity to other acid catalysts. An easy option would be to reduce Pt-loading in the catalyst, since 10wt% was used based on prior literature[9] suggesting it would have the highest rate in this type of reactions, but that does not necessarily mean that such high loading is required. In fact, knowing that the reaction is zeroth order in H_2, it is evident that hydrogenation capabilities are not heavily required, but it is required to establish first whether the zeroth order in H_2 is due to the acid-catalyzed step being rate-limiting as some literature might suggest for a similar reaction[10], or due to hydrogen being

strongly adsorbed in the catalytic surface, particularly in Pt. For this, experiments varying Pt loading in Pt-WO_x/TiO_2 catalyst are required. Assuming that dehydration is the rate-limiting step in Lgol hydrogenolysis, lowering Pt loadings will result in more affordable catalysts. Additional research may be done in replacing Pt with a base metal, such as Cu or Ni supported by WO_x/TiO_2. It should be noted that Pt performed better than Pd, Rh and Ru when supported in WO_x/TiO_2 due to the partially reduced support not overcoating the Pt nanoparticles as much as it did with the other metals[11]. Such consideration needs to be had with base metals as well. Also, additional water-tolerant supports may be considered if price allows. Supports need to be partially reducible to act as effective acid catalysts, such as ZrO_2.[12] Other reducible metals such as Mo or Re may be considered if pricing and availability is better than for W. Other water-tolerant acidic supports, such as ZrP can be considered as well, keeping in mind the effect of the acidity in the reaction chemistry. Finally, physical mixtures of separate acid and metal catalysts are shown to be able to carry out the conversion of Lgol to tetrol.[1] Further research may be done in regards whether the combination of physical mixtures of cheap catalyst alternatives such as H_2SO_4 in homogeneous catalysis, or SiO_2-Al_2O_3 or any other low-cost solid catalyst can achieve full conversion of Lgol to tetrol with reasonable catalyst loadings, temperatures and separation or replacement costs, since the solid catalysts would be expected to completely and irreversibly deactivate.

Regarding operation costs, the most important factors to consider are the number of process stages, the reaction temperature and pressure (to a lesser extent) and any additional separation costs. 10wt%Pt-(10wt%)WO_x/TiO_2 was shown to have activity at 100°C, which leaves open the question to what would the lowest process temperature that would enable conversion of Lgol to tetrol occur with reasonable catalyst mass. This is also important due to lower temperatures potentially favouring catalyst stability, particularly if catalyst deactivation occurs due to coking and/or metal

leaching. Process stage costs need to be considered as well, particularly the scenario in which a two stage process in which first an acid catalyst, even a homogeneous one such as H_2SO_4 is used to hydrolyze Lgol to its intermediates, followed by a second metal-catalyzed stage in which these intermediates are hydrogenated to tetrol selectively may be more economically feasible than a one-pot synthesis with an expensive catalyst and associated operation costs, even if catalyst replacement or separation costs is an associated factor in a two-stage process. Technoeconomic and life cycle analysis are required to further probe on this.

Finally, markets for tetrol need to be explored in order to justify its production and guarantee its commercialization. As a polyol, tetrol may be used in polymer synthesis as a chain-extender, crosslinking agent, and as a polymer precursor to polyurethanes, polycarbonates, acrylic polyols, polyether polyols, polyester polyols and other specialty polymers with myriads of applications, which need to be assessed and proven if tetrol becomes a building block for such materials. Hexan-1,2,5,6-tetrol also contains chiral centers, which as we demonstrated in Chapter 3, have an impact on the resulting polymer properties and potential applications. Moreover, the fact that tetrol itself has chirality makes it useful as a chiral reagent molecule for applications in the pharmaceutical industry or in asymmetrical synthesis.

6.2.1.2. Improved catalysts for ethanol oligomerization reactions and product selectivity control

In this work, we demonstrated that an inexpensive Mg_xAlO_y catalyst with very low amounts of Cu was able to selectively produce predominately larger linear alcohols from ethanol. The fact that it is lower loadings of Cu that enables Mg_xAlO_y to effectively perform ethanol coupling begs the question on whether other metals that enable surface hydrogen transfers might act as more effective

and selective promoters, as well as improving catalyst stability. Metals such as Ni or Pt would be a good option to try, since these metals favor C-C scission, meaning that deactivation by coking (e.g. strong binding of oligomerized species) is less likely. Coking is the main cause of deactivation for Cu-based catalysts. On the other hand, Pd has been shown to work in the ethanol coupling reaction to larger alcohols alone, or when alloyed with Cu [13,14], as well as a promoter in lower loadings for the formation of ketones[15] along with Zn, another metal to consider. Important aspects to consider are the relative activity of the metal sites to that of the support, alcohol product linearity and overall ethanol conversion rates. In addition, metal alloys that enable stabilization of active metals such as NiCu[16,17] or PtCu, or alloys that allow for higher surface hydrogen transfer rates such as PdCu[13] may be considered. These alloys may also mitigate or even eliminate catalyst deactivation by coking and/or sintering mechanisms. Finally, if the intrinsic activity of these proposed catalysts is orders of magnitude higher than Cu-based mixed metal oxides, lower reaction temperatures may be considered. To further explore the effects of using different metals, Density Functional Theory and microkinetic modelling may prove useful in guiding the rational design of new and improved catalysts, and in the understanding of the underlying alcohol coupling mechanisms, particularly on whether formal Guerbet coupling of aldehydes via aldol condensation is occurring, or direct alcohol coupling with no aldol intermediate is leading the process. Also, spectroscopical evidence for the proposed chain-growth mechanism ought to be obtained to further validate the conclusions derived from the contact time tests of ethanol oligomerization with our low loading Cu/Mg_xAlO_y catalysts. Techniques such as DRIFTS may serve for this purpose, as the presence of ethanol-based and/or acetaldehyde-based surface species may be confirmed.

On the other hand, it is desirable to further control the chemistry of the ethanol oligomerization, particularly in the production diesel fuel precursors such as higher alcohols, or higher esters. The

latter may be used as flavorings and fragrances, and since we elucidated that these are produced from alcohols and aldehydes in a series pathway, process variables such as temperature, pressure, carrier gas and even metal promoter are expected to affect the chemistry of ethanol oligomerization to one or other product. It is already known that increasing hydrogen pressure results in higher selectivity to alcohols and aldehydes at the expense of ester selectivity. Variables to explore are then, temperature and catalyst metal combinations. Another possibility to consider is the proposal of a process by which esters are the final products in the conversion of ethanol. This would be possible since higher alcohols can only couple once, and branched alcohols were shown to selectively form esters as their final products. Esters of sizes 8 and more may be blended into diesel fuel, and specific ester molecules may also be obtained from any alcohol different than ethanol, therefore making a recursive process in which ethanol is first reacted to higher alcohols in a first stage, and then the product alcohols are reacted into esters in a second stage with Cu/Mg_xAlO_y or other Cu-containing catalysts is feasible.

It is also desirable to know the elements that drive chain-growth in ethanol coupling to guide the design of catalysts. From literature we know that either higher ethanol-derived active species nucleophilicity relative to that of higher alcohols derived species is favorable to increase alcohol linearity, but not necessarily product sizes. Since ethanol coupling follows Schultz-Flory distribution, it would be desirable to know whether cofeeding small amounts of higher alcohols, such as 1-butanol would result in increased product sizes, as is the case with olefins[18]. Also, decreased relative electrophilicity of the ethanol-derived active species compared to that of higher alcohols may favor both larger alcohol product sizes and linearity, potentially at the expense of catalyst activity if the rate-determining step of the reaction is the nucleophilic attack.[5] Changing the metal may also change the reaction dynamics, as Ni-based metals (Ni/Al_2O_3)[19] were found to

fit better an interpretation of reduced electrophilicity rather than increased nucleophilicity of ethanol.

Finally, technoeconomic and life cycle analyses need to be further developed for the consideration of an economically feasible and environmentally sustainable ethanol-to-diesel process. So far, we know that ethanol prices drive the economics of our process, and that the process may generate reductions in CO_2 emissions up to 50%, while increasing eutrophication and acidification of soils due to land use to produce ethanol from biomass. It is important to assess the impact of aldehydes, ketones and esters in an acid-catalyzed subsequent step. If these compounds are found to impact the process, measures to deal, convert or remove them from the process stream may be required. Aldehydes and ketones may be hydrogenated, whereas esters would need to be separated into alcohols and aldehydes constituents. Further works needs to be done in this area as well.

6.2.2. Outlook

In this work, we have explored the selective synthesis of a biomass-derived platform molecule, as well as the selective synthesis of diesel fuel precursors from biomass-derived ethanol. Process design and scaling up considerations have been an important factor in the study of these processes, as it is desired that the knowledge acquired in this research serves as a guide for such potential processes. For this end, the obtention of important kinetic and mechanistic information from the processes, as well as the rational choice of suitable catalysts have been crucial in the development of these studies. The focus is now in determining process economics that are favorable to the scaling up of the studied processes. To this end, I put forward the following recommendations in the next paragraphs.

First, a technoeconomic analysis (TA) and life cycle analysis (LCA) are required to evaluate and de-risk any scale up of a new process. In the case of Lgol conversion to tetrol, no such analyses exist. Therefore, a formal TA and LCA be done on Lgol conversion to tetrol economics and environmental impact in order to evaluate process risks and take concrete steps to address any difficulties related to design. Scaling up itself will be challenging as well, as several difficulties not apparent at the laboratory scale such as transport effects and increased production costs start becoming increasingly significant. Rennovia Inc. provides an example of a failed scale-up of a rationally designed technology due to chiefly external factors related to funding and geopolitical events at the time.[20] We must not forget however, that several technologies that seek to address market insufficiencies, or even create new markets are being developed, such as the company Pyran[21] that is focused on scaling up 1,5-pentanediol production from biomass-derived feedstocks, which cannot be easily obtained from oil-based sources and may confer better properties to polymers such as polyurethanes. Moreover, Circa™, the first company to produce levoglucosenone at industrial scale, has also manifested its interest in producing tetrol at larger scales[22]. This motivates the development of feasible processes to this end.

Second, catalyst choice and rational design is crucial in determining whether a particular alternative has a better chance at succeeding than others. For instance, typical loadings of Cu in Mg_xAlO_y catalysts promote ethyl acetate and acetone formation from ethanol. It is known that acetone may continue coupling and form C_{5+} ketones on its own.[15] However, it is only by understanding the underlying chemistry of alcohol coupling that the proposal of low loadings of Cu made sense to make ethanol instead the building block of higher alcohols (C_{4+} alcohols). While this is a good hypothesis on its own, a more systematic approach is required to rationally design catalysts that drives the conversion of ethanol to desired products, and harness ethanol true

potential as a platform molecule. Most literature focuses on producing 1-butanol or butadiene from ethanol, and using it as a template for larger molecules, or to be blended into gasoline. Understanding molecularly on how catalysts promote ethanol chain-growth then is crucial to design catalysts that facilitate such process, which then allows the production of higher alcohols of any practical desired size. To this end, collaborations between experimentalists and theoretical scientists is required, since the former may provide data to the latter based on an initial hypothesis to understand the fundamentals of a reaction and then attempt to model it and obtain valuable fitting parameters, as well as perform calculations to determine desired surface energies, and then propose new materials and reaction conditions that may be tested in the laboratory, repeating the cycle as many times as required. TA and LCAs are currently in development for the ethanol oligomerization process, and we expect to eventually publish and use the obtained results to propose a detailed process to obtain diesel and jet fuel from ethanol. Work then would need to be done in scaling up of ethanol oligomerization similar to how it was detailed for Lgol conversion to tetrol.

6.3. References

(1) Krishna, S. H.; De bruyn, M.; Schmidt, Z. R.; Weckhuysen, B. M.; Dumesic, J. A.; Huber, G. W. Catalytic Production of Hexane-1,2,5,6-Tetrol from Bio-Renewable Levoglucosanol in Water: Effect of Metal and Acid Sites on (Stereo)-Selectivity. *Green Chem.* **2018**, *20* (19), 4557–4565. https://doi.org/10.1039/C8GC02455C.

(2) Krishna, S. H.; Cao, J.; Tamura, M.; Nakagawa, Y.; De Bruyn, M.; Jacobson, G. S.; Weckhuysen, B. M.; Dumesic, J. A.; Tomishige, K.; Huber, G. W. Synthesis of Hexane-Tetrols and -Triols with Fixed Hydroxyl Group Positions and Stereochemistry from Methyl Glycosides over Supported Metal Catalysts. *ACS Sustainable Chem. Eng.* **2020**, *8* (2), 800–805. https://doi.org/10.1021/acssuschemeng.9b04634.

(3) Eagan, N. M.; Lanci, M. P.; Huber, G. W.; Penaloza, P. A. C.; Buchanan, J. S. Processes for Producing Ethers and Olefins from Primary Alcohols. US20210363085A1, November 25, 2021.

(4) Eagan, N. M.; Moore, B. M.; McClelland, D. J.; Wittrig, A. M.; Canales, E.; Lanci, M. P.; Huber, G. W. Catalytic Synthesis of Distillate-Range Ethers and Olefins from Ethanol through Guerbet Coupling and Etherification. *Green Chem.* **2019**, *21* (12), 3300–3318. https://doi.org/10.1039/C9GC01290G.

(5) Eagan, N. M.; Lanci, M. P.; Huber, G. W. Kinetic Modeling of Alcohol Oligomerization over Calcium Hydroxyapatite. *ACS Catal.* **2020**, *10* (5), 2978–2989. https://doi.org/10.1021/acscatal.9b04734.

(6) Inui, K.; Kurabayashi, T.; Sato, S. Direct Synthesis of Ethyl Acetate from Ethanol Carried Out under Pressure. *Journal of Catalysis* **2002**, *212* (2), 207–215. https://doi.org/10.1006/jcat.2002.3769.

(7) Bravo-Suárez, J. J.; Subramaniam, B.; Chaudhari, R. V. Vapor-Phase Methanol and Ethanol Coupling Reactions on CuMgAl Mixed Metal Oxides. *Applied Catalysis A: General* **2013**, *455*, 234–246. https://doi.org/10.1016/j.apcata.2013.01.025.

(8) Moteki, T.; Flaherty, D. W. Mechanistic Insight to C–C Bond Formation and Predictive Models for Cascade Reactions among Alcohols on Ca- and Sr-Hydroxyapatites. *ACS Catal.* **2016**, *6* (7), 4170–4183. https://doi.org/10.1021/acscatal.6b00556.

(9) He, J.; Burt, S. P.; Ball, M.; Zhao, D.; Hermans, I.; Dumesic, J. A.; Huber, G. W. Synthesis of 1,6-Hexanediol from Cellulose Derived Tetrahydrofuran-Dimethanol with Pt-WO_x/TiO_2 Catalysts. *ACS Catal.* **2018**, *8* (2), 1427–1439. https://doi.org/10.1021/acscatal.7b03593.

(10) Krishna, S. H.; Assary, R. S.; Rashke, Q. A.; Schmidt, Z. R.; Curtiss, L. A.; Dumesic, J. A.; Huber, G. W. Mechanistic Insights into the Hydrogenolysis of Levoglucosanol over Bifunctional Platinum Silica–Alumina Catalysts. *ACS Catal.* **2018**, *8* (5), 3743–3753. https://doi.org/10.1021/acscatal.7b03764.

(11) He, J.; Burt, S. P.; Ball, M. R.; Hermans, I.; Dumesic, J. A.; Huber, G. W. Catalytic C-O Bond Hydrogenolysis of Tetrahydrofuran-Dimethanol over Metal Supported WOx/TiO2 Catalysts. *Applied Catalysis B: Environmental* **2019**, *258*, 117945. https://doi.org/10.1016/j.apcatb.2019.117945.

(12) Mazarío, J.; Romero, M. P.; Concepción, P.; Chávez-Sifontes, M.; Spanevello, R. A.; Comba, M. B.; Suárez, A. G.; Domine, M. E. Tuning Zirconia-Supported Metal Catalysts for Selective One-Step Hydrogenation of Levoglucosenone. *Green Chem.* **2019**, *21* (17), 4769–4785. https://doi.org/10.1039/C9GC01857C.

(13) Nikolaev, S. A.; Tsodikov, M. V.; Chistyakov, A. V.; Chistyakova, P. A.; Ezzhelenko, D. I.; Shilina, M. I. PdCu Nanoalloy Supported on Alumina: A Stable and Selective Catalyst for the Conversion of Bioethanol to Linear α-Alcohols. *Catalysis Today* **2021**, *379*, 50–61. https://doi.org/10.1016/j.cattod.2020.06.061.

(14) Goulas, K. A.; Sreekumar, S.; Song, Y.; Kharidehal, P.; Gunbas, G.; Dietrich, P. J.; Johnson, G. R.; Wang, Y. C.; Grippo, A. M.; Grabow, L. C.; Gokhale, A. A.; Toste, F. D. Synergistic Effects in Bimetallic Palladium–Copper Catalysts Improve Selectivity in Oxygenate Coupling Reactions. *J. Am. Chem. Soc.* **2016**, *138* (21), 6805–6812. https://doi.org/10.1021/jacs.6b02247.

(15) Subramaniam, S.; Guo, M. F.; Bathena, T.; Gray, M.; Zhang, X.; Martinez, A.; Kovarik, L.; Goulas, K. A.; Ramasamy, K. K. Direct Catalytic Conversion of Ethanol to C5+ Ketones: Role of Pd–Zn Alloy on Catalytic Activity and Stability. *Angewandte Chemie International Edition* **2020**, *59* (34), 14550–14557. https://doi.org/10.1002/anie.202005256.

(16) Hernández, W. Y.; De Vlieger, K.; Van Der Voort, P.; Verberckmoes, A. Ni–Cu Hydrotalcite-Derived Mixed Oxides as Highly Selective and Stable Catalysts for the Synthesis of β-Branched Bioalcohols by the Guerbet Reaction. *ChemSusChem* **2016**, *9* (22), 3196–3205. https://doi.org/10.1002/cssc.201601042.

(17) Sun, Z.; Couto Vasconcelos, A.; Bottari, G.; Stuart, M. C. A.; Bonura, G.; Cannilla, C.; Frusteri, F.; Barta, K. Efficient Catalytic Conversion of Ethanol to 1-Butanol via the Guerbet Reaction over Copper- and Nickel-Doped Porous. *ACS Sustainable Chem. Eng.* **2017**, *5* (2), 1738–1746. https://doi.org/10.1021/acssuschemeng.6b02494.

(18) Eagan, N. M.; Kumbhalkar, M. D.; Buchanan, J. S.; Dumesic, J. A.; Huber, G. W. Chemistries and Processes for the Conversion of Ethanol into Middle-Distillate Fuels. *Nature Reviews Chemistry* **2019**, *3* (4), 223–249. https://doi.org/10.1038/s41570-019-0084-4.

(19) Jordison, T. L.; Lira, C. T.; Miller, D. J. Condensed-Phase Ethanol Conversion to Higher Alcohols. *Ind. Eng. Chem. Res.* **2015**, *54* (44), 10991–11000. https://doi.org/10.1021/acs.iecr.5b02409.

(20) Rennovia's Demise, the Triple Rule, and the Pursuit of Sustainable Nylon in a World of Low Oil Prices : Biofuels Digest, 2018.

(21) Pyran https://pyranco.com/ (accessed 2022 -02 -23).

(22) Flagship EU Project aiming to Replace Toxic Solvents with Renewable Alternatives Launches today https://circa-group.com/news/2020/10/24/9axo6z01ddll227lq24abjs2g5mbyz (accessed 2021 -03 -24).

Chapter 7. Appendices

7.1. Introduction

In this chapter, the appendices for chapters 2 through 5 will be presented. Appendices reflect the supporting information relevant to the articles prepared for each of the topics treated on each chapter. Supporting information typically includes extra information about tests performed on the main chapters, additional experiments to further confirm trends, and material characterization information. Figures and tables in the previous chapters will be found here with the nomenclature Figure/Table 7-N, where N is the subnumber from start to end based on this Chapter (e.g. first figure is 7-1, then 7-2, and so on).

7.2. Appendix for Chapter 2

7.2.1. Identification of compounds and relative concentration determination by ^{13}C qNMR

The compounds levoglucosanol (Lgol), hexane-1,2,5,6-tetrol (tetrol) and hexane-1,2,6-triol (HTri) were able to be identified by NMR techniques[1]. Reactive intermediates dideoxyglucose (DDG), dideoxymannose (DDM) and dideoxyfructose (DDF) that are also tetrol precursors were not able to be identified by ^{13}C NMR. The reason for this is the number of peaks of DDM, DDG and DDF combined is 54 since these compounds present different tautomers. Therefore, by being at low concentration, the signals of these peaks are probably below the detection limits of the equipment. However, it is known from literature[1] that these compounds are formed, and their characteristic

peaks were observed to a certain degree in HPLC chromatograms and we can determine the sum of tetrol and precursors concentration from these as will be discussed later on this document.

Figures 7-1 A to E shows different zooms of the stacked 13C qNMR spectra of the initial and the final points of the reaction carried out in a batch reactor with 20wt% Lgol feed. It can be observed that as reaction time increases, the peaks corresponding to Lgol (numbers 1 – 18 for threo (t) and erythro (e) forms) disappear, while those of tetrol (19 – 38 for (*S*,*S*) and (*S*,*R*) forms) increasingly appear. HTri (39 – 47) peaks seem to be present mostly at the final time (34.5h). However, its presence can be detected at least at around 40% conversion.

Table 7-1 shows the average of the peaks obtained from ^{13}C qNMR. The evolution of reactant to products can be monitored by this technique, although HPLC is preferred for convenience and quantitative application.

Table 7-1. ^{13}C qNMR average peak areas for experiment described in Figure 7-1 A through E.

Compound	**Time (h)**			
	1.07	3.15	8.13	34.5
	Conversion (%)			
	9%	19%	43%	91%
	Average area (standard error)			
t-Lgol	1684 (3%)	1486 (1%)	1078 (2%)	120 (4%)
e -Lgol	939 (3%)	859 (1%)	644 (2%)	93 (7%)
(*S*,*S*)-tetrol	125 (6%)	464 (3%)	1241 (1%)	3522 (1%)
(*S*,*R*)-tetrol	24 (82%)	203 (9%)	611 (1%)	2068 (3%)
HTri	0	0	43 (9%)	98 (8%)

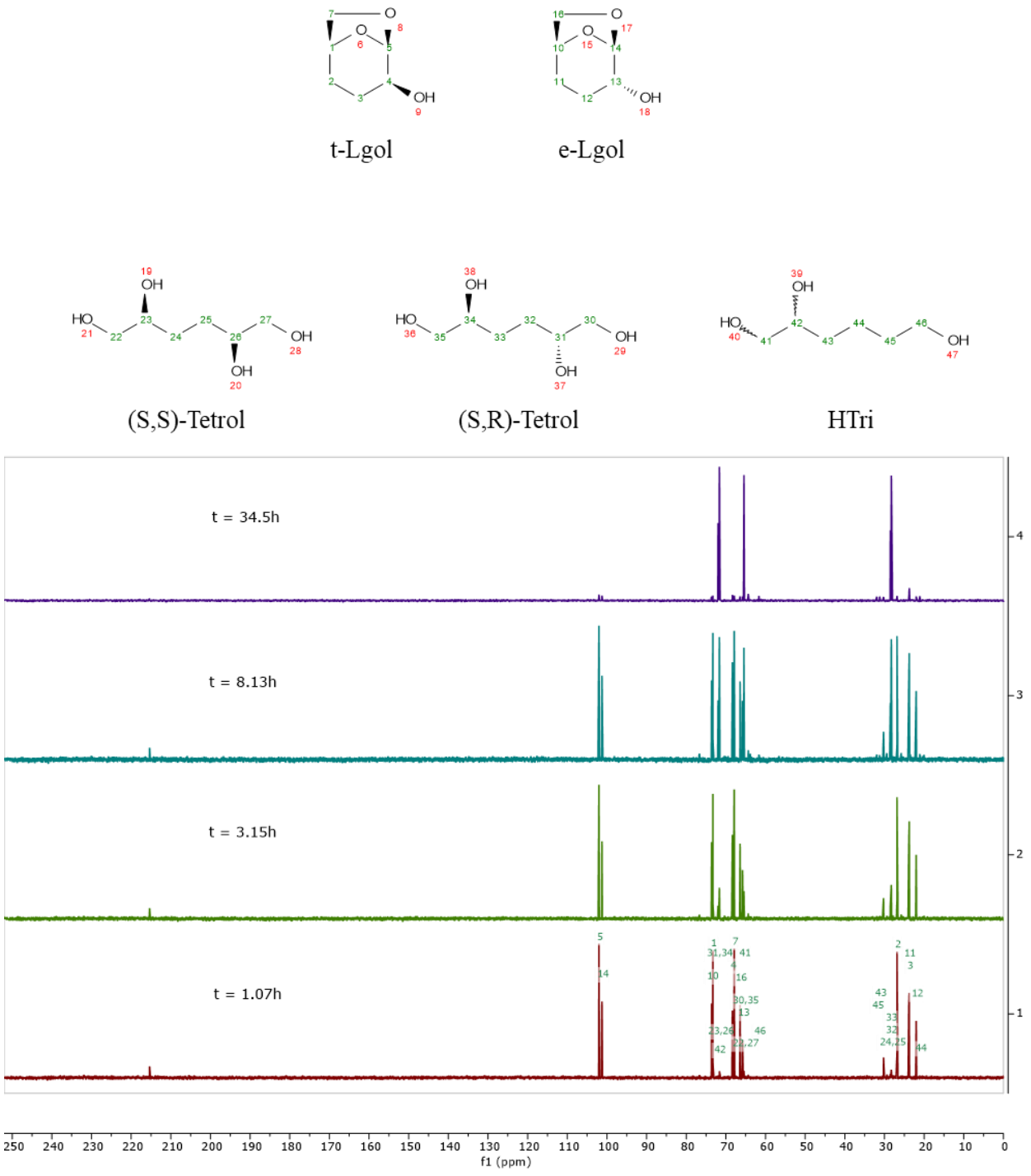

Figure 7-1A. Stacked ^{13}C qNMR describing reactants and products for aqueous Lgol hydrogenolysis - 0-250 ppm full view. **Conditions:** 120°C, 1000 psi H2, 40 mL 20wt% Lgol feed, 200 mg catalyst. For average peak values per compound NMR analysis, see details in Table 7-1 heading. Analysis details are as follows: MestreNova was used to process the spectra. Parameters are as described: 10%D2O/90%H2O solvent, NS = 112, AQ = 1s, TD1 = 30s. Referencing was done with water solvent 1H NMR peak at 4.69 ppm. Individual standards of each reactant were measured to assign.

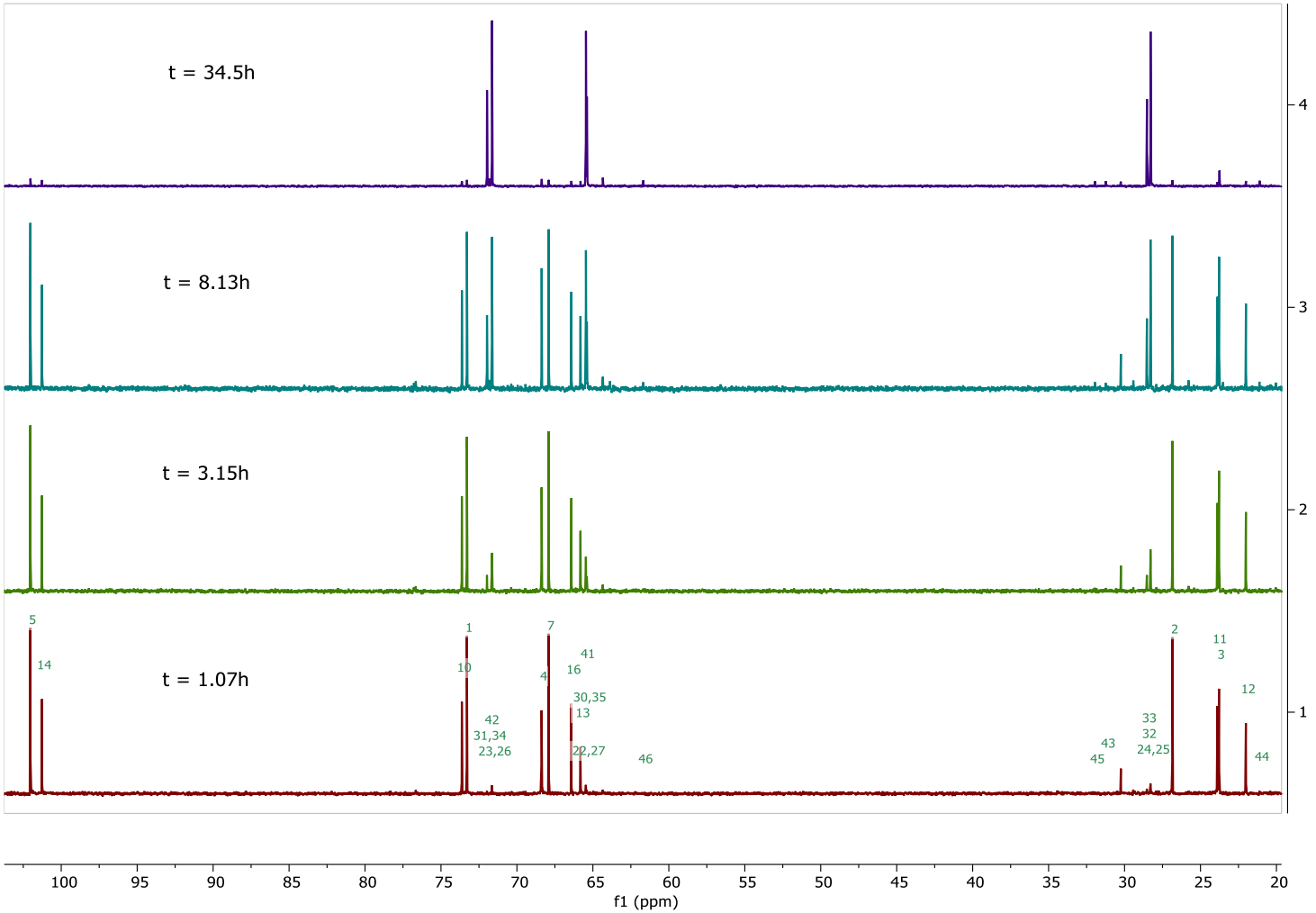

Figure 7-1B. Stacked ^{13}C qNMR describing reactants and products for aqueous Lgol hydrogenolysis – 20-110 ppm view. **Conditions:** 120°C, 1000 psi H_2, 40 mL 20wt% Lgol feed, 200 mg catalyst. For average peak values per compound NMR analysis, see details in Table 7-1 heading. Analysis details are as described in Figure 7-1A.

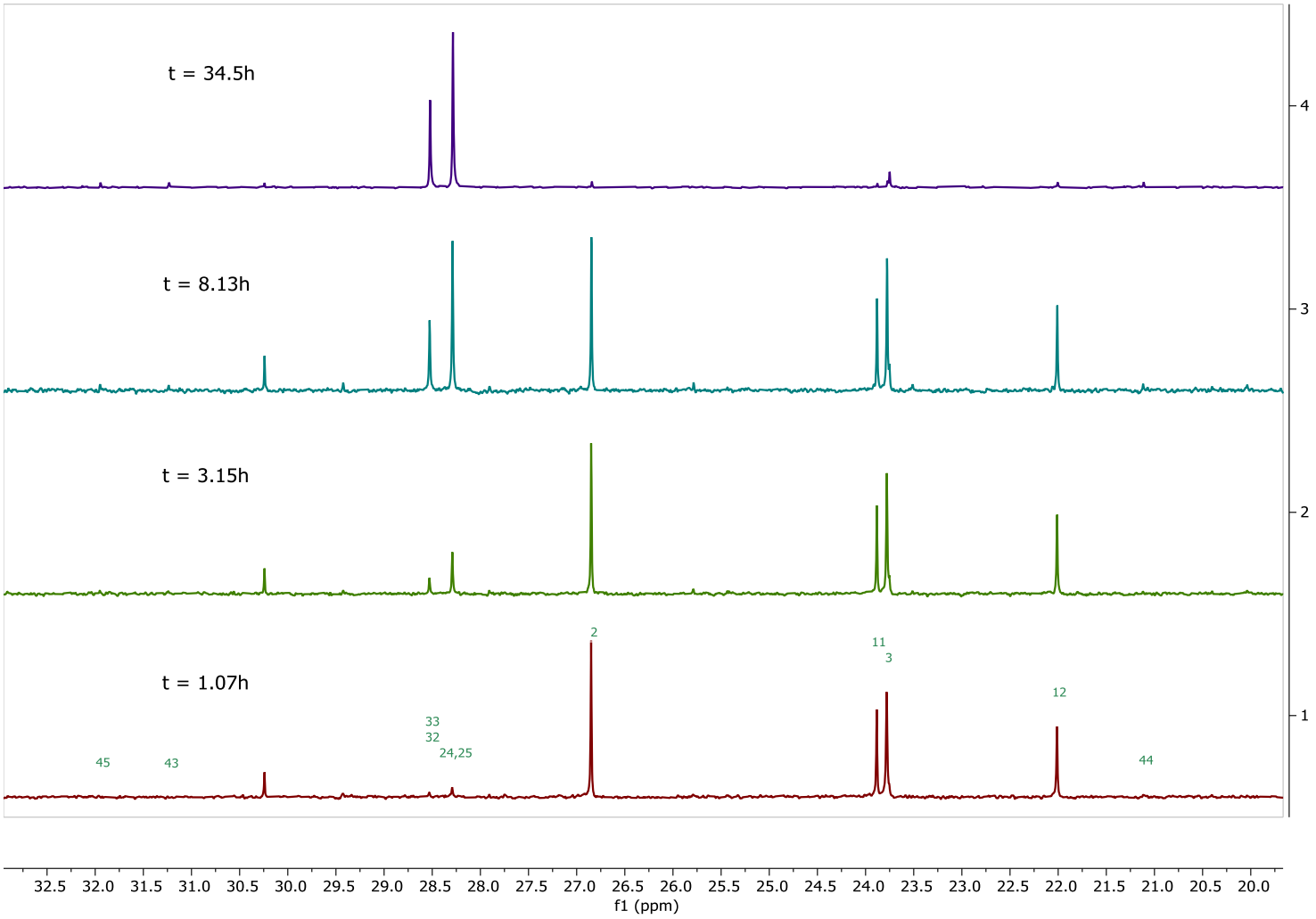

Figure 7-1C. Stacked ^{13}C qNMR describing reactants and products for aqueous Lgol hydrogenolysis - 20-35 ppm view. **Conditions:** 120°C, 1000 psi H_2, 40 mL 20wt% Lgol feed, 200 mg catalyst. For average peak values per compound NMR analysis, see details in Table 7-1 heading. Analysis details are as described in Figure 7-1A.

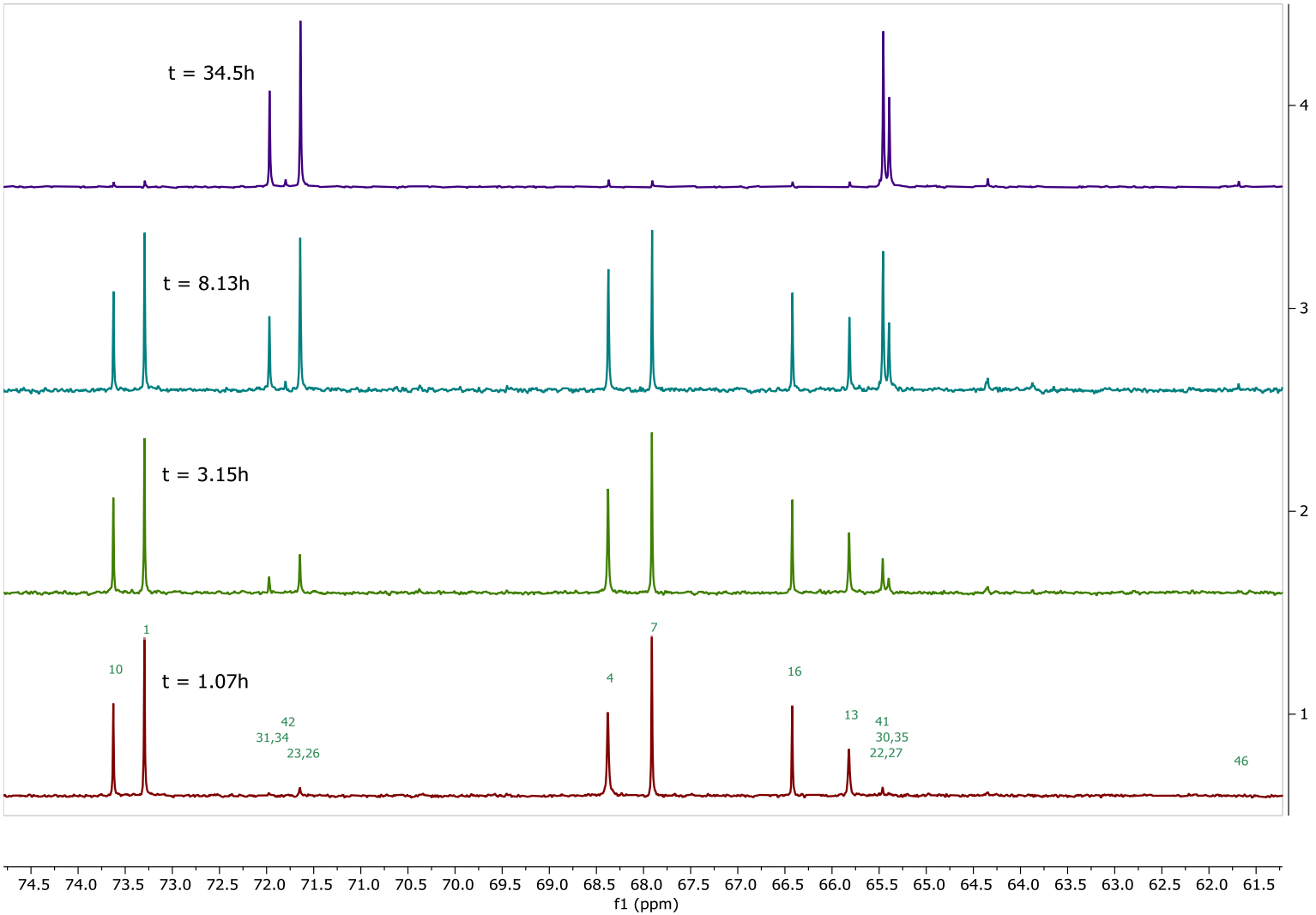

Figure 7-1D. Stacked ^{13}C qNMR describing reactants and products for aqueous Lgol hydrogenolysis - 61-75 ppm view. **Conditions:** 120°C, 1000 psi H_2, 40 mL 20wt% Lgol feed, 200 mg catalyst. For average peak values per compound NMR analysis, see details in Table 7-1 heading. Analysis details are as described in Figure 7-1A.

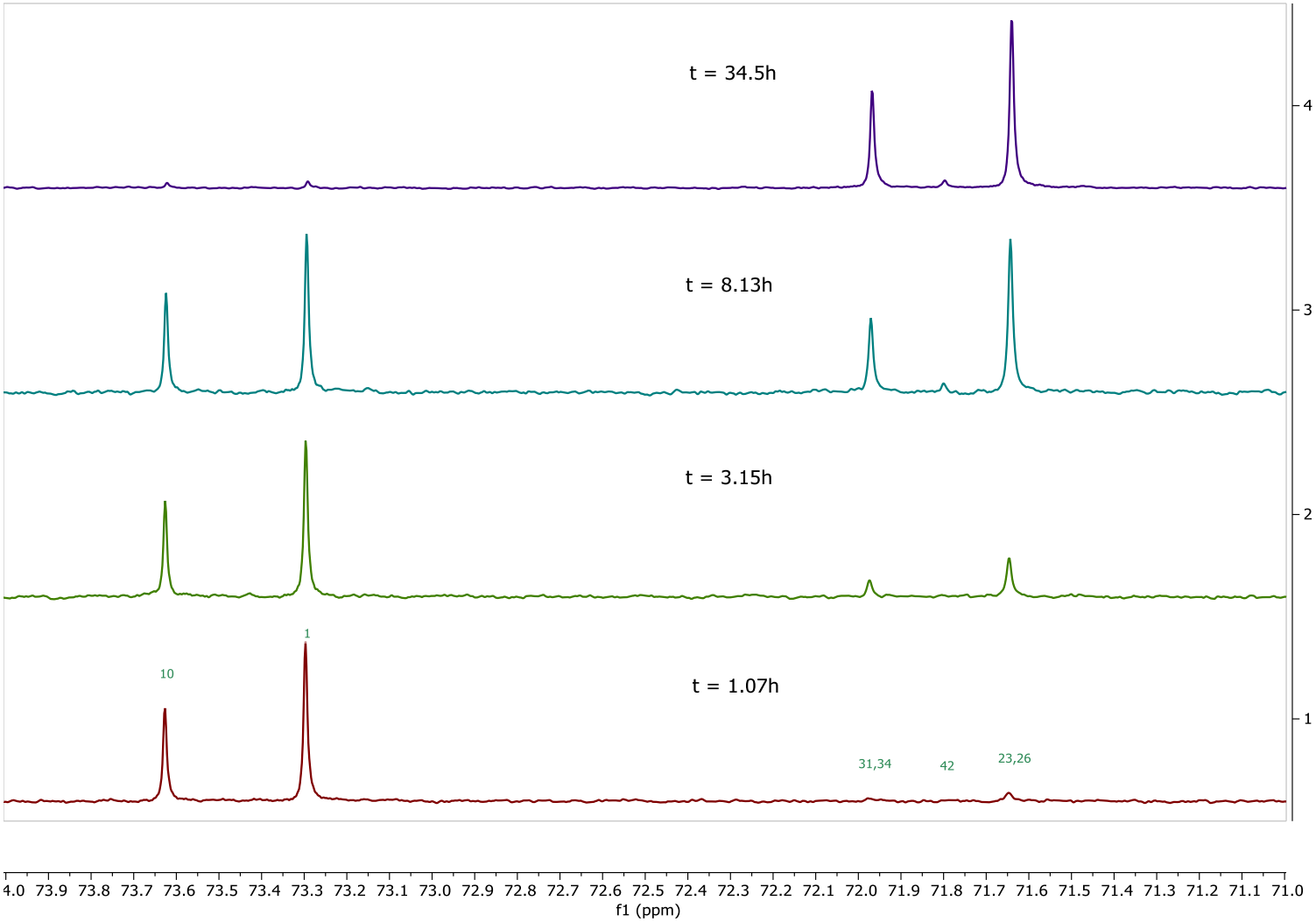

Figure 7-1E. Stacked ^{13}C qNMR describing reactants and products for aqueous Lgol hydrogenolysis - 71-74 ppm view. **Conditions:** 120°C, 1000 psi H_2, 40 mL 20wt% Lgol feed, 200 mg catalyst. For average peak values per compound NMR analysis, see details in Table 7-1 heading. Analysis details are as described in Figure 7-1A.

7.2.2. Quantitation by HPLC

Quantitative analysis was done by HPLC, which allows for the identification of all the compounds of interest. Both t-Lgol and e-Lgol forms peaks in HPLC are shown in Figure 7-2A. The peaks for all compounds are shown in the stacked chromatogram in Figure 7-2B obtained for the experiment using 20wt% Lgol aqueous feed. It can be observed that (*S*,*S*)/(*S*,*R*) tetrol and DDG completely overlap, DDM peak can be observed just beside the tetrol peak. HTri is directly observed at high conversion points (>70%). Its peak overlaps with the Lgol peaks as its concentration grows, as it can be observed with more detail in Figure 7-2c which illustrates the final data point for the 20wt% Lgol feed experiment. However, from ^{13}C qNMR we observed that HTri is present at conversions as low as 43%, but its concentration may not be high enough to be detected completely by HPLC or NMR at lower concentrations if present at lower conversion. Therefore, data deconvolution techniques were applied to have a better estimate of HTri selectivity by using Origin™ software. Particularly, the Lgol/HTri peaks between 19-23 minutes in the HPLC chromatogram were deconvoluted by using a gaussian function at data points at (or around) and after 40% conversion. An example of the result of such deconvolutions is shown in Figure 7-2d for the 34.5h data point of the 20wt% Lgol feed experiment (illustrated in Figure 7-2C). It can be observed that the Lgol and HTri peaks were successfully deconvoluted. Consequently, HTri yields and selectivities are evaluated by HPLC for all batch experiments by applying data deconvolution after 40% conversion following detection by the ^{13}C NMR analysis around this conversion.

We now note that the selectivity for HTri obtained by ^{13}C qNMR and HPLC after data deconvolution are similar. We observe that for the 20wt% Lgol feed, HTri selectivities were 5.2% and 2.2% at 43% and 91% Lgol conversion by HPLC, and 3.7% and 3.5% at those conversions

respectively by ^{13}C qNMR (as can be deduced from Table 7-1). Therefore, HTri seems to be consumed to form potentially degradation compounds since these are not observed. Nonetheless, quantitation at the start of the reaction is not possible for this product and this is crucial to be known to ascertain to what degree HTri is produced or not in a series pathway from tetrol, or if it can be produced through a parallel pathway, or both. There is literature to support either case[2–4].

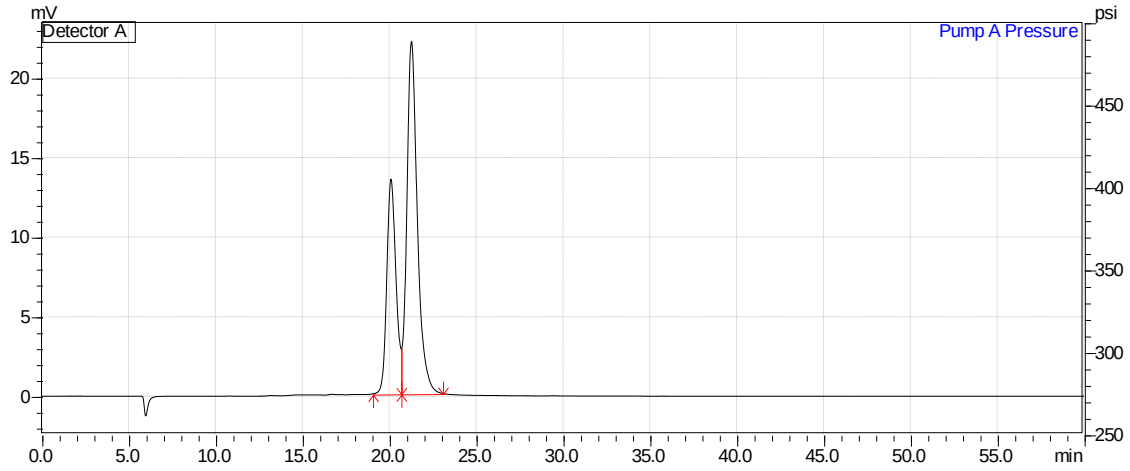

Figure 7-2A. Chromatogram for Lgol feed. Threo (t) Lgol is the largest peak, and erythro (e) Lgol is the smallest. 60 min method total time.

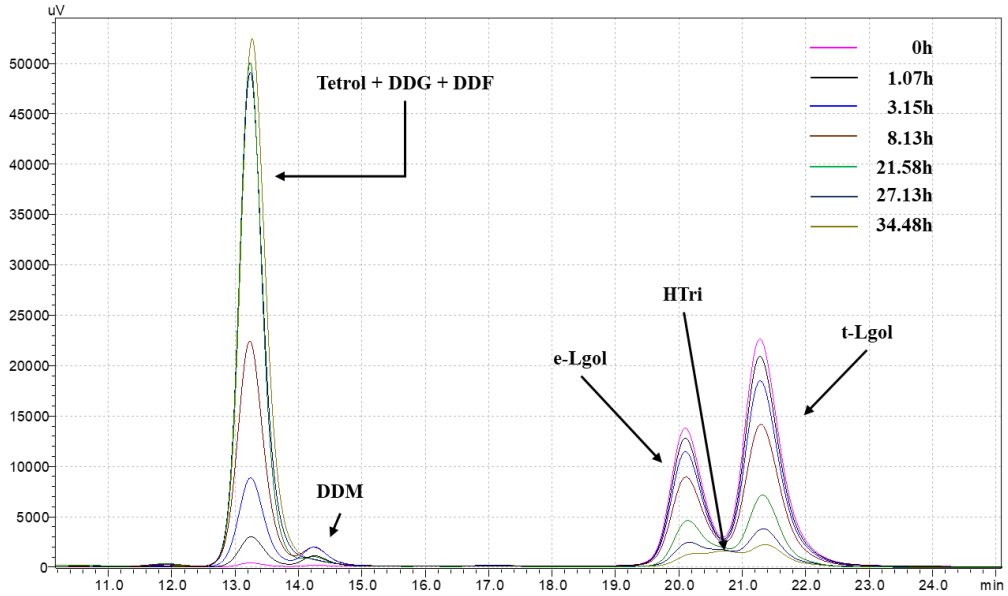

Figure 7-2B. Chromatogram stack for batch reaction with 20wt% Lgol feed. **Conditions:** 120℃, 1000 psi H_2, 40mL solution, 200 mg (10wt%)Pt(10wt%)WO_x/TiO_2 catalyst, 700 rpm. 60 min method total time.

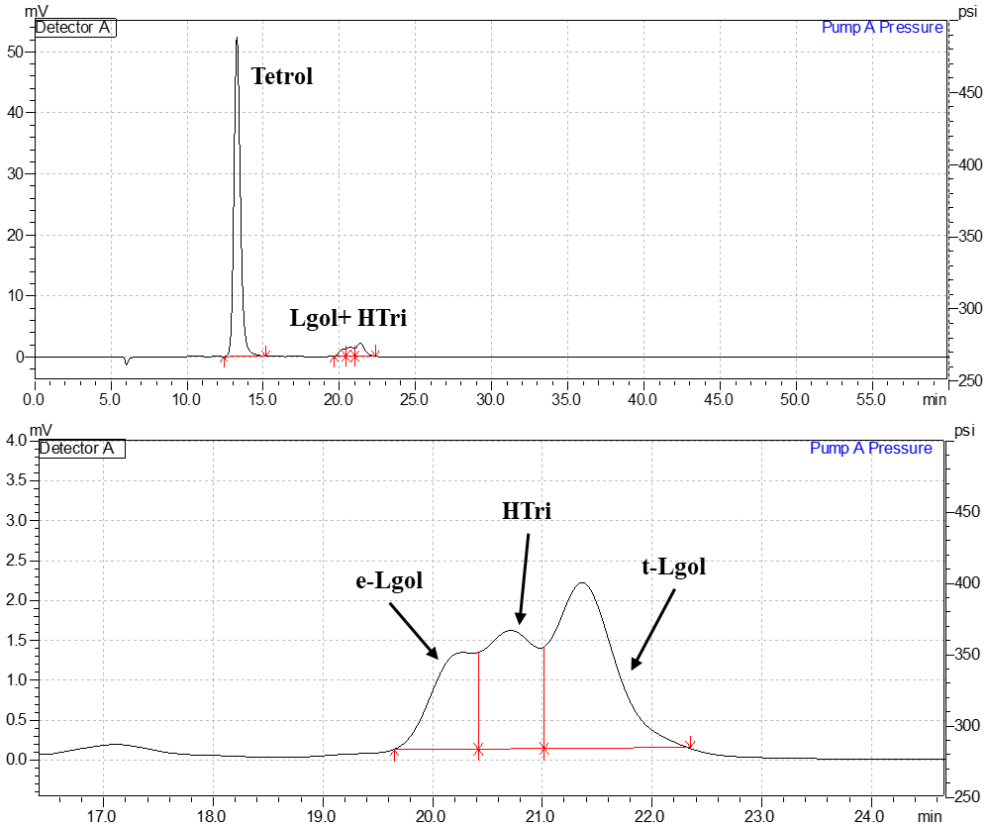

Figure 7-2C. Chromatogram stack for 34.48 h data point of batch reaction described in Figure 7-2B. Upper figure is for full chromatogram. Lower figure is chromatogram zoomed to observe Lgol and HTri peaks.

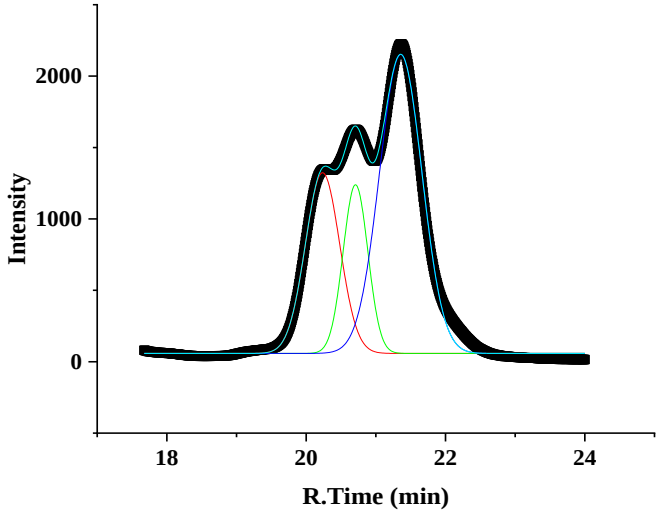

Figure 7-2D. Deconvoluted chromatogram for 34.48 h data point of batch reaction described in Figure 7-2C (lower). Red line is e-Lgol peak, green line is HTri, and blue line is t-Lgol peak.

7.2.3. First order Lgol model fitting comparisons

Reaction order for Lgol was determined by the integral method assuming a first order model. Figure 7-3 describes the first order fits made when products concentration and Lgol concentration (divided by initial Lgol concentration for convenience) are used. When the first order fit is done with the product concentrations (tetrol + precursors) compared to the reactant concentration (Lgol), very similar rate constants are obtained (0.069 vs 0.071 h^{-1} for product-based fit vs Lgol based fit), albeit the fit is more accurate for the reactant concentration since the products are difficult to deconvolute, and their sensitivities are assumed to be the same for simplicity, which may not be accurate enough at low conversion.

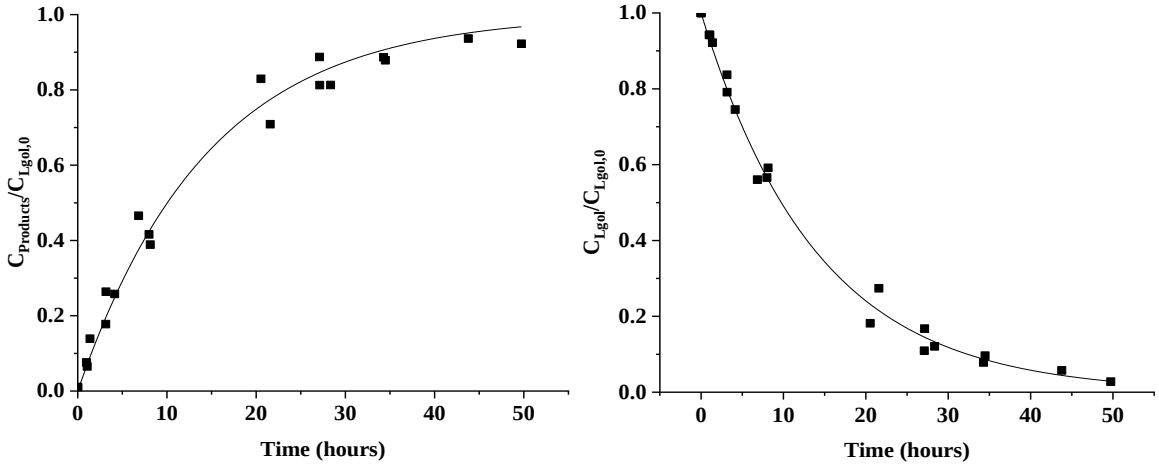

Figure 7-3. First order Lgol fit for data points obtained with 10, 20 and 30wt% Lgol feed aqueous solutions when products concentrations (tetrol + precursors) are used (left) compared to fit with Lgol concentration (right). Black squares describe data points, black line describes Lgol first order function fits, for fit of sum of product concentrations it is described by $\boldsymbol{C_{Products}/C_{Lgol,0} = 1 - \exp(-k*t)}$ where $k = 0.069 \pm 0.006$ h^{-1}, for Lgol concentration, the fit is described by $\boldsymbol{C_{Lgol}/C_{Lgol,0} = \exp(-k*t)}$ where $k = 0.071 \pm 0.004$ h^{-1}. Conditions: 120°C, 1000 psi H_2, 40 mL 20wt% Lgol feed, 200 mg catalyst.

7.2.4. Catalyst characterization data

This catalyst was synthesized according to the procedure outlined from He et al[2]. This batch, and that of He et al. were tested under similar conditions, and the conversion and product selectivities over time can be found in Figure 7-4. Both batches were found to perform very similarly in both conversion and selectivity. Hence the following characterization data (shown in Table 7-2 and Figure 7-5) is taken from the mentioned reference[2] for application to this paper too.

Table 7-2. Total acid concentration, Pt particle size, dispersion and W/Pt loadings for the 10wt%Pt(10wt%)WO_x/TiO_2 catalyst[2].

Acid concentration[a] (µmol/g)			**CO Uptake[d] (µmol/g)**	**Pt particle size (nm)**		**Metal loading (wt%)[e]**	
Total	Bronsted[b]	Lewis[b]		STEM	CO[d]	Pt	W
306	168	139	85	1.74±0.78	5.9	10.3	9.1

a. Determined by NH3-TPD; b. Determined by Pyridine-IR; c. Determined by STEM; d. Determined by CO-Chemisorption; e. Determined by ICP.

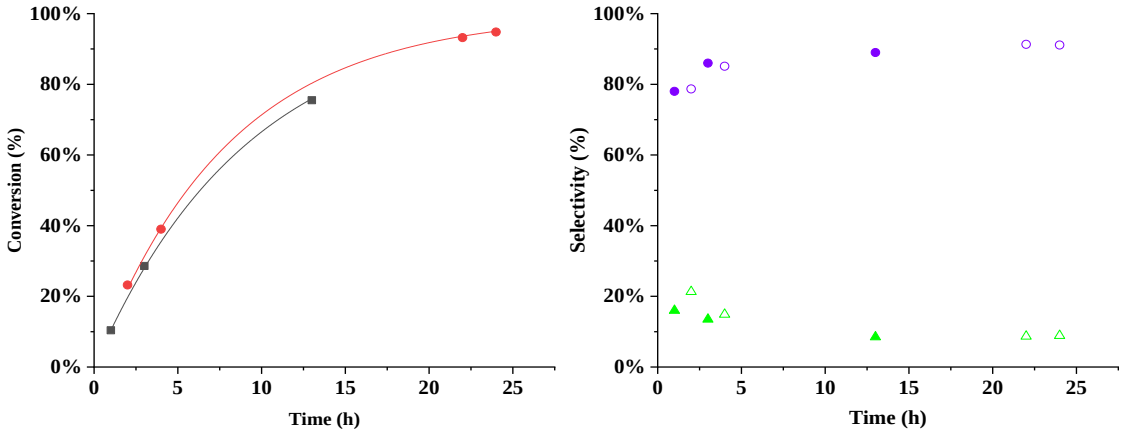

Figure 7-4. Left: Conversion vs time for He et al. (10wt%)Pt-(10wt%)WO_x/TiO_2 catalyst batch (■) compared to our catalyst batch (●). **Right:** Selectivity to tetrol + precursors (●, ○) and HTri (▲, △) over reaction time. For left figure, black and red lines are function fits in the form of ***x(%)* = 1 – exp(*k**t)***, where *x(%)* is conversion, *t* is time and *k* is a constant that was found to be 0.109 ± 0.002 h^{-1} for He et al. catalyst batch and 0.125 ± 0.004 h^{-1} for our catalyst batch. For right figure, filled markers are for He et al. catalyst batch performance, and empty markers are for our catalyst batch. **Conditions:** 120°C, 800 psi H_2, 20 mL 5% Lgol-W, 100 mg catalyst.

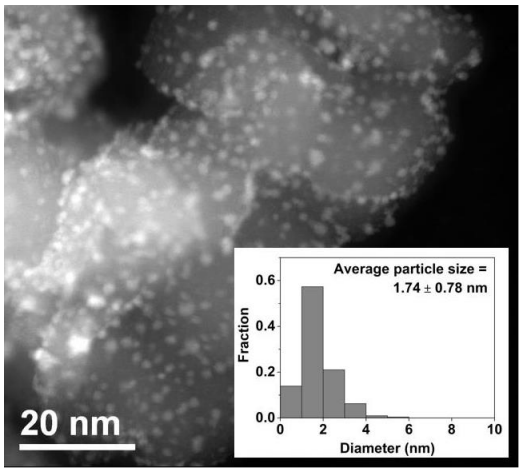

Figure 7-5. STEM picture of the 10wt%Pt(10wt%)WO_x/TiO_2 catalyst[2].

7.2.5. Carbon balances of batch experiments

Here we provide information on the carbon balances obtained at each data point on the batch experiments carried out to determine product selectivity with conversion and Lgol reaction orders. These can be observed in Figure 7-6. It can be observed that for the 10wt% Lgol feed experiment, C-balances over 100% were obtained especially at low reaction times. These may be caused individually or by a combination of the following factors: i) differences in response factors for HPLC between tetrol and intermediates DDG and DDF, since the factors of the intermediate compounds are assumed equal to that of the tetrol. Therefore, if the response factors of the latter two compounds are lower than tetrol, the overall concentration measured in the overlapping peak (see Figure 7-2B) is lower than calculated. ii) Evaporation of small amounts of water that result in slightly larger concentrations that the actual values. This would most likely occur with lower wt% aqueous solutions. We consider the first cause to be more likely than the second but acknowledge that the latter one might as well occur concurrently.

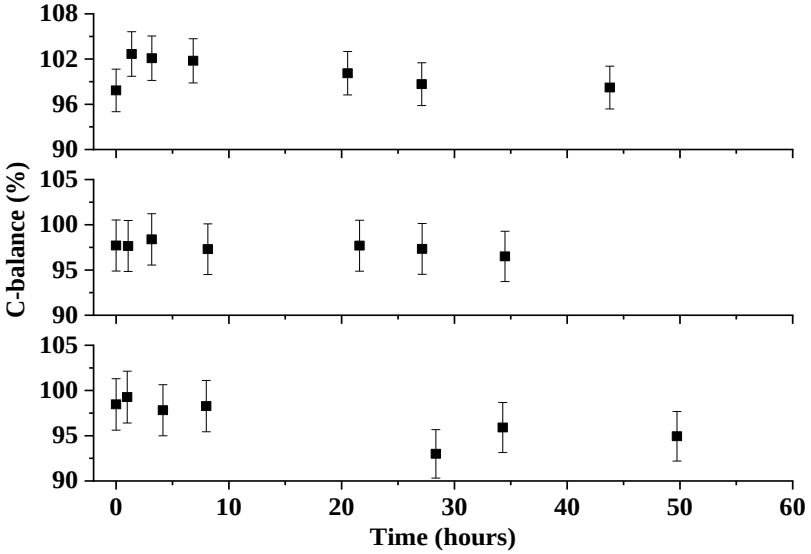

Figure 7-6. Carbon balance over time for Lgol hydrogenolysis experiments with aqueous feed concentrations of 10wt% (top), 20wt% (middle) and 30wt% (bottom). **Conditions:** 120°C, 1000 psi H_2, 40-45 mL Lgol feed, 200 mg Pt-WO_x/TiO_2 catalyst.

7.2.6. Catalyst reuse after regeneration procedure in flow reactor and characterization of fresh and spent material

The catalyst was calcined at 450°C for 4h (1°C/min) and re-tested again in the reaction at the same conditions. The result of the run is shown in Figure 7-7. It is observed that while the catalyst regained activity, recovery was not complete since it did not reach 88% at the start.

To investigate the causes of deactivation, we carried out ICP-OES of the product effluent of the first and second run. The results for the second run are shown in Figure 7-8. It is observed that the leaching rate values for the second run are relatively constant.

We also carried out ICP-OES to the fresh and spent catalyst in order to look for the relative change of Pt and W content compared to Ti. The results are summarized on Table 7-3. Essentially, a decrease of Pt and W relative to Ti is observed on the spent catalyst compared to the fresh material.

In order to determine changes in the crystalline structure of the material before and after reaction, X-ray diffraction analysis was carried out to the fresh calcined catalyst (at 400°C for 3h), the spent catalyst (after use in flow reactor) and the re-calcined spent catalyst (at 450°C for 4h) used in the flow experiments. The diffractograms can be observed in Figure 7-9. It can be observed that peaks for Pt, WO_3, and TiO_2 species appear. We also found that the spent catalyst showed peaks corresponding to $W_{18}O_{49}$ phase, which is consistent with a partial oxidation of W once re-exposed to air. This peak disappears upon re-calcination of spent material. The obtained full-width at height maximum for the largest peak is essentially the same for all diffractograms, indicating that there were no great changes in the bulk crystalline structure of the catalyst after reaction and recalcination.

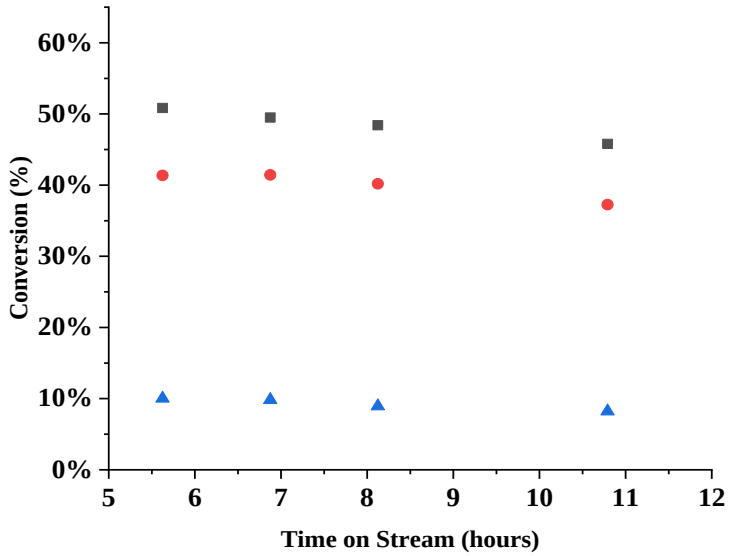

Figure 7-7. Conversion (■), and yields of tetrol + precursors (●) and HTri (▲) vs time on stream for Lgol hydrogenolysis in flow reactor using the regenerated 10wt%Pt-10wt%WO_x/TiO_2 catalyst. **Reaction conditions:** 30wt% aqueous Lgol feed, 120°C, 620 psi H_2, 500 mg catalyst, 20 μL/min liquid flow, 40 mL/min H_2 flow.

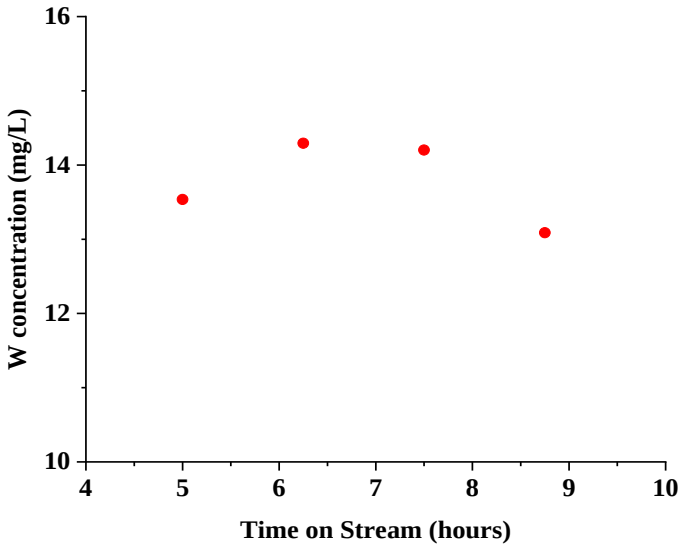

Figure 7-8. W-leached on re-run on flow reactor as shown in Figure 7-7.

Table 7-3. Ratios of Pt and W compared to Ti (fixed to 1) obtained by ICP-OES performed to fresh, spent and recalcined Pt-WO_x/TiO_2 materials studied in this work.

Material	Pt:W:Ti
Fresh Pt-WO_x/TiO_2	0.11:0.16:1
Spent Pt-WO_x/TiO_2	0.09:0.14:1
Recalcined Pt-WO_x/TiO_2	0.09:0.13:1

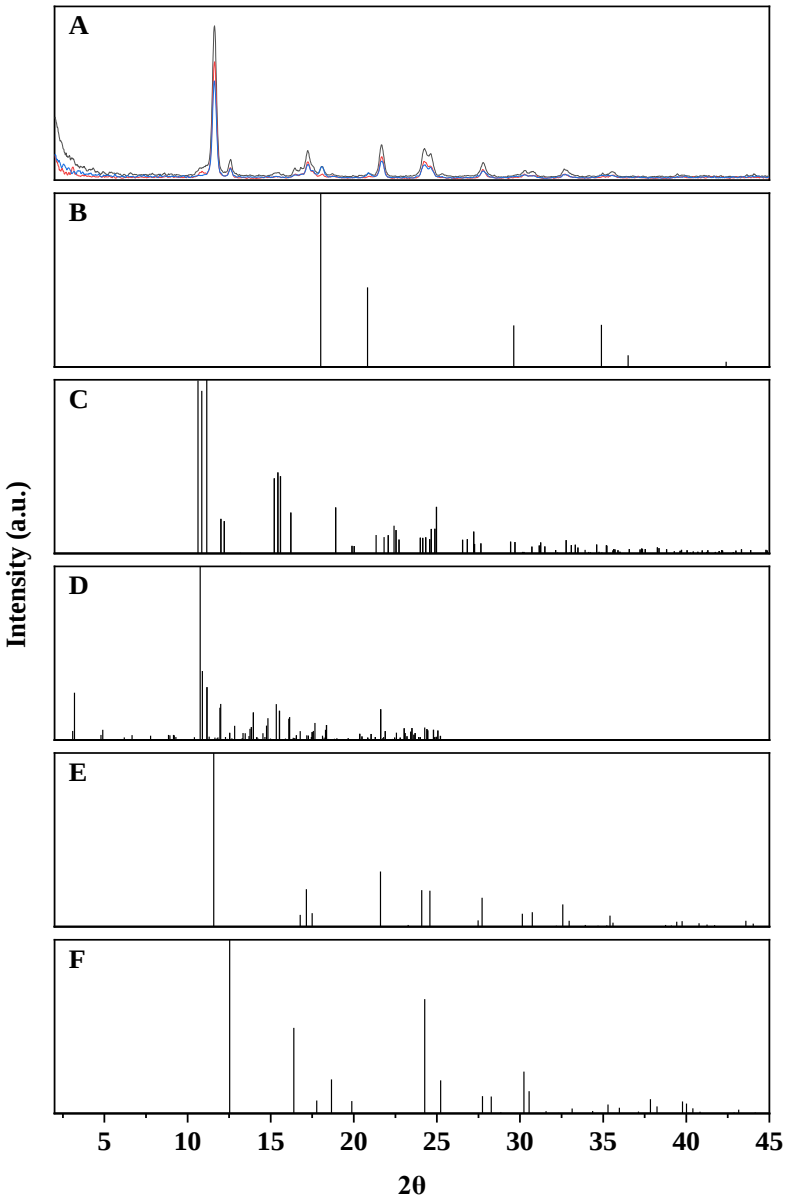

Figure 7-9. A) powder X-ray diffraction patterns of 10wt%Pt-10wt%WOx/TiO2 fresh calcined (black line), spent (red line) and re-calcined (blue line). Reference diffractograms of B) Pt, C) WO3, D) W18O49, E) TiO_2 (anatase), F) TiO_2 (rutile). Source is Mo Kα (0.707Å).

7.2.7. Stability of 5wt%Pt/SiO_2-Al_2O_3 in Lgol hydrogenolysis reaction in aqueous media

Part of the motivation of this work is to obtain a catalyst that is relatively stable in the Lgol hydrogenolysis reaction to tetrol in aqueous media. Previous related work has been done using

Pt/SiO_2-Al_2O_3 catalysts[1]. Figure 7-8 shows the result of one run with a 5wt%Pt catalyst using a low concentration aqueous Lgol feed. It is observed that deactivation proceeds with TOS. Moreover, this catalyst could not be regenerated with calcination procedures described in the current study.

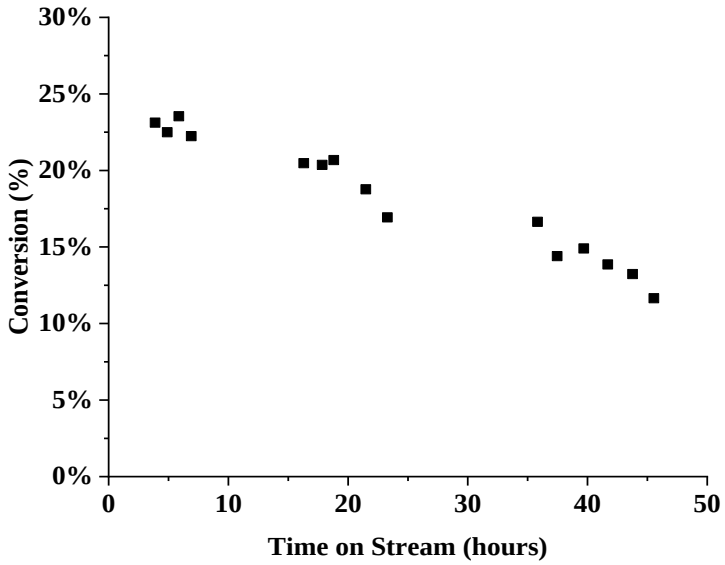

Figure 7-10. Conversion vs time on stream for Lgol hydrogenolysis in a flow reactor using the 5wt% Pt/SiO_2-Al_2O_3 catalyst. **Conditions:** 2 wt% aqueous Lgol feed, 130°C, 500 psi H_2, 200 mg catalyst, 30 μL/min feed flow, 6 mL/min H_2 flow.

7.3. Appendix for Chapter 3

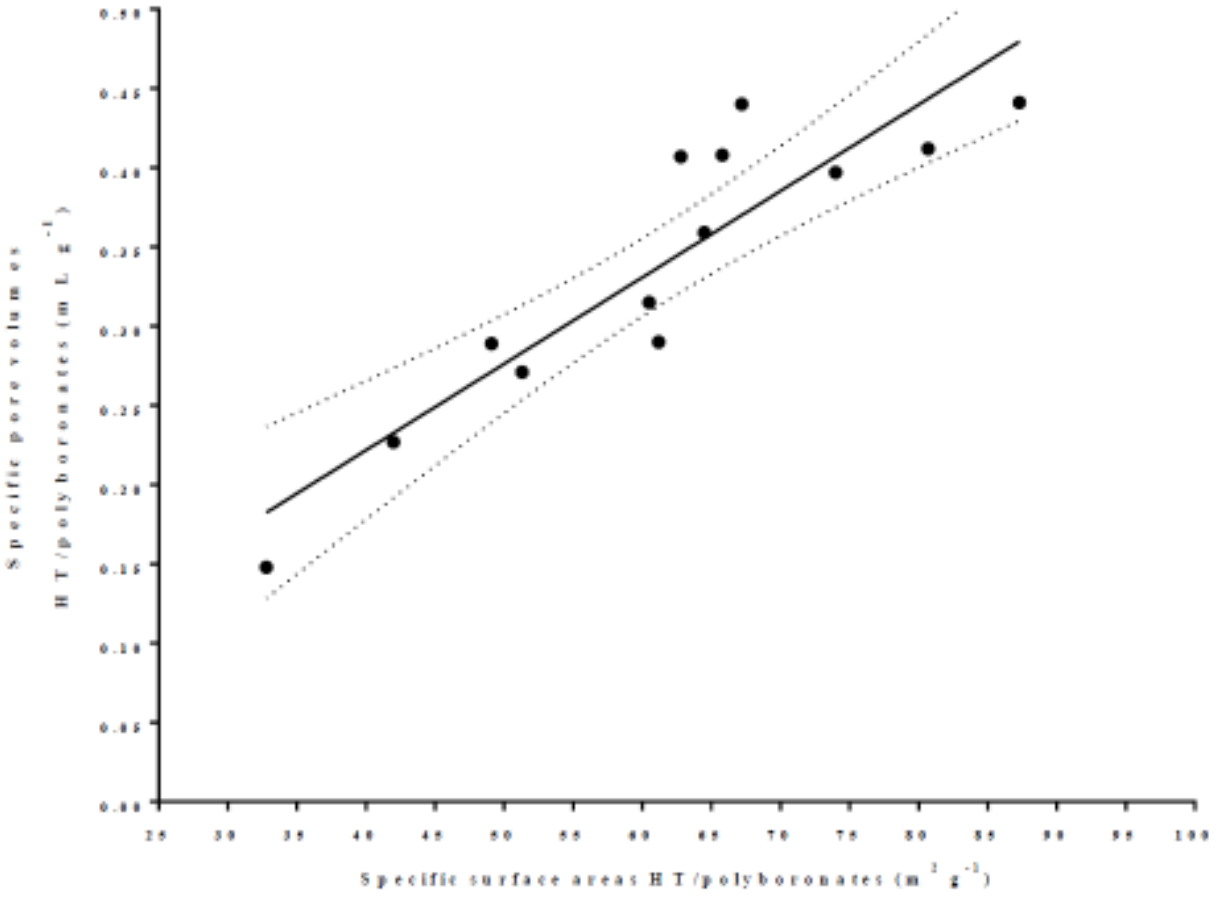

Figure 7-11. General plot of the specific surface areas of the HT/polyboronates vs their specific pore volumes. The dashed lines represent the 95% confidence intervals.

Characteristics of the fit:

Best-fit values	**± SE 95% Confidence Intervals**
Slope 0.00545 ± 0.0007669	Slope 0.003762 to 0.007138
Y-intercept 0.003719 ± 0.04843	Y-intercept -0.1029 to 0.1103
X-intercept -0.6823	X-intercept -29.09 to 14.53
1/slope 183.5	

Goodness of Fit	**Is slope significantly non-zero?**
R square 0.8211	F 50.5
Sy.x 0.03996	DFn, DFd 1, 11
	P value <0.0001
Equation Y = 0.00545*X + 0.003719 (S1)	Deviation from zero? Significant

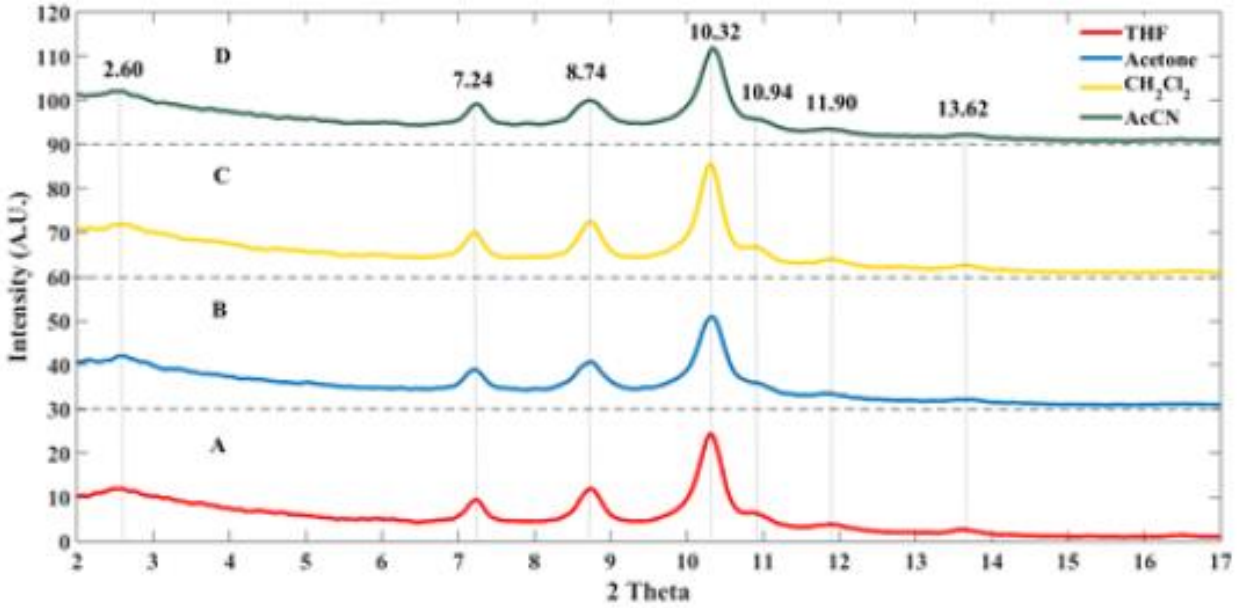

Figure 7-12. X-ray diffraction (XRD) patterns of HT/1,3-BDB (38% d.e.) for four different solvents.

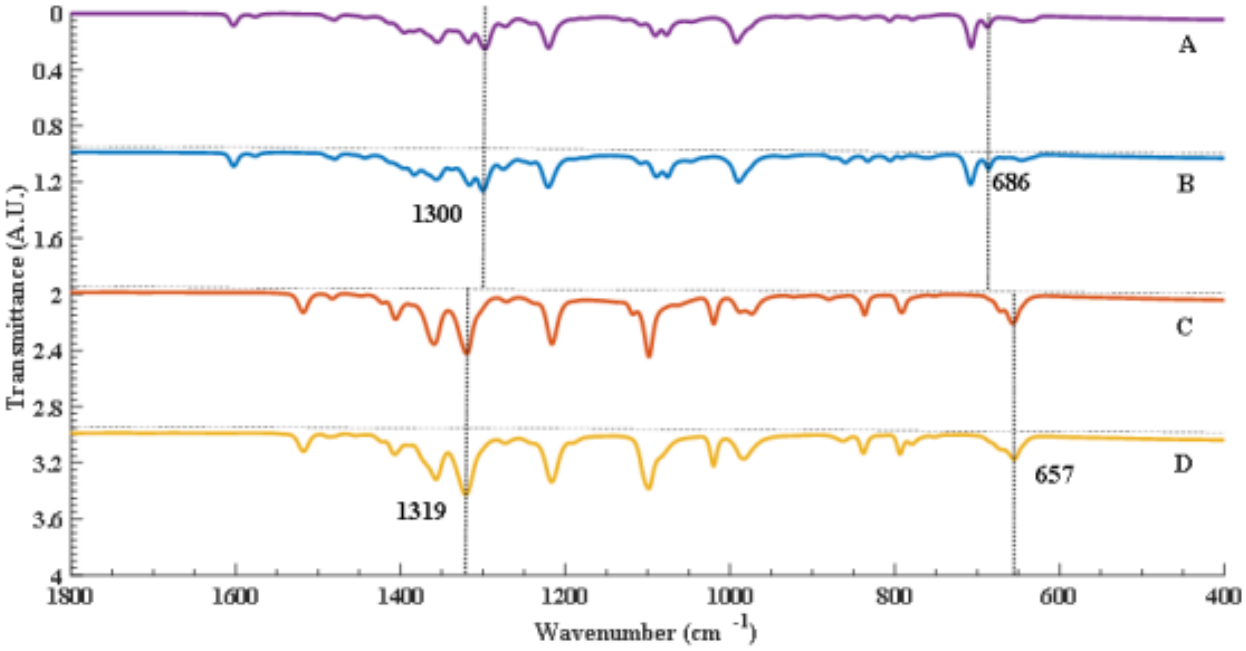

Figure 7-13A. Stacked FT-IR spectra of HT/1,3-BDB (A: 38% HT d.e. ; B: 98% HT d.e.) and HT/1,4-BDB (C: 38% HT d.e.; D: 98% HT d.e.).

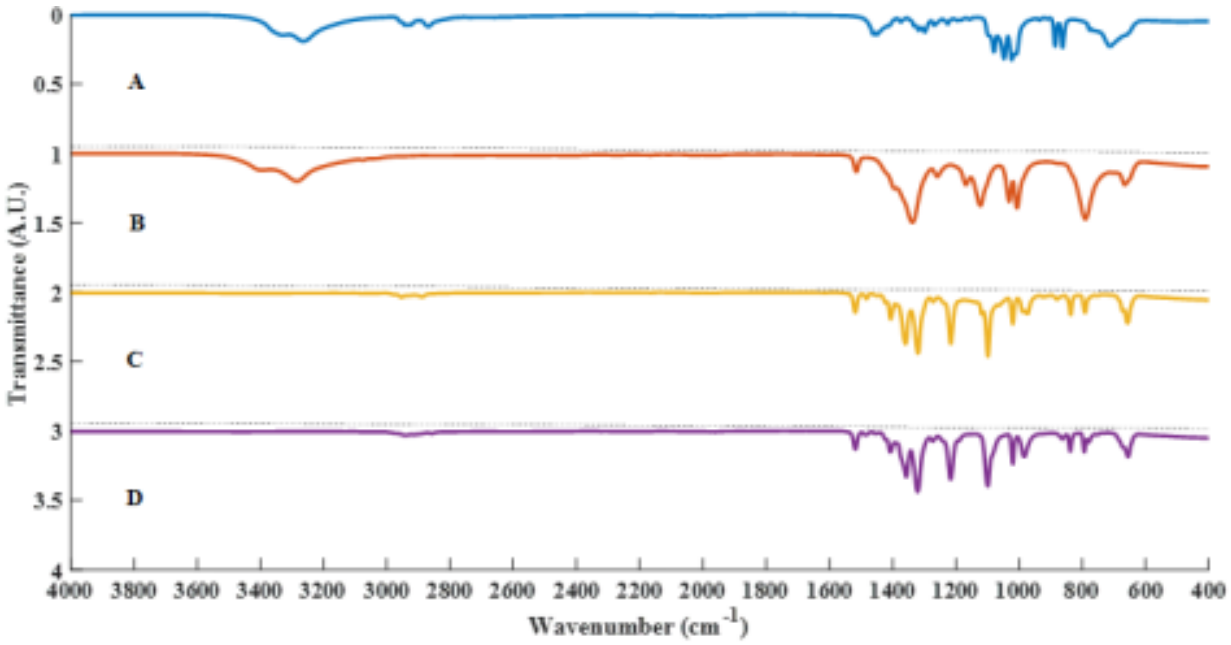

Figure 7-13B. Stacked FT-IR spectra of a range of HT/1,4-BDB polyboronates inclusive of the reference FT-IR spectra of HT and 1,4-BDB.

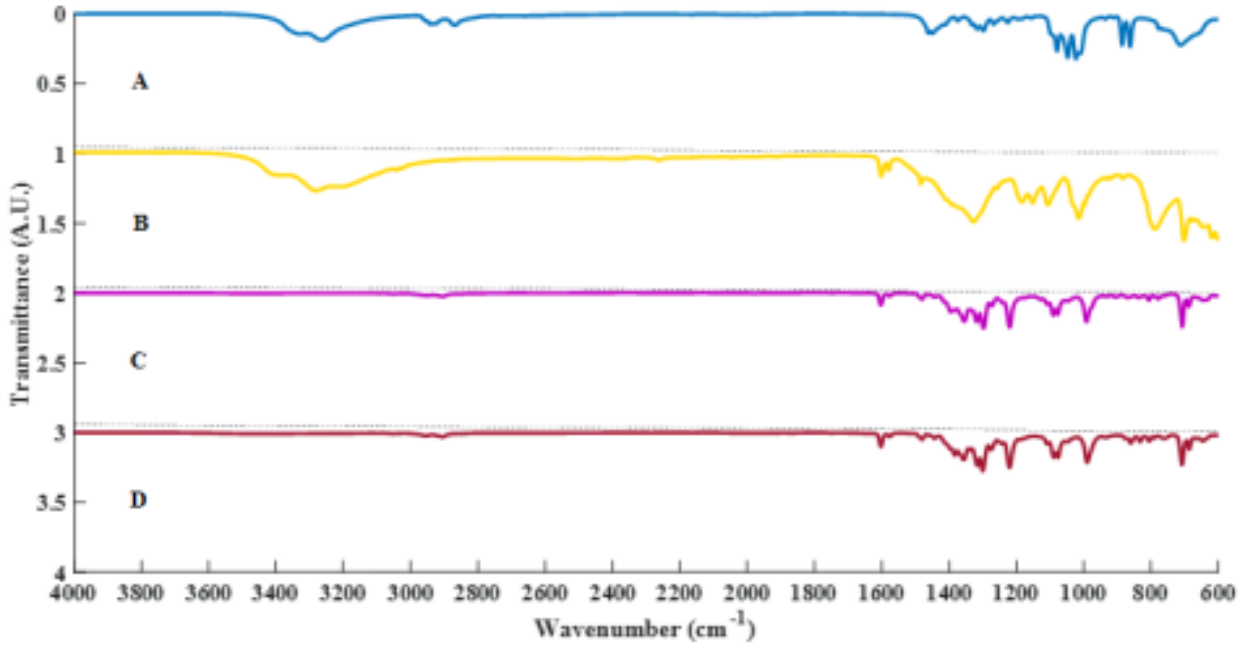

Figure 7-13C. FT-IR spectra of a range of HT/1,3-BDB polyboronates inclusive of the reference FT-IR spectra of HT and 1,3-BDB.

7.4. Appendix for Chapter 4

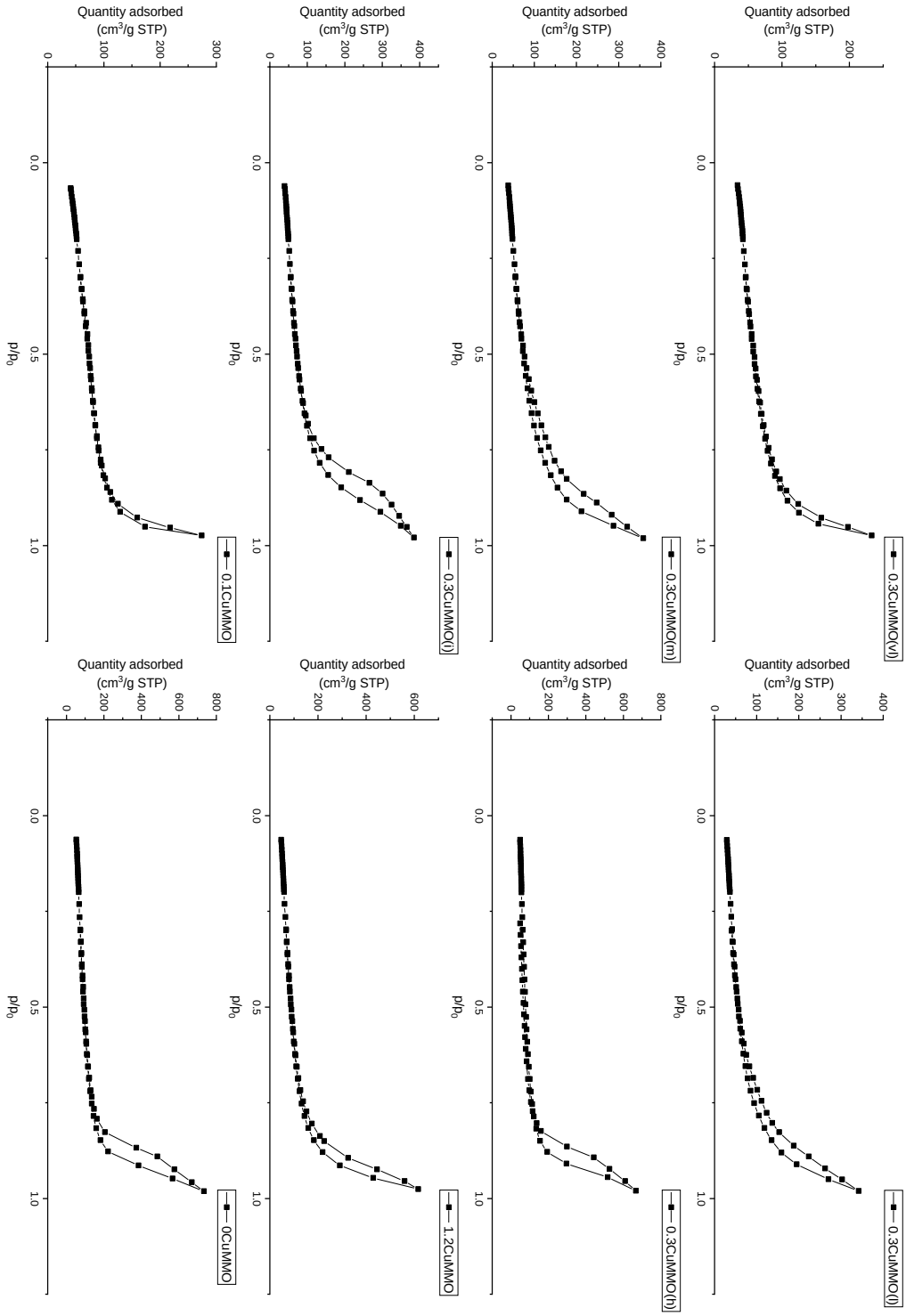

Figure 7-14. N_2 physisorption isotherms of CuMMO catalysts.

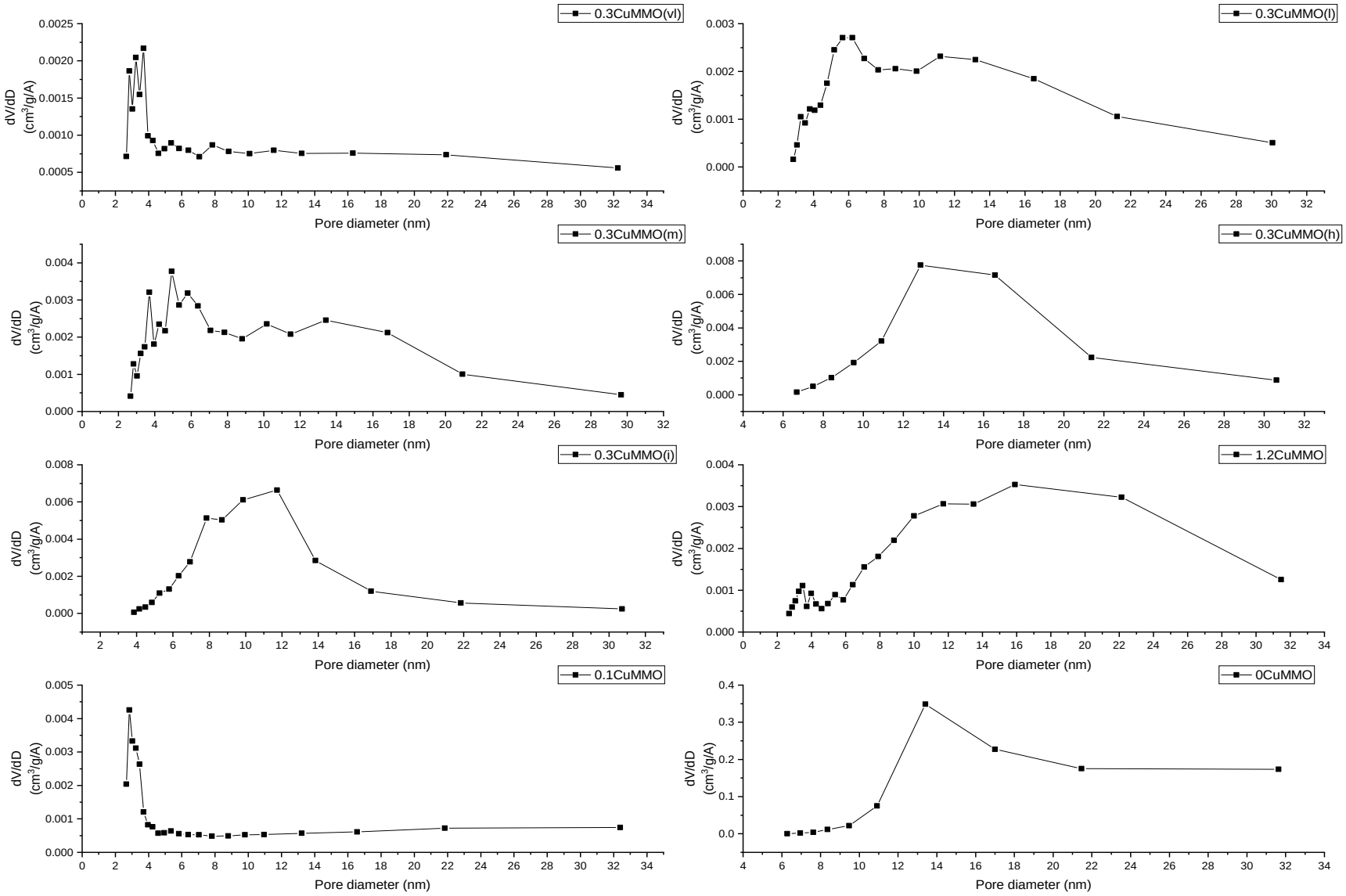

Figure 7-15. BJH Pore size distributions of CuMMO catalysts.

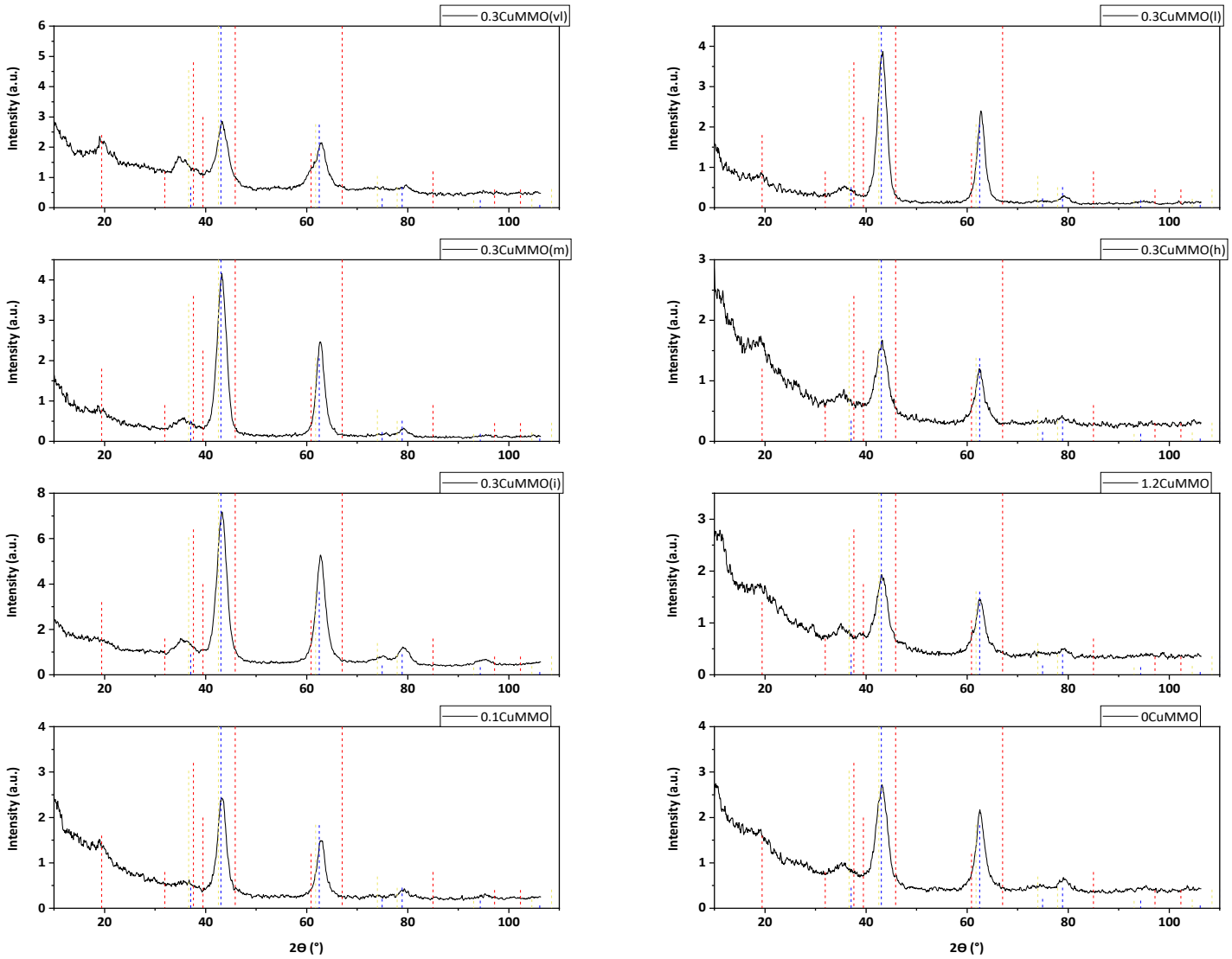

Figure 7-16. X-ray diffraction patterns of calcined CuMMO catalysts prepared for this work. Blue dashed lines denote MgO periclase peaks (PDF # 04-002-3057), red dashed line denotes Al_2O_3 peaks (PDF # 00-010-0425) and yellow dashed line denotes CuO peaks (PDF # 01-078-0428).

Table 7-4. Performance data of CuMMO catalysts at initial conversion for several Cu/Mg_xAlO_y (CuMMO) catalyst formulations.

	Catalyst	0.3CuMMO(vl)	0.3CuMMO(l)	0.3CuMMO(m)	0.3CuMMO(h)	0.3CuMMO(i)	1.2CuMMO	0.1CuMMO	0.1CuMMO(r)	0.1CuMMO(pm)
	Conversion (%)	48.63	50.92	54.19	54.10	42.92	44.38	45.36	46.91	39.42
	C-balance	92.53	95.36	97.52	95.58	94.75	93.59	97.36	93.62	97.01
	DFS(%)	75.92	80.56	75.60	77.38	74.66	50.38	80.51	78.30	84.22
Selectivities (%)	**Alcohol**	56.01	57.86	53.16	50.41	52.50	31.58	57.47	55.89	63.79
	Aldehyde	14.41	14.10	15.09	13.95	17.03	10.52	16.88	15.21	19.12
	Ester	8.74	20.02	21.46	24.80	23.31	41.87	18.23	16.99	9.34
	Ketone	2.43	3.74	3.74	5.87	4.00	12.10	3.57	3.83	2.36
	Ether	3.41	1.61	4.71	0.09	0.36	1.03	0.26	1.23	0.14
	Paraffin	0.43	0.02	0.08	0.09	0.06	0.17	0.06	0.42	0.02
	Olefin	10.04	0.60	0.42	0.33	0.27	0.26	0.28	0.65	0.40
	Aromatic	0.51	0.00	0.00	0.00	0.00	0.00	0.00	0.95	0.48
	Acetals	1.52	1.08	0.97	1.49	1.70	1.36	1.89	2.27	2.03
	Unidentified	2.51	0.97	0.36	2.97	0.77	1.11	1.36	2.56	2.32

Conditions: 325°C, 300 psi, 6.56 h^{-1}, 1.00 g catalyst, 0.139 mL/min EtOH, 18.1 mL/min H_2, p_{EtOH}:p_{H2} = 4.

Table 7-5. Detailed product selectivity of 0.3CuMMO(vl)catalyst.

# C	Total	Alcohols			Aldehydes	Ketones	Ethers	Esters	Olefins	Aromatics	Paraffins	Hemiacetals and acetals
		Primary Linear	Primary Branched	Secondary								
1	0.54	0.52	0.00	0.00	0.00	0.00	0.00	0.00	0.00	0.00	0.01	0.00
2	4.34	0.00	0.00	0.00	4.25	0.00	0.00	0.00	0.07	0.00	0.02	0.00
3	1.22	0.00	0.00	0.38	0.00	0.17	0.00	0.65	0.02	0.00	0.00	0.00
4	56.98	38.83	0.00	0.25	5.86	1.05	1.30	3.13	5.07	0.00	0.00	1.50
5	2.51	0.00	0.00	0.00	2.27	0.10	0.00	0.00	0.07	0.00	0.07	0.00
6	20.15	8.86	2.48	0.00	0.84	0.19	0.53	2.65	4.60	0.00	0.00	0.00
7	0.77	0.00	0.00	0.00	0.00	0.50	0.00	0.10	0.17	0.00	0.00	0.00
8	7.89	2.16	1.11	0.18	1.19	0.00	1.57	1.21	0.03	0.32	0.12	0.00
9	0.46	0.00	0.00	0.00	0.00	0.28	0.00	0.00	0.00	0.18	0.00	0.00
10	1.86	0.57	0.46	0.00	0.00	0.00	0.00	0.59	0.00	0.00	0.21	0.02
11	0.11	0.00	0.00	0.00	0.00	0.11	0.00	0.00	0.00	0.00	0.00	0.00
12	0.62	0.17	0.03	0.00	0.00	0.05	0.00	0.37	0.00	0.00	0.00	0.00
13	0.00	0.00	0.00	0.00	0.00	0.00	0.00	0.00	0.00	0.00	0.00	0.00
14	0.04	0.00	0.00	0.00	0.00	0.00	0.00	0.04	0.00	0.00	0.00	0.00
Total	97.49	51.11	4.09	0.81	14.41	2.43	3.41	8.74	10.04	0.51	0.43	1.52

Conditions: 325°C, 300 psi, 6.56 h^{-1}, 1.00 g catalyst, 0.139 mL/min EtOH, 18.1 mL/min H_2, p_{EtOH}:p_{H2} = 4.

Table 7-6. Selectivity to species of 0.3CuMMO(l) catalyst.

# C	Total	Alcohols			Aldehydes	Ketones	Ethers	Esters	Olefins	Aromatics	Paraffins	Hemiacetals and acetals
		Primary Linear	Primary Branched	Secondary								
1	0.99	0.98	0.00	0.00	0.00	0.00	0.00	0.00	0.00	0.00	0.01	0.00
2	3.26	0.00	0.00	0.00	3.22	0.00	0.00	0.00	0.03	0.00	0.02	0.00
3	1.75	0.00	0.00	0.01	0.00	1.74	0.00	0.00	0.00	0.00	0.00	0.00
4	61.35	42.97	0.00	0.24	6.41	0.72	0.16	9.36	0.56	0.00	0.00	0.93
5	2.31	0.00	0.00	0.00	1.96	0.33	0.00	0.00	0.03	0.00	0.00	0.00
6	19.14	7.98	2.38	0.00	1.98	0.00	0.00	6.79	0.00	0.00	0.00	0.00
7	0.73	0.00	0.00	0.07	0.00	0.66	0.00	0.00	0.00	0.00	0.00	0.00
8	5.58	1.76	0.66	0.00	0.52	0.00	0.00	2.63	0.00	0.00	0.00	0.00
9	0.19	0.00	0.00	0.00	0.00	0.19	0.00	0.00	0.00	0.00	0.00	0.00
10	1.44	0.39	0.29	0.00	0.00	0.00	0.00	0.76	0.00	0.00	0.00	0.00
11	0.07	0.00	0.00	0.00	0.00	0.07	0.00	0.00	0.00	0.00	0.00	0.00
12	0.60	0.13	0.00	0.00	0.00	0.00	0.00	0.32	0.00	0.00	0.00	0.15
13	0.02	0.00	0.00	0.00	0.00	0.02	0.00	0.00	0.00	0.00	0.00	0.00
14	0.16	0.00	0.00	0.00	0.00	0.00	0.00	0.16	0.00	0.00	0.00	0.00
Total	97.61	54.21	3.33	0.32	14.10	3.74	0.16	20.02	0.63	0.00	0.03	1.08

Conditions: 325°C, 300 psi, 6.56 h^{-1}, 1.00 g catalyst, 0.139 mL/min EtOH, 18.1 mL/min H_2, p_{EtOH}:p_{H2} = 4.

Table 7-7. Detailed product selectivity of 0.3CuMMO(m) catalyst.

# C	Total	Alcohols			Aldehydes	Ketones	Ethers	Esters	Olefins	Aromatics	Paraffins	Hemiacetals and acetals
		Primary Linear	Primary Branched	Secondary								
1	2.88	2.85	0.00	0.00	0.00	0.00	0.00	0.00	0.00	0.00	0.03	0.00
2	8.36	0.00	0.00	0.00	3.75	0.00	4.56*	0.00	0.02	0.00	0.03	0.00
3	2.24	0.00	0.00	0.42	0.00	1.78	0.00	0.03	0.02	0.00	0.00	0.00
4	58.64	38.33	0.00	0.23	8.72	0.83	0.15	9.31	0.20	0.00	0.02	0.85
5	0.49	0.00	0.00	0.00	0.00	0.36	0.00	0.00	0.13	0.00	0.00	0.00
6	18.29	6.57	1.88	0.00	2.16	0.00	0.00	7.65	0.04	0.00	0.00	0.00
7	0.92	0.00	0.00	0.28	0.00	0.64	0.00	0.00	0.00	0.00	0.00	0.00
8	5.39	1.25	0.53	0.05	0.46	0.00	0.00	3.10	0.01	0.00	0.00	0.00
9	0.21	0.00	0.00	0.21	0.00	0.00	0.00	0.00	0.00	0.00	0.00	0.00
10	1.48	0.27	0.24	0.00	0.00	0.00	0.00	0.97	0.00	0.00	0.00	0.00
11	0.08	0.00	0.00	0.00	0.00	0.08	0.00	0.00	0.00	0.00	0.00	0.00
12	0.52	0.07	0.00	0.00	0.00	0.02	0.00	0.30	0.00	0.00	0.00	0.13
13	0.04	0.00	0.00	0.00	0.00	0.04	0.00	0.00	0.00	0.00	0.00	0.00
14	0.11	0.00	0.00	0.00	0.00	0.00	0.00	0.11	0.00	0.00	0.00	0.00
Total	99.64	49.34	2.64	1.18	15.09	3.74	4.71	21.46	0.42	0.00	0.08	0.97

Conditions: 325°C, 300 psi, 6.56 h^{-1}, 1.00 g catalyst, 0.139 mL/min EtOH, 18.1 mL/min H_2, p_{EtOH}:p_{H2} = 4.

* This compound corresponds to ethylene oxide. Hence, we do not consider it a dehydration product.

Table 7-8. Detailed product selectivity of 0.3CuMMO(h) catalyst.

# C	Total	Alcohols			Aldehydes	Ketones	Ethers	Olefins	Esters	Aromatics	Paraffins	Hemiacetals and acetals
		Primary Linear	Primary Branched	Secondary								
1	0.91	0.88	0.00	0.00	0.00	0.00	0.00	0.00	0.00	0.00	0.03	0.00
2	4.64	0.00	0.00	0.00	4.59	0.00	0.00	0.02	0.00	0.00	0.03	0.00
3	2.39	0.00	0.00	0.52	0.00	1.79	0.00	0.01	0.07	0.00	0.00	0.00
4	55.16	36.64	0.00	0.31	5.69	0.88	0.09	0.22	10.01	0.00	0.03	1.28
5	3.46	0.00	0.00	0.00	1.65	1.78	0.00	0.03	0.00	0.00	0.00	0.00
6	18.76	6.72	2.01	0.00	1.59	0.00	0.00	0.02	8.41	0.00	0.00	0.00
7	0.90	0.00	0.00	0.21	0.00	0.70	0.00	0.00	0.00	0.00	0.00	0.00
8	6.61	1.46	0.67	0.08	0.42	0.00	0.00	0.02	3.93	0.00	0.00	0.02
9	0.45	0.00	0.00	0.00	0.00	0.45	0.00	0.00	0.00	0.00	0.00	0.00
10	2.15	0.39	0.31	0.00	0.00	0.00	0.00	0.00	1.27	0.00	0.00	0.18
11	0.03	0.00	0.00	0.00	0.00	0.03	0.00	0.00	0.00	0.00	0.00	0.00
12	1.03	0.14	0.07	0.00	0.00	0.10	0.00	0.00	0.72	0.00	0.00	0.00
13	0.14	0.00	0.00	0.00	0.00	0.14	0.00	0.00	0.00	0.00	0.00	0.00
14	0.40	0.00	0.00	0.00	0.00	0.00	0.00	0.00	0.40	0.00	0.00	0.00
Total	97.02	46.23	3.06	1.12	13.95	5.87	0.09	0.33	24.80	0.00	0.09	1.48

Conditions: 325°C, 300 psi, 6.56 h^{-1}, 1.00 g catalyst, 0.139 mL/min EtOH, 18.1 mL/min H_2, p_{EtOH}:p_{H2} = 4.

Table 7-9. Detailed product selectivity of 0.3CuMMO(i) catalyst.

# C	Total	Alcohols			Aldehydes	Ketones	Ethers	Esters	Olefins	Aromatics	Paraffins	Hemiacetals and acetals
		Primary Linear	Primary Branched	Secondary								
1	1.07	1.04	0.00	0.00	0.00	0.00	0.00	0.00	0.00	0.00	0.02	0.00
2	6.68	0.00	0.00	0.00	6.62	0.00	0.00	0.00	0.04	0.00	0.02	0.00
3	2.50	0.00	0.00	0.52	0.00	1.96	0.00	0.00	0.02	0.00	0.00	0.00
4	62.58	40.96	0.00	0.36	5.91	0.92	0.15	12.88	0.19	0.00	0.02	1.19
5	3.43	0.00	0.00	0.00	3.03	0.36	0.00	0.03	0.01	0.00	0.00	0.00
6	16.33	6.02	1.64	0.00	1.17	0.00	0.22	7.27	0.01	0.00	0.00	0.00
7	0.68	0.00	0.00	0.06	0.00	0.61	0.00	0.00	0.00	0.00	0.00	0.00
8	4.43	1.02	0.37	0.00	0.29	0.00	0.00	2.44	0.00	0.00	0.00	0.31
9	0.13	0.00	0.00	0.13	0.00	0.00	0.00	0.00	0.00	0.00	0.00	0.00
10	1.04	0.21	0.13	0.00	0.00	0.00	0.00	0.62	0.00	0.00	0.00	0.09
11	0.15	0.00	0.00	0.00	0.00	0.15	0.00	0.00	0.00	0.00	0.00	0.00
12	0.23	0.05	0.00	0.00	0.00	0.00	0.00	0.07	0.00	0.00	0.00	0.10
13	0.00	0.00	0.00	0.00	0.00	0.00	0.00	0.00	0.00	0.00	0.00	0.00
14	0.00	0.00	0.00	0.00	0.00	0.00	0.00	0.00	0.00	0.00	0.00	0.00
Total	99.24	49.30	2.14	1.06	17.03	4.00	0.36	23.31	0.27	0.00	0.06	1.70

Conditions: 325°C, 300 psi, 6.56 h^{-1}, 1.00 g catalyst, 0.139 mL/min EtOH, 18.1 mL/min H_2, p_{EtOH}:p_{H2} = 4.

Table 7-10. Detailed product selectivity of 1.2CuMMO catalyst.

# C	Total	Alcohols			Aldehydes	Ketones	Ethers	Esters	Olefins	Aromatics	Paraffins	Hemiacetals and acetals
		Primary Linear	Primary Branched	Secondary								
1	1.63	1.58	0.00	0.00	0.00	0.00	0.00	0.00	0.00	0.00	0.06	0.00
2	4.86	0.00	0.00	0.00	4.75	0.00	0.00	0.00	0.05	0.00	0.06	0.00
3	9.93	0.00	0.00	2.57	0.00	6.81	0.00	0.52	0.02	0.00	0.01	0.00
4	64.55	23.79	0.00	1.24	3.30	3.32	1.03	30.34	0.14	0.00	0.03	1.36
5	3.36	0.00	0.00	0.09	2.00	1.09	0.00	0.16	0.02	0.00	0.00	0.00
6	11.66	1.42	0.47	0.00	0.21	0.09	0.00	9.44	0.01	0.00	0.01	0.00
7	0.96	0.00	0.00	0.16	0.00	0.80	0.00	0.00	0.00	0.00	0.00	0.00
8	1.67	0.12	0.00	0.04	0.26	0.00	0.00	1.24	0.00	0.00	0.00	0.00
9	0.10	0.00	0.00	0.10	0.00	0.00	0.00	0.00	0.00	0.00	0.00	0.00
10	0.16	0.00	0.00	0.00	0.00	0.00	0.00	0.16	0.00	0.00	0.00	0.00
11	0.00	0.00	0.00	0.00	0.00	0.00	0.00	0.00	0.00	0.00	0.00	0.00
12	0.00	0.00	0.00	0.00	0.00	0.00	0.00	0.00	0.00	0.00	0.00	0.00
13	0.00	0.00	0.00	0.00	0.00	0.00	0.00	0.00	0.00	0.00	0.00	0.00
14	0.00	0.00	0.00	0.00	0.00	0.00	0.00	0.00	0.00	0.00	0.00	0.00
Total	98.89	26.90	0.47	4.21	10.52	12.10	1.03	41.87	0.26	0.00	0.17	1.36

Conditions: 325°C, 300 psi, 6.56 h^{-1}, 1.00 g catalyst, 0.139 mL/min EtOH, 18.1 mL/min H_2, p_{EtOH}:p_{H2} = 4.

Table 7-11. Detailed product selectivity of 0.1CuMMO catalyst.

# C	Total	Alcohols			Aldehydes	Ketones	Ethers	Esters	Olefins	Aromatics	Paraffins	Hemiacetals and acetals
		Primary Linear	Primary Branched	Secondary								
1	0.91	0.89	0.00	0.00	0.00	0.00	0.00	0.00	0.00	0.00	0.02	0.00
2	5.85	0.00	0.00	0.00	5.80	0.00	0.00	0.00	0.04	0.00	0.02	0.00
3	2.15	0.00	0.00	0.46	0.00	1.64	0.00	0.03	0.01	0.00	0.00	0.00
4	62.77	43.41	0.00	0.45	6.83	1.11	0.16	8.70	0.20	0.00	0.01	1.89
5	2.63	0.00	0.00	0.00	2.24	0.37	0.00	0.00	0.01	0.00	0.00	0.00
6	17.51	7.43	2.14	0.00	1.58	0.00	0.10	6.24	0.01	0.00	0.00	0.00
7	0.54	0.00	0.00	0.15	0.00	0.39	0.00	0.00	0.00	0.00	0.00	0.00
8	4.48	1.22	0.52	0.06	0.41	0.00	0.00	2.26	0.00	0.00	0.00	0.00
9	0.19	0.00	0.00	0.19	0.00	0.00	0.00	0.00	0.00	0.00	0.00	0.00
10	1.25	0.27	0.19	0.00	0.00	0.00	0.00	0.79	0.00	0.00	0.00	0.00
11	0.05	0.00	0.00	0.00	0.00	0.05	0.00	0.00	0.00	0.00	0.00	0.00
12	0.27	0.05	0.02	0.00	0.00	0.00	0.00	0.20	0.00	0.00	0.00	0.00
13	0.00	0.00	0.00	0.00	0.00	0.00	0.00	0.00	0.00	0.00	0.00	0.00
14	0.00	0.00	0.00	0.00	0.00	0.00	0.00	0.00	0.00	0.00	0.00	0.00
Total	98.63	53.28	2.88	1.31	16.88	3.57	0.26	18.23	0.28	0.00	0.06	1.89

Conditions: 325°C, 300 psi, 6.56 h^{-1}, 1.00 g catalyst, 0.139 mL/min EtOH, 18.1 mL/min H_2, p_{EtOH}:p_{H2} = 4.

Table 7-12. Detailed product selectivity of 0.1CuMMO(pm) catalyst (1.2CuMMO diluted with 0CuMMO to to 0.1CuMMO nominal Cu wt%).

# C	Total	Alcohols			Aldehydes	Ketones	Ethers	Esters	Olefins	Aromatics	Paraffins	Hemiacetals and acetals
		Primary Linear	Primary Branched	Secondary								
1	0.23	0.22	0.00	0.00	0.00	0.00	0.00	0.00	0.00	0.00	0.02	0.00
2	6.17	0.00	0.00	0.00	6.15	0.00	0.00	0.00	0.02	0.00	0.01	0.00
3	1.10	0.00	0.00	0.11	0.00	0.93	0.00	0.04	0.01	0.00	0.00	0.00
4	55.29	43.02	0.00	0.15	6.47	0.37	0.14	3.10	0.21	0.00	0.00	1.83
5	3.05	0.00	0.00	0.00	2.78	0.15	0.00	0.03	0.09	0.00	0.00	0.00
6	18.98	10.50	2.74	0.00	2.72	0.00	0.00	3.01	0.01	0.00	0.00	0.00
7	0.72	0.00	0.00	0.20	0.00	0.52	0.00	0.00	0.00	0.00	0.00	0.00
8	7.05	2.96	1.29	0.00	1.00	0.00	0.00	1.40	0.07	0.20	0.00	0.14
9	0.55	0.00	0.00	0.26	0.00	0.00	0.00	0.00	0.00	0.28	0.00	0.00
10	2.73	1.04	0.76	0.00	0.00	0.00	0.00	0.90	0.00	0.00	0.00	0.02
11	0.12	0.00	0.00	0.00	0.00	0.12	0.00	0.00	0.00	0.00	0.00	0.00
12	1.48	0.45	0.07	0.00	0.00	0.09	0.00	0.83	0.00	0.00	0.00	0.04
13	0.17	0.00	0.00	0.00	0.00	0.17	0.00	0.00	0.00	0.00	0.00	0.00
14	0.03	0.00	0.00	0.00	0.00	0.00	0.00	0.03	0.00	0.00	0.00	0.00
Total	97.68	58.20	4.86	0.72	19.12	2.36	0.14	9.34	0.40	0.48	0.02	2.03

Conditions: 325°C, 300 psi, 6.56 h^{-1}, 1.00 g catalyst, 0.139 mL/min EtOH, 18.1 mL/min H_2, p_{EtOH}:p_{H2} = 4.

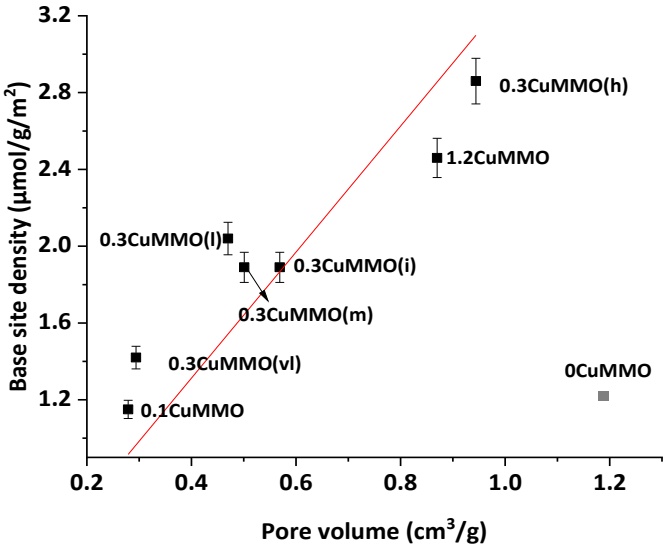

Figure 7-17. Base site density vs pore volume in Cu/Mg_XAlO_y catalysts. Red line is linear fit. Pearson's r = 0.9863, Adjusted R^2 = 0.9684.

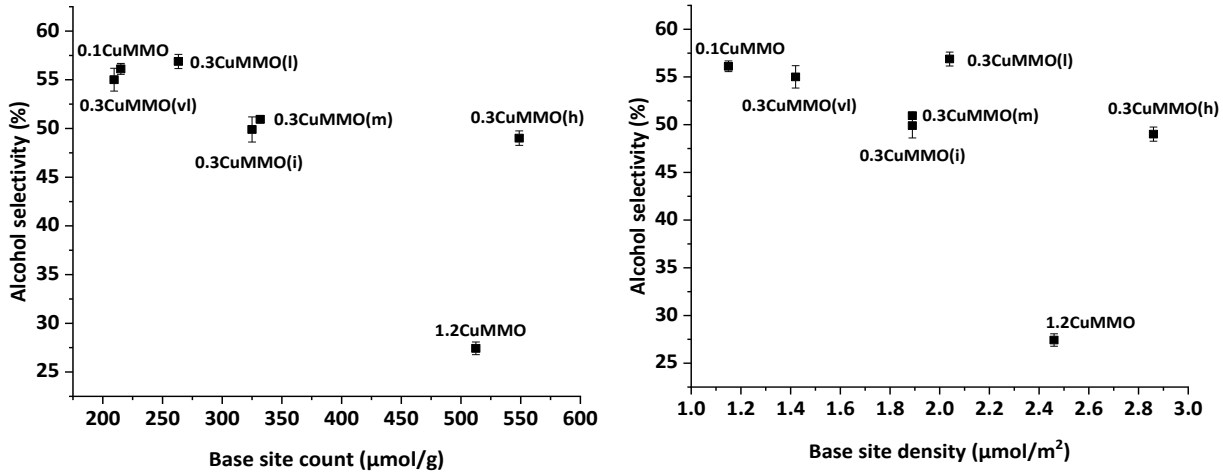

Figure 7-18. Alcohol selectivity vs base site counts (left) and density of base sites (right) in Cu/Mg_xAlO_y catalysts. Conditions as described in Table 7-4.

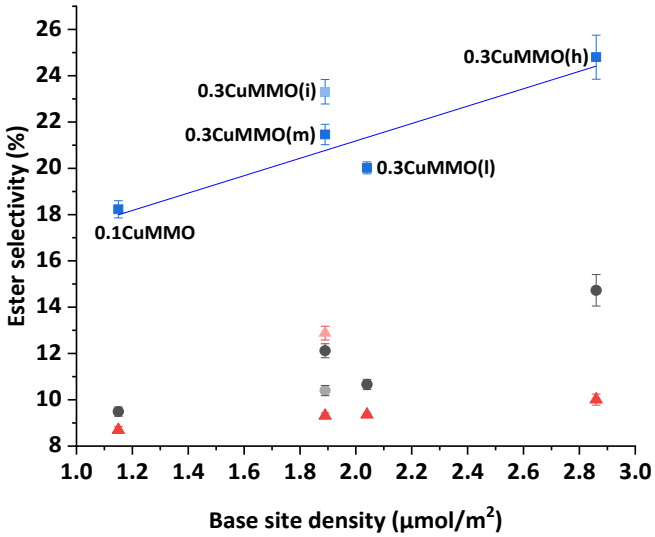

Figure 7-19. Total ester selectivity (■), C_{6+} ester selectivity (●) and ethyl acetate selectivity (▲) vs base site density in select low-loading (0.2-0.6 wt%Cu) CuMMO catalysts. Conditions as described in Table 7-4. Blue line is linear fit of total ester selectivity vs base site density excluding 0.3CuMMO(i) (shown in translucent colors). Pearson's r = 0.9467, Adjusted R^2 = 0.8444.

Table 7-13. 2104 cm^{-1} FTIR deconvoluted peak area from Gaussian function.

Catalyst	Area Peak 1
0.1CuMMO	1.22 ± 0.06
0.1CuMMO (pm)	0.73 ± 0.05
1.2CuMMO	3.35 ± 0.05

Peak 1 is the deconvoluted 2104 cm^{-1} peak from the rest of the peaks shown in Figure 4-5 for each catalysts using Gaussian function. Figure 7-20 show the deconvoluted peaks for each material.

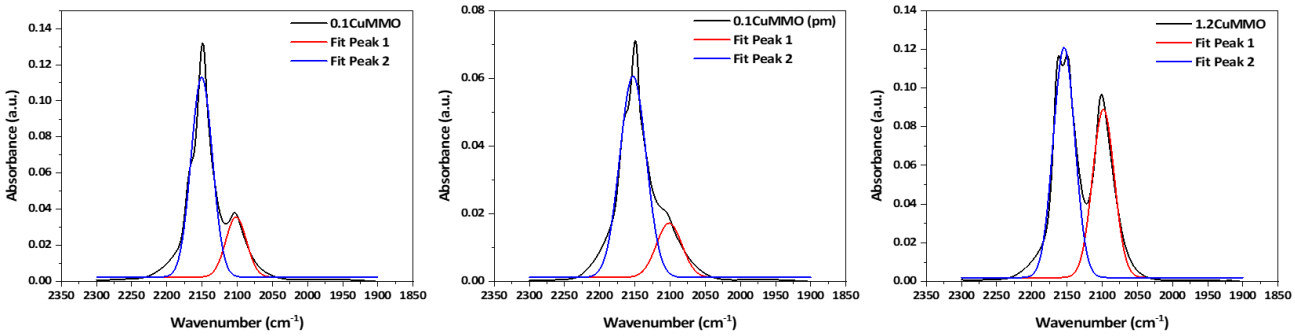

Figure 7-20. Deconvoluted 2104 cm^{-1} peak (peak 1) and 2150 + 2162 cm^{-1} peak (peak 2) for 0.1CuMMO (left), 0.1CuMMO(pm) (center) and 1.2CuMMO (right) catalysts.

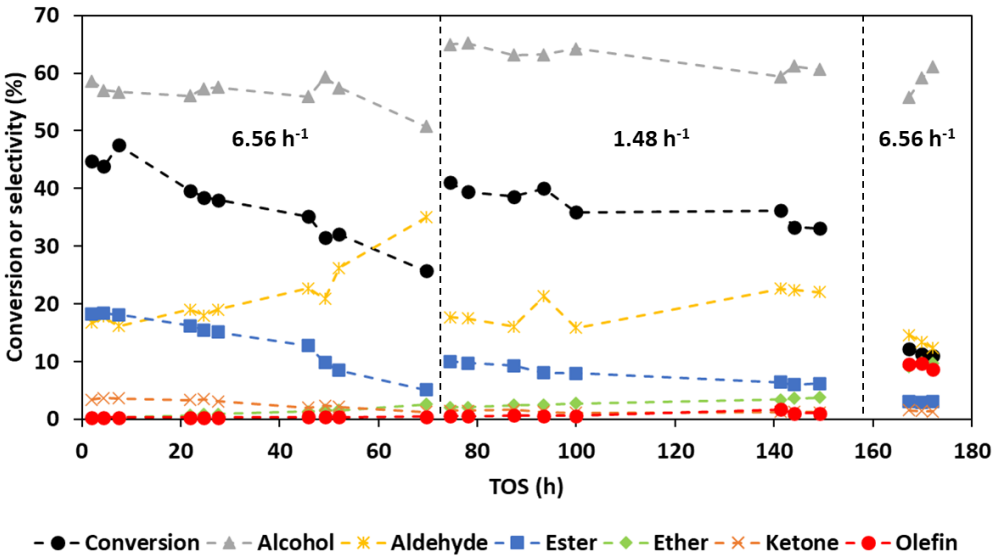

Figure 7-21. Conversion and selectivity of main species of ethanol oligomerization reaction using 0.1CuMMO. **Conditions:** 325°C, 300 psi, 1.00 g catalyst, p_{EtOH}:p_{H2} = 4.

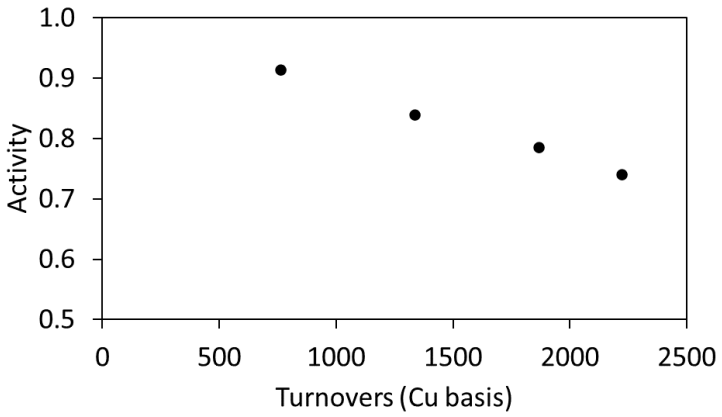

Figure 7-22. Activity vs turnover plot of 0.3CuMMO(vl) catalyst in conditions as defined in Table 7-4.

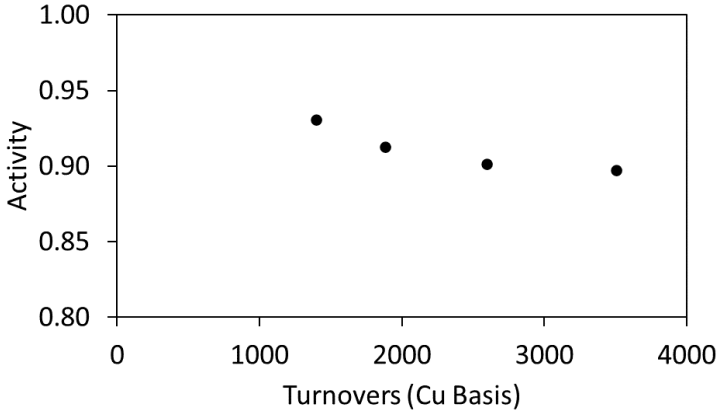

Figure 7-23. Activity vs turnover plot of 0.3CuMMO(l) catalyst in conditions as defined in Table 7-4.

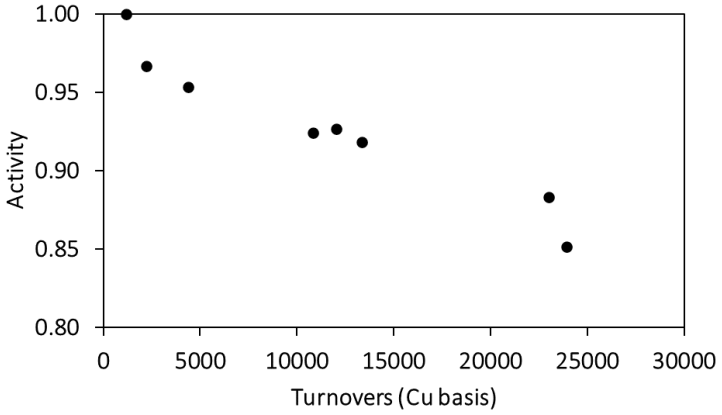

Figure 7-24. Activity vs turnover plot of 0.3CuMMO(m) catalyst in conditions as defined in Table 7-4.

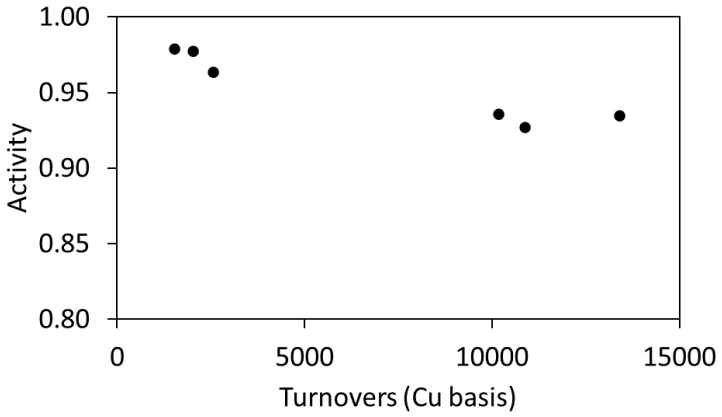

Figure 7-25. Activity vs turnover plot of 0.3CuMMO(h) catalyst in conditions as defined in Table 7-4.

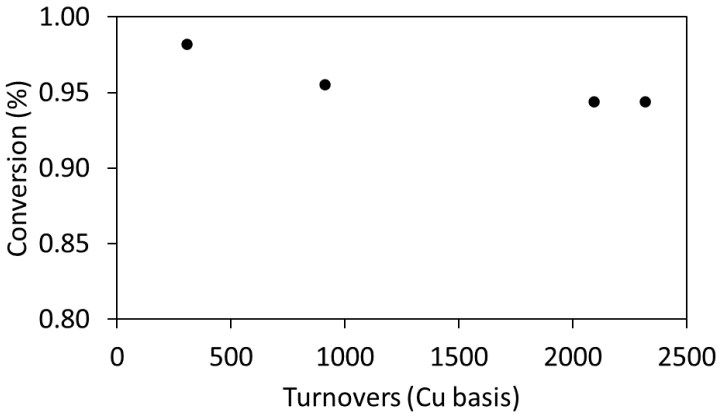

Figure 7-26. Activity vs turnover plot of 1.2CuMMO catalyst in conditions as defined in Table 7-4.

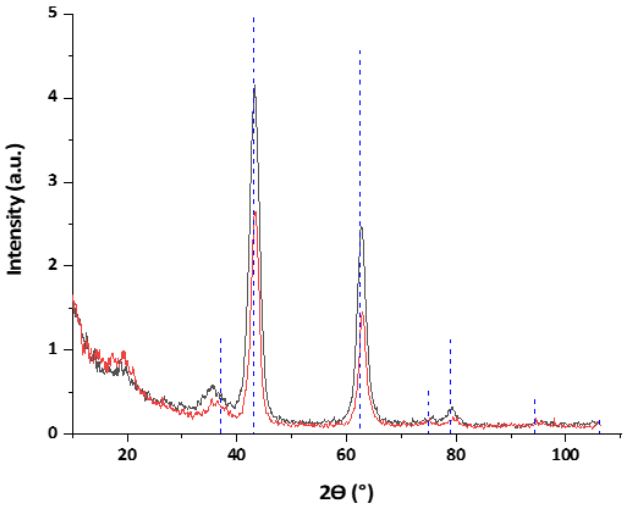

Figure 7-27. Powder XRD of fresh (black line) and spent (red line) calcined 0.3CuMMO(m). Blue dashed lines represent MgO periclase peaks (PDF # 04-002-3057). X-ray source used was Cu kα (λ = 1.54 Å).

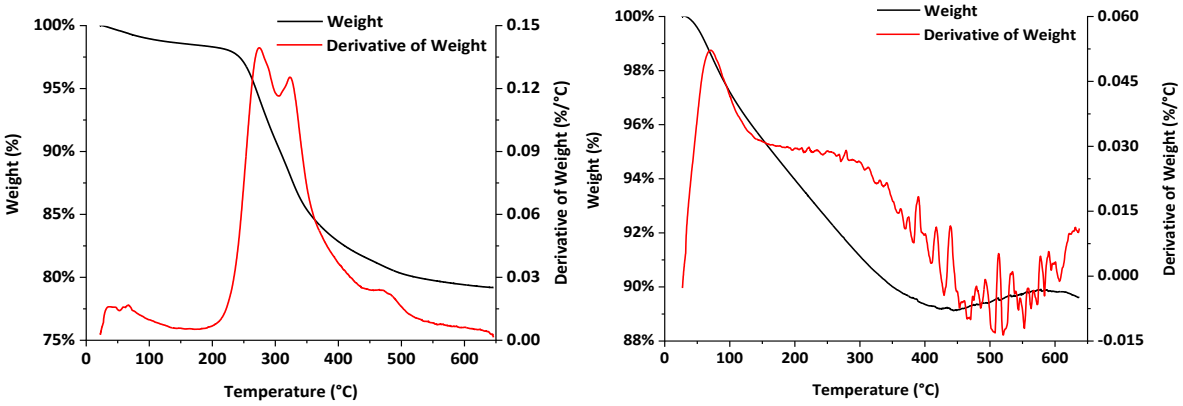

Figure 7-28. TGA of spent (left) and fresh calcined (right) 0.3CuMMO(m). **TGA conditions:** 25-650°C (10°C/min). 50mL/min O_2, 10-15 mg sample.

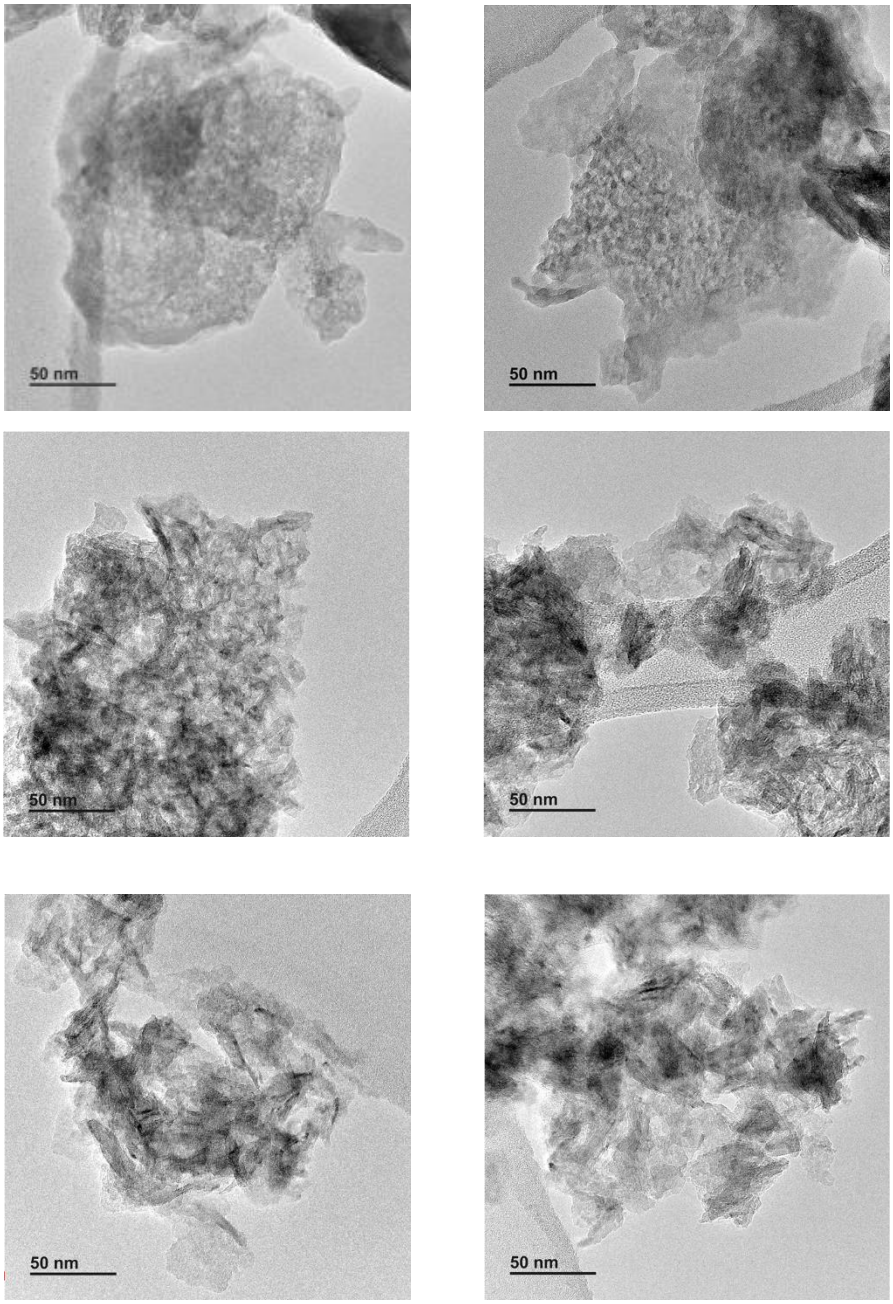

Figure 7-29. TEM micrographs of 0.3CuMMO(vl) (upper), 0.3CuMMO(l) (middle) and 0.3CuMMO(h)(lower). Micrographs to the left are of freshly calcined catalysts (600°C, 2h, 4°C/min, static air). Micrographs to the right are of reduced (50mL/min H_2, 325°C, 1.33h) then passivated (1% O_2/Ar pulses) catalysts.

7.5. Appendix for Chapter 5

Table 7-14. Contact times, conversion, C-balances and selectivities of general and specific species for tests conducted at different WHSV with 0.3wt%Cu/$Mg_{2.9}$AlO catalysts.

WHSV (h^{-1})	**328.75**	**52.70**	**26.20**	**13.22**	**6.56**	**1.33**	**0.73**
Contact time (s kg_{cat} mol^{-1})	**0.50**	**3.15**	**6.33**	**12.55**	**25.21**	**125.13**	**228.51**
Conversion (%)	**4.83**	**19.99**	**23.32**	**27.49**	**54.18**	**68.41**	**69.89**
C-balance (%)	101.9	99.9	97.0	96.1	97.5	89.8	87.3
Selectivities* (%)							
Alcohol	43.25	48.81	49.88	49.74	53.12	60.30	48.54
C_{4+} Alcohols	41.34	44.91	49.70	49.44	50.28	60.05	48.25
Primary linear alcohols	40.22	42.91	47.87	46.13	46.49	49.45	38.96
Primary branched alcohols	0.59	1.33	1.65	2.46	2.61	7.35	2.84
Secondary alcohols	0.53	0.68	0.19	0.85	1.18	3.25	2.84
Methanol	1.91	3.90	0.17	0.30	2.85	0.25	0.29
Olefin	0.22	0.43	0.17	0.25	0.42	0.59	0.25
Aldehyde	38.58	34.04	34.97	26.23	15.09	10.42	7.80
Acetaldehyde	29.75	27.39	24.99	17.66	3.75	2.60	0.76
C_{4+} Aldehydes	8.83	6.65	9.98	8.57	11.34	7.82	7.04
Ketone	6.96	2.11	2.31	3.19	3.74	4.78	13.21
Acetone	6.96	1.23	1.20	1.70	1.78	0.93	2.13
C_{4+} Ketones	0.00	0.88	1.11	1.50	1.97	3.85	11.08
Ester	3.63	7.26	8.50	12.38	21.50	19.60	26.94
Ethyl acetate	3.01	5.65	6.30	6.41	9.31	4.71	4.31
C_{6+} Esters	0.62	1.62	2.20	5.97	12.19	14.89	22.63
Ether	1.22	0.51	0.72	0.72	4.71	0.32	0.27
Paraffin	0.03	0.04	0.05	0.04	0.08	0.00	0.39
Hemiacetals and Acetals	3.76	4.84	3.10	3.20	0.97	1.31	0.68
1-ethoxyethanol	3.76	4.56	2.95	2.85	0.85	0.39	0.26
C_{6+} Acetals	0.00	0.29	0.16	0.35	0.13	0.92	0.42
Unidentified	328.75	52.70	26.20	13.22	6.56	1.33	0.73

*Selectivities of shaded general compound categories (e.g. alcohol, olefin, aldehyde, etc.) sum 100% across the column. Selectivities of specific categories add up to the general compound category (e.g. ethyl acetate + C_{6+} esters selectivities sum up to the total shown in Ester selectivity).

Table 7-15. Detailed average product selectivity of 328.75 h^{-1} test (12000 turnovers).

# C	Total	Alcohols			Aldehydes	Ketones	Ethers	Esters	Olefins	Paraffins	Hemiacetals and acetals
		Primary Linear	Primary Branched	Secondary							
1	1.93	1.91	0.00	0.00	0.00	0.00	0.00	0.00	0.00	0.02	0.00
2	29.85	0.00	0.00	0.00	29.75	0.00	0.00	0.00	0.10	0.01	0.00
3	7.49	0.00	0.00	0.53	0.00	6.96	0.00	0.00	0.00	0.00	0.00
4	52.38	36.13	0.00	0.00	8.21	0.00	1.22	3.01	0.05	0.00	3.76
5	0.07	0.00	0.00	0.00	0.00	0.00	0.00	0.00	0.07	0.00	0.00
6	5.64	3.82	0.59	0.00	0.62	0.00	0.00	0.62	0.00	0.00	0.00
7	0.00	0.00	0.00	0.00	0.00	0.00	0.00	0.00	0.00	0.00	0.00
8	0.28	0.28	0.00	0.00	0.00	0.00	0.00	0.00	0.00	0.00	0.00
9	0.00	0.00	0.00	0.00	0.00	0.00	0.00	0.00	0.00	0.00	0.00
10	0.00	0.00	0.00	0.00	0.00	0.00	0.00	0.00	0.00	0.00	0.00
11	0.00	0.00	0.00	0.00	0.00	0.00	0.00	0.00	0.00	0.00	0.00
12	0.00	0.00	0.00	0.00	0.00	0.00	0.00	0.00	0.00	0.00	0.00
13	0.00	0.00	0.00	0.00	0.00	0.00	0.00	0.00	0.00	0.00	0.00
14	0.00	0.00	0.00	0.00	0.00	0.00	0.00	0.00	0.00	0.00	0.00
Total	**97.65**	**42.14**	**0.59**	**0.53**	**38.58**	**6.96**	**1.22**	**3.63**	**0.22**	**0.03**	**3.76**

Conditions: 325°C, 300 psi, 50 mg catalyst, 0.350 mL/min EtOH, 45.0 mL/min H_2, p_{EtOH}:p_{H2} = 4.

Table 7-16. Detailed average product selectivity of 52.70 h^{-1} test (15000 turnovers).

# C	Total	Alcohols			Aldehydes	Ketones	Ethers	Esters	Olefins	Paraffins	Hemiacetals and acetals
		Primary Linear	Primary Branched	Secondary							
1	0.20	0.17	0.00	0.00	0.00	0.00	0.00	0.00	0.00	0.02	0.00
2	25.05	0.00	0.00	0.00	25.01	0.00	0.00	0.00	0.03	0.01	0.00
3	1.21	0.00	0.00	0.00	0.00	1.20	0.00	0.00	0.01	0.00	0.00
4	59.92	41.25	0.00	0.19	8.01	0.76	0.36	6.30	0.10	0.01	2.95
5	0.16	0.00	0.00	0.00	0.00	0.14	0.00	0.00	0.02	0.00	0.00
6	10.57	5.54	1.35	0.00	0.42	0.00	0.36	2.90	0.01	0.00	0.00
7	0.22	0.00	0.00	0.00	0.00	0.22	0.00	0.00	0.00	0.00	0.00
8	2.17	0.91	0.30	0.00	0.32	0.00	0.00	0.48	0.00	0.00	0.16
9	0.00	0.00	0.00	0.00	0.00	0.00	0.00	0.00	0.00	0.00	0.00
10	0.19	0.19	0.00	0.00	0.00	0.00	0.00	0.00	0.00	0.00	0.00
11	0.00	0.00	0.00	0.00	0.00	0.00	0.00	0.00	0.00	0.00	0.00
12	0.00	0.00	0.00	0.00	0.00	0.00	0.00	0.00	0.00	0.00	0.00
13	0.00	0.00	0.00	0.00	0.00	0.00	0.00	0.00	0.00	0.00	0.00
14	0.00	0.00	0.00	0.00	0.00	0.00	0.00	0.00	0.00	0.00	0.00
Total	**99.69**	**48.07**	**1.65**	**0.19**	**33.75**	**2.31**	**0.72**	**9.68**	**0.17**	**0.05**	**3.11**

Conditions: 325°C, 300 psi, 100 mg catalyst, 0.112 mL/min EtOH, 14.4 mL/min H_2, p_{EtOH}:p_{H2} = 4.

Table 7-17. Detailed average product selectivity of 26.20 h^{-1} test (4600 turnovers).

# C	Total	Alcohols			Aldehydes	Ketones	Ethers	Esters	Olefins	Paraffins	Hemiacetals and acetals
		Primary Linear	Primary Branched	Secondary							
1	0.16	0.14	0.00	0.00	0.00	0.00	0.00	0.00	0.00	0.03	0.00
2	24.19	0.00	0.00	0.00	24.14	0.00	0.00	0.00	0.03	0.01	0.00
3	1.23	0.00	0.00	0.00	0.00	1.22	0.00	0.00	0.01	0.00	0.00
4	60.09	43.01	0.00	0.31	6.68	0.50	0.40	6.24	0.09	0.01	2.85
5	0.11	0.00	0.00	0.00	0.00	0.09	0.00	0.00	0.02	0.00	0.00
6	10.37	5.48	1.34	0.00	0.28	0.00	0.41	2.85	0.01	0.00	0.00
7	0.14	0.00	0.00	0.00	0.00	0.14	0.00	0.00	0.00	0.00	0.00
8	2.14	0.89	0.28	0.00	0.27	0.00	0.00	0.47	0.00	0.00	0.23
9	1.13	0.00	0.00	0.00	0.00	0.00	0.00	0.00	0.00	0.00	1.13
10	0.18	0.18	0.00	0.00	0.00	0.00	0.00	0.00	0.00	0.00	0.00
11	0.00	0.00	0.00	0.00	0.00	0.00	0.00	0.00	0.00	0.00	0.00
12	0.00	0.00	0.00	0.00	0.00	0.00	0.00	0.00	0.00	0.00	0.00
13	0.00	0.00	0.00	0.00	0.00	0.00	0.00	0.00	0.00	0.00	0.00
14	0.00	0.00	0.00	0.00	0.00	0.00	0.00	0.00	0.00	0.00	0.00
Total	**99.74**	**49.70**	**1.62**	**0.31**	**31.37**	**1.96**	**0.81**	**9.57**	**0.16**	**0.05**	**4.21**

Conditions: 325°C, 300 psi, 100 mg catalyst, 0.056 mL/min EtOH, 7.2 mL/min H_2, p_{EtOH}:p_{H2} = 4.

Table 7-18. Detailed average product selectivity of 13.22 h^{-1} test (3000 turnovers).

# C	Total	Alcohols			Aldehydes	Ketones	Ethers	Esters	Olefins	Paraffins	Hemiacetals and acetals
		Primary Linear	Primary Branched	Secondary							
1	0.32	0.30	0.00	0.00	0.00	0.00	0.00	0.00	0.00	0.02	0.00
2	17.71	0.00	0.00	0.00	17.66	0.00	0.00	0.00	0.03	0.02	0.00
3	1.96	0.00	0.00	0.25	0.00	1.70	0.00	0.00	0.01	0.00	0.00
4	55.96	38.59	0.00	0.18	6.74	0.69	0.34	6.41	0.17	0.00	2.85
5	0.25	0.00	0.00	0.00	0.00	0.23	0.00	0.00	0.02	0.00	0.00
6	12.61	5.70	1.61	0.00	1.50	0.00	0.38	3.41	0.01	0.00	0.00
7	0.62	0.00	0.00	0.10	0.00	0.52	0.00	0.00	0.00	0.00	0.00
8	3.42	1.46	0.48	0.00	0.33	0.00	0.00	1.08	0.01	0.00	0.06
9	0.32	0.00	0.00	0.32	0.00	0.00	0.00	0.00	0.00	0.00	0.00
10	1.74	0.26	0.38	0.00	0.00	0.00	0.00	0.82	0.00	0.00	0.28
11	0.00	0.00	0.00	0.00	0.00	0.00	0.00	0.00	0.00	0.00	0.00
12	0.56	0.12	0.00	0.00	0.00	0.00	0.00	0.44	0.00	0.00	0.00
13	0.05	0.00	0.00	0.00	0.00	0.05	0.00	0.00	0.00	0.00	0.00
14	0.22	0.00	0.00	0.00	0.00	0.00	0.00	0.22	0.00	0.00	0.00
Total	**95.75**	**46.43**	**2.46**	**0.85**	**26.23**	**3.19**	**0.72**	**12.38**	**0.25**	**0.04**	**3.20**

Conditions: 325°C, 300 psi, 50 mg catalyst, 0.028 mL/min EtOH, 3.6 mL/min H_2, p_{EtOH}:p_{H2} = 4.

Table 7-19. Detailed average product selectivity of 6.56 h^{-1} test (4000 turnovers).

# C	Total	Alcohols			Aldehydes	Ketones	Ethers	Esters	Olefins	Paraffins	Hemiacetals and acetals
		Primary Linear	Primary Branched	Secondary							
1	2.88	2.85	0.00	0.00	0.00	0.00	0.00	0.00	0.00	0.03	0.00
2	8.36	0.00	0.00	0.00	3.75	0.00	4.56	0.00	0.02	0.03	0.00
3	2.24	0.00	0.00	0.42	0.00	1.78	0.00	0.03	0.02	0.00	0.00
4	58.64	38.33	0.00	0.23	8.72	0.83	0.15	9.31	0.20	0.02	0.85
5	0.49	0.00	0.00	0.00	0.00	0.36	0.00	0.00	0.13	0.00	0.00
6	18.29	6.57	1.88	0.00	2.16	0.00	0.00	7.65	0.04	0.00	0.00
7	0.92	0.00	0.00	0.28	0.00	0.64	0.00	0.00	0.00	0.00	0.00
8	5.39	1.25	0.53	0.05	0.46	0.00	0.00	3.10	0.01	0.00	0.00
9	0.21	0.00	0.00	0.21	0.00	0.00	0.00	0.00	0.00	0.00	0.00
10	1.48	0.27	0.24	0.00	0.00	0.00	0.00	0.97	0.00	0.00	0.00
11	0.08	0.00	0.00	0.00	0.00	0.08	0.00	0.00	0.00	0.00	0.00
12	0.52	0.07	0.00	0.00	0.00	0.02	0.00	0.30	0.00	0.00	0.13
13	0.04	0.00	0.00	0.00	0.00	0.04	0.00	0.00	0.00	0.00	0.00
14	0.11	0.00	0.00	0.00	0.00	0.00	0.00	0.11	0.00	0.00	0.00
Total	**99.64**	**49.34**	**2.64**	**1.18**	**15.09**	**3.74**	**4.71**	**21.46**	**0.42**	**0.08**	**0.97**

Conditions: 325°C, 300 psi, 1000 mg catalyst, 0.139 mL/min EtOH, 18.1 mL/min H_2, p_{EtOH}:p_{H2} = 4.

Table 7-20. Detailed average product selectivity of 1.33 h^{-1} test (1000 turnovers).

# C	Total	Alcohols			Aldehydes	Ketones	Ethers	Esters	Olefins	Paraffins	Hemiacetals and acetals
		Primary Linear	Primary Branched	Secondary							
1	0.28	0.25	0.00	0.00	0.00	0.00	0.00	0.00	0.00	0.03	0.00
2	1.22	0.00	0.00	0.00	1.21	0.00	0.00	0.00	0.00	0.01	0.00
3	1.42	0.00	0.00	0.21	0.00	0.94	0.00	0.15	0.02	0.11	0.00
4	43.15	32.89	0.00	1.55	5.17	0.00	0.71	2.68	0.02	0.00	0.12
5	2.22	0.00	0.00	0.25	0.16	1.21	0.00	0.00	0.44	0.16	0.00
6	23.50	11.03	3.74	0.15	2.60	0.04	0.03	5.63	0.07	0.00	0.20
7	1.23	0.00	0.00	0.25	0.00	0.93	0.00	0.05	0.00	0.00	0.00
8	11.96	3.72	1.77	0.28	1.04	0.00	0.00	4.71	0.04	0.00	0.39
9	0.97	0.00	0.00	0.56	0.00	0.41	0.00	0.00	0.00	0.00	0.00
10	5.71	1.16	0.99	0.00	0.24	0.00	0.00	2.95	0.00	0.00	0.37
11	0.44	0.00	0.00	0.00	0.00	0.44	0.00	0.00	0.00	0.00	0.00
12	3.31	0.50	0.74	0.00	0.00	0.00	0.00	1.84	0.00	0.00	0.23
13	0.49	0.00	0.00	0.00	0.00	0.49	0.00	0.00	0.00	0.00	0.00
14	1.56	0.16	0.10	0.00	0.00	0.00	0.00	1.31	0.00	0.00	0.00
15	0.33	0.00	0.00	0.00	0.00	0.33	0.00	0.00	0.00	0.00	0.00
16	0.27	0.00	0.00	0.00	0.00	0.00	0.00	0.27	0.00	0.00	0.00
17	0.00	0.00	0.00	0.00	0.00	0.00	0.00	0.00	0.00	0.00	0.00
Total	**98.06**	**49.70**	**7.35**	**3.25**	**10.42**	**4.78**	**0.74**	**19.60**	**0.59**	**0.32**	**1.31**

Conditions: 325°C, 300 psi, 1500 mg catalyst, 0.042 mL/min EtOH, 5.4 mL/min H_2, p_{EtOH}:p_{H2} = 4.

Table 7-21. Detailed average product selectivity of 0.73 h^{-1} test (1250 turnovers).

# C	Total	Alcohols			Aldehydes	Ketones	Ethers	Esters	Olefins	Paraffins	Hemiacetals and acetals
		Primary Linear	Primary Branched	Secondary							
1	0.40	0.29	0.00	0.00	0.00	0.00	0.00	0.00	0.00	0.11	0.00
2	0.92	0.00	0.00	0.00	0.89	0.00	0.00	0.00	0.00	0.03	0.00
3	2.69	0.00	0.00	0.64	0.00	1.77	0.00	0.18	0.04	0.06	0.00
4	35.42	26.90	0.00	0.25	4.09	0.23	0.27	3.35	0.19	0.01	0.12
5	4.49	0.00	0.00	0.86	0.12	3.32	0.00	0.00	0.01	0.19	0.00
6	22.50	8.15	3.58	0.31	1.84	0.13	0.00	8.39	0.01	0.00	0.09
7	3.53	0.00	0.00	0.50	0.00	2.89	0.00	0.14	0.00	0.00	0.00
8	12.32	2.44	1.55	0.07	0.76	0.14	0.00	7.20	0.00	0.00	0.16
9	2.33	0.00	0.00	0.20	0.00	2.13	0.00	0.00	0.00	0.00	0.00
10	6.28	0.79	0.80	0.00	0.13	0.00	0.00	4.30	0.00	0.00	0.26
11	1.11	0.00	0.00	0.00	0.00	1.11	0.00	0.00	0.00	0.00	0.00
12	3.04	0.29	0.60	0.00	0.00	0.00	0.00	2.09	0.00	0.00	0.05
13	0.85	0.00	0.00	0.00	0.00	0.85	0.00	0.00	0.00	0.00	0.00
14	1.36	0.09	0.21	0.00	0.00	0.00	0.00	1.06	0.00	0.00	0.00
15	0.47	0.00	0.00	0.00	0.00	0.47	0.00	0.00	0.00	0.00	0.00
16	0.22	0.00	0.00	0.00	0.00	0.00	0.00	0.22	0.00	0.00	0.00
17	0.18	0.00	0.00	0.00	0.00	0.18	0.00	0.00	0.00	0.00	0.00
Total	**98.11**	**38.96**	**6.74**	**2.84**	**7.83**	**13.21**	**0.27**	**26.93**	**0.25**	**0.39**	**0.68**

Conditions: 325°C, 300 psi, 1500 mg catalyst, 0.023 mL/min EtOH, 2.96 mL/min H_2, p_{EtOH}:p_{H2} = 4.

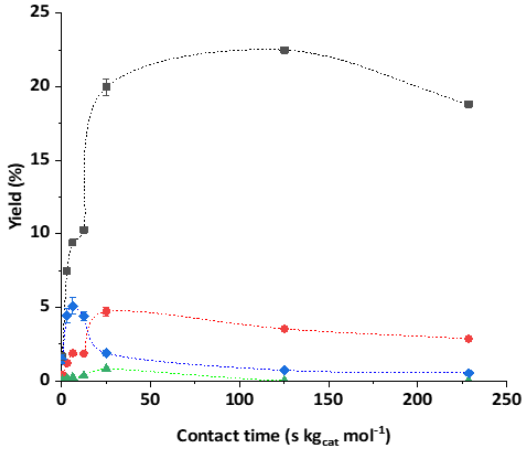

Figure 7-30. Yield vs contact time plots for 1-butanol (■), acetaldehyde (◆), butyraldehyde (●) and crotyl alcohols (▲). Conditions as described in Table 7-14 and 7-15 – 7-21.

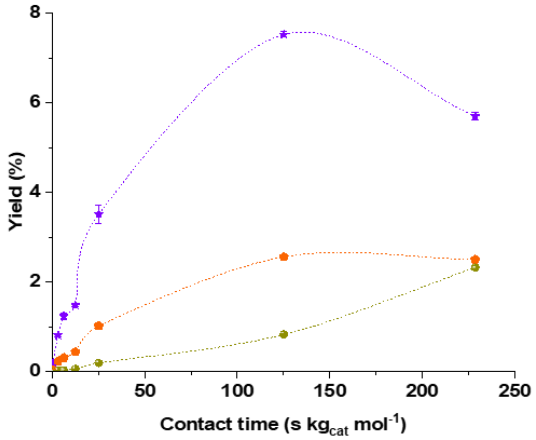

Figure 7-31. Yield vs contact time plots for 1-hexanol (★), 2-ethyl-1-butanol (⬟), and 2-pentanone (●). Conditions as described in Table 7-14 and 7-15 – 7-21.

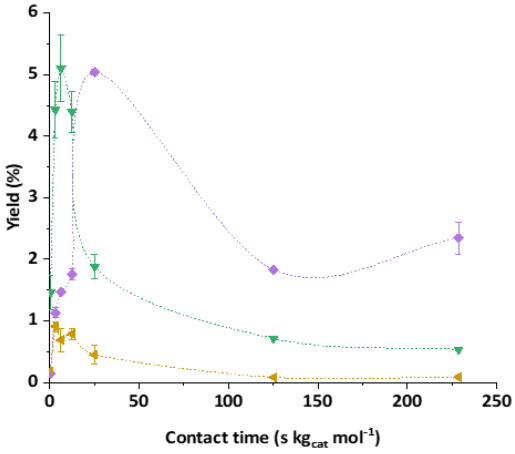

Figure 7-32. Yield vs contact time plots for acetaldehyde (▼), ethyl acetate (◆) and 1-ethoxyethanol (◀). Conditions as described in Table 7-14 and 7-15 – 7-21.

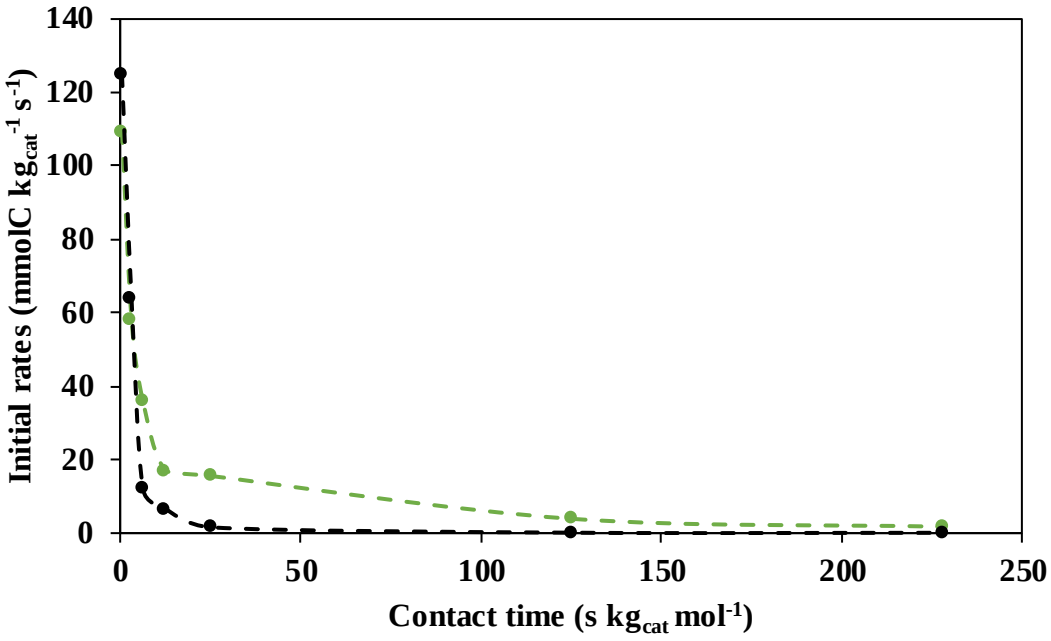

Figure 7-33. Initial rate vs contact time plot for 1-butanol (green) and acetaldehyde (black). Conditions as described in Tables 7-14 and 7-15 – 7-21 depending on the contact time.

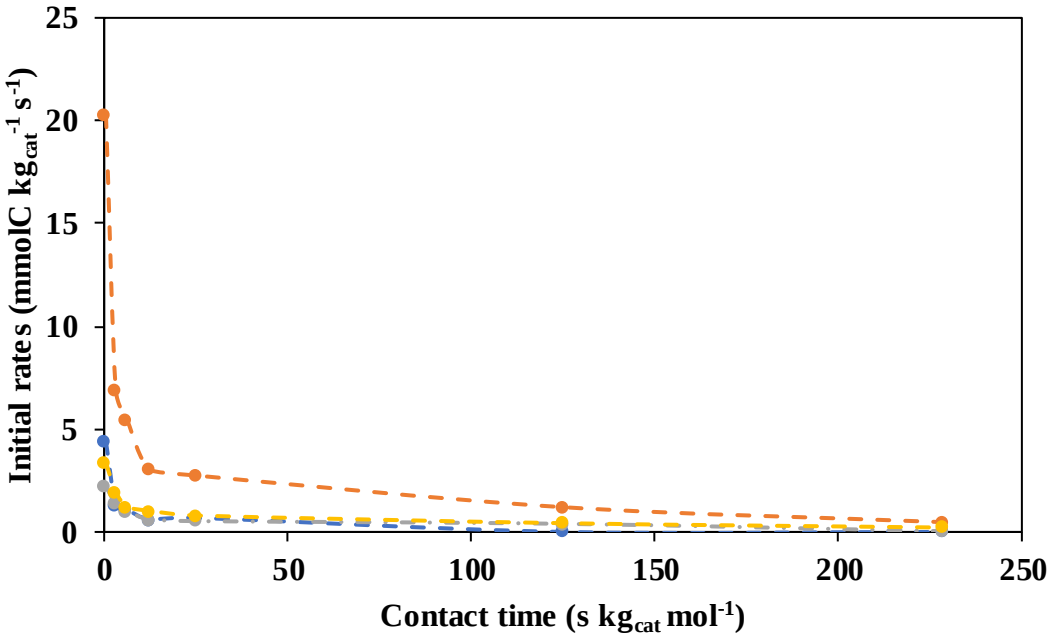

Figure 7-34. Initial rate vs contact time plot for crotyl alcohols (blue), 1-hexanol (orange), 1-octanol (gray), and 2-ethyl-1-butanol (yellow). Conditions as described in Tables 7-14 and 7-15 – 7-21 depending on the contact time.

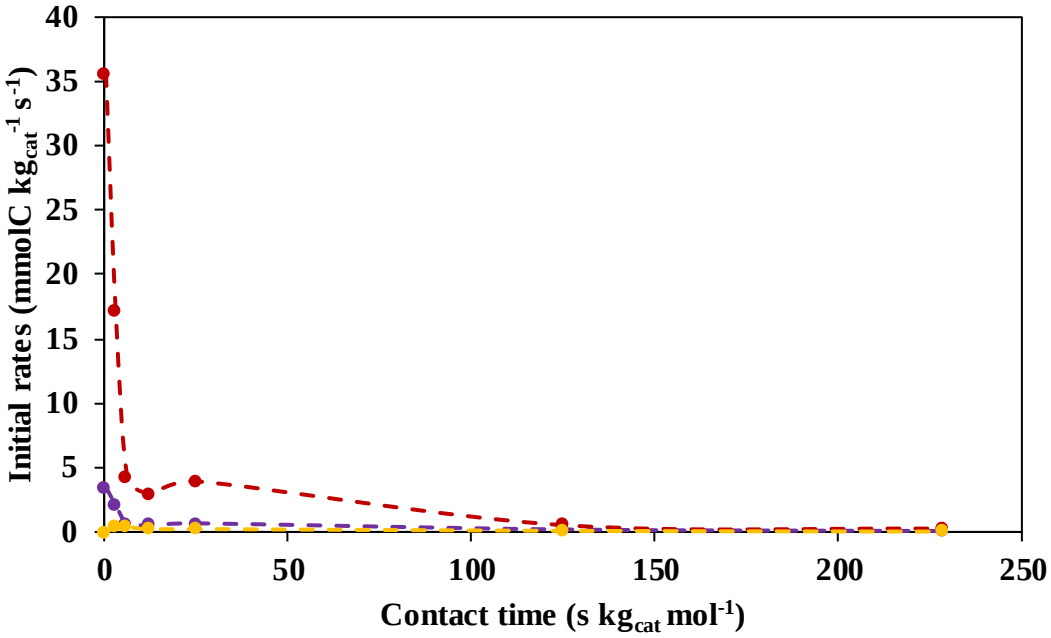

Figure 7-35. Initial rate vs contact time plot for butyraldehyde (red), hexanal (purple), and 2-ethylbutanal (yellow). Conditions as described in Tables 7-14 and 7-15 – 7-21 depending on the contact time.

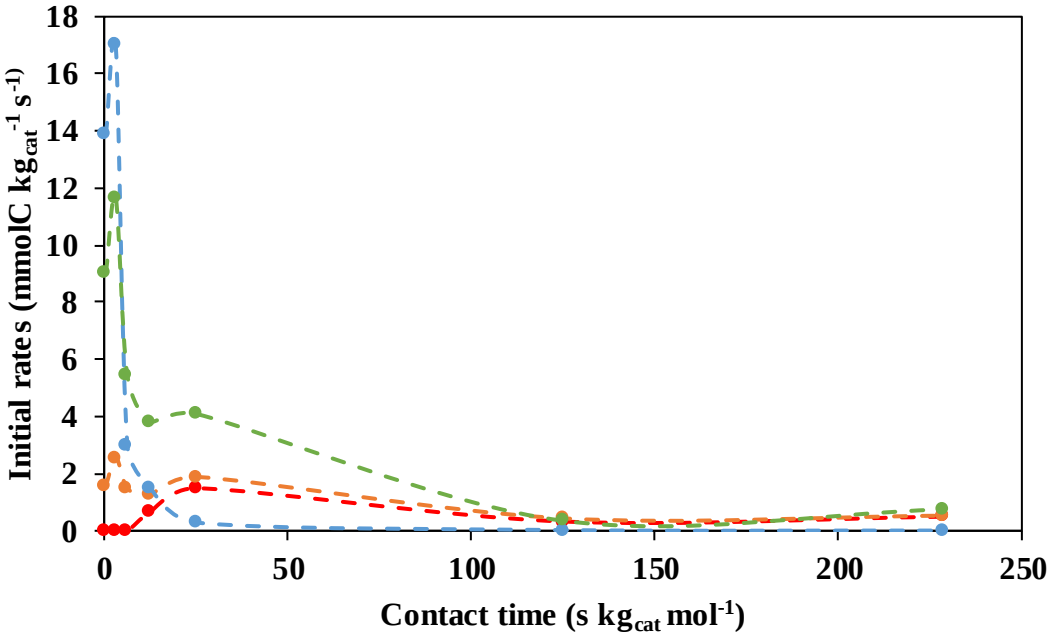

Figure 7-36. Initial rate vs contact time plot for 1-ethoxyethanol (blue), ethyl acetate (green), ethyl butyrate (orange), and butyl acetate (red). Conditions as described in Tables 7-14 and 7-15 – 7-21 depending on the contact time.

Table 7-22. Conversion, outlet partial pressures of relevant species and pressure ratio of ratios for 11mol% acetaldehyde cofeed to ethanol experiment compared to ethanol-only experiment. **Conditions:** 325°C, 300 psig total, P_{EtOH}:P_{H2} = 1, $WHSV_{EtOH}$ = 26.23 – 26.79 h^{-1}. N-hexane is added as an inert species to substitute progressively with acetaldehyde while maintaining ethanol partial pressure constant.

Acetaldehyde molar fraction	0.00	0.13
Conversion (%)	22.79	10.24
Outlet partial pressures (kPa)		
1-butanol	49.91	40.10
crotyl alcohols	1.25	2.42
2-ethyl-1-butanol	1.33	0.77
1-hexanol	5.07	3.68
butyraldehyde	8.63	22.67
2-ethylbutanal	0.41	0.49
hexanal	1.09	2.08
1-ethoxyethanol	2.51	5.75
ethyl acetate	5.32	7.16
Pressure Ratios		
$\frac{\left(\frac{p_{Ethanol}}{p_{Acetaldehyde}}\right)_{exp}}{\left(\frac{p_{Ethanol}}{p_{Acetaldehyde}}\right)_{eq}}$	9.92	3.42
$\frac{\left(\frac{p_{1-Butanol}}{p_{Butyraldehyde}}\right)_{exp}}{\left(\frac{p_{1-Butanol}}{p_{Butyraldehyde}}\right)_{eq}}$	0.94	0.29
$\frac{\left(\frac{p_{1-Hexanol}}{p_{Hexanal}}\right)_{exp}}{\left(\frac{p_{1-Hexanol}}{p_{Hexanal}}\right)_{eq}}$	1.05	0.41

7.6. References

(1) Krishna, S. H.; De bruyn, M.; Schmidt, Z. R.; Weckhuysen, B. M.; Dumesic, J. A.; Huber, G. W. Catalytic Production of Hexane-1,2,5,6-Tetrol from Bio-Renewable Levoglucosanol in Water: Effect of Metal and Acid Sites on (Stereo)-Selectivity. *Green Chem.* **2018**, *20* (19), 4557–4565. https://doi.org/10.1039/C8GC02455C.

(2) He, J.; Burt, S. P.; Ball, M.; Zhao, D.; Hermans, I.; Dumesic, J. A.; Huber, G. W. Synthesis of 1,6-Hexanediol from Cellulose Derived Tetrahydrofuran-Dimethanol with Pt-WO_x/TiO_2 Catalysts. *ACS Catal.* **2018**, *8* (2), 1427–1439. https://doi.org/10.1021/acscatal.7b03593.

(3) He, J.; Burt, S. P.; Ball, M. R.; Hermans, I.; Dumesic, J. A.; Huber, G. W. Catalytic C-O Bond Hydrogenolysis of Tetrahydrofuran-Dimethanol over Metal Supported WOx/TiO2 Catalysts. *Applied Catalysis B: Environmental* **2019**, *258*, 117945. https://doi.org/10.1016/j.apcatb.2019.117945.

(4) Chia, M.; O'Neill, B. J.; Alamillo, R.; Dietrich, P. J.; Ribeiro, F. H.; Miller, J. T.; Dumesic, J. A. Bimetallic RhRe/C Catalysts for the Production of Biomass-Derived Chemicals. *Journal of Catalysis* **2013**, *308*, 226–236. https://doi.org/10.1016/j.jcat.2013.08.008.